UNIVERSITY OF SOUTHAMPTON

Effect of Electrohydrodynamics on Thermal Dissipation for High Voltage Thermosyphons

by

Sijun Wu

A thesis submitted for the
degree of Doctor of Philosophy

in the
Faculty of Physical Science and Engineering
School of Electronics and Computer Science

August 2018

Research Thesis: Declaration of Authorship

Print name:	Sijun Wu
Title of thesis:	Effect of Electrohydrodynamics on Thermal Dissipation for High Voltage Thermosyphons

I declare that this thesis and the work presented in it are my own and has been generated by me as the result of my own original research.

I confirm that:

1. This work was done wholly or mainly while in candidature for a research degree at this University;
2. Where any part of this thesis has previously been submitted for a degree or any other qualification at this University or any other institution, this has been clearly stated;
3. Where I have consulted the published work of others, this is always clearly attributed;
4. Where I have quoted from the work of others, the source is always given. With the exception of such quotations, this thesis is entirely my own work;
5. I have acknowledged all main sources of help;
6. Where the thesis is based on work done by myself jointly with others, I have made clear exactly what was done by others and what I have contributed myself;
7. Parts of this work have been published as shown in Appendix

Signature: Date: 01/10/2018

UNIVERSITY OF SOUTHAMPTON

ABSTRACT

FACULTY OF PHYSICAL SCIENCES AND ENGINEERING

School of Electronics and Computer Science

Doctor of Philosophy

Effect of Electrohydrodynamics on Thermal Dissipation for High Voltage Thermosyphons

by Sijun Wu

Thermosyphon is a two-phase cooling approach that utilises coolant phase change to dissipate thermal energy. Selecting a suitable coolant is important to the thermosyphon design. In recent years, there has been considerable interest in selecting low global warming potential coolants to replace Hydrofluorocarbons (HFCs) and Perfluorocarbons (PFCs). Thermal properties of Hydrofluoroethers (HFE) and Fluorinated ketone (FK) are similar to HFCs, whilst they have low global warming potential (GWP). Consequently, they are considered as alternative fluids for the thermosyphon.

In order to improve overall high voltage plant efficiency, there is an increased use of thermosyphon technology to provide temperature control, replacing conventional pumps, fans and radiators. This two-phase cooling approach is not widely applied to high voltage devices due to the additional challenges that arise from electrical insulation and the introducing of electrohydrodynamics (EHD). The insulation design requires cooling fluid to have sufficient dielectric strength to avoid any electrical breakdown. Due to the presence of the electric field, electrohydrodynamics phenomena effect on thermal bubbles that further leads to the changing of the two-phase boiling behaviours and thermal dissipation. Hence, understanding of coolant dielectric behaviour and the EHD effect on boiling phenomena is integral to the development of an optimum thermosyphon design.

In this work, the AC and DC dielectric properties of HFE and FK have been characterised by dielectric spectroscopy, DC conductivity and AC breakdown measurements at different temperatures. Furthermore, in order to investigate the EHD effect on thermal bubble motion, a numerical approach has been developed by conducting force analysis upon a bubble within different electric fields, which is created by various electrode arrangements. Obtained results give predictions of the bubble trajectories for different applied fields. The pool boiling performances of both fluids are first outlined by showing the boiling curves. The effects of a DC field on the FK boiling heat transfer enhancement including bubble behaviour have been conducted under saturated temperatures.

The obtained data from this work is applicable to the design of HV thermosyphon for assessing both coolant dielectric behaviours and EHD heat transfer enhancements.

Acknowledgement

The completion of this work was associated with many great bits of help and friendship during my PhD career. It is not only the technical advice but also the mental support. In the last three years, I am very happy to work with my colleagues and friends in Southampton. Meanwhile, they lead me to become a better person.

First of all, I am very grateful to my main supervisor, Prof Paul Lewin, for his consistent help and patience. Most importantly, he taught me how to think and trained me to become a good researcher. Second, I would like to thank my secondary supervisor Dr Richard Chippendale. He guaranteed the correct path during my research. I still remember he spent the whole morning with me to correct my first deliverable. He helped me to find the correct pace of my PhD study and coffee drinking. My gratitude goes to our Friday burger team, which including Dr Matthew Praeger, Dr Thomas Andritsch and Mr Neil Palmer, they not only guide me to the pub but also provide many good ideas and suggestions for my research. I am indebted to Mr Mark Long, Mr Charlie Reed and Mr Brian Rogers for their technical assistance in equipment manufacture, without them the apparatus still stay at the blueprint stage. I also wish to express my thanks to all my colleagues and all my friends at the Tony Davies High Voltage Laboratory (TDHVL), who involved in my colourful life.

In addition, during my research, I have been consistently encouraged by my friend and Family. I am profoundly grateful for the love of my father and mother, thank for their understanding and support throughout the 6 years of study in the UK.

At last, I would like to say thank you to Dr Jaroslav and Dr Lilian Kaufmann who from ABB Switzerland corporate research. They linked my research outcomes with the industrial desires and their project gave the financial support for my PhD research.

Table of Contents

Table of Figures

Nomenclature

Symbol	Meaning	Unit
$\overrightarrow{\dot{y}_I}$	Initial velocity in the y-direction	m s^{-1}
$\vec{F}_{E(gradient\ force)}$	Electric gradient force	N
$\overrightarrow{F_B}$	Buoyancy force	N
$\overrightarrow{F_{Dx}}$	Drag force in the x-direction	N
$\overrightarrow{F_{Dy}}$	Drag force in the y-direction	N
$\overrightarrow{F_{EHD}}$	EHD force	N
$\vec{\dot{x}}$	Bubble velocity towards the grounded plate	m s^{-1}
$\vec{\ddot{x}}$	Acceleration Of The Bubble In the x-direction	m s^{-2}
$\vec{\dot{y}}$	Bubble vertical velocity	m s^{-1}
$\vec{\ddot{y}}$	Acceleration Of The Bubble In the y-direction	m s^{-2}
$A_{boiling}$	Boiling surface area	m^{-2}
C_0	Vacuum capacitance	F
C_k	Tuning Parameter	0.03m s^{-1}
C_p	Material-specific heat capacitance	J kg^{-1}K^{-1}
C_x	Capacitance of sample	F
E_0	Uniform electric field strength away from the bubble	V m^{-1}
E_A	Activation energy	J mol^{-1}
E_{vt}	The tangential electric field strength	V m^{-1}
M_{eff}	The effective mass of a spherical bubble in motion	kg
N_0	Avogadro's number	6.022×10^{23}mol^{-1}
Q_{heater}	Heater input power	W
Q_E	Transported charge	C
R_b	Bubble radius	m
R_{gas}	Molecular gas constant	8.314 J mol^{-1} K^{-1}
R_r	The radius of the rod electrode	m
S_e	The separation between the two electrodes	m
S_{wire}	Area of the wire surface	m^2
T_{amb}	Ambient temperature	K
T_{sat}	Coolant saturation temperature	K
T_w	Wall temperature of the boiling surface	K
V_{fg}	Volume function of gas	NA
V_{fl}	Volume function of liquid	NA
f_e	Force on bubble	N

f_{sn}	Normal electric stress	N m^{-2}
f_{st}	Tangential electric stress	N m^{-2}
k_B	Boltzmann constant	1.38×10^{-23}m^{2}kg s^{-2}K^{-1}
k_{cell}	Constant value for the test cell	1.241
l_c	Length of electrode	m
l_{gap}	The gap between the two electrodes	m
$\dot{m}$	Rate of vaporisation	Kg s^{-1}
p_o	Atmospheric pressure	101,325 Pa
q''	Heat flux on the wire	kW m^{-2}
q_0	Inward heat flux	W m^{-2}
q_b	Charge magnitude on the thermal bubble	C
q_s	Surface charge density	C m^{-2}
q_v	Volume charge density	C m^{-3}
r_a	The outer radius of the cylindrical test cell	m
r_b	The inner radius of the cylindrical test cell	m
t_c	Characteristic dynamical time	s
$t_{transient}$	Transient time of conductivity	s
$\vec{v}$	Liquid substantive acceleration	m s^{-2}
v_D	Charge drift velocity	m s^{-1}
x_{BD}	Cumulative probability of breakdown	
x_i	The bubble position	m
α_{BD}	Scale parameter of breakdown Weibull plot	NA
α_m	Molecular polarizability	NA
β_{BD}	Shape parameter of breakdown Weibull plot	NA
δ_s	Smoothed representation	NA
ε'	Relative permittivity	NA
ε''	The imaginary part of complex permittivity	NA
ε_0	Vacuum dielectric permittivity	F m^{-1}
ε_{air}	The dielectric constant of air	≈ 1
ε_{int}	Interface thickness	m
ε_l	Dielectric permittivity of liquid	F m^{-1}
$\varepsilon_{surface}$	Surface emissivity	NA
ε_v	Dielectric permittivity of gas	F m^{-1}
η_∞	The initial value of liquid viscosity	m^{2}s^{-1}
η_l	Coolant dynamic viscosity	m^{2}s^{-1}
λ_c	Mixing energy density	NA
λ_d	Critical wavelength	m

μ^*	Dipole moment	NA
ρ_g	Gas/bubble density	kg m^{-3}
ρ_l	Coolant density	kg m^{-3}
σ_E	Electrical conductivity	S m^{-1}
σ_o	Initial electrical conductivity	S m^{-1}
Δt_c	Collision time	s
ΔT_{unit}	Temperature gradient per unit length	K m^{-1}
ΔT	Superheated temperature	K
h	Effective transfer coefficient	W m^{-1}K^{-1}
$R(T_{amb})$	Wire resistance at ambient temperature	Ω
$R(T)$	The real-time resistance of the wire	Ω
A	Liquid cross-section	m^2
D	Electric displacement	FV m^{-2}
E	Electric field magnitude	V m^{-1}
F	Extra force	N
G	Chemical potential	NA
H	Heaviside step function	NA
I	Current	A
J	Current density	A m^{-2}
M	Molar mass	kg mol^{-1}
N	Thermal dissipation factor	NA
P	The pressure of the local fluid	Pa
Q	Heatsink	J
T	Real-time temperature	K
V	Voltage	V
b	Charge average mobility	NA
c	Charge concentration	NA
g	Gravitational acceleration	9.8 m s^{-2}
k	Thermal conductivity	W m^{-1}K^{-1}
l	The distance between the rod and the plate	m
q	Heat flux	W m^{-2}
Ψ	Equation governing parameter	NA
α	Nickel wire resistance coefficient	0.0056 K^{-1}
γ	Mobility tuning parameter	m^3 s kg^{-1}
δ	Vapour thickness	m
ε	Dielectric permittivity	F m^{-1}
η	Liquid viscosity	PI
λ	Latent heat of vaporization	J kg^{-1}

μ	Ion mobility	m^{2}s^{-1}V^{-1}
ρ	Density of material	kg m^{-3}
σ_l	Coolant surface tension	N m^{-1}
τ	Relaxation time	s
ϖ	Angular frequency	rad s^{-1}

Abbreviations

CFCs	Chlorofluorocarbon
CHF	Critical heat flux
EHD	Electrohydrodynamics
FDS	Frequency dielectric spectroscopy
FEA	Finite element analysis
FK	Fluorinated ketone
GCB	Generator circuit breaker
GWP	Global warming potential
HCFCs	Hydrochlorofluorocarbon
HFC- 134a	1,1,1,2- tetrafluoroethane
HFC-125	Pentafluoroethane
HFCs	Hydrofluorocarbons
HFE	Hydrofluoroethers
HFE-143a	Trifluoromethoxymethane
HIS	High-speed image system
HVDC	High voltage direct current
MHF	Minimum heat flux
MSDS	Material safety data sheets
ODE	Ordinary differential equation
ONB	Onset of nucleate boiling
PDE	Partial differential equations
Peek	Polyetheretherketone
PFCs	Perfluorocarbons
PID	Proportional integral differential
PTFE	Polytetrafluoroethylene
SF6	Sulphur hexafluoride
TCU	Transformer control unit
TDHVL	Tony davies high voltage laboratory
UV/Vis	Ultraviolet-visible spectroscopy

Chapter 1

Introduction

A journey to a thousand miles begins with a single step - Lao Tzu

Since the first power station was established in 1882 in London, electricity has become an integral part of our life and modern digital economy. Since 1890, the first high voltage grid was built, high voltage technologies have been introducing into the research field that aims to not only understand high voltage phenomena but also, more importantly, to assist the design of high voltage devices. For high voltage design, reliability is always the priority aim. In addition, in the last several decades, with the development of electronics and control units, cost efficiency drives the miniaturization and integration of high voltage devices has led to lower material, transportation and installation costs.

1.1 History of the Generator Circuit Breaker

The main aim of all power companies is to achieve the highest plant availability whilst having the lowest possible cost. The method to connect the high voltage grid and the power supply to auxiliaries affects the power plant availability significantly. There are two methods of connecting a generator to the high voltage transmission grid. The first approach named unit connection, whereby the generator and low voltage terminals of the main transformer form one unit. Another method is to use a generator circuit breaker (GCB). Compared with the unit connection structure, GCBs layout not only simplifies power operational procedures but also improves protection of both generator and unit transformers. Meanwhile, GCBs increase the power plant availability [1]. Due to the above advantages, increasing numbers of power plant, especially pumped storage power plants, have chosen GCBs, which significantly reduces both time and expense for erection and commissioning.

Generator circuit breakers, operating as high voltage switches, are required to control the power grid by switching lines on and off under manual or automatic supervision. When GCB switches a line on, it should synchronise the generator with the main grid and carry the load. Meanwhile, when GCB detects an unexpected overcurrent or fault power phase angle, it is required to isolate the generator and grid in a short time. Hence, GCB is an economical and efficient solution for protecting generators and transformers [2]. Since the first GCB was installed in a power station in America 1970s for a medium voltage application, GCB technology has made great developments. Particular attention has focused on arc extinguishing medium applied when the breaker disconnects the generator from the circuit [3]. From these studies, sulphur hexafluoride (SF_6) gas has been successfully applied to GCBs due to its outstanding performance on extinguishing arcs and reliability. With the achievement of the advanced arc-extinguishing medium, modern SF_6 GCBs have achieved 57,000 A rated current (2000 MW generating units) and 210,000 A fault current [1]. Furthermore, with the developing scale of renewable energy such as offshore wind farms, high voltage direct current (HVDC) power transmission has gained great attention due to its advantage of long-distance transmission. Hence, manufacturers are focusing on designing HVDC GCBs, which are located in between the voltage source converter and the power grid. Today the HVDC GCBs are available up to 5000 A rated current according to 2500 MW generating units [4].

1.2 Thermal Issues and Thermosyphon Concept

The higher current rating means that GCB can potentially connect to a larger power-rating generator. Hence, the current rating is an important parameter when the power plant assesses and selects GCBs. Thermal issues restrict the increase of the GCBs current rating. It is because both normal and surge currents generate considerable heat due to resistive losses. The overheat may lead to a thermal failure of GCB internal components. To guarantee GCBs have a high reliability and a long service life, the standard IEC 62271 has defined the operating temperature limitations of GCBs that according to different contact materials as detailed in Table 1-1.

Table 1-1 Temperature limits of generator circuit breaker [5]

	Temperature Limits °C Above a 40°C Ambient			
	IEC 62271		**IEEE C37**	
Description	**Air**	**SF_6**	**Air**	**SF_6**
Bare-copper contacts	75	105	70	90
Silver-coated contacts	105	105	105	105
Bare-copper connections	90	115	70	100
Silver-plated connections	115	115	105	115
Tin-plated connections	105	105	105	105
Bare-copper to silver-plate	115	—	70	—
Normally touched parts	70	—	50	—
Not normally touched parts	80	—	70	—

For increasing the current rating of GCBs, either the power losses have to be minimized or the thermal dissipation must be intensified. Considerable research has previously focused on minimising the electrical resistance through novel materials [6]. While the research is processing steadily, the majority of solutions are applying the various cooling devices on the GCBs, to keep the operating temperature below the limit. Fans and pumps have been widely equipped on the GCBs but it has several undesirable factors, such as operating noise and extra energy consumption. To avoid these defects, manufacturers desire to apply the thermosyphon concept to GCBs. Thermosyphon is a wickless heat pipe that utilizes the latent heat of evaporation to dissipate thermal energy with a very small temperature gradient. Hence, thermosyphon is a simple but effective thermal transfer device. Since thermosyphons have high thermal dissipation efficiency and reliability, they have been used in many different applications, which includes heat exchangers, de-icing roads and turbine blade cooling etc. [7], [8]. However, the thermosyphon concept is not widely applied to high voltage devices yet. This is because of the additional challenges arise from the electrical insulation of these devices and the introducing of electrohydrodynamic phenomena.

1.3 Research Motivation

To design a reliable HV thermosyphon for GCBs applications, dielectric performance is the most important consideration. Insulation defects such as partial discharge or breakdown can either degrade the service life or directly cause internal components failure of GCBs. The failure of GCBs further results in significant economic losses to the power plant.

The dielectric design of HV thermosyphon should not only withstand the normal operating voltage but also even higher voltages, for example, those introduced by fault impulses. The technologic demand requires that coolant have sufficient dielectric strength as well as solid insulators. Lack of information of candidate coolants motivates the researcher to investigate coolants' thermal, dielectric and environmental properties. A good compromise has to be made between these properties while selecting the candidate coolants. Understanding the candidate coolants dielectric properties forms the first aim of this research. This information can help manufacturers to have a reliable design without having any insulation failure.

Thermosyphon thermal exchange is attributed to the latent heat of evaporation, which means the phase change has to occur in the HV thermosyphon. Many publications have reported the thermally induced bubbles, in the two-phase material, cause insulation failure when they form a gas column [9]–[12]. Understanding the gas-liquid failure mechanism motivates the studies to explore the coolant bubble motion under different electric fields.

Finally, since the aim of HV thermosyphon is to dissipate heat, the heat transfer characteristics of coolant is another important aspect. After selecting the candidate coolants, it is necessary to characterise their boiling behaviours, which can explain the heat transfer performance directly. Furthermore, due to the presence of an electric field, heat transfer is expected to be affected by electrohydrodynamics (EHD). The exact contribution of EHD on boiling heat transfer of candidate coolants are not well understood and so it motivates the experimental evaluation.

1.4 Contributions

In answering the research motivation, this thesis makes three significant contributions to assist coolant selection and optimization design for future HV thermosyphon applications.

The limitation given by the Kyoto protocol leads to a keen desire to phase out hydrofluorocarbons in HV thermosyphon. After reviewing and comparing the thermal and environmental factors, two new coolants i.e. Hydrofluoroethers (HFE) and Fluorinated ketone (FK) have been selected as the potential coolants for the future thermosyphon applications. The most important contribution of this thesis is to determine both HFE and FK boiling curves. The experiments were conducted on a flat boiling surface configuration, which is more relevant to the industrial application, such as chips or evaporators. Hence, these valuable results have made a great contribution to the two- phase heat transfer technology. Furthermore, the boiling curves for FK material have been obtained with different magnitude of DC electric fields, and the field effects have been analysed and discussed. The results show that EHD could promote thermal dissipation in a thermosyphon and encourage its use in high voltage practical devices.

In addition, the dielectric characteristics of HFE and FK, including AC dielectric spectroscopy, DC conductivity, AC breakdown and repeated breakdown effects, have been determined. These valuable data assist manufacturers to evaluate dielectric loss and control the maximum electric field. Hence, it is a significant contribution to the dielectric design of HV thermosyphon. Furthermore, this data also provides information for the apparatus design in the future.

Last, based on the literature review, gas pockets in the HV device may cause electrical insulation failure. Understanding the bubble trajectories at different electric fields helps to locate gas pockets. This thesis has developed a numerical model to predicted FK thermal bubble trajectories under different electric fields. The theoretical results are compared with experimental observations. The results have shown a good agreement. Hence, this study gives an applicable method to predict potential bubble location in the thermosyphon.

1.5 Thesis Structure

This chapter has outlined the introduction of the generator circuit breaker and novel thermosyphon concept. In order to increase thermal dissipation efficiency, manufacturers aim to equip thermosyphon on the generator circuit breaker. To assist design a reliable HV thermosyphon and understanding the coolant different behaviours under electric field form the great research motivations and corresponding research outcomes.

Chapter 2 aims to provide the research background that guides the future direction of this study. After reviewing the variety of coolant properties, HFE and FK coolants are selected as the research materials. Furthermore, the key findings of the boiling curves and corresponding experimental design have been critically reviewed. At last, a comprehensive review of the literature on thermal transfer enhancements has been undertaken.

Chapter 3 introduces the experimental approaches to investigate the dielectric properties of both candidates coolants. By comparing different standards and experiment methodologies, the appropriate methods were selected for measuring dielectric spectroscopy, DC conductivity and AC dielectric strength at different temperature conditions.

Chapter 4 introduces a numerical prediction on bubble trajectory under different electric fields. Meanwhile, two experimental platforms were designed and manufactured with the aim to validate the theoretical analysis.

Chapter 5 presents a series of experimental investigations into the effects of different electric fields on the two-phase heat transfer of candidate coolants. A novel electrode system has been designed and manufactured. To validate and assist the design, an FEA thermal model has been developed. The boiling curves of both HFE and FK coolants have been obtained. Furthermore, the EHD effect on onset nucleate boiling, nucleate heat transfer and critical heat flux of FK coolant have been in-depth analysed.

Chapter 6 presents a numerical method for simulating bubble production, which can provide both thermal and two-phase flow information during the boiling phenomena. An experimental apparatus, which is identical with the model geometry, has been manufactured with the aim to validate numerical results.

Chapter 7 summarises the research findings, contributions and raises the potential investigations that could be developed from this study.

Chapter 2

A Review of Thermosyphon and Boiling Phenomena

I do not care that they stole my idea. I care that they do not have any of their own. - Nikola Tesla

This chapter contains an introduction to thermosyphon technology and boiling phenomena. Coolant is the operating media in the thermosyphon and variety of coolants have different boiling behaviours. In order to select a suitable coolant for HV thermosyphon applications, the thermal, dielectric and environmental parameters of candidate coolants have been investigated and compared.

Hydrofluoroethers (HFE) and Fluorinated Ketone (FK) have been considered as materials to be used instead of chlorofluorocarbon (CFCs) and hydrochlorofluorocarbon (HCFCs). A comparison of these two candidate coolants demonstrates that they provide good thermal properties whilst being environmentally friendly. The boiling phenomena of typical coolants are introduced in detail and the boiling curves of both HFE and FK have been reviewed. Finally, heat transfer enhancing strategies are discussed.

2.1 Thermosyphon Technology

Power devices are following the trend of becoming smaller and durable, while at the same time incorporating a higher energy load. This developing tendency raises thermal issues. This is because in most cases, the high-energy load and large heat flux are concomitant. Hence, this thermal issue promotes the development of cooling devices.

The cooling devices that apply to power equipment are categorized as “active” or “passive”. The active cooling device involves external energy to dissipate heat flux, such as fans or pumps, which shown in Figure 2.1i. In contrast, the passive cooling device utilises gravity or imbalanced pressure as the driving force. A typical passive cooling device named thermosyphon, shown in Figure 2.1ii, has been applied to electronics in order to provide a better thermal energy control [13]–[16]. Nowadays, this technique is attracting the attention of manufacturers, who are attempting to apply this device to HV equipment, such as generator circuit breakers (GCBs), to assist with cooling [17].

i ii

Figure 2.1 Cooling device category; i. active cooling device for a transformer, ii. Passive cooling device for generator circuit breakers

There are advantages to using thermosyphon technology. The thermosyphon requires minimum maintenance and is quieter than active cooling devices due to its unique structure and working principle. Moving parts do not exist in the thermosyphon; instead, an evaporator, transport pipe and condenser are the three main components. The cross-section structure and two-phase boiling cycle of the thermosyphon are shown in Figure 2.2. To allow for an efficient heat transfer, the evaporator must be in good thermal contact with the heat source and the condenser has to be located in the cooler ambient. Thermal dissipation is attributed to the two-phase boiling cycle. Thermal energy is absorbed during the phase change process due to the latent heat of evaporation. The hot vapour then moves to the condenser by a pressure gradient and buoyancy forces. Subsequently, vapour reaches the condenser and releases heat to ambient through condensation. The condensate fluid which flows back to the evaporator, relies on gravity, and starts the next heat dispatching cycle and dissipates thermal energy continually.

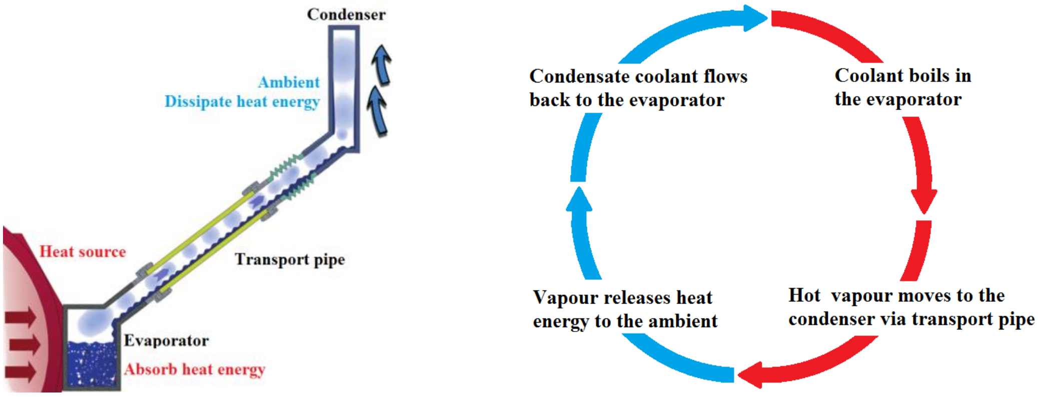

Figure 2.2 Thermosyphon cross-section and two-phase boiling circle

2.1.1 Thermal Transfer Advantages

It has been reported that the following advantage on the thermosyphon thermal transfer aspect. Peterson et al. experimentally investigated the efficiency of a thermosyphon and compared it to simple metal cooling fins [18]. The results, plotted in Figure 2.3, showed that compared to thermally conductive metal, thermosyphon can dissipate thermal energy with a smaller temperature gradient. Hence, it can be concluded that thermosyphons have higher effective thermal conductivity than thermal conductive solid materials. This conclusion can be proved by Fourier's law i.e.

$$\vec{q} = -k\Delta T_{unit} \tag{2.1}$$

where q is the heat flux, ΔT_{unit} is the temperature gradient per unit length and k is the effective thermal conductivity. Thus, given that q is constant and ΔT_{unit} is lower for a thermosyphon, it must have larger effective thermal conductivity than a metallic cooling fin.

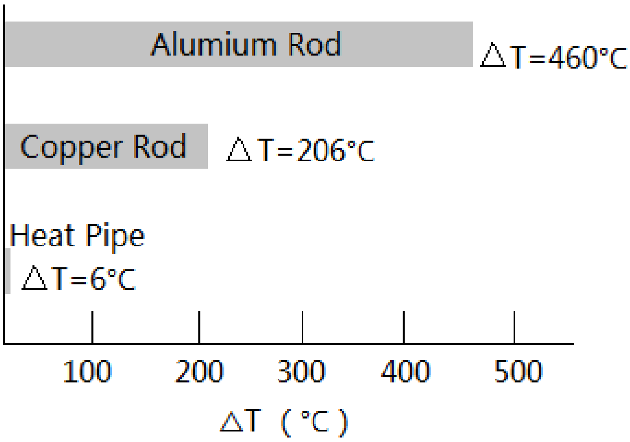

Figure 2.3 Temperature gradient of different materials after dissipating 20 W thermal energy

2.1.2 Operating Limitations

In practice, five operating limitations affect the application of thermosyphon technology.

Vapour pressure limit:

This limit links to the thermosyphon lowest operating temperature. In general, a lower operating temperature results in a greater value of coolant viscosity. When the viscous force of the coolant is stronger than the thermal pressure gradients, a viscous limitation occurs. The reason for this is that the high viscosity fluid resists vapour formation and therefore reduces heat dissipation. This limitation can be minimised to a certain extent by heating up the coolant. This limit needs to be taken into account when utilising thermosyphon technology in very cold climates such as northern Canada and Russia.

Dry out limit:

This limit links to the thermosyphon highest operating temperature. When an excessive heat flux is applied to the evaporator, all the coolant may turn into the gas phase in a short time. Therefore, no coolant remains in the evaporator to drive the boiling cycle. This situation is defined as the dry out limit. To avoid this occurring, the coolant filling ratio needs to be monitored and different corresponding filling ratios should be defined for different circumstances.

Sonic limit:

This limit is viewed as the upper bound of the heat transport capacity. With the increasing heat flux, the vapour velocity reaches the speed of sound and forms a shock wave at the outlet of the evaporator. This shock wave decreases condenser pressure significantly and decreases the thermal dissipation efficiency of the heat transfer boiling cycle.

Boiling limit:

This limit happens under high heat fluxes in the evaporator section. When the high heat fluxes are applied to the evaporator, the coolant nucleate boiling turns into film boiling. Film boiling results in the production of an unstable vapour film, which covers the evaporator surface and reduces the evaporation heat transfer coefficient.

Counter-current flow limit:

This limitation occurs under high axial heat flux. The high heat flux leads to an excessive velocity vapour flow, which interacts with the counter-current condensate flow. Consequently, this limit slows down the boiling cycle and reduces the maximum heat transfer.

In summary, thermosyphon performance relies on the two-phase boiling cycle. Five limits of thermosyphons can be avoided by either modifying the thermosyphon design or varying the heat flux input. Coolant properties also dominate the thermosyphon working performance and therefore the choice of coolant is discussed in greater detail in the following section.

2.2 Coolant Selection

To select an ideal coolant for thermosyphon applications, several main aspects should be considered. They are coolants' operating temperature range, thermal properties, dielectric properties, environmental properties, stability, flammability and toxicity.

In the real world, a perfect material does not exist. Therefore, during selection, there has to be some compromises. In this study, the first four key parameters listed above are primarily considered.

2.2.1 Operating Temperature Range

The theoretical operating temperature range for a thermosyphon application is from the coolant triple point to critical temperature. Figure 2.4 illustrates four distinct temperature windows for commercial coolants. They are the cryogenic temperature (< 150 K), low temperature (150 K to 300 K), intermediate temperature (300 K to 1000 K) and high temperature (1000 K to 3000 K) windows. Peterson has shown the typical operating temperature of electrical device is from 250 to 375K [18], which is covered by the low temperature and intermediate temperature coolants. The most common coolants for these two groups are ammonia, acetone and fluorides such as CFCs and HCFCs.

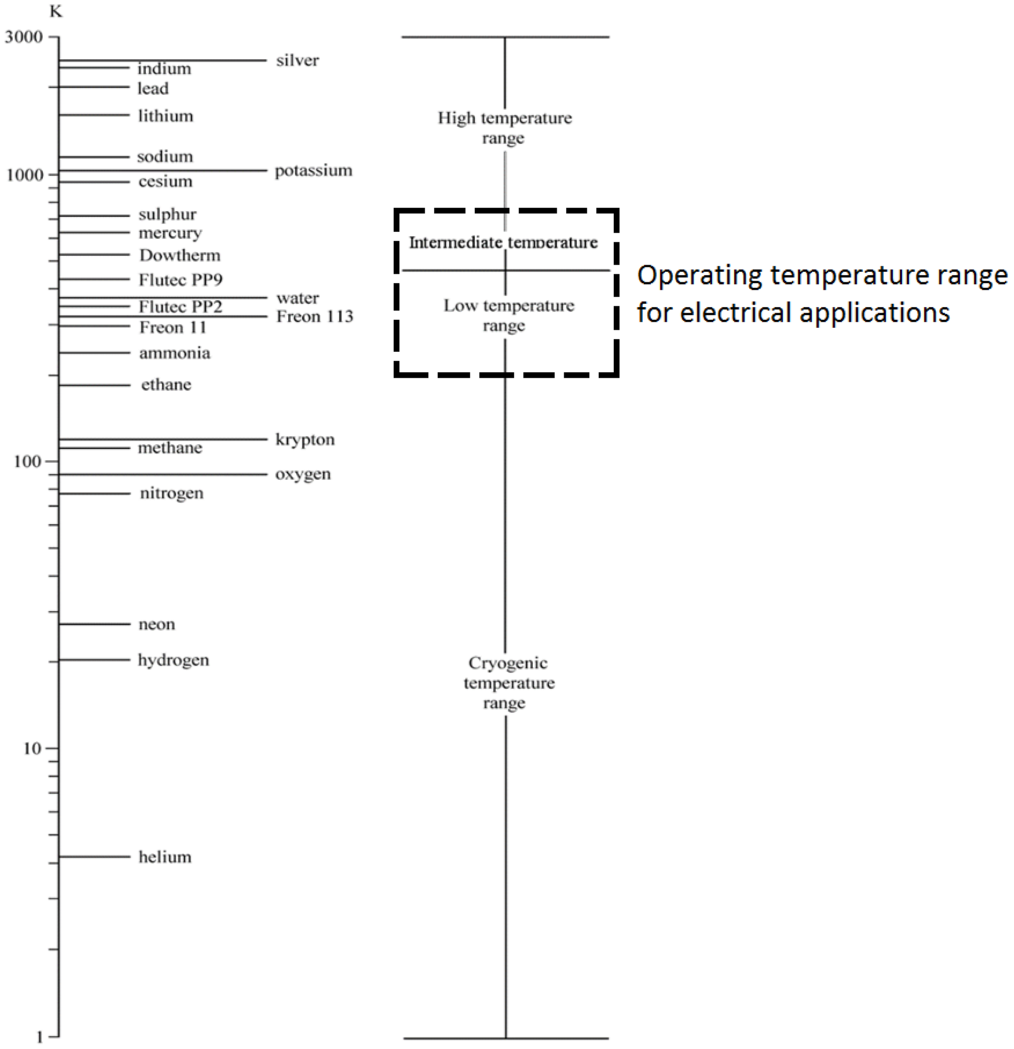

Figure 2.4 Operating temperature ranges of various coolants [19]

2.2.2 Thermal Properties

Coolant thermal transfer is attributed to two-phase boiling transfer. Instead of thermal conduction in the solid material, thermal convection and phase change absorption dominates heat transfer in coolants. In order to quantify the thermal convection and phase change contributions on the thermal transfer in a two-phase material, a parameter named thermal dissipation factor, *N*, is defined as [20]:

$$N = \frac{\rho_l \sigma_l \lambda}{\eta_l} \tag{2.2}$$

where ρ_l is the coolant density, σ_l is the coolant surface tension, λ is the latent heat of vaporization and η_l is the coolant dynamic viscosity. A high value of thermal dissipation factor indicates a greater permissible heat flux can be removed for the heat source by two- phase heat transfer. From 2.2, ρ_l, σ_l and λ need to be high whereas η_l needs to be low to ensure greater turbulence and larger thermal conductive flow.

2.2.3 Electrical Properties

In HV applications, the coolant electrical properties are as important as their thermal performance. This is because in most cases the coolant in HV devices is not only the heat transfer media but also has to provide electrical insulation. The HV thermosyphon also belongs to this case. Since the condenser is usually mounted on the grounding case, the HV thermosyphon is likely to bridge a high electric field. In order to avoid any undesired insulation failures, a candidate coolant must have good dielectric behaviour and be capable of withstanding high electrical stress. Specifically, relative permittivity [21], [22], AC dissipation factor [23], DC conductivity [24] and breakdown strength [25]–[27] are the four key parameters that are used to evaluate coolant dielectric properties.

2.2.4 Environmental Properties

The Montreal protocol [28] limits the use of CFCs and is phasing out HCFCs, due to their ozone depleting behaviour. Furthermore, the Kyoto protocol [29] now limits the use of high global warming potential (GWP) coolants. This protocol aims to slow down global warming. Consequently, for environmental aspects, an ideal coolant should be non-ozone depleting and have a relatively low GWP. Meanwhile, in terms of manufacturing, in order to protect staff health and safety, the ideal coolant should have low toxicity and low flammability.

2.2.5 Candidate Coolants Selection

After considering various properties, Table 2-1 shows characterises of an ideal coolant. In the real world, it is less possible to satisfy all characterises, a list of commercial coolants for selection is summarised in Table 2-2. The properties detailed above have been considered when selecting a candidate coolant. The thermal dissipation factor shows the evidence that

Chlorofluorocarbons (CFCs) and Hydrochlorofluorocarbons (HCFCs), such as R- 11, R-12; Perfluorocarbons (PFCs), for example, FC-72, PFC-116, and Hydrofluorocarbons (HFCs), for instance, R- 134a, and n-pentane are good two-phase heat transfer media.

On the electrical aspect, CFCs, HCFCs, PFCs and HFCs have a high magnitude of volume resistivity and large value of dielectric strength. These parameters show that these coolants are suitable for HV applications.

After considering environmental factors, several groups of coolants have to be deleted from the candidate list. These groups are CFCs and HCFCs, the reason is that they have ozone depletion potential. HFCs and PFCs now are widely applied in refrigeration systems [26], but most of them have very high GWP. The EU F-gas is set to phase out 80% HFCs by 2030 [30]. Consequently, HFCs and PFCs are also a not an ideal choice for future thermosyphon applications. The n-pentane is non-ozone depleting and has low GWP. However, the flash point of n-pentane is -49 ℃ and its fluid and vapour are extremely flammable. Since a discharge spark can cause fire and therefore n-pentane is not a good choice for HV plant.

Ultimately, there are two new possible coolants, which offer comparable thermal properties to CFCs, while they are non-ozone depleting and having a low GPW. They are Hydrofluoroethers (HFE) and Fluorinated ketone (FK). They are environmentally friendly and are regarded as an alternative cooling fluid for HV thermosyphon applications. As these materials are relatively new, little information is available with regard to their dielectric performance under different conditions. Therefore, additional material characterizations have been undertaken and the obtained results are detailed in Chapter 3.

Table 2-1 Ideal coolant characterises

Properties	Parameters	Requirement
Environmental properties	Ozone depleting	No
	GWP	Low (<10)
Electrical properties	Conductivity	Low (<10^{-10} S m^{-1})
	Dielectric strength	High (~20 kV mm^{-1})
Thermal properties	Latent heat of evaporation	High (>100)
	Boiling point	Low (< 50 ℃)

Table 2-2 Candidate coolants properties

coolants	Physical				Thermal				Dielectric			Environmental		Reference
	Boiling Point ATM	Absolute viscosity cP	Surface tension mN/m 25℃	Density g/cm^3	Specific heat J/kg K at 25℃	Latent heat kJ/kg	Thermal conductivity w/m K at 25℃	Thermal dispassion factor based on SI unit	Dielectric strength kV/mm at 25℃ ATM	Dielectric constant at 1kHz	Volume Resistivity Ω ·m at 25℃	Ozone depletion potential	GWP	
FC-72	56	0.64	10	1.68	1100	88	0.057	2.31×10^{8}	>15	1.75	10^{15}	0	>5000	[31]
R-11	23.6	0.42	62.07	1.48	876.2	180.17	0.093	3.94×10^{9}	3.71*	3.1	10^{10}	1.0	4680	[32]
R-12	29.8	0.206	56.98	1.49	973	165.61	0.071	6.83×10^{9}	2.46*	2.4	10^{12}	1.0	10720	[32]
R-13	-81.27	0.760	50.56	1.6	1204.12	149.67	0.011	1.59×10^{9}	1.65*	1.7	10^{12}	10	14190	[33]
R-22	-40.83	0.013	64.23	0.52	1242.22	233.76	0.106	6.01×10^{10}	1.27*	2.0	10^{10}	0.05	1780	[33]
R-113	47.6	0.011	30	1.58	891.36	167.47	0.068	7.22×10^{10}	2.6*	2.6	10^{11}	0.8	4800	[34]
R-123	27.8	0.408	16	1.46	975.1	170.26	0.096	9.75×10^{8}	38	<2	10^{10}	0.02	76	[35]
R-124	-12.05	0.2568	9.66	1.37	1109	164.21	0.0701	8.46×10^{8}	1.55*	<2	10^{9}	0.02	599	[36]
R134a	-26.0	0.2156	8.92	1.26	1409.27	217	0.0803	1.13×10^{9}	0.8-1.1*	9.5	10^{8}	0	1430	[37]
PFC-116	-78.2	1.013	13.42	1.608	1728	117.04	0.0134	2.49×10^{8}	1.4*	2.6	10^{8}	0	9200	[32]
n-pentane	36	0.214	15.30	0.63	1626	353.55	0.136	1.59×10^{9}	111	1.844	10^{11}	0	<15	[38]
HFE	61	0.58	13.6	1.52	1183	112	0.069	3.99×10^{8}	≤15	7.4	10^{8}	0	297	[39]
FK	49	0.64	10.8	1.6	1103	88	0.059	2.38×10^{8}	>15	1.84	10^{12}	0	1	[40]
R-1234yf	-30	0.22	5.76	1.1	1196	145	0.032	4.18×10^{8}	4.72	7.7	10^{7}	0	4	[41]

*Relative to nitrogen which is approximant 20 kV mm^{-1} [42]

2.3 Coolant Boiling Behaviour

Having outlined the working principle and candidate coolants for HV thermosyphon, this section considers their boiling behaviour.

2.3.1 Boiling Curve

The boiling phenomenon that occurs in a two-phase material can be divided into two categories, i.e. free boiling and forced boiling. Free boiling is a phase change phenomenon that occurs in a quiescent pool of liquid. Forced boiling is defined as the extra forces determine the liquid boiling on the heating surface. In a thermosyphon there is a minimal force boiling, hence this study focuses on free boiling behaviour.

A boiling curve is a typical method to characterize the boiling behaviour of the coolant, and it presents the relationship between the heat flux (q) and wall superheated temperature (ΔT). The 'superheated temperature' is because the wall temperature is greater than the liquid saturated temperature. Figure 2.5 shows a typical boiling curve, which shows that the pool boiling process is divided into subcooled boiling and saturated boiling. When the wall temperature (T_w) is below the saturation temperature (T_{sat}), the boiling process is defined as subcooled boiling. When the wall temperature is greater than the saturation temperature, the boiling process is called saturated boiling.

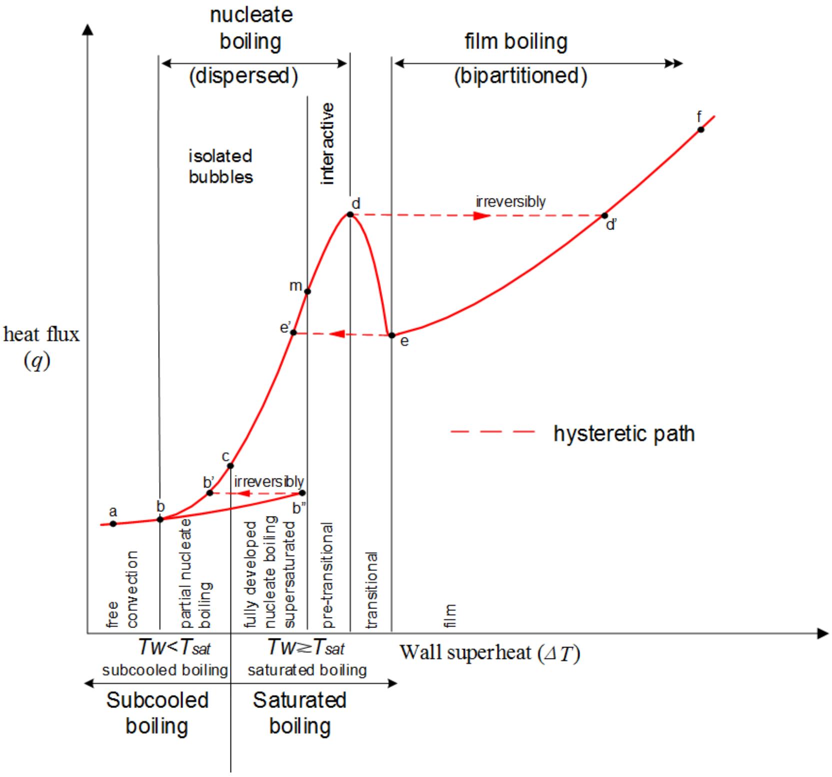

Figure 2.5 Pool boiling curve of coolant

In order to give a direct impression, an illustration of different boiling stages is demonstrated in Figure 2.6. In this illustration, the heating surface is located at the bottom and the letters refer to points on the boiling curve detailed in Figure 2.5.

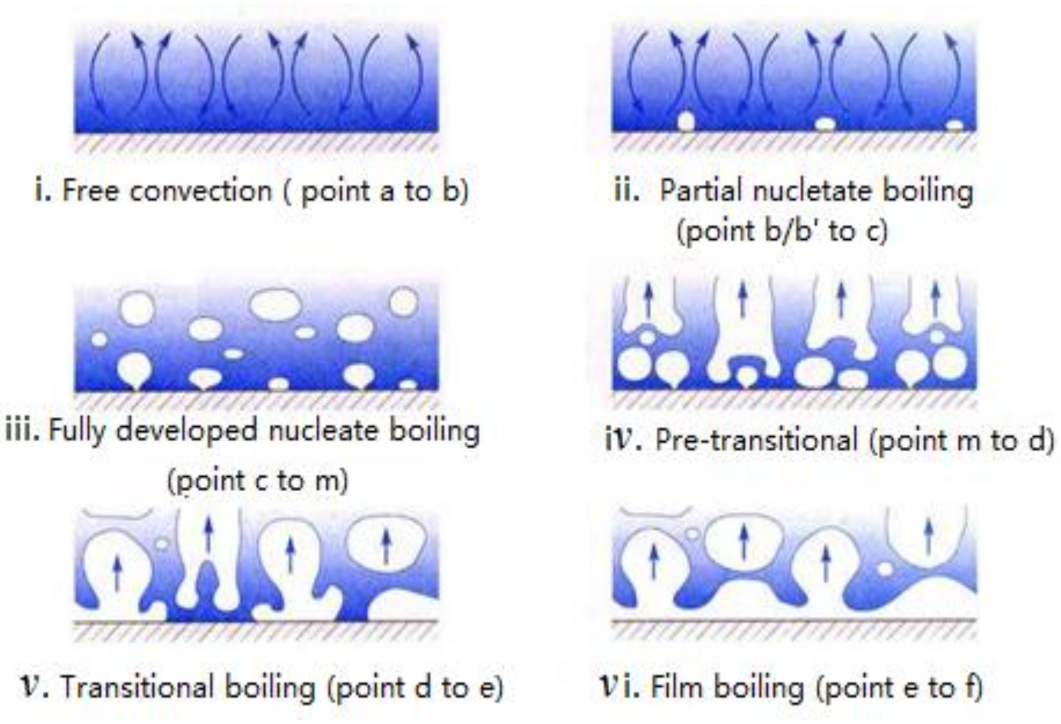
i. Free convection (point a to b)

ii. Partial nucletate boiling (point b/b' to c)

iii. Fully developed nucleate boiling (point c to m)

iv. Pre-transitional (point m to d)

v. Transitional boiling (point d to e)

vi. Film boiling (point e to f)

Figure 2.6 Illustration of the fluid boiling response [43]

2.3.1.1 Subcooled Boiling

Free convection and partial nucleate boiling are the subdivisions of subcooled boiling. The path a to b in Figure 2.5 expresses the free convection period and Figure 2.6i shows the coolant convection phenomenon. In this stage, the density of the coolant is heterogeneous; the thermal energy heats the bulk coolant locally. The buoyancy force results in the hotter fluid moving upwards away from the heat source and forces down the cool liquid to replace it.

Partial nucleate boiling is the second stage of subcooled boiling. This stage is shown by the path b-b′ in Figure 2.5 and the boiling behaviour is illustrated in Figure 2.6ii. Bubbles start forming due to a localized heat pulse above the liquid saturation temperature [44]. Surface tension is a factor that affects both bubble production and heat flux dissipation. This effect can be explained by the paths b to c and a to b′′ in Figure 2.5. The large value of the coolant surface tension decreases the coolant contacting area with the bubble cavity. Hence, in this circumstance, onset nucleate boiling only needs a small temperature gradient i.e. path b-c. As surface tension decreases, bubbles require a higher temperature gradient to initiate nucleate boiling, this produces a temperature overshoot that shown by the path a-b′′. This is also defined as the boiling hysteresis.

2.3.1.2 Saturated Boiling

When the fluid temperature reaches the saturated boiling point, the boiling regime turns into saturated boiling, which is further divided into four parts.

With the increasing heat flux, nucleation increases on the boiling surface and further causes increased bubble production. This phenomenon is defined as fully developed nucleate boiling; this course is shown by path c-m in Figure 2.5. The bubble formation is a phase change process, which reduces the local temperature. As discussed previously, the same as with natural convection, buoyancy drives bubbles away from the boiling site and cool liquid replaces the bubbles' location. After a waiting period, the local temperature increases and new bubbles form again. This causes plumes of bubbles to emerge from each bubble site as this process repeats. In this regime, the heat flux increases significantly with minimum superheated temperature, this is attributed to the phase change phenomenon absorbs thermal energy and prevents wall temperature rising.

The spacing of nucleation sites decreases as more cavities begin to produce bubbles with a higher heat flux. Once the distance between cavities is small enough that neighbouring bubbles touch, bubbles begin to coalesce. This phenomenon represents a new boiling regime called pre- transitional boiling shown by path m-d in Figure 2.5 and Figure 2.6i*v*. In this region, heat flux increases continually. This is because of the enhancement of natural convection, which is caused by the bubbles longitudinal and lateral movements. The lateral movement causes a large vapour pocket formation on the heater surface and eventually forms a vapour layer. These large vapour layers now produce bigger bubbles. The heat flux, therefore, increases rapidly, and finally reaches the critical heat flux (CHF) i.e. point d in Figure 2.5.

A path that connects the CHF point d and the minimum heat flux (MHF) point e in Figure 2.5 represents the transitional boiling regime, which as shown in Figure 2.6*v*. When the temperature reaches MHF point, highly turbulent flow is generated above the heater, which causes a decrease in heat flux. This is because the turbulent flow causes dry patches to be formed on the heater surface. With an increasing temperature gradient, the heat flux reaches CHF point d the boiling regime can jump upwards to the film boiling regime directly via an irreversible path d-d′. However, with decreasing temperature gradient, the heat flux can also drop back to the nucleate boiling regime with the path e-e′.

By continuing to increase heat flux, eventually vapour pockets will begin to coalesce, which results in a stable film of vapour covering the heater surface, shown by the e-f path in Figure 2.5 and Figure 2.6*v*i. In this region, the heat flux increases significantly due to the evaporation at the liquid vapour interface.

2.3.2 Boiling Curve of Candidate Coolants

After showing the typical boiling curve, there is a strong motivation to investigate the boiling curve of selected candidate coolants. Since both FK and HFE are relatively new, only a few studies have reported their boiling behaviours and corresponding boiling curves. The boiling curve results and experimental apparatus are presented in this section.

2.3.2.1 Pool Boiling Curve of FK

Whilst numerous publications have investigated the boiling curve for traditional coolant FC- 72 [45], [46], little work, has been reported on the pool boiling performance of FK. One study which has considered FK was published by Eric Forrest [47]. This study investigated the boiling curve of this alternative coolant and compared the results with traditional coolant FC- 72. The experimental apparatus is depicted in Figure 2.7.

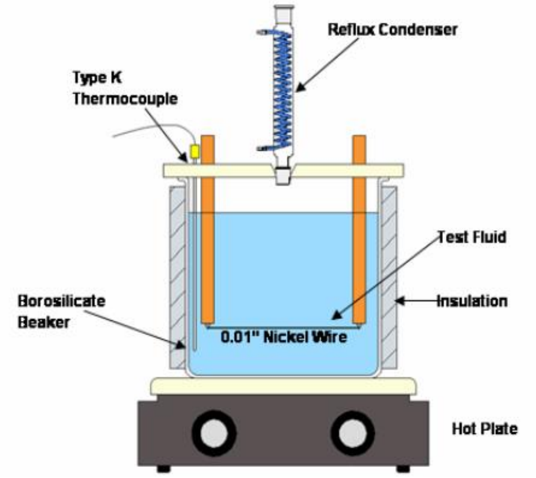

Figure 2.7 Schematic of the wire boiling setup [47]

The pool boiling experiments were conducted at standard atmospheric pressure. In this experiment, a 0.01-inch diameter nickel wire is the heating element. It was connected to a DC supply to generate heat energy and boil the coolant. The wire surface was degassed by supplying a low heat flux. The bottom hot plate raised the bulk coolant temperature to its saturation temperature, which is 322 K. The temperature of the test bath was monitored by a K-type thermocouple. The heat flux of the wire was obtained by measuring the current flow and calculated using Equation 2.3

$$q = \frac{IV}{S_{wire}} \tag{2.3}$$

where I is the current flowing in the wire for an applied voltage V and S_{wire} is the area of the wire surface. Figure 2.8 shows the boiling curve of the FK coolant. In the boiling curve q'' is the heat flux on the wire, T_w is the wall temperature of the boiling surface and the T_{sat} is the coolant saturation temperature. In this study, T_w was predicted using the resistance temperature coefficient method i.e.;

$$R(T) = R\,(T_{amb})\;[\,1 + \alpha(T - T_{amb})] \qquad (2.4)$$

where $R(T)$ is the real time resistance of the wire, $R(T_{amb})$ is the wire resistance at ambient temperature, T is the real time temperature, T_{amb} is the ambient temperature and α is the linearized temperature coefficient of resistance for the nickel wire. The value of α was experimentally determined and it is equal to 0.0056 K^{-1} from 25 ℃ to 75 ℃.

From Figure 2.8 can be seen that the natural convection and nucleate boiling regimes are apparent. In the natural convection regime, the wall temperature increased in an approximately linear function. There were no significant heat flux increases for both FK and FC-72. Hence, there is a large boiling hysteresis before the nucleate boiling regimes. This is because both FK and FC-72 have a low surface tension and the nucleate site is wet. In contrast, when the regime transferred into nucleate boiling there is a dramatical wall temperature drop. In the full nuclear boiling regime, the heat flux and superheated temperature follow a linear function:

$$q''=26.5(T - T_{amb}) - 120 \qquad (2.5)$$

The slope of the boiling curve can reflect the thermal dissipation performance. The larger slope indicates a higher thermal dissipation ability. Figure 2.8 shows that the boiling curves' slopes of FK and FC-72 are similar. This result indicates that, within this experiment apparatus, the effective heat transfer of FK and FC- 72 are comparable. Nevertheless, the saturated temperature of FK is 7 ℃ lower than FC-72, meaning it allows a larger permissible heat flux than FC-72. The experimental results show that CHF was 220 kW m^{-2} for FC-72 and 200 kW m^{-2} for FK, with a wall superheat of about 13 ℃.

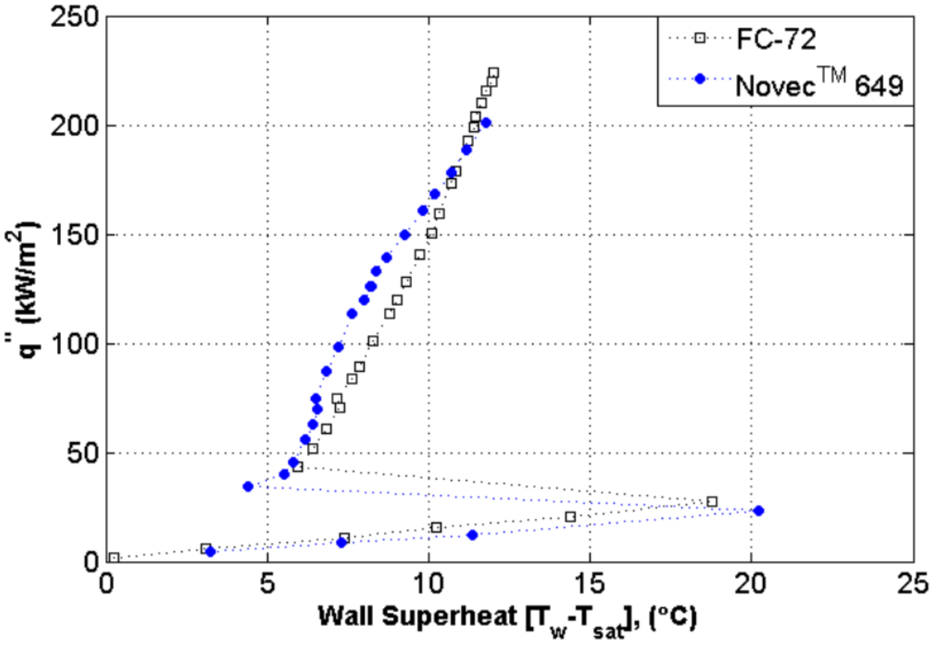

Figure 2.8 Pool boiling curves of FK and FC-72 [47]

This experiment has three main advantages: First, the arrangement only requires a small volume sample. Since the sample volume is small, it is convenient to maintain the bulk coolant temperature equal to the saturated temperature. Second, a glass beaker provides good light transmissivity for the imaging system to record boiling phenomena. Third, the thermal insulation layer and condenser are a convenient way to maintain bulk liquid temperature and recycle the vapour.

This simple arrangement also has some disadvantages: First, the bottom hot plate cannot maintain the coolant saturated temperature precisely. This is because a typical commercial hot plate is designed to control the temperature within a certain range rather than at a value. Hence, the hot plate input power should be varied with monitored temperature and this process may cause an error. Second, the method to predict heat flux is not ideal. The wire surface area is calculated by the wire length, which is hard to define due to the wire terminals that are welded on the two conductors. Furthermore, at high temperature, since the wire surface area is very small the thermal expansion cannot be negligible. Third, the nickel wire resistance may not only vary by temperature but also other factors such as impurities or oxidation. Hence, using the variation of resistance to predict boiling surface temperature may not be accurate.

In conclusion, this study used a simple and convenient approach to investigate the FK boiling curve. Conclusions from this approach are that the volume of the coolant should be as small as possible. The condenser and thermal insulation are necessary to maintain temperature, but a hot plate is not an ideal tool to control the bulk coolant temperature.

2.3.2.2 Pool Boiling Curve of HFE

Genk et al. have investigated the pool boiling phenomenon of HFE on a copper heat surface [48]. The experimental arrangement is shown in Figure 2.9.

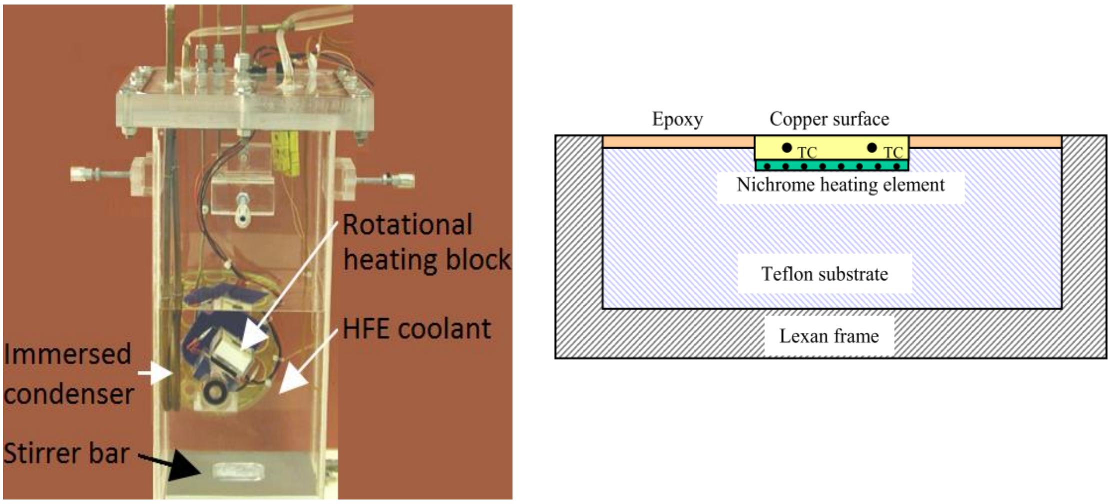

i ii

Figure 2.9 HFE pool boiling experimental facility; i. Pool boiling test cell, ii. Heating block cross-section

The experiments were conducted at atmospheric pressure and the HFE sample was heated from saturation temperature and 10 K, 20 K and 30 K subcooling temperature (i.e. the bulk liquid below the saturation temperature). A water bath system is applied to control the bulk coolant temperature. In this experiment, the heating element is a 1 cm^2 smooth copper surface. Two thermocouples are installed, their average readings are taken as the boiling surface temperature. The power of the heating element is equal to the product of current and voltage. Another research interest of their study was to investigate the angle of the boiling surface effects on the HFE boiling curve. Hence, the heater surface rotated from 0° (lying horizontally) to 180° (lying inversely). The experimental results are shown in Figure 2.10.

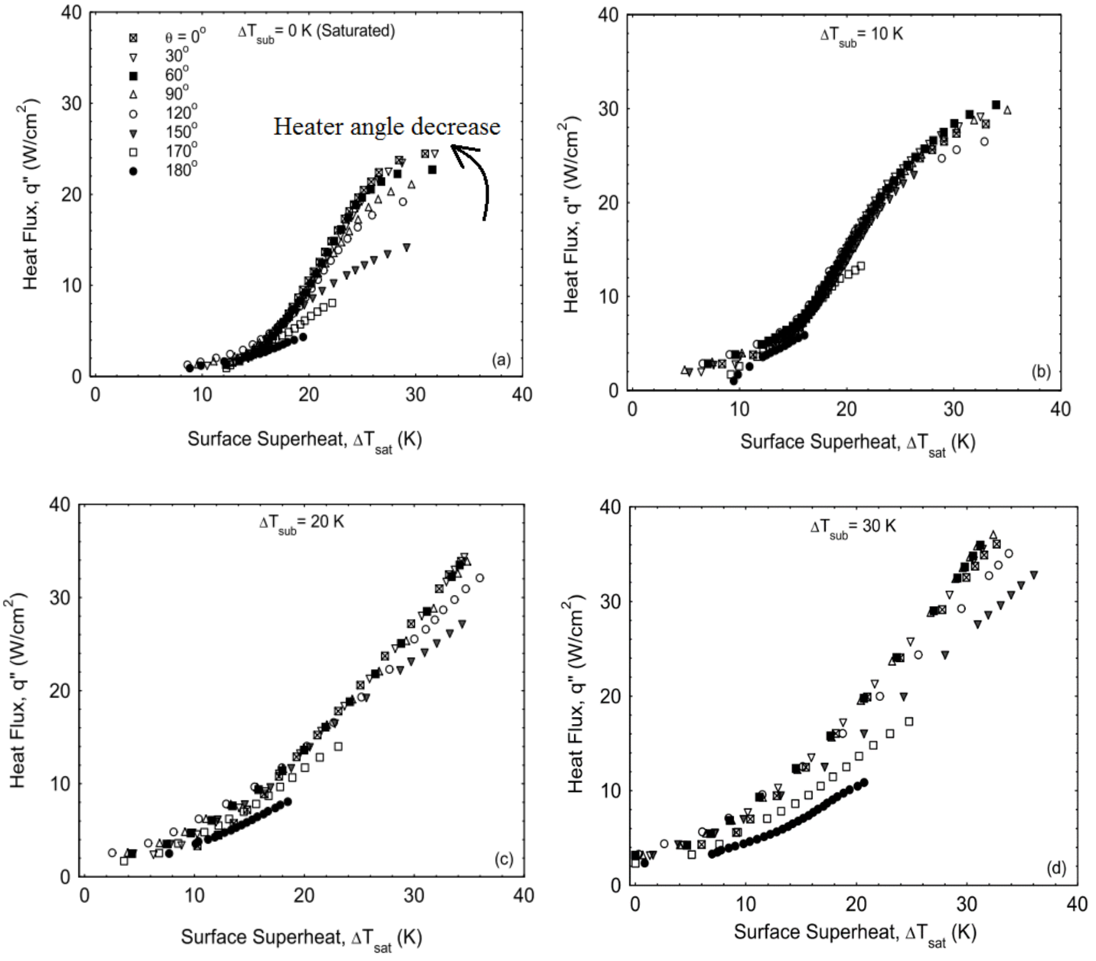

Figure 2.10 Nucleate boiling curves for HFE at different inclination angles and subcooling [48]

From published results, the heater inclination angle has an effect on the HFE boiling curves and CHF points. Specifically, at the saturation temperature, the horizontally positioned heater (i.e. θ=0), the HFE boiling curve has the largest slope and the highest CHF value, which is 24.45 W cm^{-2}. This result indicates that a horizontal heater surface is the ideal position for the maximum thermal dissipation. The second observation is the bulk liquid temperature effects on HFE boiling curve and CHF point. Specifically, the greater subcooling temperature results in a larger thermal dissipation and higher CHF value.

The design of this experiment also has both advantages and disadvantages. The advantage of this experimental design is the temperature control system. The water bath can control the bulk coolant temperature precisely. What is more, the embedded thermocouples are a good approach to determine the boiling surface temperature. However, this design also has a defect, which is the heater block design. Since the Teflon can still dissipate thermal energy by thermal conduction, in reality, the total heat energy is not only applied to the boiling surface. For experiments in this thesis, the need to isolate heat flux has been considered as part of the design process.

In conclusion, these experiments provide detailed information on HFE and FK boiling curves. These studies generate significant motivation to improve the apparatus design in order to obtain more actuate data for future research. The boiling curve obtained is only valid for corresponding heater arrangements and may change due to the different heater configurations.

2.4 Boiling Heat Transfer Enhancement

The aim of heat transfer enhancement is to increase the thermal dissipation within a minimum temperature window. There are two main technologies for modifying the boiling curve and enhancing two-phase heat transfer. These are boiling surface modification and electrohydrodynamics (EHD).

2.4.1 Boiling Surface Modification

Modifying the boiling surface roughness and bubble cavity chemical continuity are two strategies commonly employed. A rougher boiling surface provides a higher number of bubble nucleation sites. Hence, with the same heat flux, a rougher boiling surface results in a higher bubble production than a smooth boiling surface. It further leads to a larger heat absorption [49]. Surface abrasion and porous coatings are two technologies that have been widely used to increase boiling surface roughness. These two technologies have been reviewed in [50]. Results show that compared with abrasion treatment, a porous coating can provide a long-term enhancement to the boiling heat transfer coefficient. Ventola increased the boiling surface roughness by utilizing laser sintering [51]. The experimental results show that heat transfer on the rough surface was enhanced by a factor of 63% and 35% on average compared with flat surfaces and finned surfaces respectively.

The other strategy is to change the bubble cavity chemical continuity. The aim of this technology is to increase the heat exchange area between bubbles and the nucleate cavity. Resulting in a bigger size bubble and more thermal absorption than the untreated surface. Young et al. increased the water boiling heat transfer by polytetrafluoroethylene (PTFE) coating, which reduces the wettability of the bubble nucleate cavity [52]. Tuma showed an increased value of both heat transfer and CHF for both HFE and FK samples by applying the metallic microparticle coatings on the boiling surface [53], [54].

In conclusion, a rough boiling surface can increase the thermal absorption of HFE and FK samples. However, the rough boiling surface may not be suitable for HV applications; this is because the rough boiling surface can lead to a local high electric field, which may cause partial discharge. Furthermore, this second approach cannot increase HFE and FK heat transfer dramatically, this is because both HFE and FK samples already have relatively low surface tension and will effectively wet most boiling surfaces.

2.4.2 Electrohydrodynamics

Electrohydrodynamics (EHD) detail the electric field effect on the fluid. Studies have proven that the EHD technique can increase the boiling heat transfer [55]–[63]. EHD has several advantages such as a quick response to control, a significant increase in the rate of heat transfer and reduced energy consumption. Consequently, the EHD technique is of interest to this research project.

2.4.2.1 EHD Mechanism

The magnitude of the EHD effect is determined by the electric field involved in the coolant pool boiling. The foundational electrostatic equations are:

$$curl\ E = 0 \tag{2.6}$$

$$D = \varepsilon E \tag{2.7}$$

$$\nabla \cdot D = q_v \tag{2.8}$$

$$J = \sigma_E E + q_v u_l + \frac{\partial D}{\partial t} \tag{2.9}$$

$$\nabla \cdot J = 0 \tag{2.10}$$

where E is the electric field magnitude, D is the electric displacement, ε is the dielectric permittivity, q_v is the electrical volume charge density, J is the current density, σ_E is the electrical conductivity and u_l is the bubble velocity. Equation 2.9 shows that current density consists of three parts, $\sigma_E E$ is the electrical conduction in the coolant, $q_v u_l$ is due to the free charge convection, and $\frac{\partial D}{\partial t}$ is the electric displacement variations with time. Equation 2.10 indicates the conservation of free charges. Under steady state, the electrical free charge density is obtained.

$$q_v = \frac{1}{\tau} D \cdot \nabla \tau \tag{2.11}$$

where τ is defined as relaxation time, which is the ratio between the material dielectric permittivity ε and electrical conductivity σ_E. Relaxation time represents the time required for free charge relaxation to the bubble wall interface. The other important parameter is the characteristic dynamical time t_c, which is the time of the imposed electric field, the period of the mechanical oscillations on the liquid-vapour interface or bubble detachment period [62], [63]. By comparing the τ to the t_c, the liquid can be judged to be a conductor or an insulator.

If the relaxation time is longer than the characteristic dynamical time, the electric field does not have enough time to affect the coolant and bubbles. Hence, the coolant can be treated as an insulator and there is no charge that builds up on both coolant and bubble. If the relaxation time is shorter than characteristic dynamical time, this condition represents a conducting fluid where the voltage drops at the bubble surface. It coincides with the electrical free charge appearing. In order to understand EHD mechanisms on coolants, the values of relaxation time and characteristic dynamical time, of different coolants, have been reviewed and are summarized in Table 2-3.

Table 2-3 shows that, for both R11 and R113, the relaxation time is much larger than the dynamical time. Hence, they are treated as dielectric coolants. In order to enhance the EHD phenomenon, previous experiments have shown that by mixing a conductive liquid, such as ethanol with the dielectric coolants, the relaxation time can be decreased significantly [55]. At present, no literature reports the relaxation time of HFE and FK material. If EHD does effect HFE and FK samples, the enhancement of boiling heat transfer is attributed to the changing of bubble shape and bubble movement.

Table 2-3 Electrical properties of cooling fluid at 1 atm

Name of fluid	Tsat (℃)	τ (s)	t_c (s)	Refs
R11	25	1.3	0.02	[57]
R113	47	2.12/0.97/10	0.01	[55], [60], [64]
C2H5OH	78	1.9×10^{-3}	NA	[65]
R11+C2H5OH (2wt%)	NA	9.2×10^{-3}	NA	[65]
R113+C2H5OH (4wt%)	NA	5.7×10^{-3}	NA	[65]
R123	28	0.9×10^{-3}	0.017	[66]
n-pentane	36	2.4×10^{-3}	NA	[55]
FC-72	56	156	0.02	[60]

2.4.2.2 EHD Effect on Bubble Shape

The electric stress affects the bubble interface, which further results in changing its boiling behaviour [56], [57]. The dielectric forces as a pressure term, which is attributed to the difference of two-phase material. These forces are predominant at the bubble wall since the interface has the highest permittivity gradient. The electric stress can be divided into normal and tangential components, as shown in the following equations:

Normal electric stress:
$$f_{sn} = \frac{9\varepsilon_0 {E_0}^2}{2(2+\frac{\varepsilon_v}{\varepsilon_l})^2}\{[(\frac{{\varepsilon_l}^2+4\varepsilon_l-2}{3})(\frac{\varepsilon_v}{\varepsilon_l})^2-\frac{(\varepsilon_l-2)^2}{3}]\,cos\theta+\frac{(\varepsilon_l-1)^2}{3}\} \qquad (2.12)$$

Tangential electric stress:
$$f_{st} = q_s E_{vt} \qquad (2.13)$$

where ε_0 is the vacuum dielectric permittivity, E_0 is the uniform electric field strength away from the bubble. ε_l and ε_v are the dielectric permittivity of liquid and gas respectively. θ is the angular coordinate which is shown in Figure 2.11. q_s is the electrical charge density appearing at the liquid- gas interface and E_{vt} is the tangential electric field strength of the vapour phase.

Whether the bubble is dielectric or conductive, the normal electric stress will result in a distortion of the bubble [57], [64], [67]. The normal electric stress can be decomposed into horizontal (f_{snx}) and vertical (f_{snz}). Their directions are shown in Figure 2.11. The maximum horizontal component occurs at the bubble equator and towards to the gas phase. The vertical component has the maximum value at the top of the bubble and towards the liquid phase. Hence, the bubble is elongated in the direction of the electric field [67], [68]. Equation 2.12 shows that the normal electric stress is proportional to electric field squared, therefore, this force effect on bubble deformation is independent of electric field polarity but it shows a positive correlation with electric field magnitude [55], [67].

The tangential electric stress is attributed to the Coulomb stress on the liquid-vapour interface. If the fluid is an insulating material, no free charges act on the bubble surface. Therefore, only the normal electric stress acting on the liquid-vapour interface contributes to the bubble deformation. For the other case, if the fluid is deemed as a conducting material, the electric stress has a normal component. There is no tangential electric stress on the highly conducting bubble surface through electrical charges exist on the bubble surface. Between these two extreme cases, the tangential electric stress can affect the bubble surface. Most literature regards the fluid as either a perfect insulator or conductor [57], [67], [69]; therefore, the tangential stress is normally neglected in the past studies.

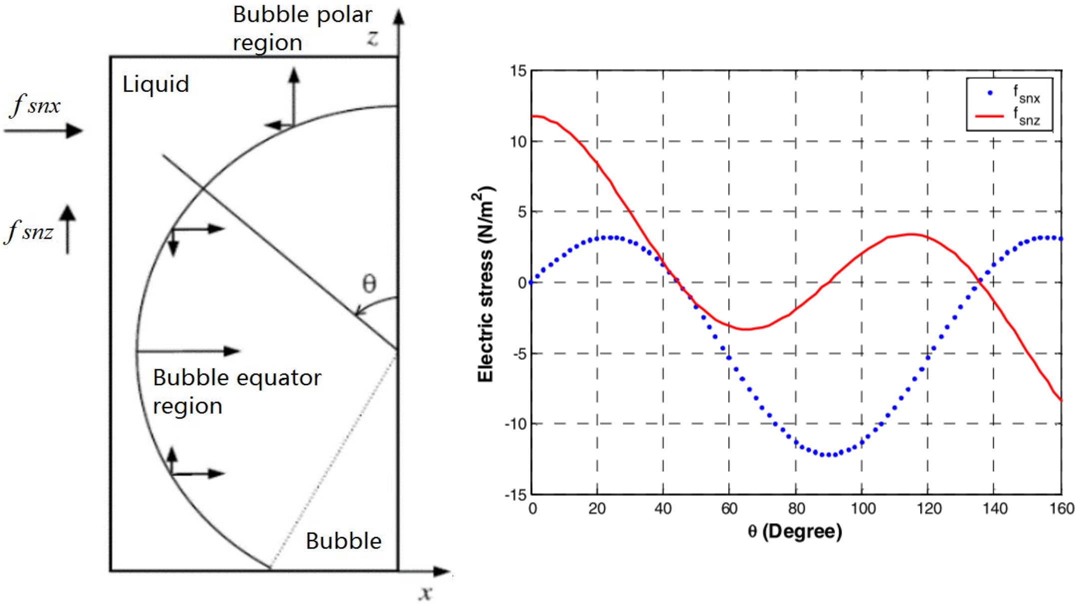

Figure 2.11 Horizontal and vertical components of the normal electric stresses [67].

2.4.2.3 EHD Changing Bubble Movement

Numerous published experiments have demonstrated bubble motion due to the presence of an electric field [55], [65], [70], [71]. The bubble movement is due to the force defined as;

$$f_e = 2\pi R_b{}^2 \frac{\varepsilon_v-\varepsilon_l}{\varepsilon_v+2\varepsilon_l} \varepsilon_0\varepsilon_l\nabla(E^2) \tag{2.14}$$

where f_e is the force on the bubble, $R_b$is the bubble radius, ε_0 is the absolute permittivity of vacuum. As relative permittivity of a liquid is normally higher than that of a gas, the term $\frac{\varepsilon_v-\varepsilon_l}{\varepsilon_v+2\varepsilon_l}$ is negative in most cases. Hence, the electric force drives the bubble to a lower electric field region.

Most experimental apparatus have the same design, which is that a heater is embedded inside the grounded electrode as shown in [11], [72], [73]. Therefore, both thermal and electrical field influence the bubble movement. The results show that within the uniform electric field, bubbles are pushed against the grounded electrode for a longer time.

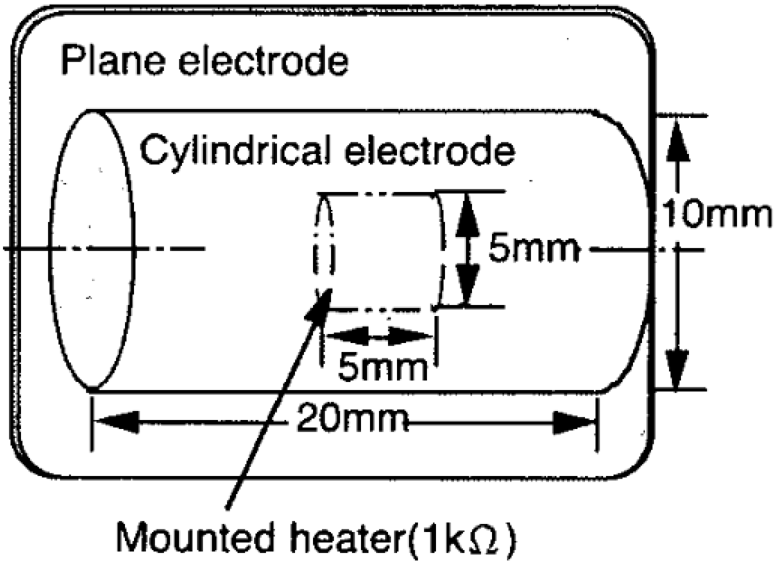

Figure 2.12 Electrode system arrangement [72]

In order to decouple the thermal effect on bubble movement, a novel experiment, designed by Kweon and Kim, investigated only the electric field effect on bubble behaviour in cyclohexane by using a syringe as the gas source [74]–[76]. The experimental apparatus is shown in Figure 2.13. It shows a 0.1 mm diameter needle injected a bubble into the field area. The needle is vertically located at the centre of the bottom electrode. The bubble departure volume can be recorded by a micrometre. There are two parallel copper electrodes with 144 cm^2 area, where the distance between the two electrodes is up to 36 mm. A 30 kV DC potential was placed across the electrodes. The electric field uniformity was varied by changing the height of the needle.

Under the uniform electric field, the results demonstrate that the bubble departure volume grows with an increasing voltage. This result is also proved by Wang's study of the boiling behaviour of liquid Nitrogen [67]. Under non-uniform electric field. The electric strength was the greatest at the needle tip resulting in bubble crossed a larger electric field gradient. With an increasing voltage, the bubble departure time and volume decrease continuously [76].

The effect of polarity on bubble movement has also been considered. The results indicate that under a uniform electric field the bubble movement and liquid velocity are independent of the polarity of the electric field [67], [74]. However, in a non-uniform field, the negative polarity has a greater effect on bubble movement than a positive polarity with the same magnitude. Ashe reports a polarity-dependent bubble motion in Freon-113, the possible reason for this observation could be issues of impurity layers and bubble charge [77].

There are also several disadvantages of this design, which may influence the results. Firstly, the needle diameter is much larger than a real thermal bubble seed. Secondly, the needle edge is sharper than a bubble cavity. It reduces the bubble contact area and therefore the bubble departure frequency is higher than the frequency of a real bubble boiling process from a flat surface.

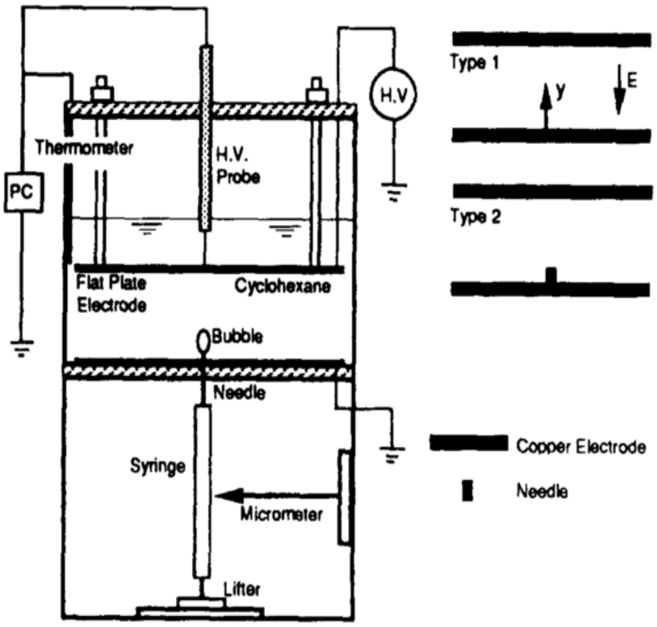

Figure 2.13 experimental apparatus and the electrode systems [74]

2.4.2.4 EHD Effect CHF Enhancement

Published literature also demonstrates that EHD increases the CHF value [61], [78]–[81]. This is because EHD destabilizes the blanketing bubble layer that covers the boiling surface. Without EHD intervention, when the heat flux reaches the CHF point, the vapour columns form a blanket covering the boiling surface. Since the gas blanket has very small thermal conductivity, the rapidly increased temperature may damage the heater. To avoid CHF, there is a maximum vapour rate limitation, which is represented by the critical wavelength;

$$\lambda_d = 2\sqrt{3}\pi\sqrt{[\frac{\sigma}{(\rho_l-\rho_g)g}]} \tag{2.15}$$

where λ_d is the critical wavelength, ρ_g is the gas phase density, g is the gravitational acceleration. The wavelength expression is changed when the electric field effect is taken into account, i.e.

$$\lambda_{dE} = \frac{6\sqrt{2}\pi\delta}{G^2+\sqrt{(G^4+3{B_o}^2)}} \tag{2.16}$$

where λ_{dE} is the critical wavelength with EHD effect, δ is the vapour thickness that covers the heated surface. G and Bo values are given by

$$G = \sqrt{\frac{\varepsilon_v E^2\delta}{\sigma}} \tag{2.17}$$

$$B_o = \sqrt{\frac{\rho_l g\delta^2}{\sigma}} \tag{2.18}$$

It can be seen that the electric field reduces the most critical wavelength and increases the CHF value. More heat energy is dissipated by the liquid-gas phase exchange before the heat flux reaches the CHF point.

2.4.2.5 EHD Heat Transfer Enchantment on Various Coolants

Previous sections have explained and discussed that the EHD effect on the liquid-gas phase boiling behaviours. This section aims to give a summary of the EHD enhancement on heat transfer and CHF values of various commercial coolants. From numerical values, which are summarised in Table 2-4, three observations can be made:

First, the EHD has a minimal boiling enhancement of R-11 and liquid nitrogen. This is because the relaxation time of these fluids is higher than the bubble detachment period. Consequently, there is no free charge on the bubble surface and both vapour and liquid behave like dielectrics so that the EHD force does not affect their behaviour significantly. In contrast, R-11+C_2H_5OH and R-123 has much shorter relaxation time and behaves conductively, and therefore EHD effects on the heat transfer significantly. Second, under the same pressure, lower heat flux has an obvious EHD heat transfer enhancement. The possible reason for this is that a lower level of heat flux produces fewer bubbles. Hence, the electric field can affect individual bubbles more sufficiently. Finally, at the same voltage and heat flux supply, reducing pressure is an alternative way to increase EHD heat transfer enhancement.

Table 2-4 Heat flux and CHF enhancements by EHD

Cooling fluid	The voltage supplied (kV)	Heat flux (kW/m^2)	Fluid Pressure kP$_a$	Heat flux enhancement by EHD	CHF enhancement by EHD	Reference
R-11+C_2H_5OH	25	5.8	101	8.5 times	-	[55], [65]
R-123	25	5	101/82	9.2/9.9 times	-	[66]
		10	101/82	5.8/6.2 times	-	
		13	101	4.9 times	-	
		15	101	4.5 times	-	
		20	101/82	3.9/4.1 times	-	
R-123*	25	8.6	101	5.25 times	3 times	[56]
		32.3		2.6 times		
		194		1.4 times		
R-11	14.8	8.8	101	1.5 times	-	[58]
R-11*	0	10	101	≤1.05 times	-	[66]
	10				-	
	25				-	
R114	30	1.3	101	1	-	
	30	1.6	101	3	-	[82]
HCFC-123	1.5	25	101	1.15 times	1.15 times	[61]
n-pentane	25	9.6	101	1.5 times	1.17 times	[56]
		36.2		1.3 times		
		181		1.13 times		
R-113	25	19.2	101	1.71 times	1.23 times	[56]
		34.5		1.5 times		
		187.2		1.13 times		
Liquid nitrogen	40	33.3	101	1.1 times	1.13 times	[83]

* Represents different suppliers

2.5 Summary

This chapter introduced a passive cooling device named thermosyphon. Compared with active cooling devices, it has many advantages such as smaller, quieter and less energy consuming. Since thermosyphon heat transfer relies on the coolant boiling, selecting an appropriate coolant is essential to ensure good thermosyphon performance.

Several candidate coolants have been evaluated that based on their thermal, dielectric and environmental impacts. After compromising, HFE and FK are two candidate coolants, which are selected as the research samples. Their boiling behaviours and heat transfer characters have been investigated by their pool-boiling curves, which have been experimentally obtained by other researchers. Results indicate that if the evaluation was based on their thermal properties only, both FK and HFE may not the best choice. Nevertheless, after considering the environmental factors, their comprehensive properties are better than the congeneric coolants.

In order to maximize the heat transfer capabilities of both FK and HFE coolants, heat transfer enhancing techniques have been discussed. According to HFE and FK physical parameters, EHD can be seen as one of the best options to enhance their boiling heat transfer. This enhancement is attributed to the electric field effect on two-phase boiling behaviours, in particular, EHD results in bubble movements on the evaporator boiling surface due to Maxwell stress [55], [65], [84]. EHD spreads bubble gas pockets on the boiling surface [85], [86] and increases the bubble amount by breaking up large gas bubbles so decreasing bubble departure volume and creating turbulence [87]. EHD eliminates boiling hysteresis, thereby nucleate boiling starts at a lower superheat [63], [88], [89] and decreases surface tension that results in higher wetting of the bubble cavities [90], [91]. EHD also generates perturbations at the boiling surface due to the instability of the gas-liquid interface [92]–[94].

Chapter 3

Dielectric Properties of Candidate Coolants

An experiment is a question which science poses to Nature, and a measurement is the recording of Nature's answer. - Max Planck

The AC and DC dielectric properties of Hydrofluoroethers (HFE) [$C_4F_9OCH_3$] and Fluorinated Ketone (FK) [$C_2F_5C(O)CF(CF_3)_2$] at different temperatures are investigated by frequency dielectric spectroscopy (FDS), DC conductivity and AC electrical breakdown measurements. The repeated breakdown effects on AC dielectric strength also been experimentally investigated. These measurements can provide adequate information of HFE and FK dielectric behaviours. Obtained experimental results are important for manufacturers to define the operating loss, dielectric distance and therefore the data give by this chapter makes great contribution to HV thermosyphon design.

3.1 Dielectric Spectroscopy Analysis

The dielectric spectroscopy results of HFE and FK samples at different temperatures are analysed in this section.

3.1.1 Introduction

Dielectric spectroscopy is a nondestructive technique that can provide the information on materials' molecular interactions, orientation and polarization at different frequencies. This technology has been widely applied to analysis AC response of a dielectric material. Previous studies have shown that the dielectric response could vary with the applied electric field and measuring environments, such as temperature and pressure [95], [96]. Therefore, it is important to define the methodology and standard.

3.1.2 Methodology and Standard

In this study, dielectric spectroscopy of samples was measured by a direct capacitance method, which is based on the Standard BS 60247 [97]. The spectroscopy is deduced by measuring sample capacitance. A two parallel electrodes system, encompassing a sample, can be regarded as the equivalent to a capacitor. By applying an alternating voltage with angular frequency ϖ an alternating current is produced which is;

$$I = j\,\varpi C_0 V \tag{3.1}$$

Where C_0 is the vacuum capacitance of the test cell and j is defined as $\sqrt{-1}$. After filling the dielectric material, the capacitance value of the capacitor becomes larger and equal to C_x. The relative permittivity of the dielectric material (ε') is defined as the ratio of C_x to C_0:

$$\varepsilon' = \frac{C_x}{C_0} \tag{3.2}$$

The relative permittivity indicates the dipole polarization or interaction. During these processes, energy dissipation in the form of heat is defined as a loss. In order to characterise both polarization and loss, the AC dielectric response is usually represented by the relative complex permittivity i.e.;

$$\varepsilon^* = \varepsilon'(\varpi) - j\,\varepsilon''(\varpi) \tag{3.3}$$

The real part of the complex permittivity is the relative permittivity (ε') and the losses are represented by the imaginary component (ε'').

From the theory of the molecular polarizability, the real part of complex permittivity is related to the dipole moment of a liquid such that [98]:

$$\frac{(\varepsilon'-1)(2\varepsilon'+1)}{9\varepsilon'} = \frac{N_0}{3}\left(\alpha_m + \frac{\mu^{*2}}{3\varepsilon_0 k_B T}\right)\frac{\rho}{M} \tag{3.4}$$

where M is the relative molar mass of the material, ρ is the material density, N_0 is Avogadro's number, which is 6.023×10^{23}, α_m is the molecular polarizability, k_B is the Boltzmann constant, which is 1.381×10^{-23} and μ^* is the dipole moment. From Equation 3.4, it can be seen that the value of the relative permittivity is influenced by the sample's temperature, density and molecular activity.

The dielectric loss may generate undesirable heat. Hence, for an ideal dielectric material, the imaginary component should be as small as possible. In engineering, another parameter is defined to assess the losses. This is the dielectric dissipation factor (tan δ) and is determined by the dielectric loss angle (δ), which is the angle between the applied voltage and current. The dielectric dissipation factor is equal to the ratio of the imaginary component of complex permittivity (ε'') to the relative permittivity (ε').

3.1.3 Apparatus and Settings

In this study, a Solartron 1296 dielectric interface device and model 1260A impedance/gain- phase analyser was used to measure sample spectroscopy. These devices measured the sample impedance and the lag angle to calculate sample relative and imaginary permittivity. Figure 3.1 shows the schematic diagram of the test cell, which consists of two parallel copper electrodes. The separation between two electrodes was set equal to 1 mm. To minimise any edge effects [99] a guard ring was connected to the bottom electrode. In order to hold the liquid sample, the bottom electrode was encased in a PTFE ring to act as a sample reservoir. For each measurement, 5 ml sample was slowly injected into the test cell by a syringe to avoid the formation of air bubbles. After sample loading, both electrodes were submerged by the liquid sample and therefore the sample thickness is equal to the electrodes' separation, which is 1 mm. Each measurement was started 1 minute after filling the samples. No air bubbles were observed during the measurement.

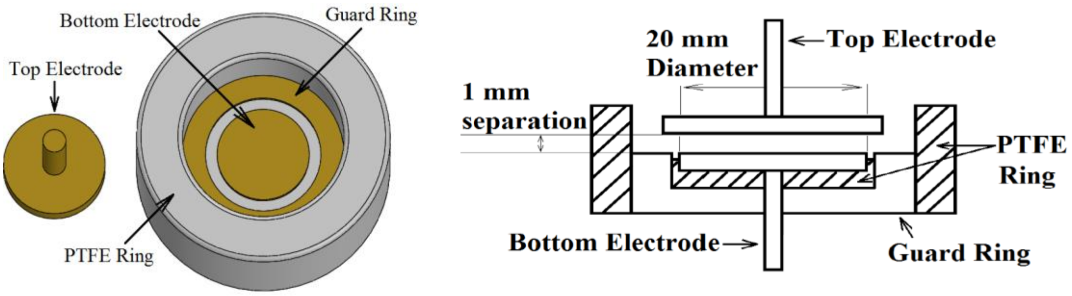

Figure 3.1 Liquid test cell with parallel electrodes system

In this study, the electric potential across the sample was 7 V (RMS) the measuring frequency was from 0.1 Hz to 100 kHz covering most applications' operating frequencies. The higher numbers of measuring cycles contribute to precise results. The whole frequency array was divided into two ranges aims to allow different settings. The first frequency range is from 100 Hz to 100 kHz. In this frequency range, there are five measuring points per frequency decade and the integration period was set equal to 20 seconds. The second frequency range is from 0.1 Hz to 100 Hz. In this frequency range, there are three measuring points per frequency decade and 25 cycles were chosen as the integration period. It can be seen that, in the whole frequency range, there are at least 25 measuring cycles were conducted for each measuring point. These settings guarantee a precise data set.

Besides the appropriate settings, good variable control methods are also indispensable for an accurate measurement, these methods are shown in the next section.

3.1.4 Variable Control and Sample Preparation

Temperature and humidity are two variables in this measurement. Since, both HFE and FK coolant have relatively low saturated temperatures (334 K and 322 K at atmospheric pressure) [100], all measurements were conducted not higher than the lab ambient temperature (i.e. 295 K). To achieve this, samples were packaged in 10 ml sealed phials and placed in a modified freezer. A T-type thermocouple was applied to monitor the sample temperature. The temperature readings are shown in Figure 3.2 and it can be seen that after three hours all the samples reach thermal equilibrium. Therefore, the low-temperature measurement started three hours after the sample was put into the freezer.

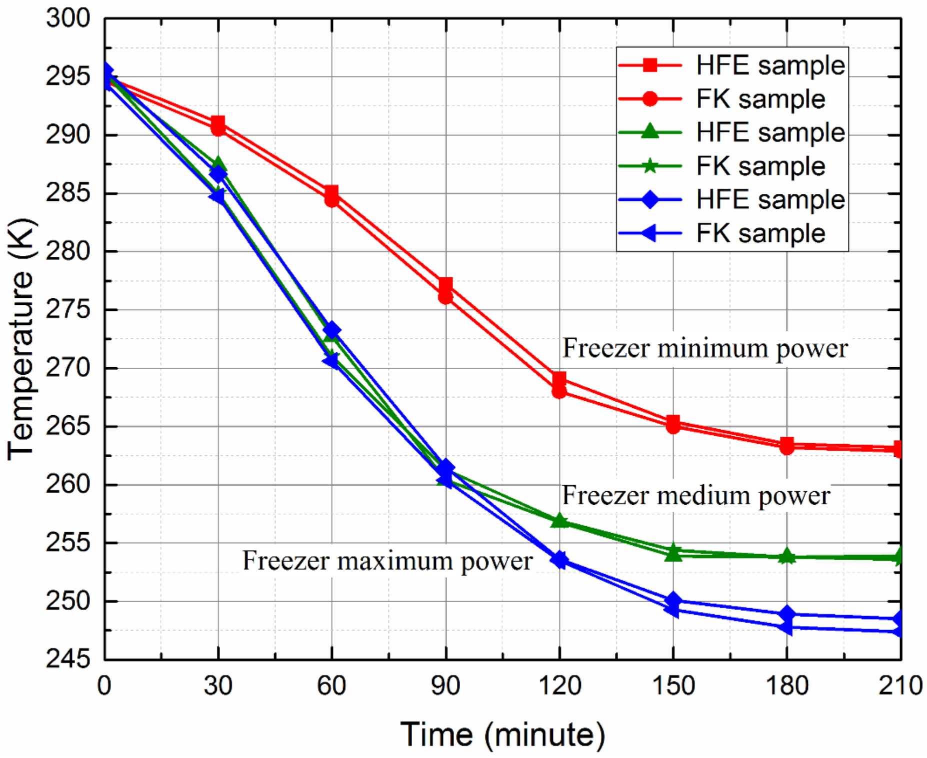

Figure 3.2 Freezer temperature as a function of time

The Material Safety Data Sheets (MSDS) state that both HFE and FK do not have strong water solubility and hydrophilicity [39], [40]. In order to avoid any water moisture effect on the measuring results, the sample humidity was still controlled during the measurement. Two dehumidifiers were placed in the freezer to absorb any water moisture. The humidity curve is shown in Figure 3.3 and it can be seen that after two hours the humidity became stable and dropped to only 6 % in the freezer.

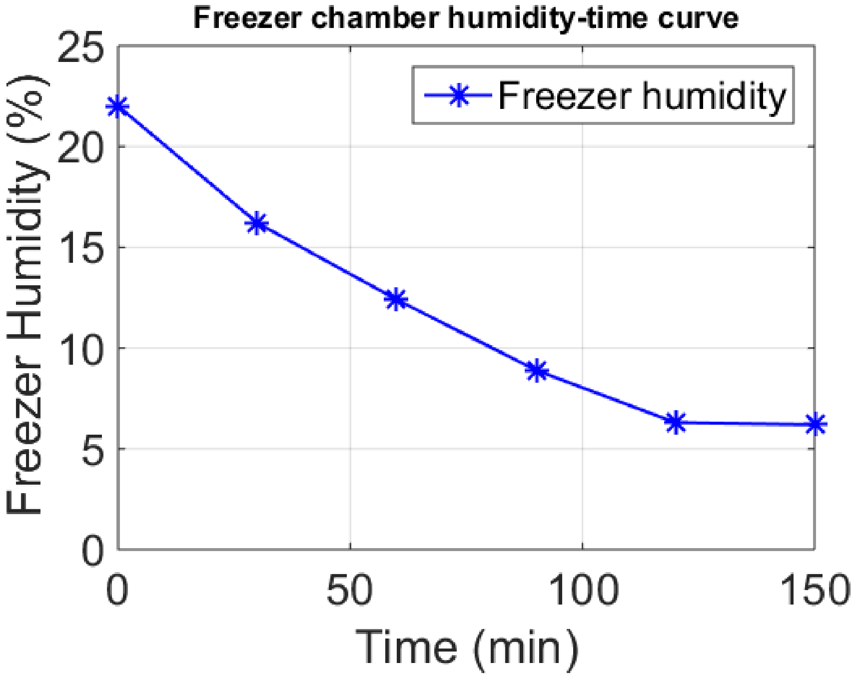

Figure 3.3 Freezer chamber humidity as a function of time

3.1.5 Results

The results, presented in this section, are the average values of five repeated measurements with a standard deviation of less than 5%.

The real part of the complex permittivity of HFE is shown in Figure 3.4. The value that obtained by the measurements of HFE at 1 kHz and 295 K is 7.3. This value is in a close agreement with the reference value given by the manufacturer, which is 7.4 [100]. This large magnitude of the real permittivity could indicate the formation of ionic charge layers at the electrodes.

Description of the results is carried out by dividing the measurements into high frequency ($>$ 80 Hz) and low-frequency domains ($\leq$ 80 Hz). Considering the high-frequency domain, results show the real permittivity of HFE is negatively correlated with increasing temperature. On the contrary, in the low-frequency domain, the real permittivity is positively correlated with increasing temperature. Furthermore, the turning point of the real permittivity shifts to a higher frequency value with increasing temperature.

The imaginary part of the complex permittivity of HFE is plotted in Figure 3.5. As observed from the results, the value of the imaginary permittivity decreases with increasing frequency. Furthermore, the slope of the value in a log-log plot is -1 for all temperature ranges. This result indicates electrical conduction dominates the dielectric behaviour. The temperature also effects on the imaginary part of complex permittivity. As temperature increases so do the imaginary permittivity

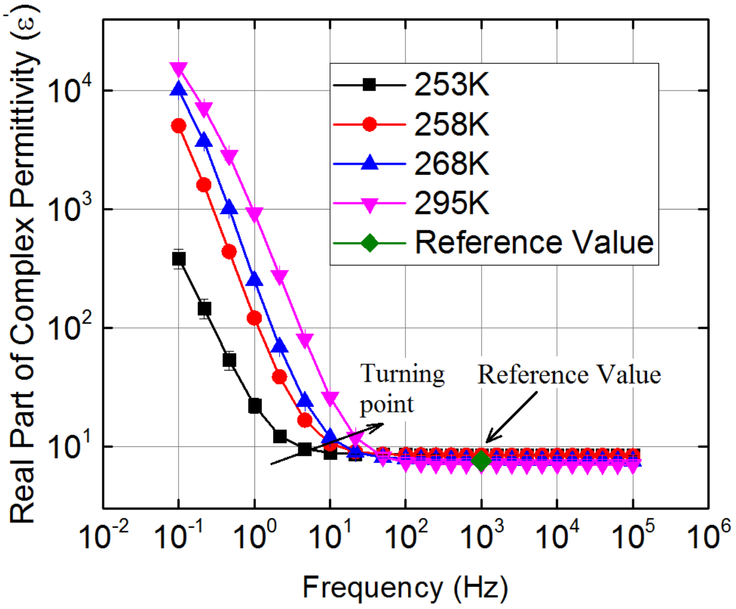

Figure 3.4 The real permittivity of HFE against frequency

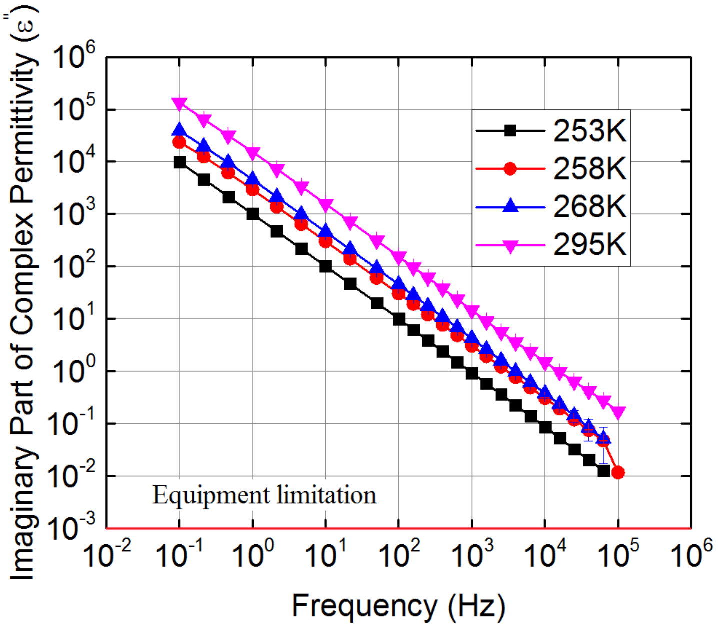

Figure 3.5 The imaginary permittivity of HFE against frequency

The dielectric dissipation factor of HFE is plotted in Figure 3.6. It can be seen that there is a turning point on the dissipation factor curves at all measured temperatures. The frequency that corresponds to the turning point is defined as the critical frequency. Three observations can be drawn from the dissipation factor results. Firstly, the critical frequency shifts to a higher value with the increasing temperature. Secondly, when the frequency is higher than the critical frequency the dissipation factor and frequency are in a negative correlation. When the frequency is lower than the critical frequency, the sample dissipation factor and temperature are positively correlated. Thirdly, in the high-frequency range (80 Hz), a higher temperature results in a larger value of the dielectric dissipation factor.

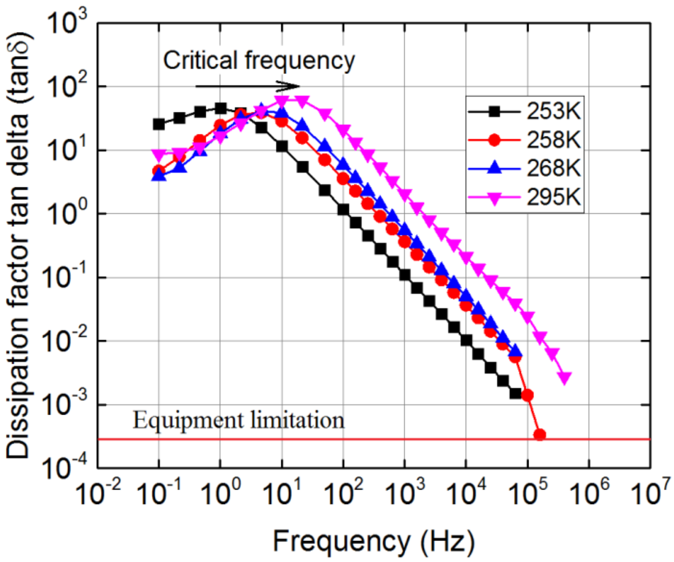

Figure 3.6 Dissipation factor of HFE against frequency

The results of the real part and the imaginary part of the complex permittivity of FK are shown in Figure 3.7 and Figure 3.8. Figure 3.7 indicates that when the frequency is higher than 10 Hz, the real permittivity is approximately frequency independent. The measured real permittivity of FK was 1.84 at 1 kHz. It is in close agreement with the reference value, which is 1.8 [100].

The results indicate that the real part of the complex permittivity of FK sample is negatively correlated with an increasing temperature. A high temperature has the positive effect on increasing imaginary part of complex permittivity. Significant fluctuations can be seen in the imaginary permittivity plot when the frequency is above 100 Hz. This is because the imaginary part of the complex permittivity of FK at the high-frequency range is too small and it is below the equipment measurement limit.

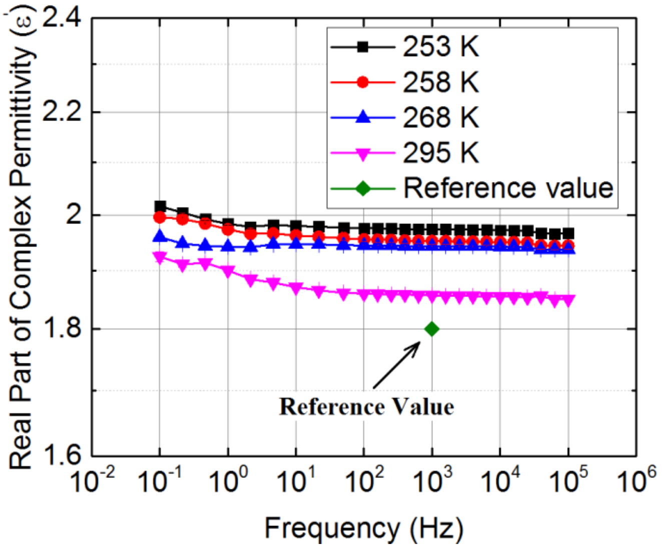

Figure 3.7. The real permittivity of FK against frequency

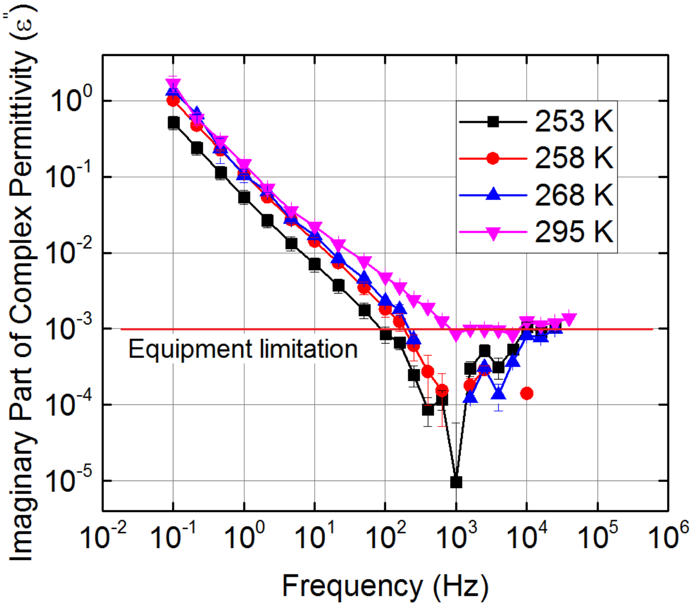

Figure 3.8. The imaginary permittivity of FK against frequency

Figure 3.9 presents the dissipation factor of the FK sample. The results show the dissipation factor of the FK sample increases with rising temperature. With the same temperature, the dissipation factor of the FK sample increases with reducing frequency.

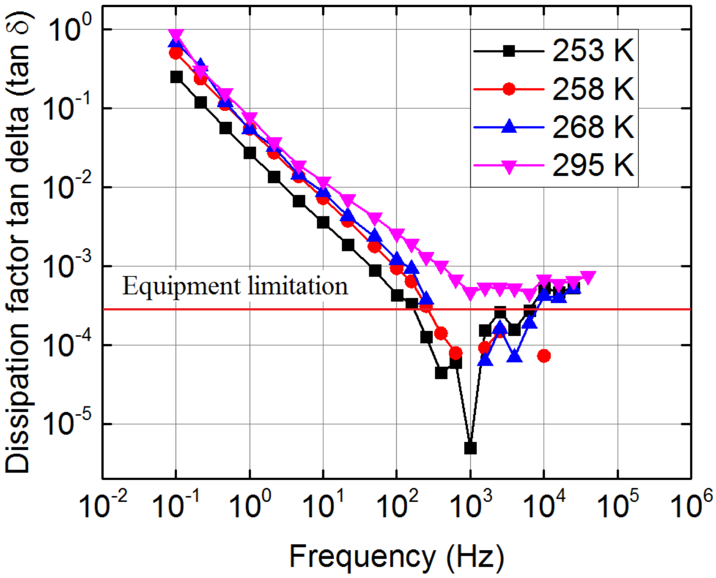

Figure 3.9. Dissipation factor of FK against frequency

3.1.6 Discussion of Results

The real part of the complex permittivity of HFE and FK samples, in the high-frequency domain (>80 Hz), is negatively correlated with increasing temperature. The reason for this is that higher temperature results in a stronger thermal motion of dipoles. Hence, random thermal motion decreases the electric field effect on dipole alignment. As a result, dipoles are less closely aligned with each other, the polarisation becomes weaker and causes a decreased real part of the complex permittivity. This behaviour has also been found in HFC coolants such as 1,1,1,2- Tetrafluoroethane (HFC- 134a), Pentafluoroethane (HFC-125) and trifluoromethoxymethane (HFE-143a) [98], [101]. Figure 3.6 shows that the real part of the complex permittivity of HFE increases significantly over the low frequency domain (<80 Hz). This phenomenon is due to the ion drift occurrence at low frequencies, resulting in the formation of double charge layers near to the electrodes. Since higher temperatures lead to higher ion mobility, ion drift starts at a higher frequency. It further leads to the turning point shifts to a higher frequency. The imaginary part of the complex permittivity of both HFE and FK samples decreases with increasing temperature. The answer to this phenomenon is the viscosity of HFE and FK decreases with increasing temperature. The lower viscosity results in a stronger dipole mobility. Thus, a higher temperature leads to a larger value of the imaginary part of the complex permittivity.

3.1.7 Summary of Dielectric Spectroscopy Measurement

In conclusion, the AC dielectric response of both HFE and FK fluids have been measured from 0.1Hz to 100 kHz. The dielectric spectroscopy results have shown a qualitatively different behaviour of HFE and FK fluids. The FK behaves as a dielectric fluid due to the capacitive current, a well-defined dielectric constant with value 2 and relatively smaller dielectric loss than HFE via measuring frequency range. In contrast, HFE behaves like an ionic conductor because the conduction current dominates the displacement current for all measured frequencies below 1 kHz and results in hetero charge formation near to the electrodes.

The temperature effect on the AC responses of HFE and FK have also been investigated, the results show that higher temperature results in a lower value of real part of complex permittivity but leads to a larger magnitude of the imaginary part of complex permittivity and greater value of dissipation factor.

3.2 DC Conductivity Analysis

This section introduces an investigation of DC conductivity of HFE and FK samples at different temperatures.

3.2.1 Introduction

DC conductivity is an important parameter to characterize the charging phenomenon and current flow in a dielectric material. Charging phenomenon occurrence in a dielectric liquid remains a concern for high voltage equipment due to the electrostatic hazards [102] and introduces the electrohydrodynamic phenomenon [60]. Therefore, knowledge of DC conductivity of a dielectric liquid is crucial for the safe and reliable design of high voltage thermosyphon.

3.2.2 Methodology and Standard

With the constant electric potential, a high conducting current results in a larger DC conductivity value. The DC conductivity is mainly attributed to the motion of numerous charge carriers. According to the type of charge carrier, electrical conduction can be subdivided into ion conduction and electron conduction. Ion conduction can be distinguished in terms of ions, which are the main charge carriers that contributes to electrical conduction. Generally, ions are generated by the dissociation of impurities or sample ionization under the electric field. Electrons are the other main charge carrier, which contributes to electron conduction. Different types of materials contain different charge carriers. Electron conduction dominates electric conduction in metals. However, there is minimum electron conduction, at low electric fields. In dielectric liquids, ions are the main charge carriers instead [103], [104]. Hence, ion drift dominates conductivity in liquids and the methodology is introduced as follows [105];

With a DC field, the current density J in the dielectric liquid is determined by the derivative of transported charge Q_{E} with respect to time t per unit cross-section area of the liquid A by;

$$J = \frac{1}{A}\,\frac{dQ_{\mathrm{E}}}{dt} \tag{3.5}$$

Charge drift velocity v_{D} can be derived by extending Equation 3.5 by d_x which is expressed by;

$$J = \frac{1}{A}\,\frac{dQ_E}{d_t}\,\frac{d_x}{d_x} = \frac{dQ_E}{dVol}\,\frac{d_x}{d_t} = \frac{dQ_E}{dVol}\,v_D = q_v v_D \tag{3.6}$$

The drift velocity v_D can also be expressed as a function of charge concentration c, charge average mobility b and electric field, by;

$$v_{\mathrm{D}} = c\,b\,E \tag{3.7}$$

Therefore, the product of c and b is more commonly referred to as ion mobility μ;

$$\mu = cb \tag{3.8}$$

$$J = q_v\,\mu\,E \tag{3.9}$$

Then current density is defined as the electrical conductivity multiplied by an electric field,

$$J = \sigma_{\mathrm{E}} E \tag{3.10}$$

Now by combining Equation 3.9 and 3.10, the electrical conductivity is expressed as:

$$\sigma_{\mathrm{E}} = q_v\,\mu \tag{3.11}$$

From Equation 3.11, it can be seen that ionic conductivity is equal to the ion mobility multiplied by the charge density. Numerous studies have demonstrated that the electrical conductivity is strongly dependent on temperature by changing the liquid viscosity and charge mobility [106], [107]. The relationship between temperature T and liquid viscosity η is expressed by Arrhenius equation [108], [109]:

$$\frac{1}{\eta} = \frac{1}{\eta_\infty}\, e^{-\frac{E_A}{k_\mathrm{B} T}} \tag{3.12}$$

where E_A is activation energy, and η_∞ is the initial value of liquid viscosity. E_A represents the minimum energy required for processing a chemical reaction. It depends on the chemical bond between atoms and structure. Based on Stokes' law the mobility of ions in a dielectric liquid is inversely proportional to the liquid viscosity η. In the limit of small ionic concentration, this phenomenon is described as Walden's Rule i.e. [104]

$$\mu \cdot \eta = constant \tag{3.13}$$

By combining Equation 3.12 and Equation 3.13 the temperature influence on the electrical conductivity can be expressed by;

$$\sigma_E = \sigma_0\, e^{-\frac{E_A}{k_\mathrm{B} T}} \tag{3.14}$$

From Equation 3.14 it can be seen that higher liquid sample temperature results in a greater value of DC conductivity.

Furthermore, ion drift is a transient process. The typical relationship between the electrification time and conductivity is shown in Figure 3.10, which shows that the conductivity has three domains, i.e. initial conductivity, transient ion conductivity and steady state conductivity.

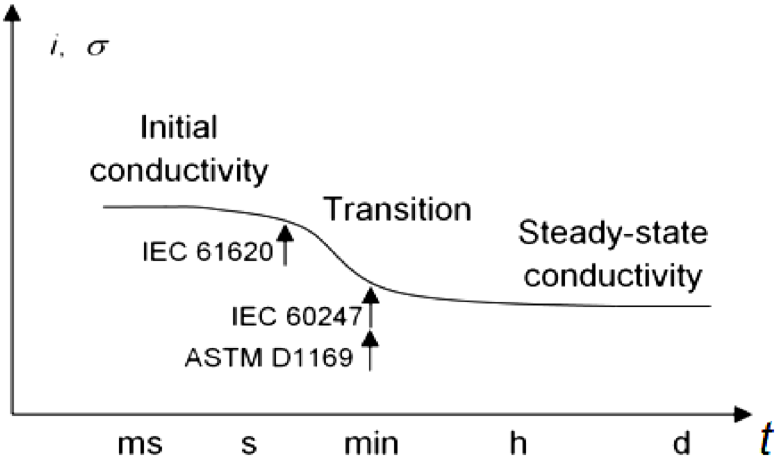

Figure 3.10 Typical relationships between the electrification time and conductivity [104], [110], [111].

At the instant of energization, the free charge drift dominates the magnitude of the conductivity. This process results in higher conducting current. This phase is defined as the initial conductivity and it is determined by the concentration of free charge carriers. When the majority of free charges deplete from the bulk liquid and accumulate at the electrodes, the current density and DC conductivity value decay with increasing electrification time. Eventually, the DC conductivity value of the material flattens and turns into steady-state conductivity.

In order to measure DC conductivity magnitude of samples, studies have introduced two approaches [112], [113]. They are Wheatstone bridge and series circuit.

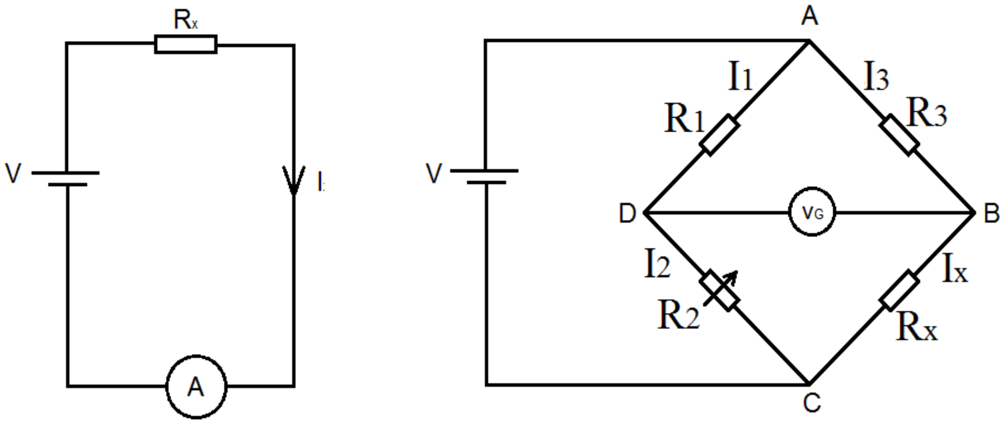

i. ii.

Figure 3.11 Circuit for testing DC conductivity

A diagram of a series circuit is shown in Figure 3.11i. This circuit is comprised of a DC power supply, the test sample (R_X) and an ammeter (A). By measuring the conducting current I the conductivity σ_E of the sample can be calculated by;

$$\sigma_E = \frac{1}{k_{\text{cell}}}\frac{I}{V} \tag{3.15}$$

where k_{cell} is a constant value for the test cell, it is calculated from the capacitance of the test cell by [111];

$$k_{\text{cell}} = \frac{C}{\varepsilon_0} \tag{3.16}$$

Various standards have defined the time of electrification and electric field for the series circuit. A measuring field strength is 100 V mm^{-1} with 5 second energization time is recommended by IEC 61620 [110]. IEC 60247 advises the electric field strength is from 50 to 250 V mm^{-1} and the electrification time is 1 minute [97]. ASTM D1169-11 suggests field strength is 200 to 1200 V mm^{-1} with 5 minutes of electrification. The standard also defines the uncertainty limitation, which is 35% of the highest value between two consecutive measurements.

The second method is the Wheatstone bridge which is shown in Figure 3.11ii. By measuring the material resistivity R_x the corresponding conductivity can be calculated. In the circuit R_1, R_2 and R_3 are known value resistors and R_2 is adjustable. A voltage meter is placed for measuring the voltage across the bridge from point B to D which is equal to;

$$V_G = \left(\frac{R_2}{R_1 + R_2} - \frac{R_x}{R_x + R_3}\right)V \tag{3.17}$$

When both sides of the circuit are balanced, there is no potential difference across the bridge and therefore the V_G is equal to zero, i.e.;

$$\frac{R_2}{R_1 + R_2} - \frac{R_x}{R_x + R_3} = 0 \tag{3.18}$$

$$R_x = \frac{R_3 R_2}{R_1} \tag{3.19}$$

Studies have shown that the Wheatstone bridge approach can measure the resistivity of a sample to high precision [114]. However, due to the transient behaviour of dielectric liquid conductivity, R_2 value also varies with time. Hence, a fast control system is required to link the value of R_x and R_2.

By comparing the above two measuring approaches, the series circuit is selected to measure the transient conductivity and Standard BS 60247 [97] directed the experimental procedures.

3.2.3 Apparatus and Settings

This section introduces the test cell and circuit. A cylindrical test cell is applied in this study. The sketch of the test cell and its dimension is shown in Figure 3.12.

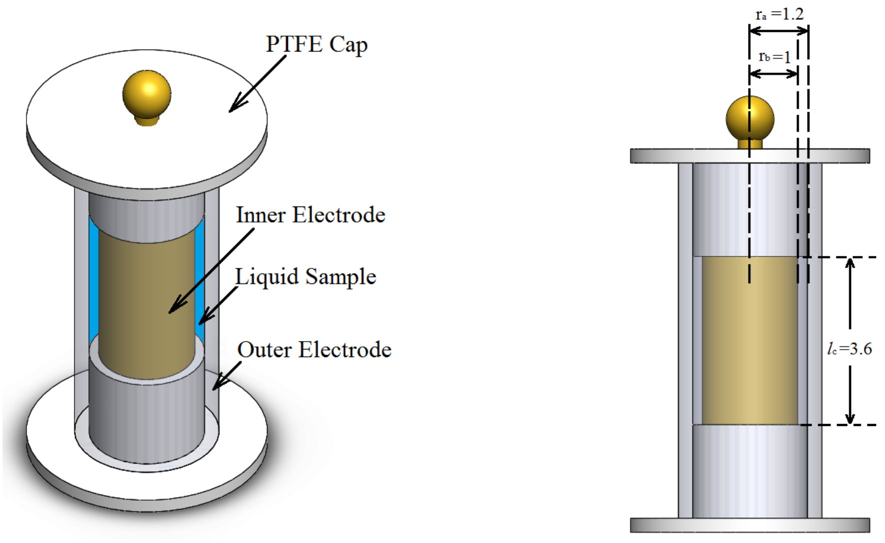

Figure 3.12 DC conductivity test cell and its dimension in (cm)

The test cell consists of two concentric electrodes and two polytetrafluoroethylenes (PTFE) caps. Two PTFE caps fixed the position of two electrodes. The gap between the two electrodes is a reservoir for the liquid sample. A spherical fitting was connected to the inner electrode for HV connection and avoids any corona discharge.

The conductivity of samples was measured by the series circuit, shown in Figure 3.13. A DC voltage source, a protection resistor (90 MΩ), a pico-ammeter and the cylindrical test cell were connected in series. A pico-ammeter was chosen for higher measurement precision. The inner electrode was connected to the high potential side and the outer electrode was serially connected to the low potential side via the pico-ammeter.

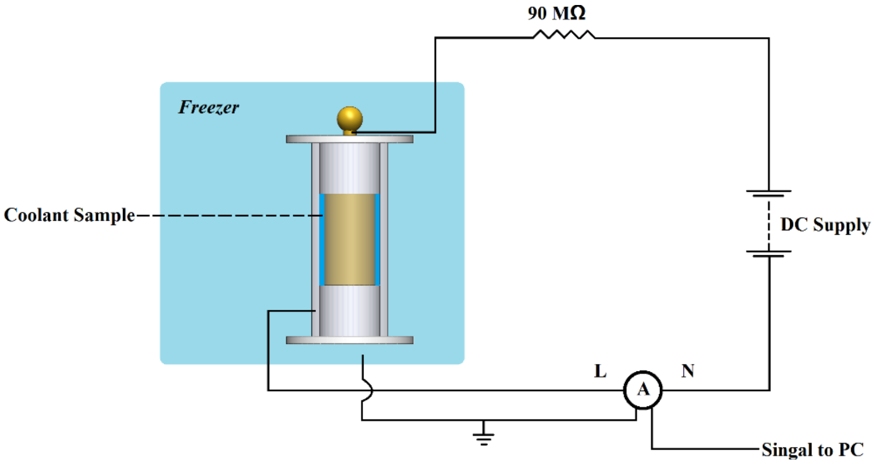

Figure 3.13 Series testing circuit with a cylindrical text cell

The DC conductivity of the dielectric liquid was calculated by substituting the conducting current and electrical potential into Equation 3.15. The capacitance of a typical cylindrical test cell, $k_{\text{cethe ll}}$ is equal to;

$$k_{\text{cell}} = \frac{2\pi\ \varepsilon_{\text{air}}\ l_{\text{c}}}{ln\dfrac{r_{\text{a}}}{r_{\text{b}}}} \tag{3.20}$$

where r_{a} and r_{b} are the outer and inner radius of the cylindrical test cell respectively, l_{c} is the length of the electrode and ε_{air} is the dielectric constant of air, which is equal to 1. According to the test cell dimensions k_{cell} value is equal to 1.241. After substituting k_{cell}, Equation 3.15 becomes;

$$\sigma_e = \frac{1}{1.241}\frac{I}{V}\ (S\ m^{-1}) \tag{3.21}$$

According to the Standard BS 60247 [97], the electric field was set equal to 250 V mm^{-1}. The energization time was set equal to 3 hours (10800 seconds), which is much longer than the standard requires, to investigate the conductivity decay process. During the experiment, sample DC conductivity was recorded every 12 seconds, hence the first measuring point was 12 seconds after energization.

3.2.4 Variable Control and Sample Preparation

Temperature and humidity are two variables that can affect the measurement. The variable control methods are as same as that introduced in section 3.1.4. The sample was injected into the test cell and left to settle for 2 minutes in order to remove any bubbles.

3.2.5 Results

An initial experiment was conducted to investigate errors of equipment. The DC conductivity of the HFE sample was measured on different days and the results are shown in Figure 3.14. The results show that the trend of the two set DC conductivities is similar but the value of the conductivity is slightly different. The possible reason for this variation could be either the different resistances that caused by the circuit connection or the temperature variation of two different days. The deviation of the steady state DC conductivity is less than 15%, which is in the standard acceptable range (<35%). Therefore, the errors in the experiment are acceptable.

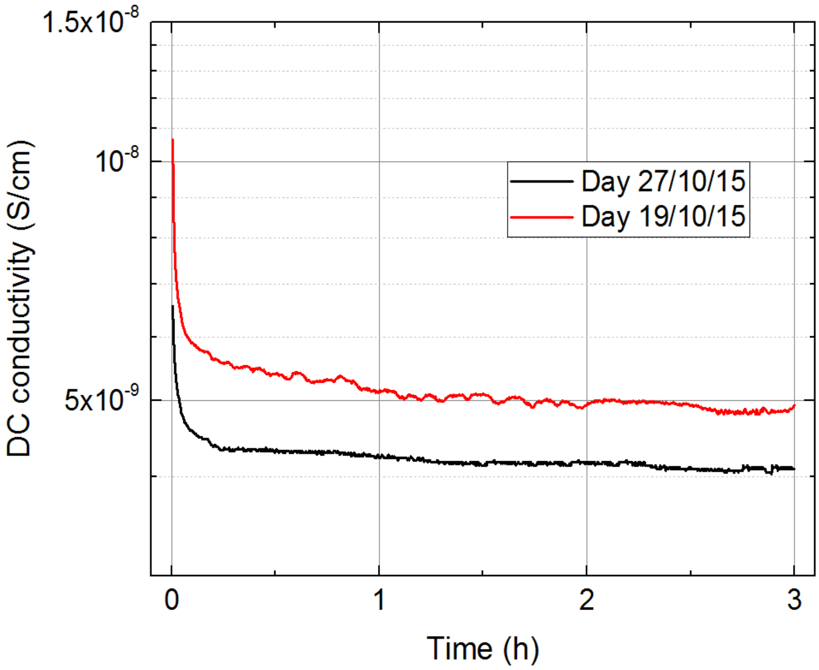

Figure 3.14 The conductivity of HFE at 295 K

After investigating the errors, both HFE and FK samples' conductivities have been measured, with a constant electric field (250 V mm^{-1}). In order to investigate the temperature effect on the DC conductivity, the experiments were conducted at different temperatures. The measured results are shown in Figure 3.15 and Figure 3.16. The results indicate that the higher temperature value results in a greater magnitude of steady-state DC conductivity

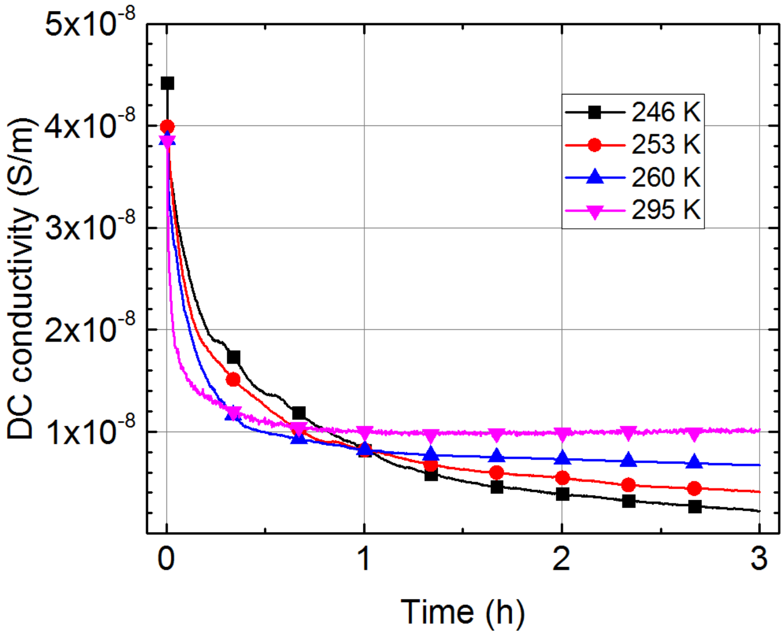

Figure 3.15 The DC conductivity of HFE at a different temperature under 250 V mm^{-1} field

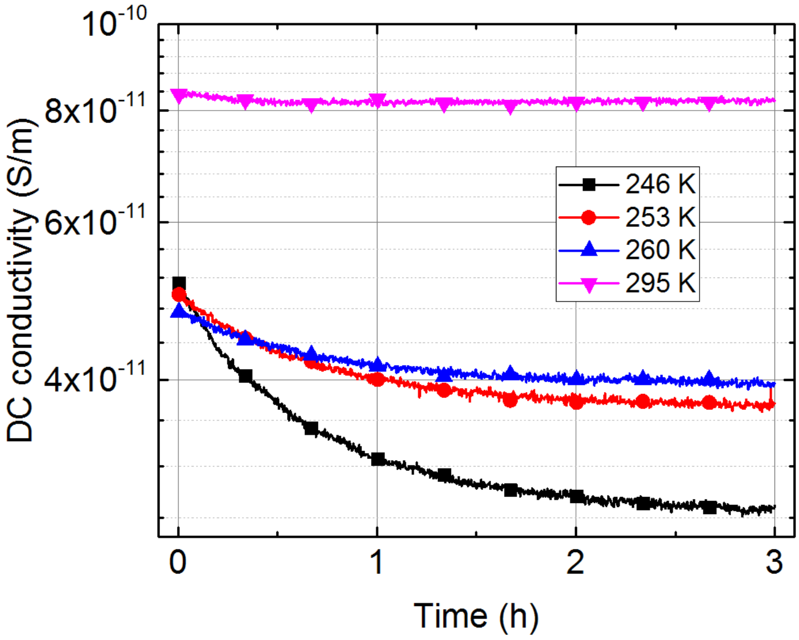

Figure 3.16 The DC conductivity of FK at a different temperature under 250 V mm^{-1} field

With an aim to investigate DC conductivity transient time, two conductivity ratios are plotted in Figure 3.17. From the plot, it can be seen that the short-term conductivity value of HFE (at 12s) is at least 4 times the 3 hours value. In contrast, the conductivity ratio of the FK sample is much lower than the HFE sample, which indicates the DC conductivity of the FK sample is less time-dependent. For both FK and HFE samples, the conductivity ratios after 1 hour are lower than 4, which indicates after one hour of energization the transient conductivity is close to the steady state conductivity.

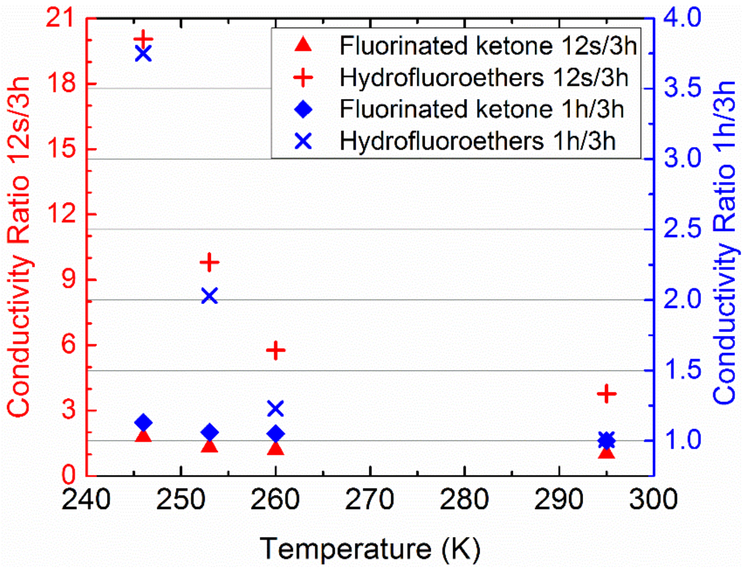

Figure 3.17 Conductivity Ratio of HFE and FK

3.2.6 Discussion of Results

Experimental results also showed the same conclusion with published literature [106], [107]. Specifically, DC conductivity magnitudes of both HFE and FK samples increase with increasing temperature, and this phenomenon can be explained by ion drift theory. Higher temperature results in a lower sample viscosity, which leads to a higher average charge mobility. The stronger charge mobility further increases the DC conductivity value of the sample. The results also show the transient time of conductivity drops with increasing temperature. This phenomenon is explained by the relationship published by [115], which is:

$$t_{transient} = \frac{l_{gap}}{\mu E} \tag{3.22}$$

where l_{gap} is a gap between two electrodes. From Equation 3.22 it can be seen that with a constant sample thickness and electric field, a higher temperature results in a greater ion mobility and further leads to a shorter transient time.

3.2.7 Summary of DC Conductivity Measurement

The measured values of FK and HFE samples' conductivities have a good agreement with the reference values [100]. The results indicate that, over the measuring temperature range, DC conductivity magnitude of HFE is at much higher than FK. Furthermore, the HFE's DC conductivity value is more time-dependent than that of FK. One possible reason for this is that the charge concentration of FK is lower than that in the HFE. The temperature effect on the DC conductivity of the samples is also been investigated. The results show that a higher temperature contributes to a greater value of DC conductivity of both HFE and FK samples.

3.3 AC Electrical Breakdown Strength

This section discusses the AC dielectric strength of HFE and FK samples at different temperatures.

3.3.1 Introduction

The dielectric strength of a material is defined as the maximum electric field that dielectric material can withstand without losing its insulating characteristics. When the applied field stress exceeds the material dielectric strength, the dielectric either temporarily or permanently loses its insulating property by forming a conductive channel. The dielectric strength values of both HEF and FK samples have not been widely published, with only a few reference data that provided by the manufacturers [100]. The data sheets present the breakdown fields of HFE and FK samples are 11.02 kV mm^{-1} and 15.7 kV mm$^{- 1}$ respectively.

3.3.2 Methodology and Standard

The typical relationship between the voltage and current of a dielectric material during the breakdown process is shown in Figure 3.18. Initially, there are a few charge carriers inside the dielectric material, caused by photoionization. These charge carriers move toward the electrodes by electrostatic force producing the initial current. With increasing electric field, the charge carriers obtain higher velocity due to the greater electrostatic force, which results in a higher current. This phenomenon is demonstrated by curve O-a in Figure 3.18. After the initial current increase, the current is independent of the applied voltage as shown by the curve a-b in Figure 3.18. This is because there are no free charge careers inside the dielectric fluid. Consequently, the current magnitude is only influenced by the external photoionization intensity and the material presents good insulating characteristics. This region is defined as the non-self-maintained discharge area. By further increasing the applied voltage, electrons are accelerated to a higher velocity, which triggers inelastic collisions between neighbouring electrons. These inelastic collisions introduce more electrons, which participate in the reaction and further increases the current as shown by the b-c curve in Figure 3.18. The process is described as an avalanche. By continually increasing the voltage, the dielectric material eventually cannot resist electric stress hence, the current increases dramatically. This is defined as an electric breakdown. A breakdown is always accompanied by sound and light energy as the conducting path between the two electrodes forms, and gas expansion occurs. After the breakdown, the conducting current is not dependent on external photoionization and is positively correlated to an external voltage. Hence, it is defined as a self-maintained discharge.

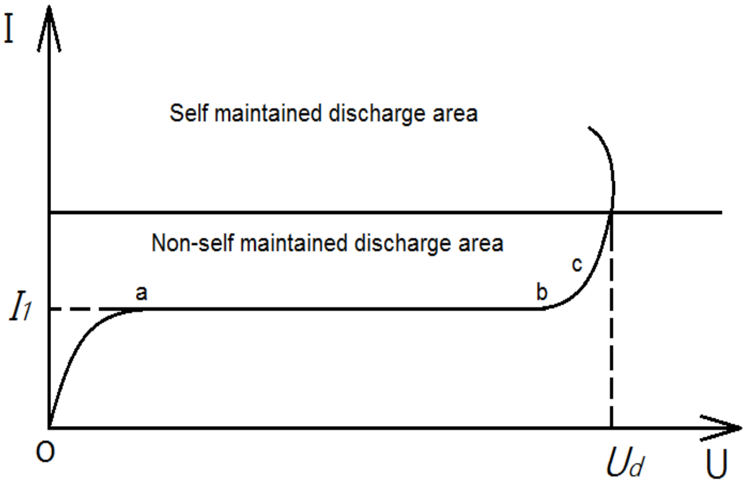

Figure 3.18 Typical V-I characteristic of dielectric material

Measuring the dielectric strength of a liquid sample is more difficult than in solid or gaseous materials. The main reason is that the breakdown phenomenon in the dielectric liquid is more dependent on random factors. Among these factors, the most important variables are temperature, impurity, electrode configuration and voltage ramp rate [116], [117]. These factors have been well defined by various standards.

In this study, the experiment operation referred to Standard BS 60156 [118]. The testing voltage was provided by an AC transformer and the measuring frequency was 50 Hz. The electric potential started from an initial voltage and was gradually increased with 2 kV s^{-1} ramp rate. The trigger current was defined as 5 mA, which is lower than the Standard value of 10 mA [118]. A lower value was chosen because it is high enough to identify a breakdown phenomenon while reducing the risk of a liquid spill.

3.3.3 Apparatus and Settings

The sample AC dielectric strength was measured in a cylindrical polycarbonate test cell, which is shown in Figure 3.19. The test cell has a 30 mm inner diameter that holds 25 ml samples for each test. The electrodes are two 25 mm diameter stainless steel ball bearings each in contact with a copper rod and sheet to provide an electrical connection. A micrometre gauge was used to measure a 2.5 mm separation along the central axis of spherical electrodes.

The dielectric strength measurement circuit, as shown in Figure 3.20, consists of a transformer control unit (TCU), a variable transformer, a 230 V/100 kV step-up transformer, a current limiting resistor R_1 and the liquid test cell [119].

To obtain an average value of AC dielectric strength, 25 breakdown measurements were registered for both HFE and FK liquids in a set of 5 measurements. Testing samples and electrodes were changed after 5 measurements. During each set measurement, the applied voltage was increased from 5 kV at a rate of 2 kV s^{-1} until breakdown occurred. The breakdown value isolated the high voltage supply from the test sample was defined by a trigger current, which is set equal to 5 mA. When the cell current is greater than the trigger current, the TCU interrupts the supply voltage to the step-up transformer and the digital voltmeter, connected to the secondary transformer tap, records breakdown voltage.

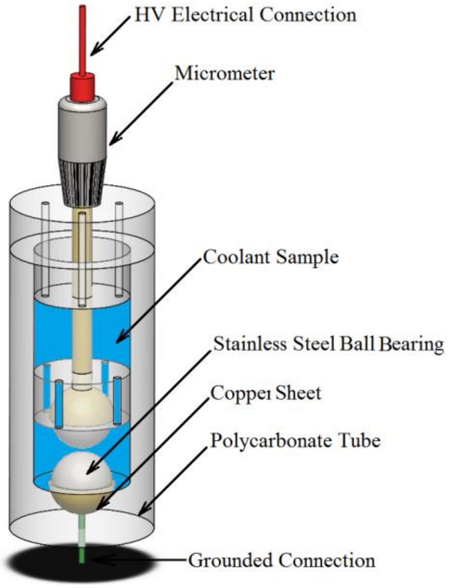

Figure 3.19 AC dielectric strength cylindrical test cell

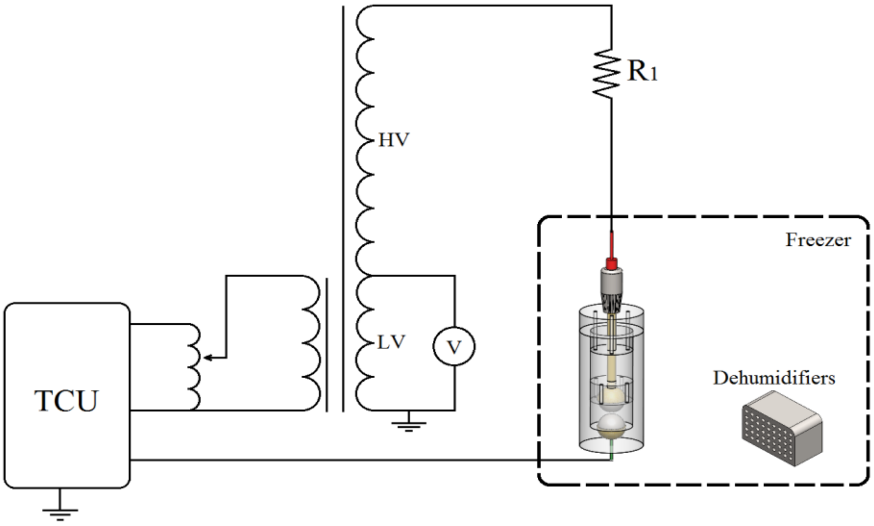

Figure 3.20 Schematic of dielectric breakdown circuit and test cell [119]

3.3.4 Variable Control and Sample Preparation

Similar as the FDS measurement, temperature and humidity are the two main variables in the measurement. Literature indicates temperature has a significant impact on the sample's water content and viscosity, which further changes the sample dielectric strength [120], [121].

In this study, the AC breakdown measurements were conducted in a modified freezer. The temperature and humidity control results have been shown in Figure 3.2 and Figure 3.3.

3.3.5 Results

The AC dielectric strength is a statistical value, but it can indicate liquid dielectric performance and assist HV equipment design. The Weibull distribution is widely used in reliability and life data analysis due to its versatility and it was used to show the breakdown probability of HFE and FK samples. For this study, 3-parameters Weibull plot was conducted. Compared with 2-paramters plot, 3-parameters Weibull plot can fit the data point into a curve, instead of a line, through the data points using nonlinear regression. The density function of a 3- parameters Weibull plot is according to

$$f(x_{BD}) = \frac{\beta_{BD}}{\alpha_{BD}} \left(\frac{x_{BD}-\gamma_{BD}}{\alpha_{BD}}\right)^{\beta_{BD}-1} e^{-\left(\frac{x_{BD}-\gamma_{BD}}{\alpha_{BD}}\right)^{\beta_{BD}}} \qquad (3.23)$$

where $f(x)$ is the cumulative probability of breakdown, x_{BD} is the AC breakdown voltage, α_{BD} is the scale parameter, β_{BD} is the shape parameter and γ_{BD} is the location parameter. . The Gauss-Newton method can be used to solve for the parameters, α_{BD}, β_{BD} and γ_{BD}, by performing a Taylor series expansion on F $(x_{BD}, \alpha_{BD}, \beta_{BD}, \gamma_{BD})$. Then the nonlinear model is approximated with linear terms and ordinary least squares are employed to estimate the parameters. This procedure is iterated until a satisfactory solution is reached. The AC breakdown results of HFE and FK samples are plotted in Figure 3.21 and Figure 3.22. In figures, solid lines are adjusted lines and dashed lines are unadjusted lines.

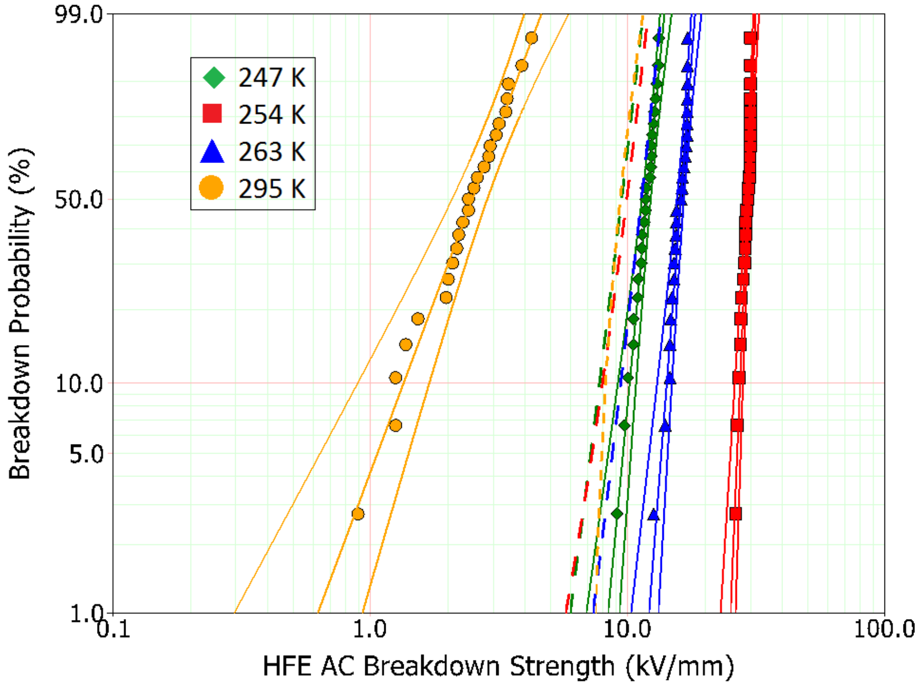

Figure 3.21 AC breakdown Weibull plot of HFE sample

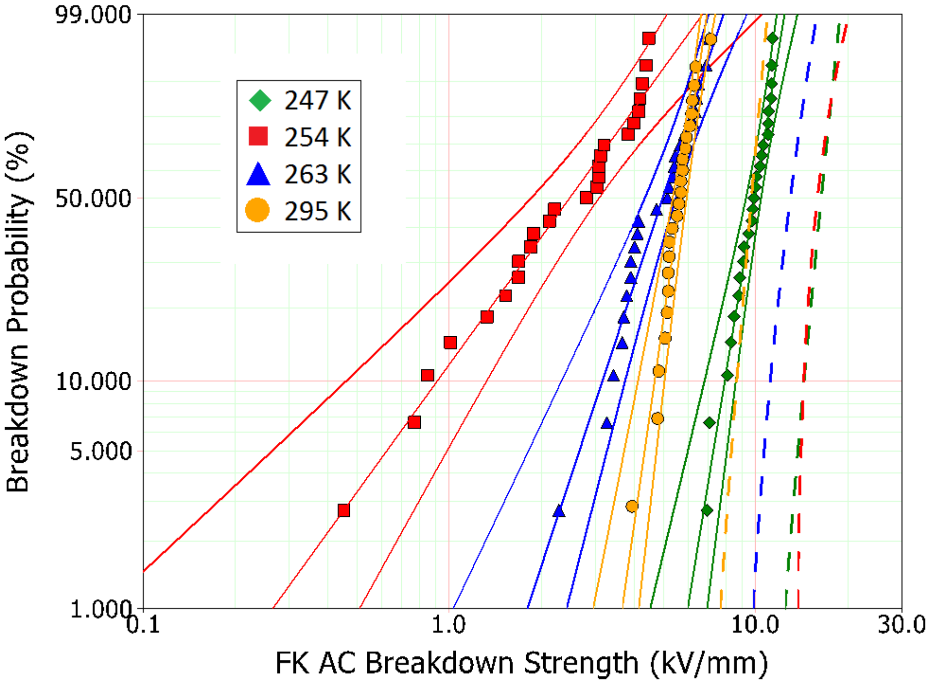

Figure 3.22 AC breakdown Weibull plot of FK sample

The corresponding breakdown values are summarised in Table 3-1. With 0.9 reliability, were summarized. It can be seen that at ambient temperature (i.e. 295 K), HFE and FK samples have relatively close AC breakdown values, which are around 8.5 kV mm^{-1}. Furthermore, reliable breakdown voltages of the HFE sample is independent of the temperature, as reliable breakdown voltages (BDV) of both HFE and FK samples contrast; the reliable breakdown voltages of FK sample has a distinct increase at a lower temperature. Hence, decreasing temperature could be a potential way to increase FK reliable breakdown value.

Table 3-1 Electrical breakdown results

Temperature	HFE				FK			
	α_{BD}	β_{BD}	γ_{BD}	Reliable BDV (R=0.9)	α_{BD}	β_{BD}	γ_{BD}	Reliable BDV (R=0.9)
295 K	3.06	2.80	6.85	8.20	9.61	5.91	3.99	8.66
263 K	14.88	16.4	-4.78	9.38	4.15	5.43	7.98	11.14
254 K	27.5	29.6	-19.35	7.97	1.89	2.99	13.42	14.33
247 K	12.13	12.24	-2.40	7.76	8.41	10.35	6.45	14.37

3.3.6 Discussion of Results

Published literature has reported three typical temperature dependent phenomena, which affect liquid dielectric strength. The breakdown voltage of an insulating oil increases with high temperature [122]. This is caused by the reduction of water content with increasing temperature. However, for low boiling point fluids, low temperatures contribute to high values of breakdown strength [123]. This is because the low temperature reduces both potential bubble size and numbers in the liquid. Furthermore, the low-temperature samples have a higher viscosity. Hence, the average charge mobility decreases and the conducting path is harder to form, which results in a higher dielectric strength.

Since both HFE and FK samples are not hydrophilic, the temperature has minimal effect on sample water content. Therefore, temperature dependent dielectric strength of FK, could be caused by the reduction of charge mobility, which is due to the samples higher viscosity at low temperature. The HFE sample has a comparable viscosity with FK sample at ambient temperature. However, at low temperatures, there was not an increase in dielectric strength. The possible reason is the conducting behaviour of HFE sample. Since the HFE sample has reasonably high conductivity, during the breakdown test the high current passing through the sample may cause local heating and produce bubbles, which results in a low dielectric strength.

3.3.7 Summary of AC Electric Breakdown Strength measurement

At ambient temperature, reliable breakdown voltages of both HFE and FK samples are 8.2 kV mm^{-1} and 8.66 kV mm^{-1} respectively. Compared with HFE, FK has a higher dielectric strength with lower fluctuation at ambient temperature.

The dielectric strength of FK is negatively correlated with increasing temperature, this is because the lower temperature sample has a higher viscosity, which further results in a lower charge mobility. The temperature does not affect the dielectric strength of the HFE sample significantly. The possible reason could be attributed to the conducting behaviour of HFE.

3.4 Electrical Ageing through Repeated Breakdown

This section investigates the repeated breakdown effects on HFE and FK samples' dielectric behaviours.

3.4.1 Introduction

The processes of electrical breakdown in candidate fluids are not fully understood. A number of factors have been identified which may affect fluid dielectric strength such as fluid impurity (water content), bubbles or electrode roughness [123], [124]. Furthermore, both HFE and FK samples have long molecule chain, which is shown in Figure 3.23. The discharge or local breakdown may occur in the dielectric fluid, the hypothesis is that breakdown energy results in some of the C-C or C-H bonds being broken and thereby producing extra ions [124]. Hence, these ions, which are generated by the breakdown process, may decrease dielectric strength. At present, results from the repeated breakdown effects on HFE and FK have not been published. Hence, electric breakdown ageing has been conducted and the dielectric strengths according to different breakdown times have been recorded.

i.

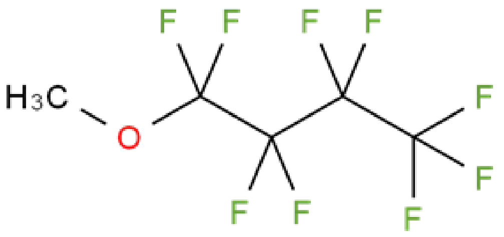

ii.

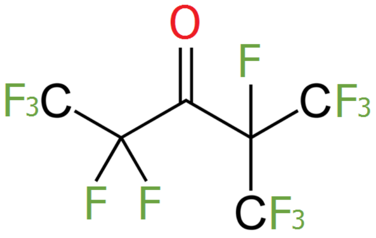

Figure 3.23 Sample molecule chain i. HFE sample ii. FK sample

3.4.2 Methodology and Standard

The repeated breakdown strengths were recorded according to the 5 set breakdown phenomena. The DC conductivity values of breakdown aged samples were also measured. Furthermore, tentative experiments show the transmittance of the HFE sample was changed with the increasing breakdown times. In order to quantify the samples perceived transmittance, the samples' transparencies were measured by ultraviolet-visible spectroscopy (UV/Vis).

3.4.3 Apparatus and Setting

The UV/Vis spectroscopies were performed using a Perkin-Elmer Lambda 35 instrument. The schematic of a spectrophotometer is shown in Figure 3.24. The sample was shaken sufficiently before being injected into a quartz test cell, which has a 10 mm path length. In this experiment, the double beam light was produced by a tungsten bulb, and the light wavelength is from 300 to 1100 nm, which is primarily used for liquid samples.

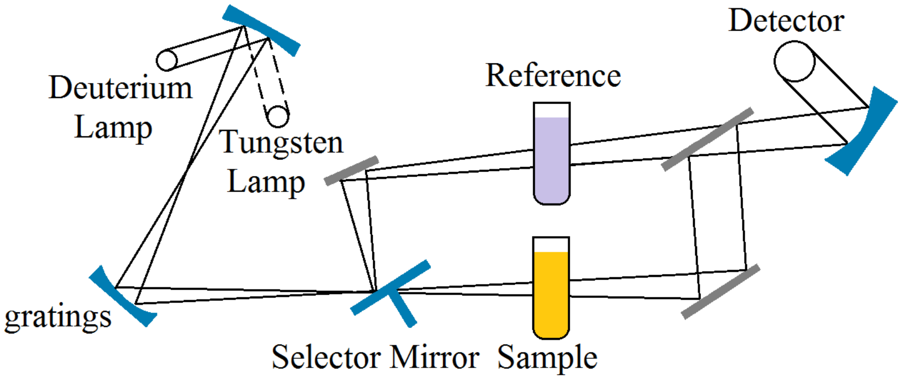

Figure 3.24 Simplified schematic of a double beam UV/Vis spectrophotometer

3.4.4 Variable Control and Sample Preparation

Repeated AC breakdown and DC conductivity were conducted at ambient temperature (i.e. 295 K). Twenty repeated electrical breakdowns were applied to HFE and FK samples. During these experiments, samples were taken after 5 repeated breakdowns to assess any change in dielectric performance.

3.4.5 Results

After 20 repeated electrical breakdowns, the most notable phenomenon is the change in transmittance of the HFE samples as shown in Figure 3.25.

$$\text{Virgin sample} \xrightarrow{5\ repeated\ breakdowns} \text{20 repeated breakdowns}$$

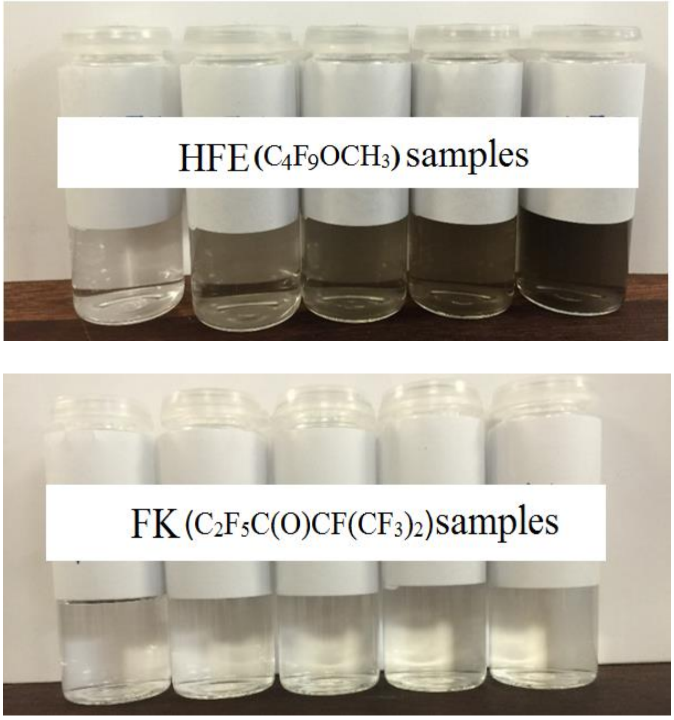

Figure 3.25 Sample colour after repeated electric breakdowns

The results show that the HFE sample becomes visibly darker after 20 repeated breakdowns, due to the suspended black particulates. Over a period of seven days, the particulate settled at the bottom of the phials, and the HFE fluid became clear again. On the contrary, the colour of FK samples did not change after 20 repeated breakdowns.

With the aim of quantifying sample transmittance, light transmittance through the samples of different light wavelengths was measured by UV/Vis spectrometry. The results are shown in Figure 3.26. The results show that the HFE transmittance drops dramatically with increasing numbers of repeated breakdown at all light wavelengths. This is because of the black particulates, produced by repeated electrical breakdown, block the light passing through the sample. However, compared with the HFE sample, the transmittance boundaries of FK sample remain at approximately 88 % and independent of the numbers of electrical breakdowns. This result indicates that minimal numbers of particles were generated in FK in accompaniment with an electrical breakdown.

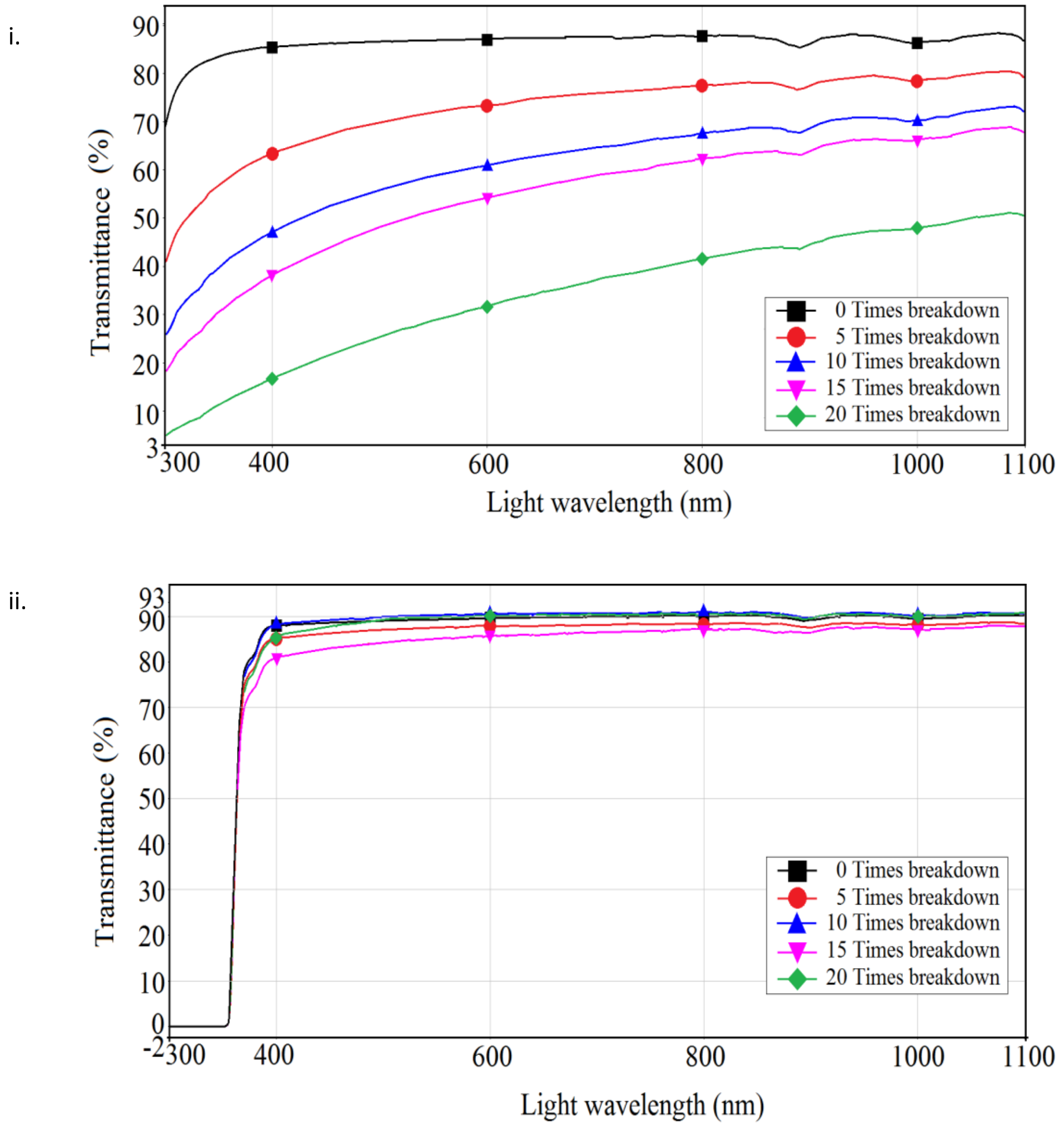

Figure 3.26 UV/Vis data from the homogenised sample after the repeated electric breakdown;

i. HFE sample ii. FK sample

The DC conductivity of both HFE and FK samples after different numbers of breakdown have been registered. The results are shown in Figure 3.27 and Figure 3.28, which indicate that the value of the DC conductivity of HFE sample becomes larger with the increasing numbers of repeated electrical breakdown. This result indicates that the black particulates, generated by the repeated breakdowns, are not only reducing sample transmittance but also contribute to a higher sample DC conductivity. Contrarily, repeated breakdown did not have a significant effect on FK samples' DC conductivity results. Hence, it shows that repeated electrical breakdowns did not generate additional conductive particulates in FK sample.

Finally, a comparison of breakdown strength from each different set, i.e. 5 repeated electrical breakdowns, is shown in Figure 3.29 and Figure 3.30. The results indicate that after 20 repeated breakdowns, for both HFE and FK samples, although the DC conductivity values of HFE increased with repeated breakdown, the AC dielectric strength value did not degrade. The AC dielectric strength of FK sample is also nearly independent of numbers of repeated breakdown.

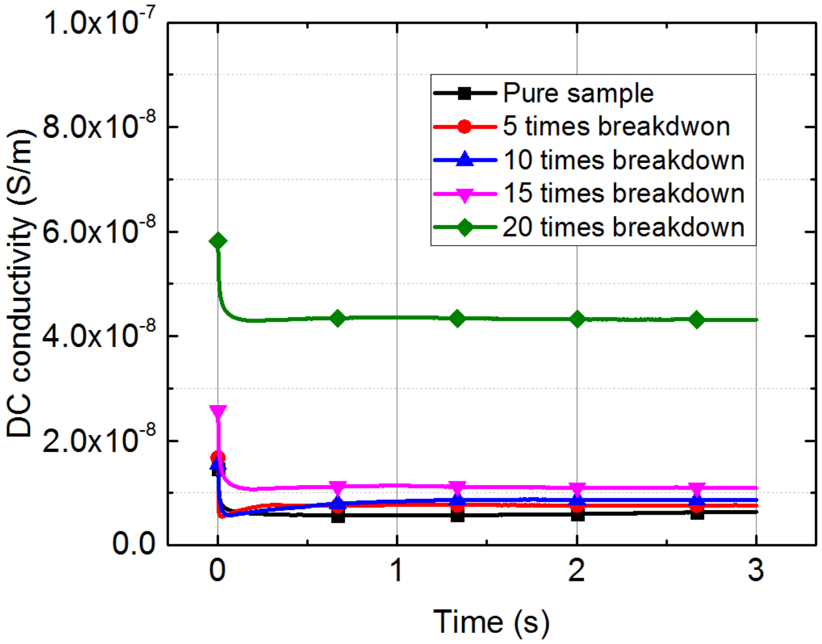

Figure 3.27 DC conductivity value of HFE after different numbers of electrical breakdown

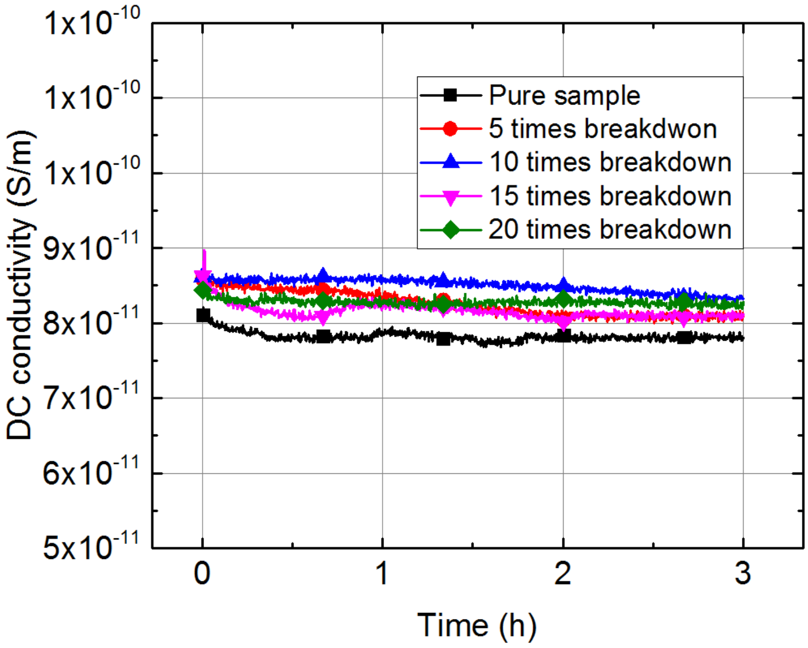

Figure 3.28 DC conductivity value of FK after different numbers of electrical breakdown

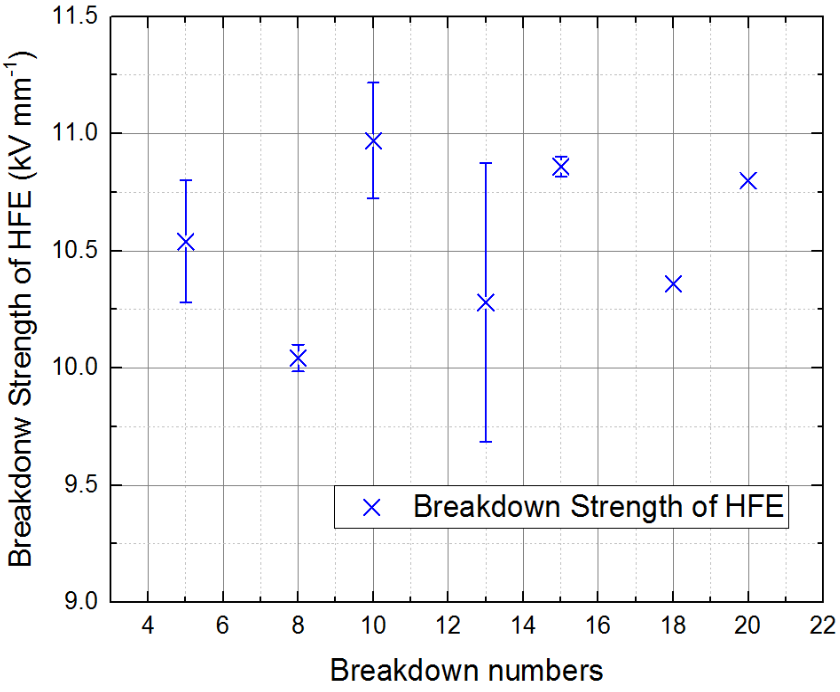

Figure 3.29 HFE dielectric strength of repeated breakdown

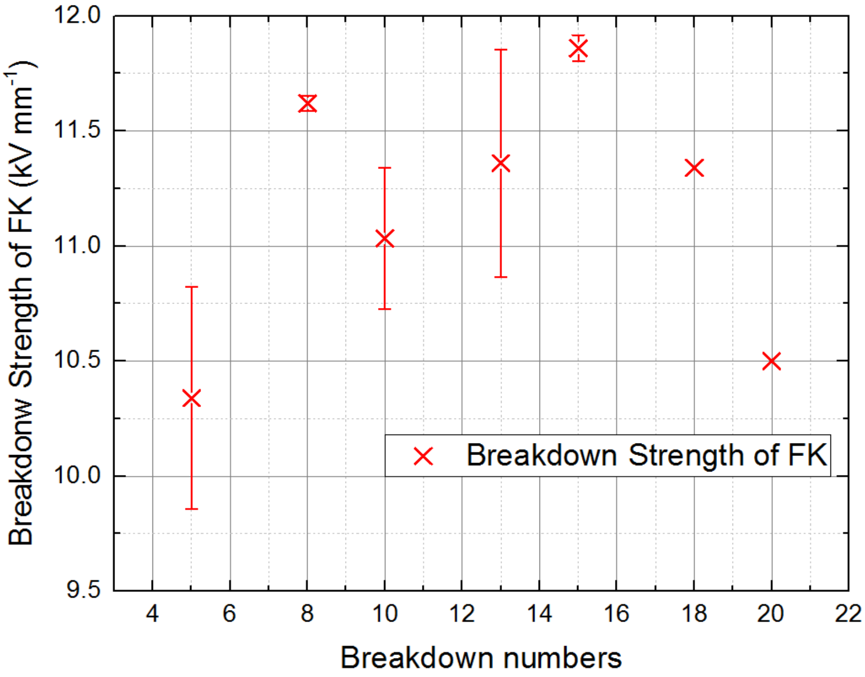

Figure 3.30 FK dielectric strength of repeated breakdown

These experimental results indicate that the repeated breakdowns have a minimal effect on AC dielectric strength of both HFE and FK samples. However, the DC conductivity value of HFE becomes larger with repeated breakdowns due to the creation of conducting particulates.

3.4.6 Summary of Repeated Breakdown Measurement

After repeated breakdown, the colour of the HFE sample becomes dark and there is not a significant transmittance variation of FK sample. The transmittance change of the HFE sample is due to the particulates that are generated by the electrical breakdown. The DC conductivity measurements further prove that the particulates in the HFE sample contribute to a higher value of DC conductivity. The conducting particulates did not form a conducting path and therefore the breakdown ageing does not present a significant degeneration of both HFE and FK breakdown strengths.

3.5 Summary

Three dielectric properties of HFE and FK fluids have been measured at different temperatures.

AC spectroscopy results show that FK coolant behaves as a dielectric fluid whereas HFE sample is an ion conductor. In addition, higher temperature results in a lower value of real part of the complex permittivity, while it leads to a greater value of imaginary part of the complex permittivity for both HFE and FK samples.

The DC conductivity results show that FK sample has a significant lower DC conductivity than HFE coolant. The conducting current of the FK fluid is less time-dependent than HFE sample. A higher temperature results in a larger value of DC conductivity for both HFE and FK samples.

The AC dielectric strength results indicate that at ambient temperatures, HFE and FK samples have comparable values, which are approximately 10 kV mm^{-1}. However, reducing temperature is an effective method to increase the breakdown voltage of the FK sample. In contrast, the breakdown voltage of HFE fluid is less temperature dependent.

Repeated breakdown measurement demonstrates that breakdown ageing does not show a significant effect on the value of AC dielectric strength of both HFE and FK samples. However, repeated breakdown can generate conducting particulates in the HFE sample. These conducting particulates contribute to a larger DC conduction of HFE sample and greater loss. In comparison, after repeated breakdown, there is no significant change in the FK sample.

Chapter 4

The Effect of DC field on the Bubble Motion

When you can measure what you are speaking about, and express it in numbers, you know something about it - Lord Kelvin

This chapter presents an investigation to observe FK thermal bubble motion under different DC electric fields.

4.1 Introduction

It is known that heat extraction, achieved through the phase change process, can be promoted due to the presence of a DC electric field [51], [67]. This is attributed to electrohydrodynamics (EHD). In addition, studies have reported that EHD forces, acting upon a thermal bubble, may lead to the formation of gas columns [10]. Since in the most case the dielectric strength of gas is much lower than liquid dielectric strength, the gas columns could provide an electrical breakdown path. Hence, EHD may be a cause of electrical insulation failure in two-phase gas liquid systems [11], [72]. For HV thermosyphon applications, the coolant is both a heat transfer medium and the electrical insulation. Therefore, it is necessary to investigate thermal bubble motion in the coolant.

In this study, Fluorinated Ketone (FK) is selected as the research sample. The reason behind the material selection is due to its dielectric behaviour, which was detailed in Chapter 3. Hydrofluoroether (HFE) shows a high relative permittivity in the low-frequency range and behaves as an ion conductor. Therefore, with a high electric field, the conducting current generates thermal turbulence, which adversely effects on bubble trajectory prediction. In contrast, FK shows a well-defined relative permittivity over the low frequency range and behaves like a dielectric fluid.

4.2 Electrohydrodynamics (EHD)

Electrohydrodynamics is the study of the motion of particles and their interactions with electric fields and the surrounding fluid. By neglecting hydro-stir and bubble collisions, an expression of electric body force density can be expressed by the following equation [125]–[127]:

$$\overrightarrow{F_{EHD}} = \underset{\substack{\uparrow \\ \text{Coulomb force}}}{\boxed{q_v \vec{E}}} \; \underset{\substack{\uparrow \\ \text{Gradient force}}}{\boxed{-\frac{1}{2}\vec{E}^2 \, \nabla \varepsilon_l}} \; \underset{\substack{\uparrow \\ \text{Electrostrictive force}}}{\boxed{+\frac{1}{2}\nabla\left[\vec{E}^2\left(\frac{\partial \varepsilon}{\partial \rho_l}\right)\rho_l\right]}} \tag{4.1}$$

The electric body forces can be further divided into three forces. They are Coulomb force, gradient force and electrostriction force.

The Coulomb force is an electrophoretic force, which is caused by the generation of net free charges, which is determined by the scale of relaxation time and bubble detachment period. The method has been discussed in Section 2.4.2.1. The Coulomb force only contributes to the charged bubbles and vice versa.

The gradient force is a dielectrophoretic force, which is exerted on an insulating material in a non-uniform electric field. The gradient force effects by the spatial gradient of permittivity due to the multiple phases, hence it does not require the bubble to be charged.

The last term is the electrostrictive force, which is also a dielectrophoretic force. It is caused by the variation of dielectric permittivity and non-uniformity of the electric field. This force can be thought of as the compressing pressure on a bubble, which results in a bubble deformation.

In this study, only Coulomb force and gradient force are considered. The electrostrictive force is neglected to simplify the prediction. The reasons for this are because the bubble size is relatively small and this force cannot generate any vorticity in the fluid.

4.3 Thermal Bubble Motion in a Uniform Electric Field

This section aims to investigate FK thermal bubble motion under the uniform electric field. The gradient force acting on a spherical bubble is caused by the inhomogeneous electric field. Hence, under the uniform electric field, only the Coulomb force leads to bubble motion.

4.3.1 Electrode Arrangement and Cartesian coordinate system

Parallel plates and co-axial cylinders are the two typical arrangements used to create the uniform electric field. With the aim to observe bubble motion conveniently, in this study, the parallel plate arrangement was selected and is shown in Figure 4.1. In order to study the thermal bubble motion, force analysis is indispensable. To assist force analysis, a three-axis

Cartesian coordinate system is defined. As shown in Figure 4.1, the *x*-axis is normal to the ground plate, the *y*-axis is vertical upwards, and the *z*-axis is along the parallel side of the grounded plate.

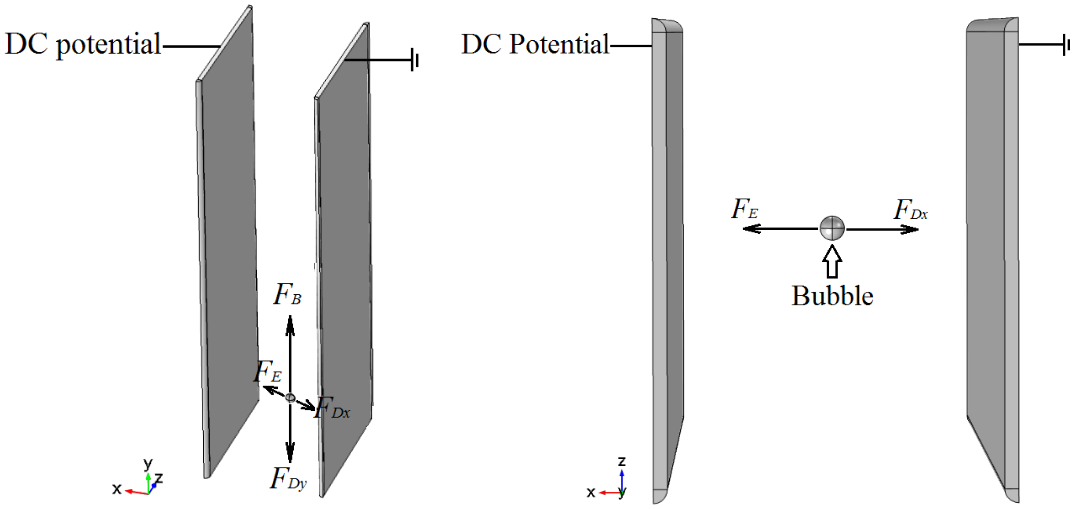

Figure 4.1 Parallel plate electrode arrangement and Cartesian coordinate system

4.3.2 Theoretical Analysis of Bubble Motion under Uniform DC Field

This section aims to give a force analysis on each bubble moving direction. Two forces result in bubble motion along the *x*-axis. They are EHD force and drag force. In this case, the EHD force is the Coulomb force. The magnitude of the EHD force is calculated by;

$$|F_{EHD}| = |q_b|E \tag{4.2}$$

where q_b is the charge magnitude on the thermal bubble. The direction of the Coulomb force is determined by the net charge polarity. If the charge acting on the bubble is positive the force is applied in the same direction as the field lines and vice versa.

The drag force resists bubble acceleration and therefore it is in opposite direction with bubble velocity. The magnitude of the drag force $\overrightarrow{F_{Dx}}$ is attributed to the fluid dynamic viscosity, bubble size and bubble instant velocity. The bubble *x*-direction drag force is defined as;

$$\overrightarrow{F_{Dx}} = -4\pi\eta_l R_b \vec{\dot{x}} \tag{4.3}$$

where, $\vec{\dot{x}}$ is the bubble horizontal velocity.

Buoyancy and drag force are the two forces that result in vertical bubble displacement. The magnitude of the buoyancy force is caused by the difference in density between the gas-liquid two phases. Since the gas density is smaller than liquid density, the buoyancy direction is against the gravity direction. The magnitude of buoyancy is calculated [128];

$$\overrightarrow{F_B} = \frac{4}{3}\pi\, R_b{}^3(\rho_l - \rho_g)\,\vec{g} \tag{4.4}$$

The drag force in *y*-direction restricts bubble vertical motion. It can be calculated by;

$$\overrightarrow{F_{Dy}} = -4\pi\eta_l R_b \vec{\dot{y}} \tag{4.5}$$

where $\vec{\dot{y}}$ is the bubble vertical velocity.

The force acting on the *z*-direction results in bubble movement parallel to the side of the plate electrode. The principle forces in this direction are the same as those in the *x*-direction. Assuming the initial bubble location is on the symmetric plane between the electrodes. The forces acting upon the bubble in this direction are balanced, which results in the net force in the *z*-direction being zero.

This is the ideal case for this study. Hence, the bubble displacement in the *z*-direction is minimal and will not be discussed further in this study. Nevertheless, in reality, the bubble may not always be on the symmetric plane between electrodes due to convection heat flux, a slight displacement will cause a force unbalancing in this direction.

According to Newton’s law, by substituting previous forces, the kinematic equations for both *x* and *y* directions are defined as follows;

x-direction:

$$M_{eff}\,\vec{\ddot{x}} = \overrightarrow{F_{EHD}} + \overrightarrow{F_{Dx}} \tag{4.6}$$

$$M_{eff}\,\overrightarrow{\ddot{x}} = |q|E - 4\pi\eta_l R_b \vec{\dot{x}} \tag{4.7}$$

y-direction:

$$M_{eff}\,\vec{\ddot{y}} = \overrightarrow{F_B} + \overrightarrow{F_{Dy}} \tag{4.8}$$

$$M_{eff}\,\vec{\ddot{y}} = \frac{4}{3}\pi\, R_b{}^3(\rho_l - \rho_g)\,\vec{g} - 4\pi\eta_l R_b \vec{\dot{y}} \tag{4.9}$$

In the above equations, M_{eff} is the effective mass of a spherical bubble in motion, which can be calculated using [128].

$$M_{eff} = \frac{4}{3}\pi\, R_b{}^3\left(\rho_g + \frac{1}{2}\,\rho_l\right) \tag{4.10}$$

After discussing the theoretical kinematic equations, it can be seen that the bubble motion depends on gas-liquid material properties. In addition, the bubble parameters, such as bubble size and charge characterises, also have a great effect on bubble behaviour. To investigate these unknown factors, an experimental platform was constructed that allows observation of single bubble movement under a uniform DC field.

4.3.3 Experimental Analysis of Bubble Motion under Uniform DC Electric Field

The experimental platform is shown in Figure 4.2. The platform consists of three main parts, which are a custom-built glass vessel, parallel plate electrodes and a high-speed image system.

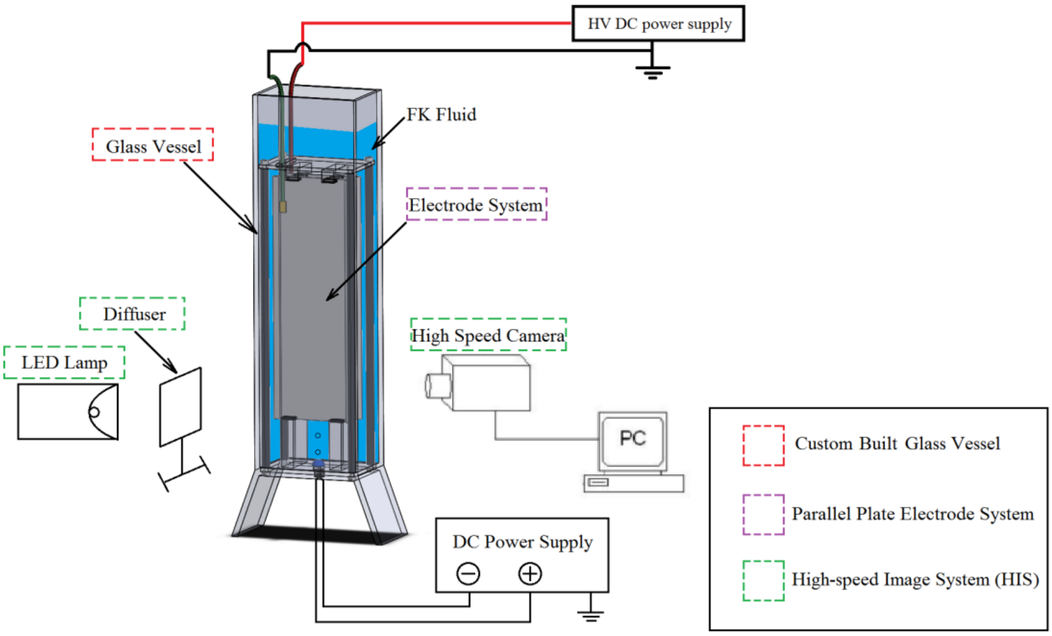

Figure 4.2 Parallel plate experimental platform arrangement

The experiments were conducted in an 84×54×300 mm custom-built cuboid vessel, which is shown in Figure 4.3.

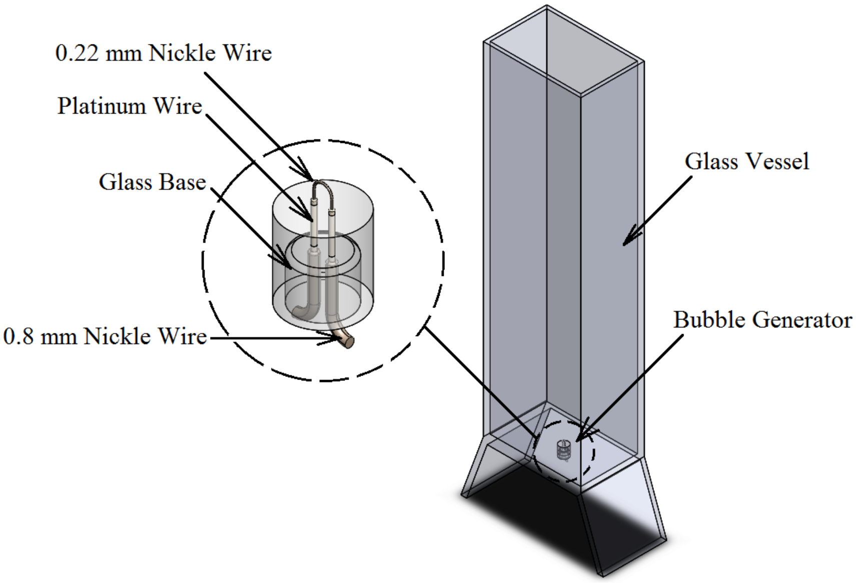

Figure 4.3 Custom build cuboid glass vessel

The vessel was made of optical glass that makes it possible to observe bubble motion. In order to generate a thermal bubble, a bubble generator was joined in the centre of the vessel bottom surface. The bubble generator was based on a glass tube. Two platinum wires were embedded within the glass tube. The platinum material was chosen because its thermal expansion is as same as the glass. Hence, differential expansion is minimized and it avoids any damage to the glass base. Two different diameter nickel wires are then connected at either end of the platinum wire. The 0.8 mm diameter wire was connected to a DC supply. The 0.22 mm diameter wire is the heating element, which was submerged in the FK liquid. The smaller diameter results in a higher resistance, which increases the thermal loss so that generates more heat and produces bubbles.

A parallel plate electrode system was manufactured to create a uniform DC field. The sketch of the electrode system is shown in Figure 4.4. The electrode system consists of two identical 195×65×2 mm aluminium plates. The edges of the plates were curved to reduce the surface charge density and avoid any discharge. There are two pairs of plate slots allowing 5, 12, 20 mm electrode separations and they hold the electrodes in parallel. Two cables were attached to the electrodes back surface for the electrical connection.

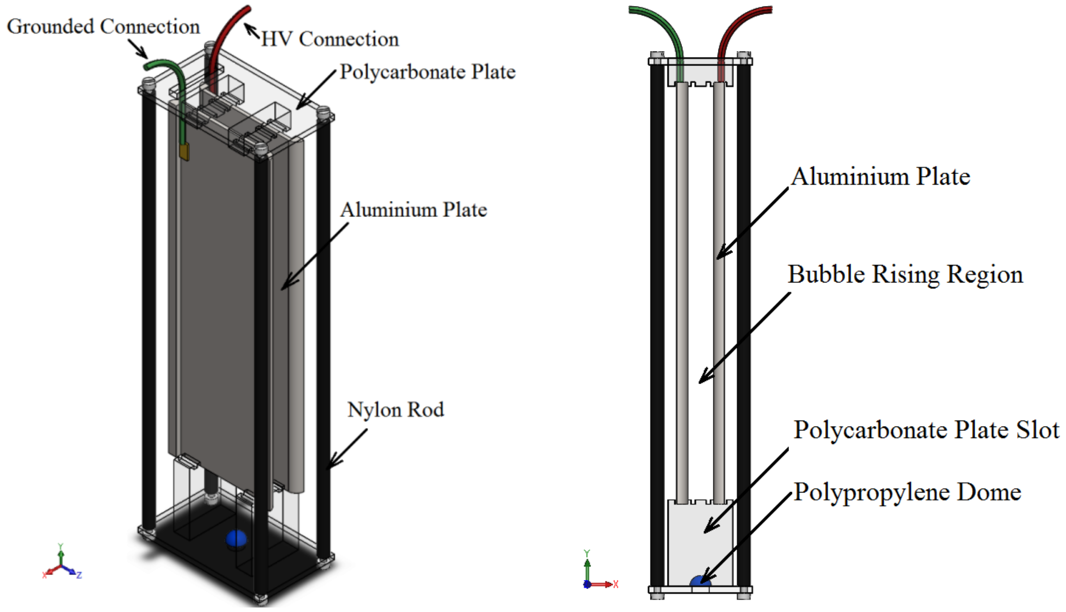

Figure 4.4 Parallel plate electrode system

Furthermore, with the aim to control the initial bubble size and position, a polypropylene dome is located in the centre between two electrodes. A 0.5 mm diameter hole was machined on the top of the dome. The arrangement is shown in the following Figure 4.5. It can be seen that the parallel electrode system is placed in the vessel and the dome was located above the heater.

For recording the bubble motion for subsequent analysis, a high-speed image system (HIS) was employed. The HIS system consists of a high-speed camera, a 100 Watt LED lamp and a light diffuser. In this study, the speed of the high-speed camera shutter is 1000 fps.

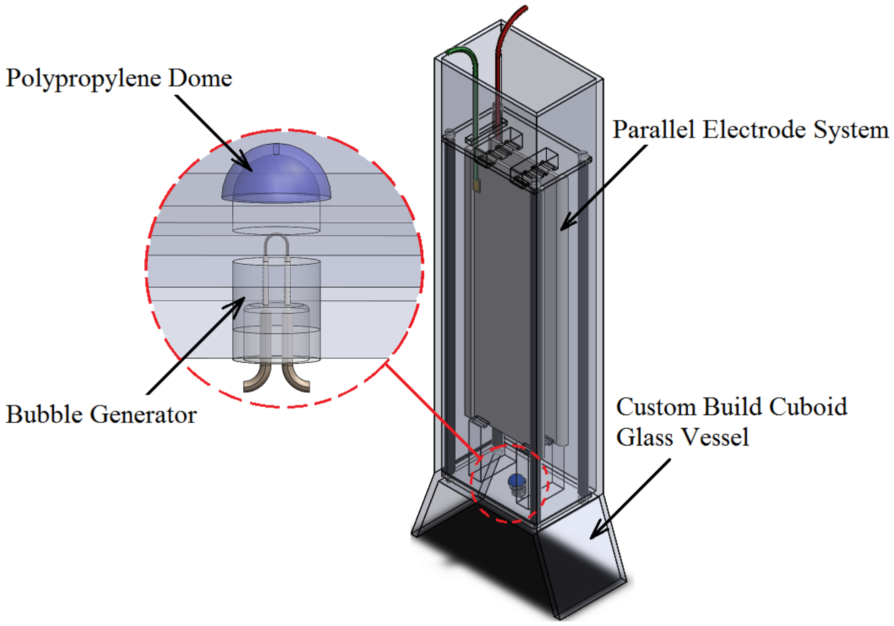

Figure 4.5 Experimental vessel and electrode system arrangement

4.3.4 Electric Field Simulation by Finite Element Method

The profiles of the electric field *E* applying to the experiments have been simulated by a 2D finite element model, which reproduces a cross section of the parallel plate electrode system. The modelling geometry and boundary conditions are plotted in Figure 4.6.

In the model, electrodes consist of two 65×2 mm plates placed in the centre of a glass vessel, which has 80×50 mm inner dimension and 2 mm wall thickness. The separations between the plates are 5, 12, 20 mm, which is as same as experimental arrangements. A square with 150 mm sides, representing air, surrounds the vessel.

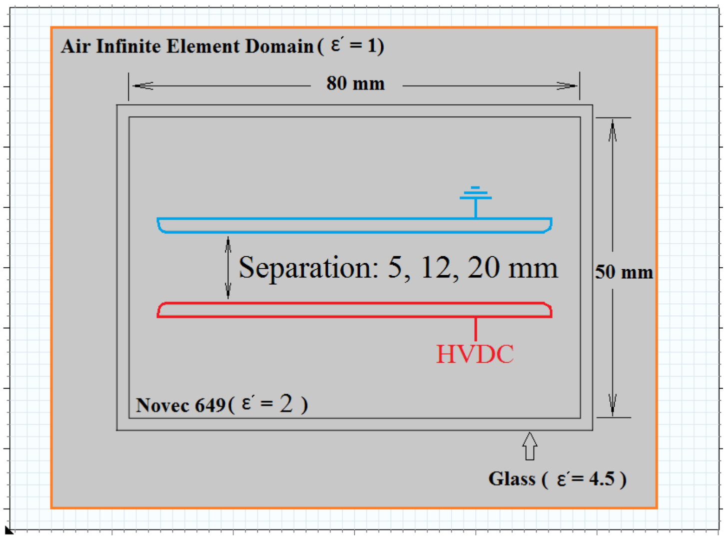

Figure 4.6 Parallel plate geometry and boundary conditions

The model assumes that the electric medium exists in the steady state. Charges do not build up on the external boundaries (i.e. orange lines), and the initial potential is 0 V for all domains. The air domain is defined to have an infinite element to mimic a virtual air box. With this approach, the air boundaries are defined away from the centre glass vessel. Then the zero charge external boundaries have minimal effect on the field of the bubble raising area. The one electrode (blue) is connected to the ground, meaning the electrical potential remains at 0 V. The other electrode (red) connects the HVDC power supply. Electric potentials ranging from 1 kV to 4 kV are applied to the electrode at 1 kV intervals.

As an example, the pattern of electric field distribution with 4 kV potential applied on the electrode is plotted in Figure 4.7. The profile shows the electric field is uniform in the bubble motion area; some field enhancements appear at the edge of both electrodes.

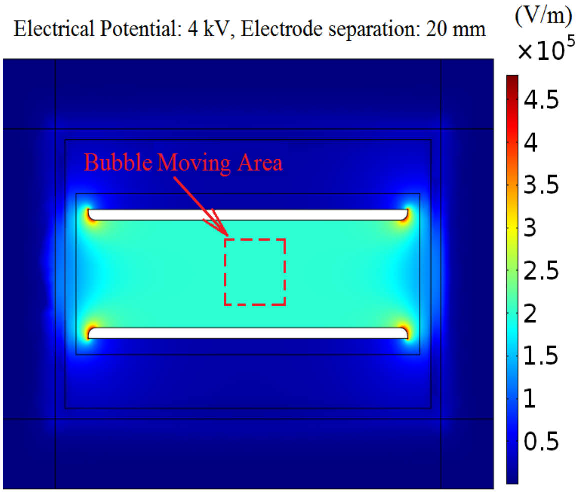

Figure 4.7 Electric field distribution with 4 kV potential applied to the electrode

Furthermore, by applying different electric potentials and electrode separations, there are 11 different electric potentials. The values are plotted in Figure 4.8.

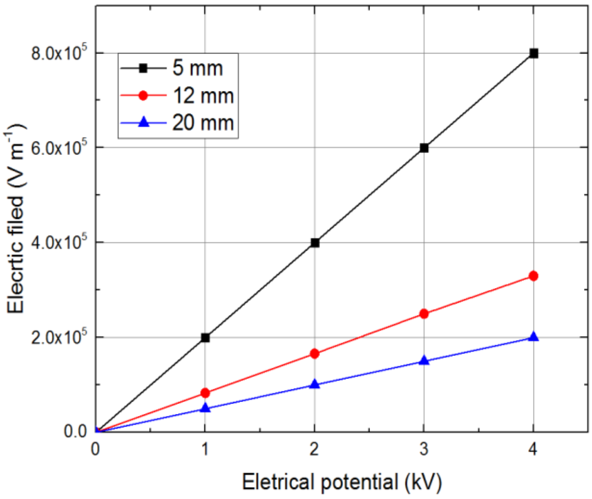

Figure 4.8 Electric field as a function of electric potential with different electrode separations

4.3.5 Results of Bubble Motion under Uniform DC fields

Bubble motion under different DC fields has been investigated by a series of experiments. The first step of the experiment was to calibrate the optical system. In this step, there was not an electric potential applied to the electrode. Hence, only vertical forces affect bubble motion. This step aims to make sure the high-speed camera and experimental vessel are on the same focusing plane. A level was used to guarantee the testbed was placed vertically to the ground. The results of the calibration are shown in Figure 4.9.

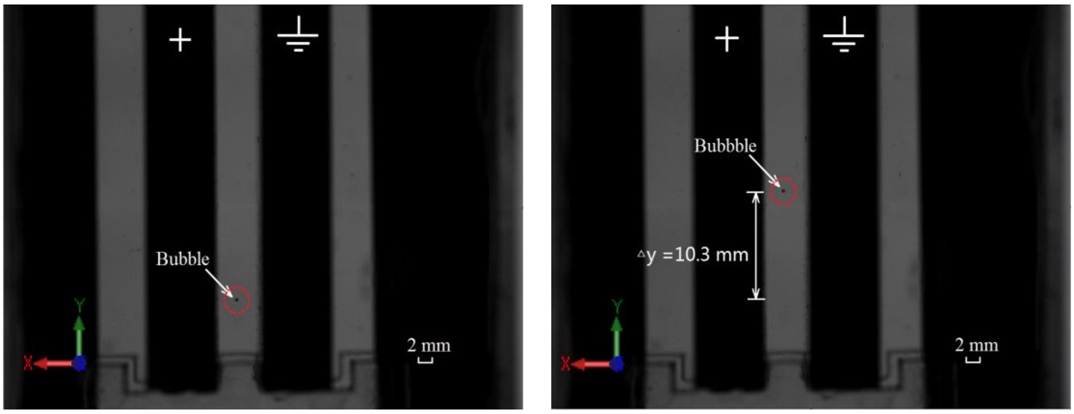

Positive 0 kV Δt = 0.1 s

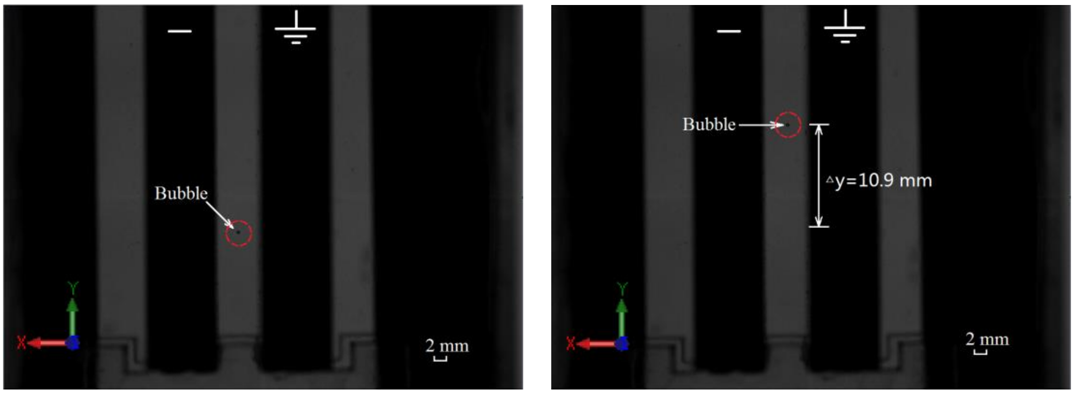

Negative 0 kV Δt = 0.1 s

Figure 4.9 Calibration results with positive and negative electric potential

These pictures show the continual frames at 0.1 seconds (Δt = 0.1 s). There are two main observations from these experimental results. The first finding is the diameter of the bubble. By counting the pixels, the bubble diameter was approximately 0.2 mm. The second conclusion is that the horizontal (i.e. *x*-direction) net force on the bubble is zero. This is because the bubble raised vertically in the centre of two electrodes.

In order to further investigate bubble charging behaviour, both positive and negative electrical potentials were applied to the electrode to create different electric field polarities. Then the bubble motions were recorded using the HIS and the series results are shown in Figure 4.10. It can be seen that the bubble moves horizontally under both a positive and negative electric fields. This phenomenon indicates that the net force in the *x*-direction is not zero and therefore

Coulomb force effects on bubble displacement. The existence of the Coulomb force proves that charges exist on the bubble surface. Furthermore, experimental results show that the bubble moves against the direction of the electric field. Hence, it can be determined that the polarity of the charge is negative. Nevertheless, this experiment cannot give a precise conclusion of the charge magnitude.

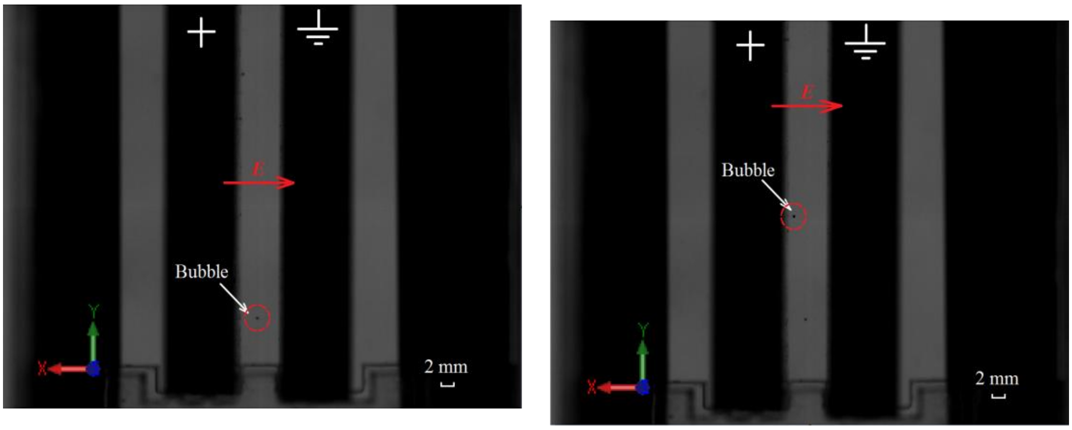

Positive 0.5 kV Electrode separation 5 mm $\Delta t = 0.2$ s

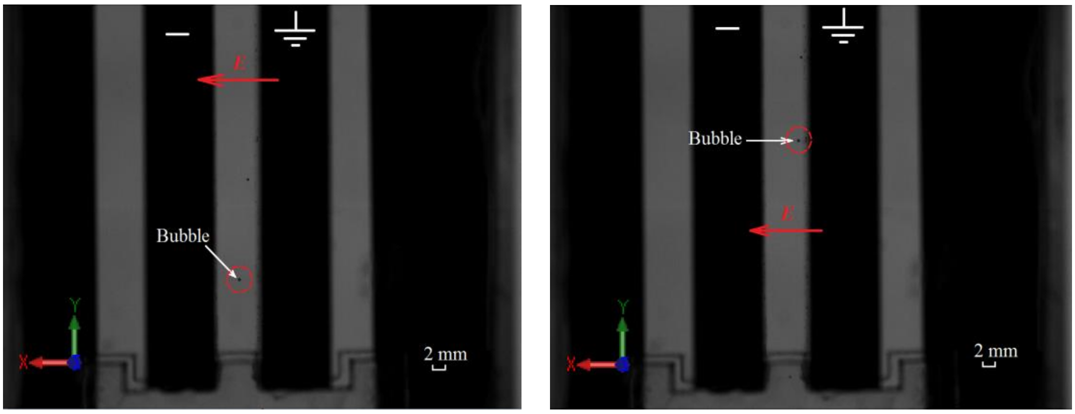

Negative 0.5 kV Electrode separation 5 mm $\Delta t = 0.2$ s

Figure 4.10 Bubble motion under different electric field polarities

To further investigate charge magnitude, the bubble motions under different magnitude electric fields were observed by the experiments. A positive electric potential was applied to one electrode, the other electrode was grounded. The different electric fields were created by varying electric potential and electrode separations. The magnitude of the electric field has been simulated by FEA models, which were discussed in Section 4.3.4. Then HIS recorded the bubble motions under eight different electric fields. By counting the number of the image frame, the collision time Δt_c (i.e. the time before the bubble collides with the electrode) was obtained. With the assistance of collision time, the bubble average velocities and accelerations can be calculated by the following equations.

$$\bar{\dot{x}} = \frac{S_e}{\Delta t_c} \tag{4.11}$$

$$\bar{\ddot{x}} = \frac{2S_e}{{\Delta t_c}^2} \tag{4.12}$$

where S_e is the half separation between two electrodes. In this study, bubble motion is assumed to have a constant acceleration and the initial bubble horizontal (x-direction) velocity is zero. In real life, since the drag force is positively proportional to the bubble velocity, initially the bubble should have higher value of acceleration. However, since Coulomb force dominates bubble motion, this assumption should not lead to a significant error. As an example, the image frames of bubble collision positions with 12 mm electrode separation and different magnitude electric fields are shown in Figure 4.11.

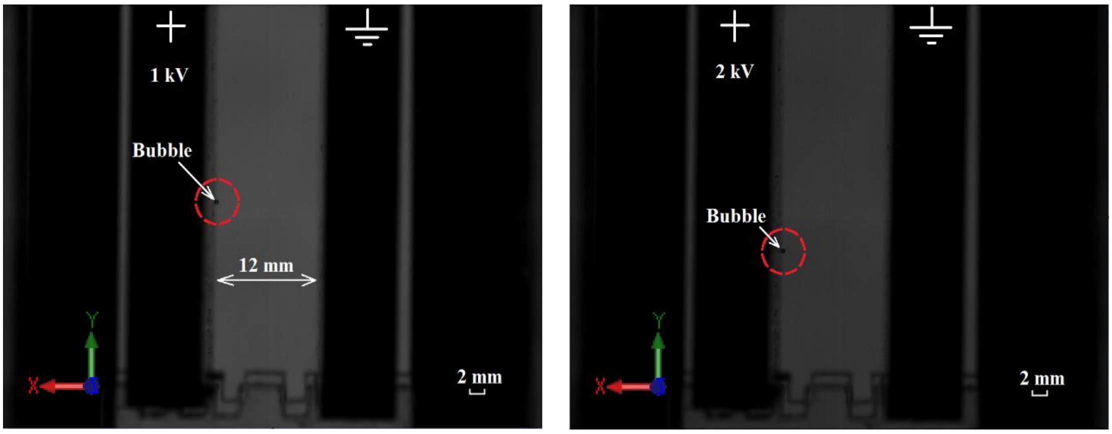

Positive 1 kV Δt_c=0.33 s

Positive 2 kV Δt_c=0.18 s

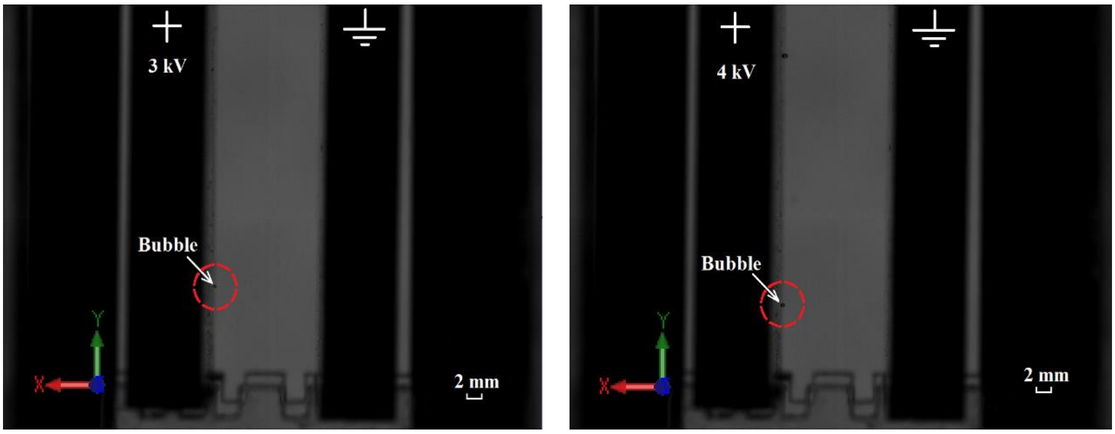

Positive 3 kV Δt_c=0.11 s

Positive 4 kV Δt_c=0.08 s

Figure 4.11 Bubble collision time with different electric fields

These experimental image frames show that the higher the electric field between two electrodes the shorter the bubble collision time. The explanation for this phenomenon is because the higher electric field results in greater Coulomb forces, which further lead to a higher *x*-direction bubble velocity and acceleration. After analysing the collision times of eight different electric fields, the bubble average velocities and accelerations were calculated as the average values and plotted in Figure 4.12 and Figure 4.13.

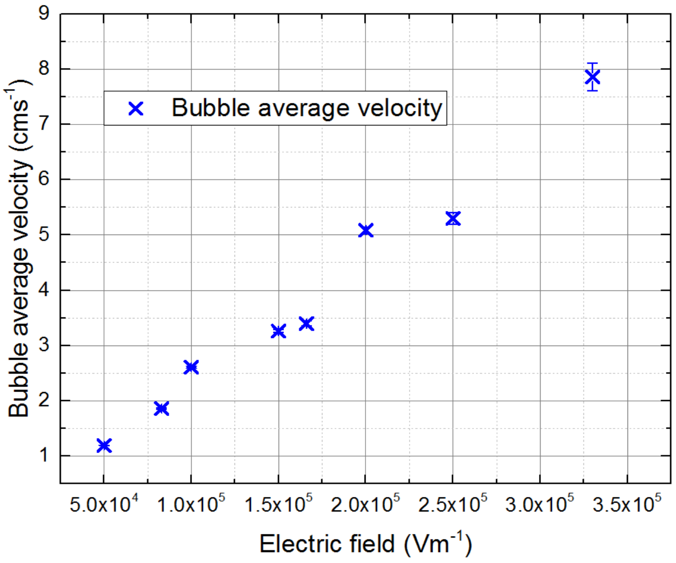

Figure 4.12 Bubble average velocity

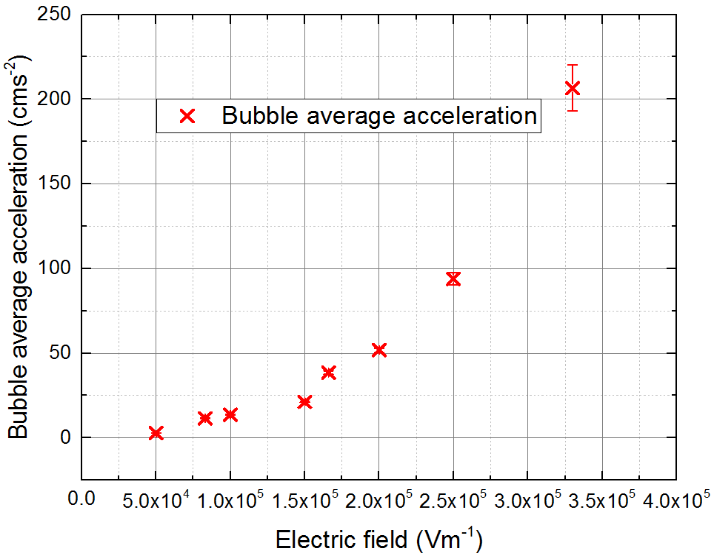

Figure 4.13 Bubble average acceleration

Figure 4.13 shows the bubble velocity and acceleration are positively correlated with electric fields. The bubble charge magnitude q_b can be calculated by substituting bubble average velocity and acceleration into;

$$q_b = \frac{\frac{4}{3}\pi R_b{}^3\left(\rho_g + \frac{1}{2}\rho_l\right)\ddot{\vec{x}} + 4\pi\eta_l R_b \dot{\vec{x}}}{E} \tag{4.13}$$

The bubble charge magnitudes according to different electric fields are plotted in Figure 4.14. It shows that the charge magnitudes on the bubble surface are between 0.2 pC and 0.3 pC. The average value of the charge magnitude is 0.253 pC, which will be used in later analysis.

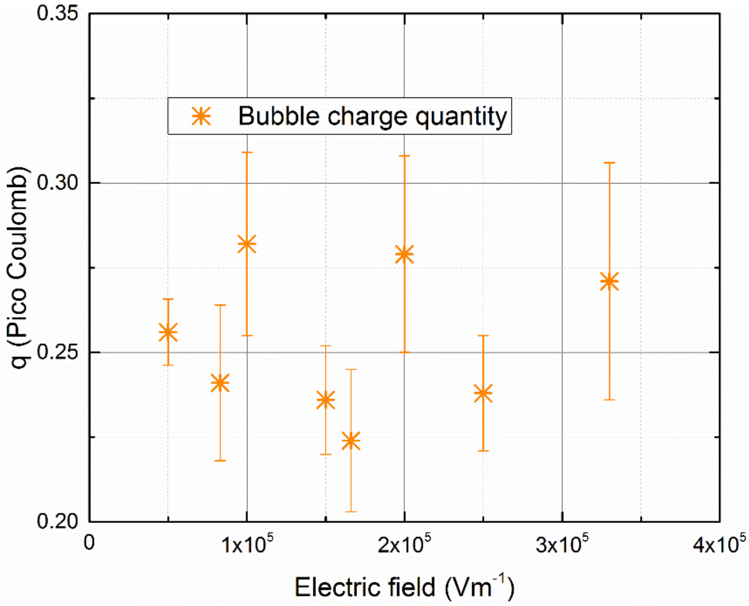

Figure 4.14 Bubble charge magnitude under different electric fields

4.3.6 Summary of Bubble Motion under Uniform DC field

This section investigated bubble motion under different uniform DC fields. The experimental results can draw three conclusions. First, the bubble moves horizontally under the DC electric field. This phenomenon indicates the existence of the Coulomb force due to the charges on the bubble surface. Second, by changing field polarities, bubble motion is against the electric field line, indicating that the polarity of the bubble charge is negative. Finally, by analysing the bubble velocities and accelerations, the average charge magnitude on the bubble was calculated. It is approximentaly 0.25 pC

4.4 Thermal Bubble Motion in a Non-uniform Electric Field

This section investigates the effect of both electrophoretic and dielectrophoretic forces on bubble motion in a non-uniform electric field. The dielectrophoretic force is attributed to the electric field gradient. In order to create an electric field gradient, the non-uniform electric field was usually created by three electrode arrangements. They are rod-plate electrode arrangement [128], inclined plane electrode [129] or a needle-plate arrangement [74]. The rod-plate electrode arrangement was applied in this study.

4.4.1 Electrode Arrangement and Cartesian coordinate system

The rod-plate electrode arrangement applied in this study is shown in Figure 4.15. As same as in Section 4.3.1, a three-axis Cartesian coordinate is also defined. In this coordinate system, the *x*-axis is normal to the ground plate; *y*-axis is vertically upwards, and the *z*-axis is along the parallel side of the grounded plate.

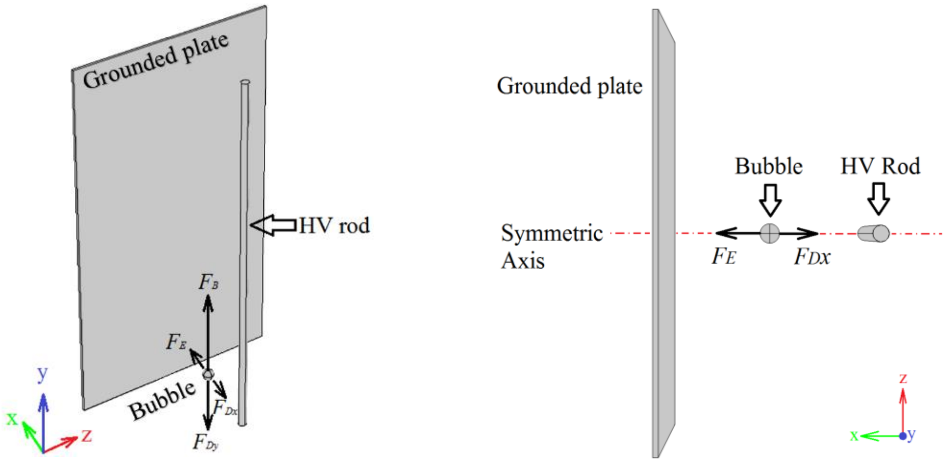

Figure 4.15 Rod-plate electrode arrangement and Cartesian coordinate system

4.4.2 Theoretical Analysis of Bubble Motion under a Non-uniform DC Field

Consider the force analysis and kinematic equations for bubble motion under non- uniform electric field: The bubble motion in the *x*-direction is attributed to two forces, which are EHD force and drag force. In the non-uniform electric field, EHD force consists of both dielectrophoretic force and electrophoretic force.

Pohl suggests that the dielectrophoretic force acting on a spherical bubble of radius R_b and permittivity ε_g in a surrounding liquid with the permittivity of ε_l is given by [130];

$$\vec{F}_{E(gradient\ force)} = 2\pi {R_b}^3 \frac{\varepsilon_l(\varepsilon_g-\varepsilon_l)}{\varepsilon_g+2\varepsilon_l} \nabla \vec{E}^2 \tag{4.14}$$

Furthermore, the electrophoretic force also affects bubble motion in a non-uniform DC field. This is because the charge exists on the bubble surface, which has been discussed in the last section. Hence, the EHD force due to the non-uniform electric field is the sum of two forces.

$$\overrightarrow{F_{EHD}} = \overset{\text{Dielectrophoretic Force}}{\overset{\Downarrow}{\boxed{2\pi {R_b}^3 \frac{\varepsilon_l(\varepsilon_g-\varepsilon_l)}{\varepsilon_g+2\varepsilon_l} \nabla \vec{E}^2}}} \mp \overset{\text{Electrophoretic Force}}{\overset{\Downarrow}{\boxed{\vec{E}q_b}}} \tag{4.15}$$

Equation 4.15 shows that the direction of the dielectrophoretic force is attributed to gas liquid two-phase material permittivity. Since the permittivity value of the gas is usually lower than the liquid, the dielectrophoretic force will act towards the low electric field region. For this study, the dielectrophoretic force direction points to the grounded plate. This is because the electric field is higher around the rod electrode. The direction of the electrophoretic force is dependent on the electric field polarity. In order to observe bubble displacement clearly, negative electric potentials are applied to this study and therefore the direction of the electrophoretic force is the same as the dielectrophoretic force. Then Equation 4.15 transfers into;

$$\overrightarrow{F_{EHD}} = 2\pi R_b{}^3 \frac{\varepsilon_l(\varepsilon_g-\varepsilon_l)}{\varepsilon_g+2\varepsilon_l} \nabla\vec{E}^2 + \vec{E}q_b \tag{4.16}$$

The drag force is also involved in bubble *x*-direction displacement and explained as

$$\overrightarrow{F_{Dx}} = -4\pi\eta_l R_b \dot{\vec{x}} \tag{4.17}$$

The bubble motion in the *y*-direction is also governed by the bubble buoyancy force and drag force. These forces are calculated by the following equations;

$$\overrightarrow{F_B} = \frac{4}{3}\pi\, R_b{}^3(\rho_l - \rho_g)\, \vec{g} \tag{4.18}$$

$$\overrightarrow{F_{Dy}} = -4\pi\eta_l R_b \dot{\vec{y}} \tag{4.19}$$

The force acting on the *z*-direction results in bubble movement parallel to the side of the ground electrode. As discussed in Section 4.3.2, if the bubble rising on the symmetric plane between the electrodes (red dashed line in Figure 4.15) the forces acting upon the bubble in this direction are balanced. Hence, the net force in the *z*-direction is zero.

The net force in the *x*-direction is attributed to EHD force and drag force. Hence, Newton's equation is formed as;

$$M_{eff}\, \ddot{\vec{x}} = \overrightarrow{F_{EHD}} + \overrightarrow{F_{Dx}} \tag{4.20}$$

The net force in the *y*-direction is caused by the buoyancy force and corresponding drag force. Therefore, the kinematic equation in the *y*-direction is given by:

$$M_{eff}\, \ddot{\vec{y}} = \overrightarrow{F_B} + \overrightarrow{F_{Dy}} \tag{4.21}$$

By substituting the required forces into Equation 4.20 and 4.21, the bubble component kinematic equations can be rearranged such that;

$$\begin{cases} \ddot{\vec{x}} + \alpha_x\dot{\vec{x}} + \beta_x\nabla\vec{E}^2 + \gamma_x\vec{E} = 0 & (4.22) \\ \ddot{\vec{y}} + \alpha_y\dot{\vec{y}} + \beta_y = 0 & (4.23) \end{cases}$$

where

$$\begin{cases} \alpha_x = \frac{3\eta_l}{R_b{}^2(\rho_g+\frac{1}{2}\rho_l)} \\ \beta_x = -\frac{3\varepsilon_l(\varepsilon_g-\varepsilon_l)}{2\left(\rho_g+\frac{1}{2}\rho_l\right)(\varepsilon_g+2\varepsilon_l)} \\ \gamma_x = -\frac{3q_b}{4\pi R_b{}^3(\rho_g+\frac{1}{2}\rho_l)} \end{cases} \tag{4.24}$$

$$\begin{cases} \alpha_y = \frac{3\eta_l}{R_b{}^2(\rho_g+\frac{1}{2}\rho_l)} \\ \beta_y = -\frac{(\rho_l-\rho_g)g}{(\rho_g+\frac{1}{2}\rho_l)} \end{cases} \tag{4.25}$$

4.4.3 Equation Solving and Theoretical Results

There are four assumptions considered for solving the numerical equations to predict bubble trajectory under different DC fields;

i. Initial bubble position

Initially, the bubble is released on the symmetric plane between the electrodes. Hence, the bubble is released with an initial x-direction displacement x_i. Furthermore, the initial bubble location is defined as the origin point of both the *y* and *z* axis. Therefore, the initial bubbles coordinate is defined as $(x_i, 0{,}0)$.

ii. Bubble size and shape

A polypropylene dome regulates thermal bubble diameter and the bubble diameter is 0.2×10^{-3} m. Furthermore, since the bubble volume is small there is no significant deformation. Hence, in this study, the bubble is treated as a perfect sphere.

iii. Initial bubble velocity

In this study, before the bubble entering the electric field region, the buoyancy force results in a bubble initial vertical velocity $\overrightarrow{\dot{y}_I}$. The magnitude of $\overrightarrow{\dot{y}_I}$, which is investigated by a preliminary experiment, is 0.08 m s^{-1}. In contrast, there is not a significant bubble displacement in both *y* and *z* axis. Therefore, the velocities in the *x* and *z* direction are defined as 0 m s^{-1}.

iv. Gas bubble density

The gas phase density of FK material is three orders of magnitudes smaller than the liquid phase density. The liquid density is the decisive parameter on bubble motion and therefore the gas density of FK is neglected.

In addition, the FK material parameters are required for solving the Equation 4.22 and Equation 4.23. These parameters are summarised in Table 4-1

Table 4-1 The parameter of FK

ρ_l = 1607 kg m^{-3}	η_l = 0.46× 10^{-3} kg m^{-1} s^{-1}	$\varepsilon_l = 2.0\varepsilon_0$
$\rho_g \approx$ 0 kg m^{-3}	ε_0 = 8.854× 10^{-12} F m^{-1}	$\varepsilon_g = 1.0\varepsilon_0$

From Equation 4.22 it can be seen that bubble motion is not only dependent on material properties but is also a function of the electric field E and square of the electric field gradient (∇E^2). The traditional formula and finite element model are the two approaches that were used, to investigate electric field distribution around the rod-plate electrode arrangement.

Previous studies [64] and [71] introduce an analytical formula to predict the electric field around the rod-plate electrode;

$$E = \frac{2\sqrt{l^2 - R_r^2}}{(l^2 - R_r^2 - (l - x_i)^2)\ln[(l + \sqrt{l^2 - R_r^2})/R_r]} V \tag{4.26}$$

where l is the distance between the rod and the plate, R_r is the radius of the rod electrode and x_i is the bubble horizontal position. ∇E^2 is given by;

$$\nabla E^2 = \frac{[-16V^2(l^2 - R_r^2)](l - x_i)}{\ln[(l + \sqrt{l^2 - R_r^2})/R_r]^2[(l^2 - R_r^2) - (l - x_i)^2]^3} \tag{4.27}$$

The second approach is using a 2D Finite Element Analysis (FEA), model. This 2D model is designed to reproduce a cross-section of the rod-plate arrangement. The model geometry and boundary conditions are shown in Figure 4.16.

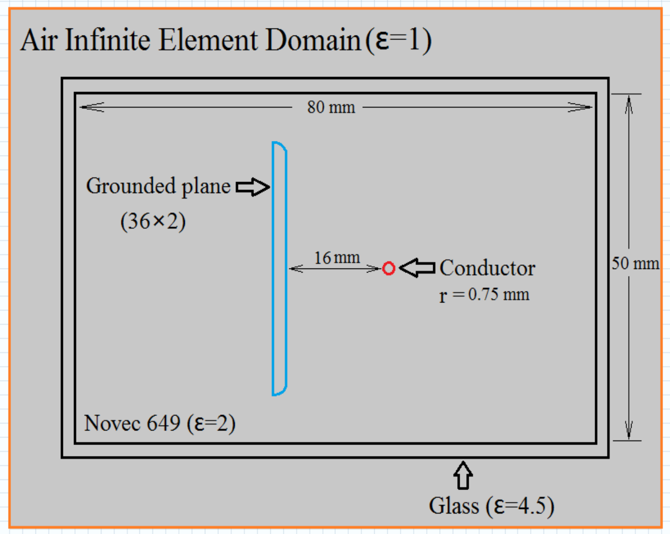

Figure 4.16 Modelling geometry and boundary conditions

The simulation investigates the steady-state electric field profile of the rod-plate arrangement. The electrode is placed in the centre of a glass vessel and submerged by FK material. The electrode system consists of a 1.5 mm diameter rod and a 36×2 mm plate. The separation between the rod and plate is 16 mm. Furthermore, the relative permittivity of FK and glass are set equal to 2 and 4.5 respectively. The last step is to define boundary conditions. There is no charge built up on the external boundaries (i.e. orange lines), and the initial potential of all domains is 0 V. The blue boundary of the plate electrode is grounded and therefore the electrical potential is 0 V. The red line is the boundary of the rod electrode with 1 V electric potential. By carrying out this process, the electric field can be defined as a function of applied electric potential.

The simulation results of both electric field E and the square of the electric field gradient ∇E^2 are plotted in Figure 4.17 and Figure 4.18. It can be seen that the magnitude of the electric field and square of electric field gradient are both according to bubble position.

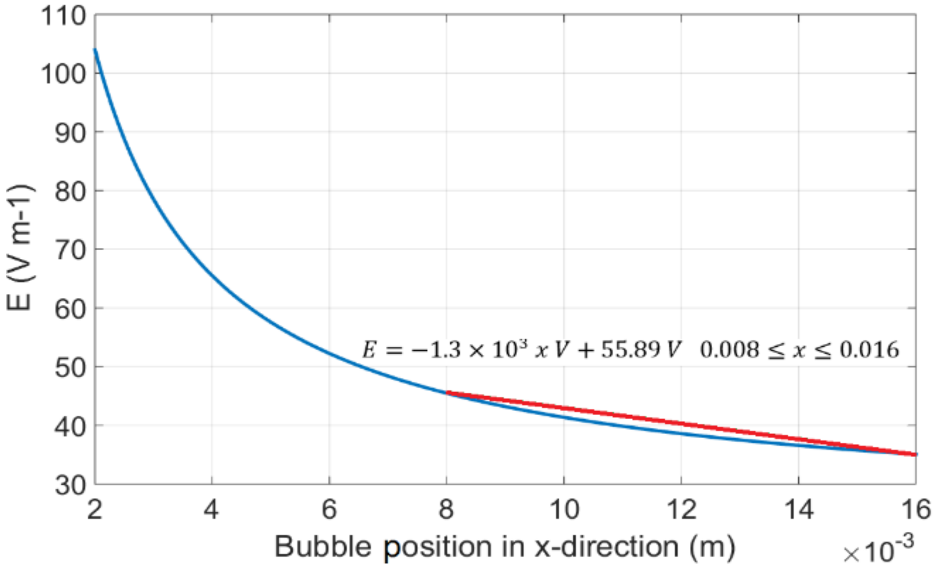

Figure 4.17 Electric field versus bubble position

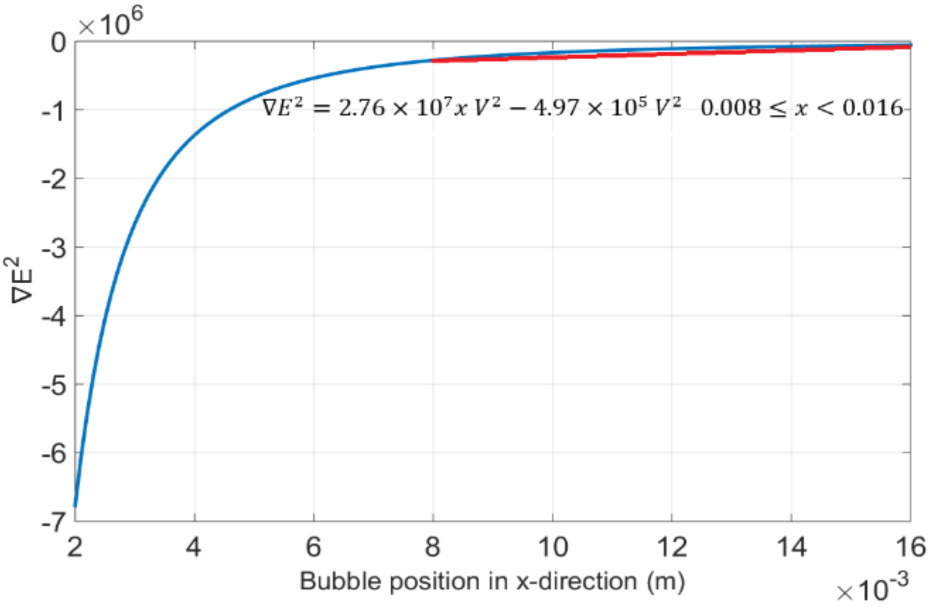

Figure 4.18 Square of electric field gradient versus bubble position

By fitting the second order polynomials to E and ∇E^2 the following formulas are derived:

$$E = (0.23x^{-0.94} + 23.82)V \tag{4.28}$$

$$\nabla E^2 = -4.04x^{-2.31}V^2 \tag{4.29}$$

From Equation 4.28 and 4.29, it can be seen that the inclusion of electric potential allows both E and ∇E^2 to be scaled to represent the field for any voltage applied to the rod electrode.

It is necessary to compare and investigate the error of both approaches in this study. Hence, the error between the two methods is calculated and plotted in Figure 4.19.

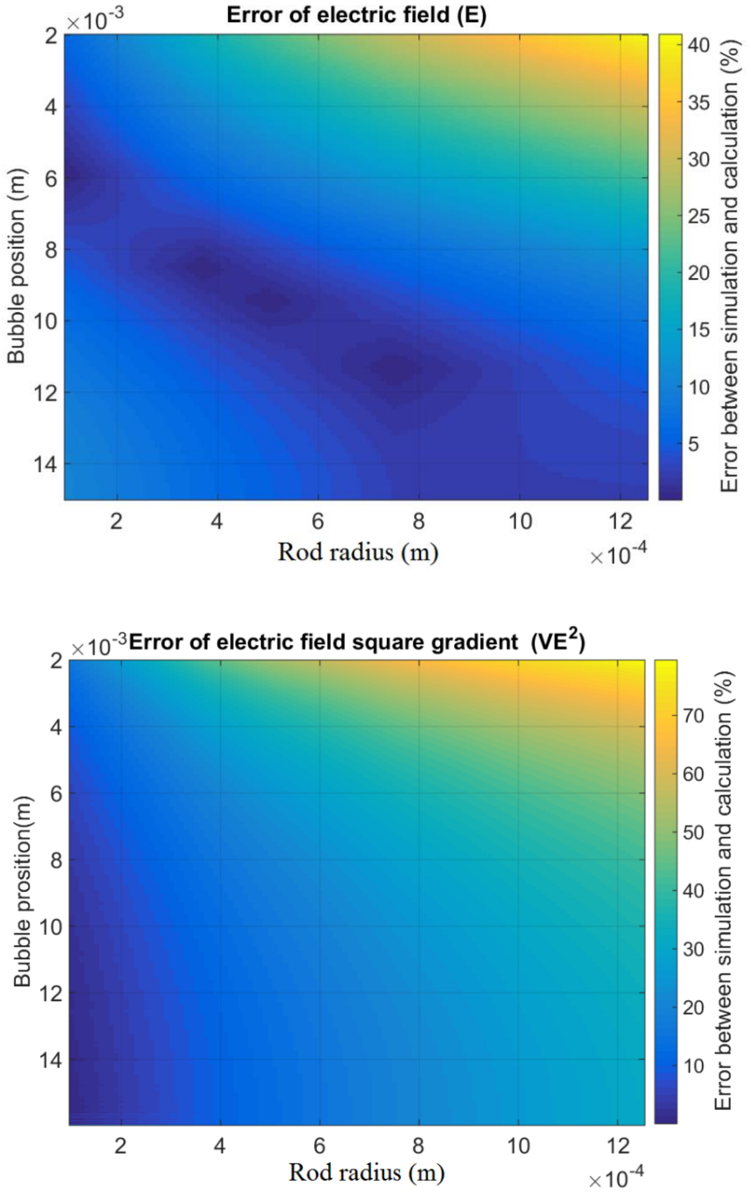

Figure 4.19 Error of electric field (E) and electric field square gradient (∇E^2) between two methods

In Figure 4.19 the colour bar represents the error between the two approaches as a percentage, which can be calculated by;

$$Error\ (E) = \frac{E(F) - E(S)}{E(S)} \times 100\% \tag{4.30}$$

$$Error\ (\nabla E^2) = \frac{\nabla E^2(F) - \nabla E^2(S)}{\nabla E^2(S)} \times 100\% \tag{4.31}$$

where (*F*) and (*S*) are the values, which are obtained by the formula and simulation method respectively. It can be seen that with the increasing rod diameter the errors of the E and ∇E^2 between two approaches become bigger, especially when the bubble is close to the HV rod. In this study, the rod radius is 7.5× 10^{-4} m, so the errors between the two approaches are a minimum of 10 %. This is because the real electrode arrangement does not conform to the ideal condition for the formula, which is the line voltage source and an infinite separation between rod and plate. Hence, a simulation method was applied for this study.

In order to predict bubble *x*-direction displacement, the simulation of E and ∇E^2 profiles, which defined are by Equation 4.28 and 4.29, are substituded in *x*-direction kinematic Equation 4.22 and transfers into:

$$\ddot{\vec{x}} + \alpha_x \dot{\vec{x}} + \beta_x(-4.04x^{-2.31}V^2) + \gamma_x(0.23x^{-0.94} + 23.82)V = 0 \tag{4.32}$$

The inclusion of *V* allows bubble motion prediction to be scaled for any high voltage applied to the electrode. Since Equation 4.32 is a second-order nonlinear ordinary differential equation (ODE), there are no specific solutions. To solve this, two linear approximations of *E* and ∇E^2 have been made which are covered to region 0.008 ≤ x ≤ 0.016 m and plotted by the red lines in Figure 4.17 and Figure 4.18. These linear functions are defined as;

$$\begin{cases} \nabla E^2 = -4.04x^{-2.31}V^2 \approx 2.76 \times 10^7 xV^2 - 4.97 \times 10^5 V^2 & 0.008 \le x \le 0.016 \\ E = (0.23x^{-0.94} + 23.82)V \approx -1.3 \times 10^3 x\, V + 55.89\, V & 0.008 \le x \le 0.016 \end{cases} \tag{4.33}$$

By substituting 4.33 into 4.32, the *x*-direction equation becomes

$$\ddot{\vec{x}} + \alpha_x \dot{\vec{x}} + (2.76 \times 10^7 V^2 \beta_x - 1.3 \times 10^3 V \gamma_x)x + (55.89\, V\gamma_x - 4.97 \times 10^5 V^2 \beta_x) = 0 \tag{4.34}$$

$$\begin{cases} \alpha_x = \dfrac{3\eta_l}{{R_b}^2(\rho_g + \frac{1}{2}\rho_l)} \\ \beta_x = -\dfrac{3\varepsilon_l(\varepsilon_g - \varepsilon_l)}{2\left(\rho_g + \frac{1}{2}\rho_l\right)(\varepsilon_g + 2\varepsilon_l)} \\ \gamma_x = -\dfrac{3q_b}{4\pi {R_b}^3(\rho_g + \frac{1}{2}\rho_l)} \end{cases}$$

The general form of 4.34 is expressed as

$$\ddot{\vec{x}} + A\dot{\vec{x}} + Bx + C = 0 \tag{4.35}$$

The solution of the general form ODE, Equation 4.35 can be expressed as

$$x(t) = C_{x1}e^{\frac{1}{2}t(-\sqrt{A^2-4B}-A)} + C_{x2}e^{\frac{1}{2}t(\sqrt{A^2-4B}-A)} - \frac{C}{B} \tag{4.36}$$

For solving Equation 4.36 two initial conditions are needed and shown in Equation 4.37. Since the bubble is released in the centre between two electrodes, the initial displacement is 0.008 m. Furthermore, the initial bubble *x*-direction acceleration is 0 m s^{-2}.

$$\begin{cases} x_{|t=0} = x_i = 0.008 \\ \dot{\vec{x}}_{|t=0} = 0 \end{cases} \tag{4.37}$$

The y-direction kinematic Equation 4.23 is the general form ODE and the solution can be expressed as:

$$\mathrm{y(t)} = \frac{C_{y1}e^{-\alpha_y t}}{\alpha_y} - \frac{\beta_y}{\alpha_y}\mathrm{t} + C_{y2}$$

$$\begin{cases} \alpha_y = \frac{3\eta_l}{{R_b}^2(\rho_g+\frac{1}{2}\rho_l)} \\ \beta_y = -\frac{(\rho_l-\rho_g)g}{(\rho_g+\frac{1}{2}\rho_l)} \end{cases} \tag{4.38}$$

There are also two initial conditions for calculating C_{y1} and C_{y2}. These conditions are:

$$\begin{cases} y_{|t=0} = 0 \\ \dot{\vec{y}}_{|t=0} = 0.08 \end{cases} \tag{4.39}$$

After calculating the solutions C_{x1}, C_{x2} and C_{y1} C_{y2} the theoretical bubble trajectories of horizontal and vertical directions are plotted in Figure 4.20 and Figure 4.21.

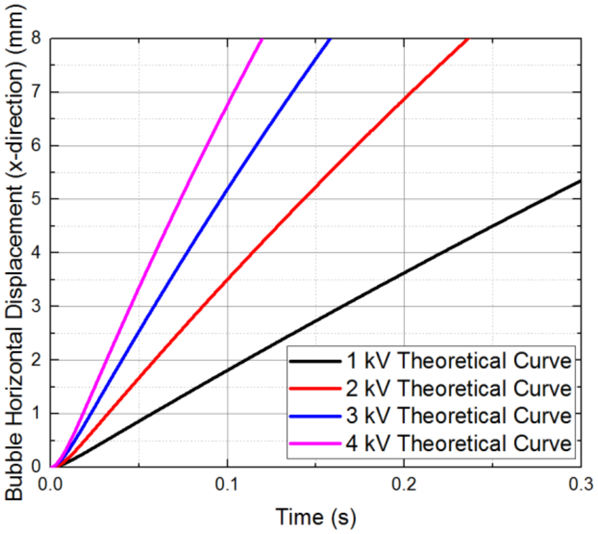

Figure 4.20 Theoretical results of thermal bubble horizontal motion

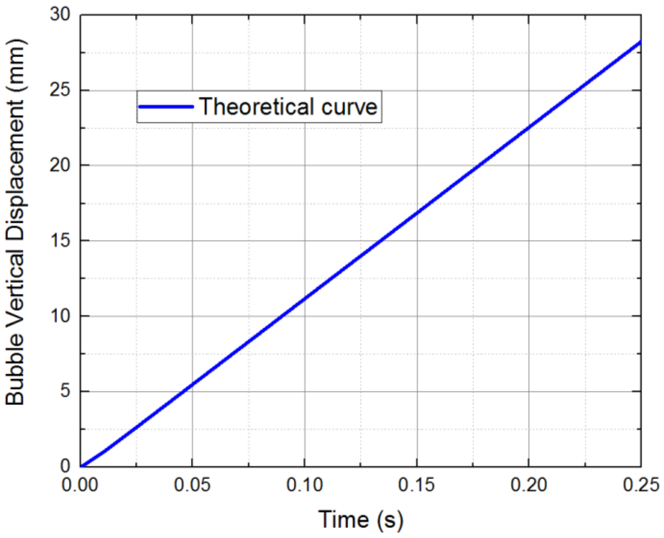

Figure 4.21 Theoretical results of thermal bubble vertical motion

The theoretical results show that when a higher electric potential is applied to the rod electrode, there is a greater EHD force acting upon the bubble, this is reflected by the larger displacement in the *x*-direction. Furthermore, since the net force on the vertical is independent of the electric field, the bubble *y*-direction velocity is kept as a constant. An experiment has been designed to provide a comparison between the calculated trajectory and the real case.

4.4.4 Experimental analysis of Bubble Motion under Non-uniform DC Electric Field

The experimental platform arrangement is shown in Figure 4.22.

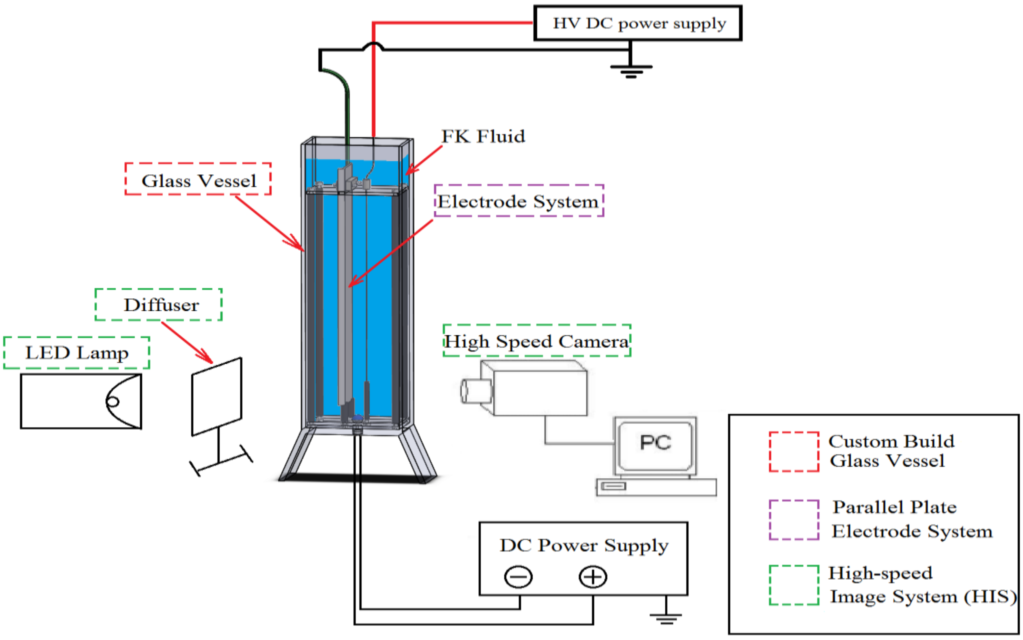

Figure 4.22 Rod-plate experimental platform arrangement

The custom build glass vessel and HIS system are the same as introduced in Section 4.3.3. A rod-plate electrode system, which is shown in Figure 4.23, was placed in the centre of the glass vessel. The electrode system consists of a 1.5 mm diameter rod and a 250×36×2 mm plate. The separation between rod and plate is 16 mm. A negative electric potential from 1 to 4 kV was applied to the rod and the plate electrode was grounded. The bubble motion between two electrodes was recorded by HIS and the results are shown in the next section.

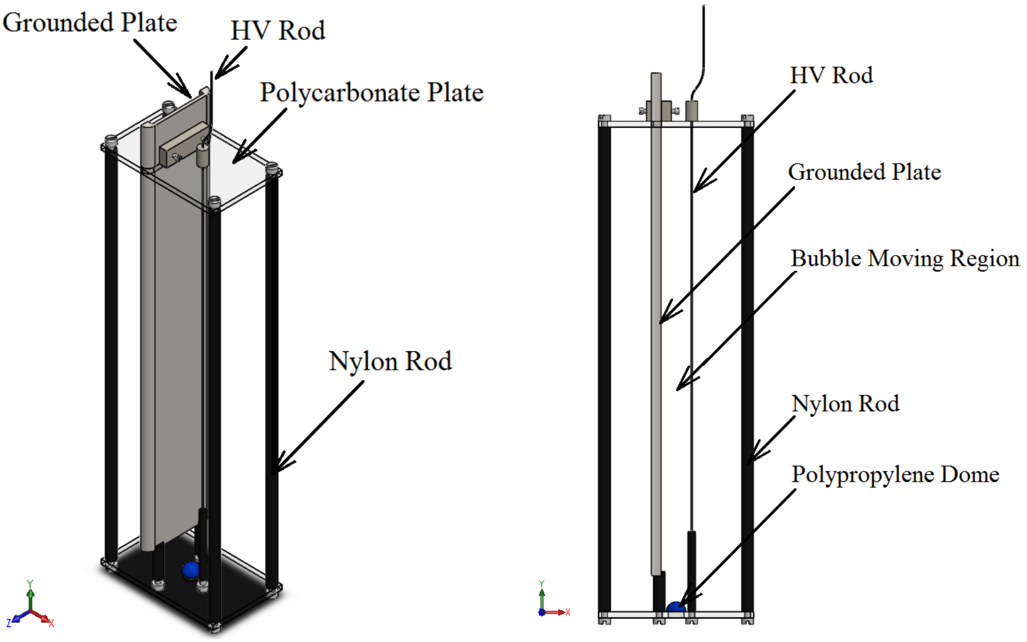

Figure 4.23 Rod-plate electrode system

4.4.5 Results of Bubble Motion under Non-uniform DC fields

The bubble motions under different magnitude non-uniform electric fields were recorded and shown in this section. This section firstly investigates bubble vertical displacement. During the experiment, no electric field was applied. The recorded images are shown in Figure 4.24.

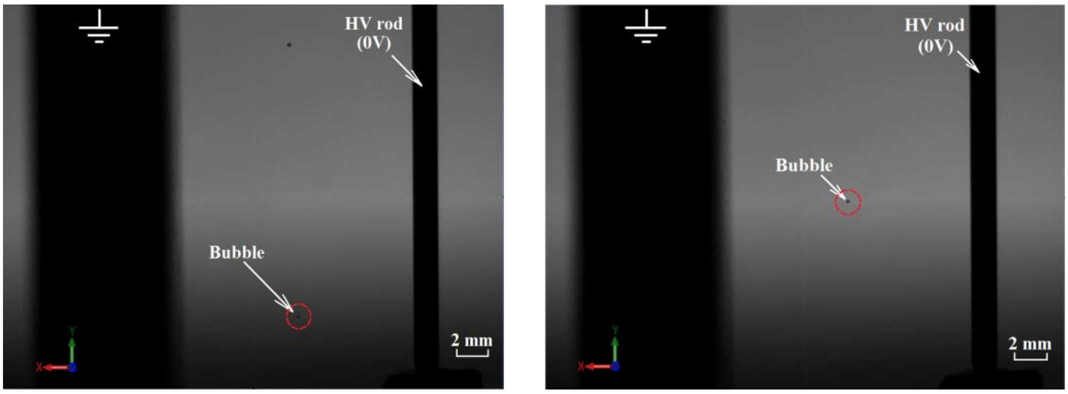

0 kV, $\Delta t = 0.1$ s, bubble vertical displacement is 8.4 mm

Figure 4.24 Bubble vertical motion without electric field

Figure 4.24 shows two bubble motion frames and the time difference between two frames (Δt) is 0.1 s. The images show that without electric potential applied to the rod electrode; there was not a significant horizontal bubble displacement. Furthermore, the bubble rose vertically on the middle plane between two electrodes. Within 0.1 s the bubble rose 8.4 mm vertically. This result is in good agreement with the initial kinematic conditions of theoretical studies.

In order to validate the theoretical prediction, thermal bubble motions under different non- uniform DC fields were recorded and analysed. The results are shown in Figure 4.25 and Figure 4.26. When −1 kV was applied to the rod electrode, the bubble moved horizontally towards to grounded plate. Since the time difference between each image is 0.05 s, the duration between the first image and the last image is 0.15 s. During this time, the bubble displacement in *x*-direction was 3.1 mm and the bubble vertical displacement was 13.2 mm.

When −3 kV was applied to the rod electrode, there was a larger bubble displacement in the *x*-direction, which is 7.9 mm. This is due to the larger EHD force. This trend agrees with the theoretical prediction that shown in Figure 4.20. Within 0.15s, bubble vertical displacement is 14.3 mm. It can be seen that the bubble *y*-direction displacement is nearly independent of electric potential.

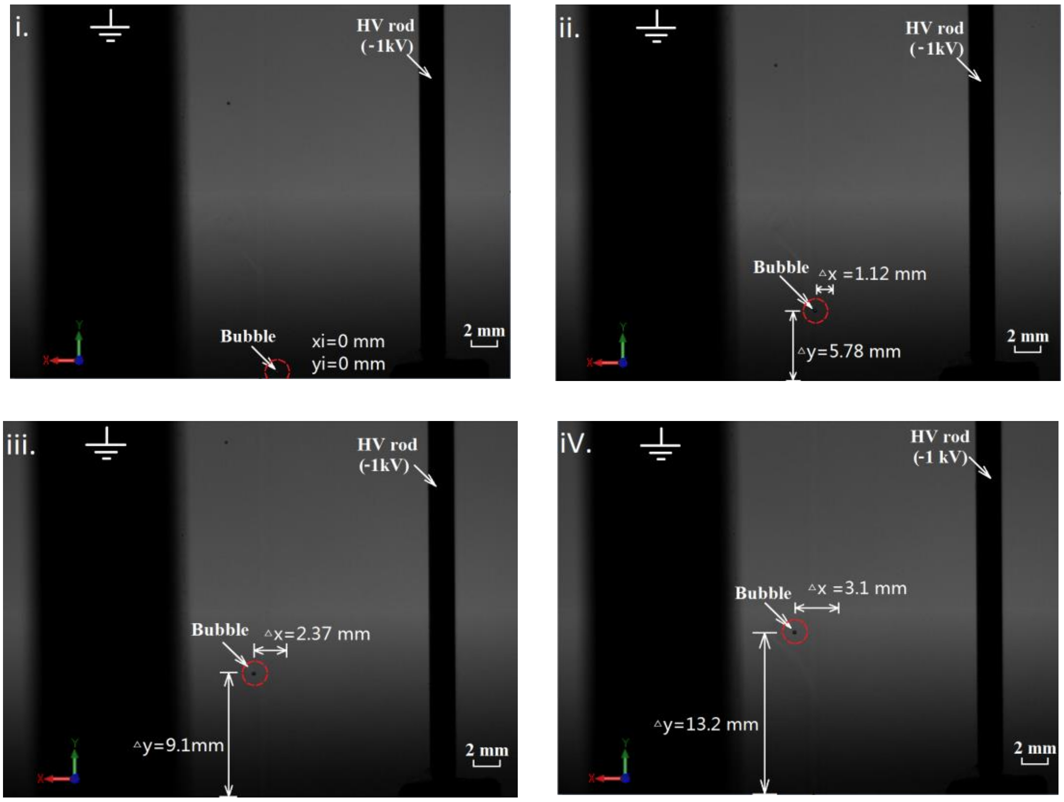

Time difference between each frame Δt =0.05 s

Figure 4.25 Bubble motion under −1 kV electric potential

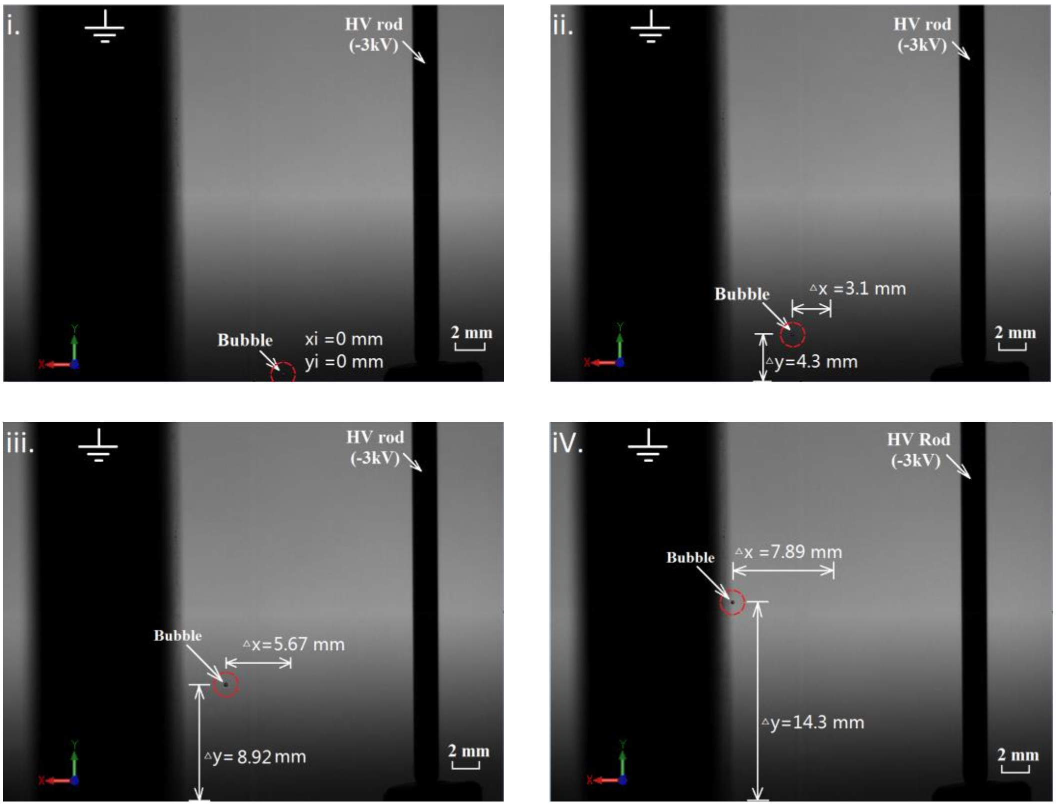

Time difference between each frame Δt =0.05 s

Figure 4.26 Bubble motion under −3 kV electric potential

4.4.6 Comparison between Theoretical and Experimental Results

The comparison between theoretical and experimental results is shown in Figure 4.27 and Figure 4.28.

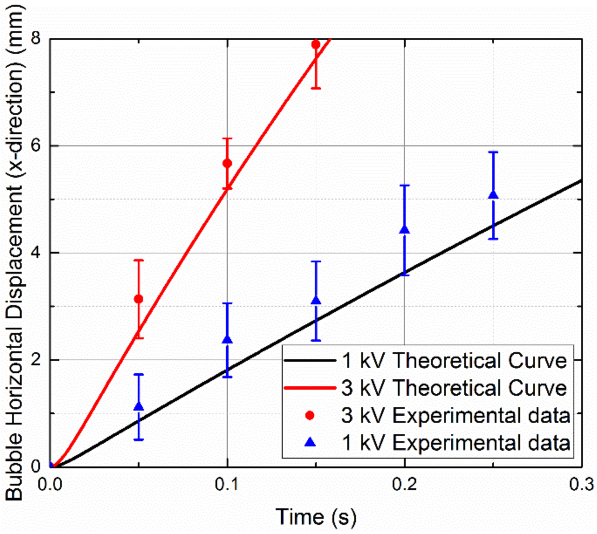

Figure 4.27 Results comparison of bubble motion in the x-direction

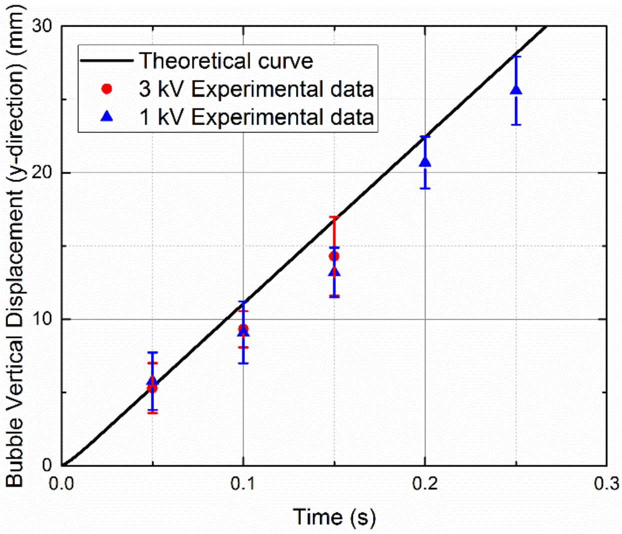

Figure 4.28 Results comparison of bubble motion in the y-direction

Figure 4.27 and Figure 4.28 show that the experimental results have a reasonable agreement with the predictions in both the horizontal and vertical directions. These results indicate that the horizontal bubble velocity is positively correlated with the increasing electric potential. However, the vertical bubble velocity is independent of the electric field. In addition, the results show that horizontal bubble speeds, which are given by experiments, are slightly higher than the prediction value. A possible explanation for this is that the charge density applied to simulated bubbles is slightly smaller than that applied in reality. This error could cause by the assumption of average velocity and acceleration. The experimental results also show that in the 1 kV experiment the bubble has a higher vertical displacement before 0.1 s. The reason is possible turbulent flow due to natural convection which contributes to the bubble rising.

4.5 Summary

Fluorinated Ketone (FK) thermal bubble motion under different uniform and non-uniform electric fields have been investigated by both theoretical analysis and experimental observation. Electrohydrodynamic (EHD) forces, dominate bubble motion in an electric field. It can be subdivided into electrophoretic force and dielectrophoretic force. Different electrode arrangements have been designed with the aim of decoupling these two forces and their corresponding effects.

The uniform electric field is generated by a parallel plate electrode arrangement, which aims to analyse electrophoretic forces individually. By analysing the bubble motion under different field polarity, it can be seen that the bubble moved against the electric field line. It indicates FK thermal bubbles easily attract electrons and therefore bubble behaves with negative polarity. The magnitude of the negative charges is calculated by analysing the bubble average velocities and accelerations, which are obtained by the high-speed images. The calculated results show that the charge magnitude is approximately 0.25 pC.

In addition, a rod-plate electrode arrangement was designed to create a non-uniform electric field. It allows for both electrophoretic force and dielectrophoretic force effects on bubble motion under different electric fields. In the theoretical analysis, the electric field profile is simulated by using an FEA model. Then the experimental results show that larger EHD forces lead to a greater bubble motion along the field direction. However, the bubble vertical motion is nearly independent of electric field magnitude.

Finally, the theoretical bubble velocities in both horizontal and vertical directions according to different field magnitudes have been compared with experimental results. A comparison of these results shows a strong correlation, which demonstrates the accuracy of the theoretical prediction. Hence, it can be seen that in this chapter an applicable numerical approach to predict not only FK thermal bubble motion but also any other material thermal bubble trajectory under various types of DC fields.

Chapter 5

The Effect of DC Field on Boiling Heat Transfer

A fool is a man who never tried an experiment in his life
- Erasmus Darwin

This chapter presents an experimental investigation on pool boiling behaviours of both Hydrofluoroethers (HFE) and Fluorinated ketone (FK). Furthermore, the effects of a DC field on FK boiling heat transfer enhancement have been observed under saturated temperature.

5.1 Introduction

In order to improve overall HV plant efficiency, there is an increased use of thermosyphon technology to provide temperature control, replacing conventional pumps, fans and radiators. HFE and FK are two low global warming potential coolants. One use of these fluids in high voltage plant is as the coolants within a thermosyphon. The working principle of the thermosyphon has been discussed in Section 2.1. Although thermosyphon is a very effective method of heat transfer [131], engineers are committed to developing approaches to enhance the thermal dissipation.

Two approaches to promote liquid-gas two-phase heat transfer have been discussed in Section 2.4. This chapter focuses on discussing the electrohydrodynamic (EHD) heat transfer enhancement. Early publications focus on the enhancement of single-phase convection [132]. Over the last two decades, researchers realized the greater potential of EHD in enhancing boiling heat transfer [60], [69], [133], [134].

While studies on EHD boiling have proceeded steadily, there is no publication that considers the EHD effects on both HFE and FK coolants boiling heat transfer. Thus, it is necessary to investigate electric field effects on pool boiling in the nucleate, transitional and minimum film boiling regimes of these coolants. Unfortunately, the material characteristic experiments that are shown in Chapter 3 indicate HFE coolant has poor dielectric properties and may not be ideally suited for use in high electric field environments [135]. Hence, in this report, only the FK sample is selected to investigate the EHD effects on boiling phenomena and heat transfer.

5.2 Experimental Apparatus

This section introduces the experimental apparatus design. Moreover, a heat transfer Finite Element Analysis (FEA) model based on the grounded electrode geometry has been developed to obtain temperature profiles and assist calculations.

5.2.1 Aims

There are three aims of the experiments. The first aim is to investigate the inherent heat transfer behaviours of both HFE and FK coolants during the phase change process. Therefore, the apparatus must allow the capture of real-time temperature data to assist in plotting the boiling curve, which is a scientific approach to explain the heat transfer performance of a two-phase system. The second aim is to observe the uniform DC electric field effect on the FK pool boiling regime. Hence, the apparatus should not only obtain the real-time temperature data but also facilitate application of a uniform DC field within the fluid under test. The last aim is to observe the boiling behaviour over each boiling regime, as the result, the apparatus design should allow access for equipment to record boiling phenomena.

5.2.2 Schematic of the experimental platform

A schematic diagram of the experimental apparatus platform is shown in Figure 5.1.

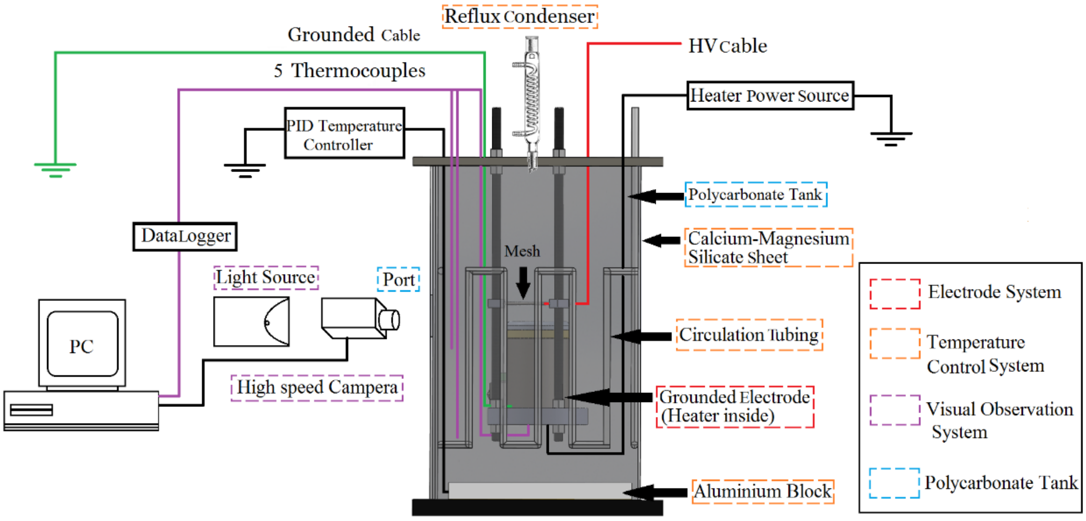

Figure 5.1 Schematic diagram of experimental arrangement

With reference to Figure 5.1, the platform consists of four main systems, which are labelled by different coloured dashed boxes. The design details of each section will be introduced in the following sections.

5.2.3 Electrode System

The investigation of EHD phenomena undertaken using a uniform DC electric field. There are two typical configurations to generate the uniform electric field. The first arrangement is the co-axial wire and tube [62], [66]. The second approach is the parallel plate [56], [76]. In this study, parallel plate electrodes were selected. There are two reasons that led to this decision. First, a significant field distortion always occurs at the HV wire terminals and therefore it may result in a non-uniform field and errors. Second, the parallel plate arrangement is convenient for the optical device to capture boiling phenomena without refraction.

5.2.3.1 Design of High Voltage Electrode

The high voltage electrode is made of a perforated steel sheet with 33% open area, which is sketched in Figure 5.2. This design minimises the restricted bubble flow and reduces its effect on boiling heat transfer. The centre diameter of the HV electrode is 80 mm and the edge was connected to a 3 mm diameter ring to avoid any undesired partial discharges.

Figure 5.2 Sketch of HV perforated steel sheet

5.2.3.2 Design of Grounded Electrode

The grounded electrode is a hollow cylindrical block. The cross-section engineering plot is shown in Figure 5.3. A mushroom-shaped aluminium block, polyetheretherketone (Peek) ring and a stainless steel base are the three components of the electrode.

The top central surface of the mushroom shape aluminium block serves as the boiling surface where the boiling process takes place. The area of the boiling surface is 7.07×10^{-4} m^2. Since the high thermal conductivity of aluminium, the temperature along the central axis of the aluminium block should be linear correlated with the distance to the heater. This hypothesis makes it possible to predict boiling surface temperature by using a thermocouple array.

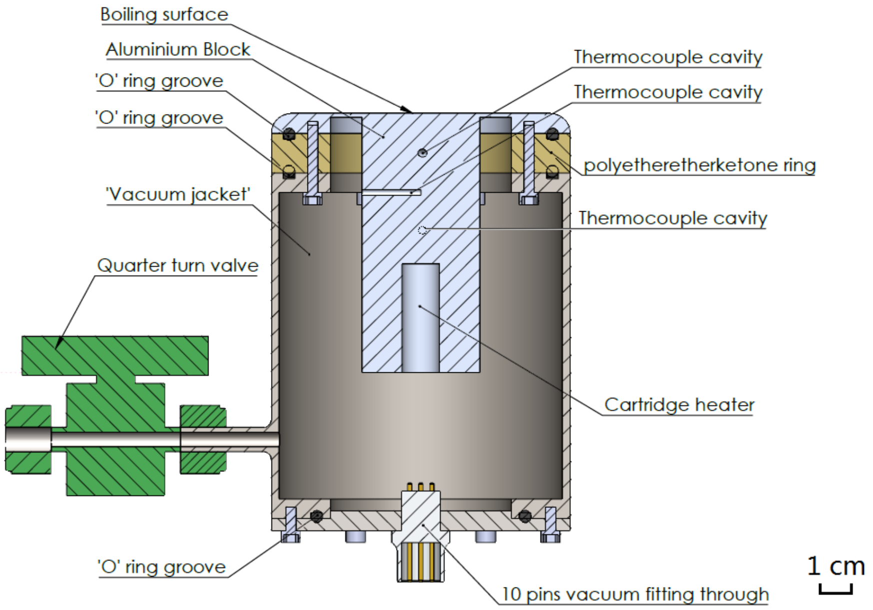

Figure 5.3 Cross section of the grounded electrode

To guarantee this boiling surface area, a thermal obstructive groove was machined which is shown in Figure 5.4. In order to generate the heat flux a 200 W cartridge heater, which was embedded inside the aluminium block. The peak heater input power can provide 283 kW m^{-2} heat flux on the boiling surface. To predict the temperature of the boiling surface three identical T- type thermocouples were positioned at a different height along the central axis of the aluminium block, also they were placed apart by 120° to reduce their effect on the measurement.

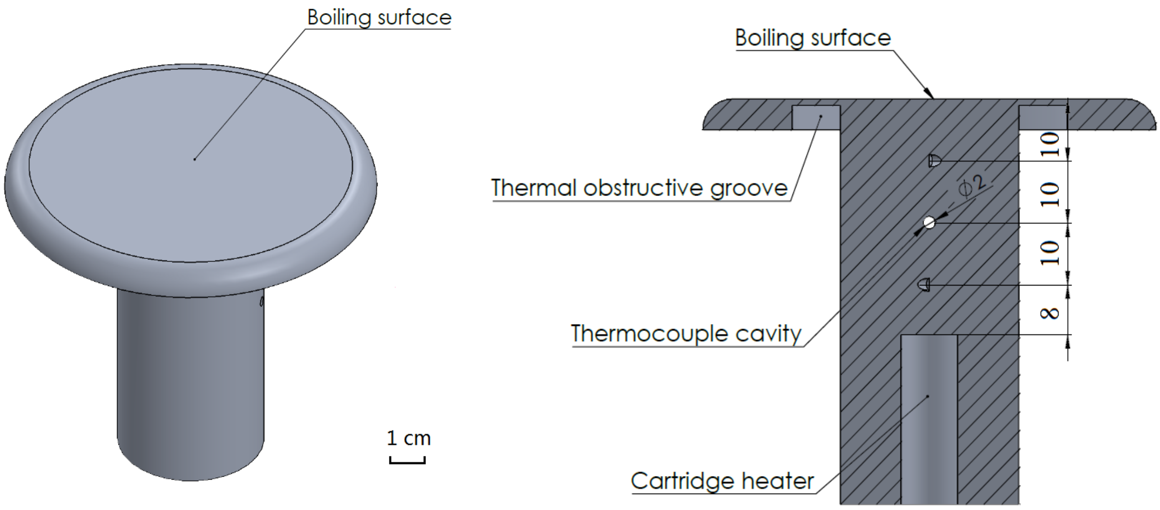

Figure 5.4 Sketch and cross-section of the aluminium block (unit in mm)

The polyetheretherketone (Peek) ring is the adapting piece which is shown in Figure 5.5. It splices the aluminium block and stainless steel base. The selection of Peek material is because of its outstanding mechanical strength and very low thermal conductivity. Therefore the maximum heat flux is always on the boiling surface.

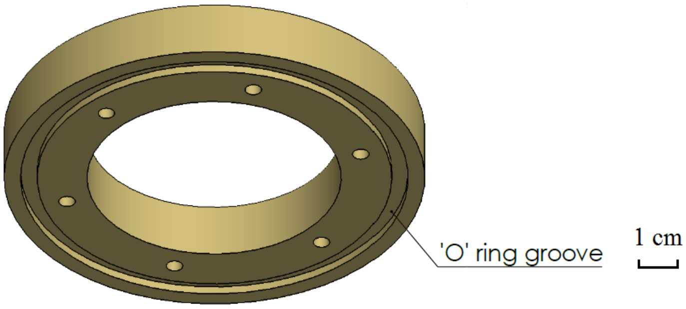

Figure 5.5 Peek ring

The last component is a stainless steel base that shown in Figure 5.6. It supports the aluminium block. ‘O’ rings were placed between interfaces and therefore, after vacuumization, a ‘vacuum jacket’ can be created. This ‘vacuum jacket’ is an excellent thermal insulation to minimise heat transfer. A vacuum fitting plug was equipped at the bottom to provide a means for electrical connection.

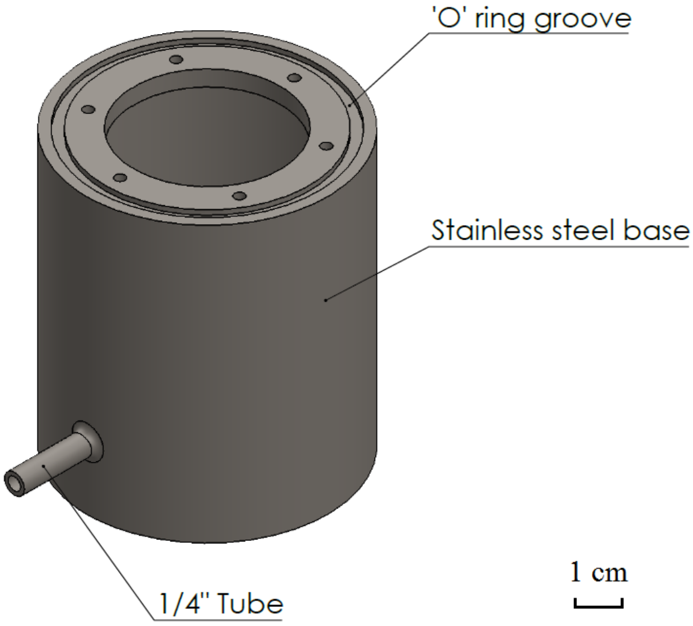

Figure 5.6 Stainless steel base

5.2.3.3 Modelling Verification of Electrode design

In order to verify the temperature profile hypothesis of the grounded electrode, a static heat transfer Finite Element Analysis (FEA) model was developed.

The geometry implemented into the FEA model is as same as the electrode blueprint. Since the rotational symmetry of the electrode, 2D axial symmetry is the model spatial dimension. The model geometry and material filling are shown in Figure 5.7.

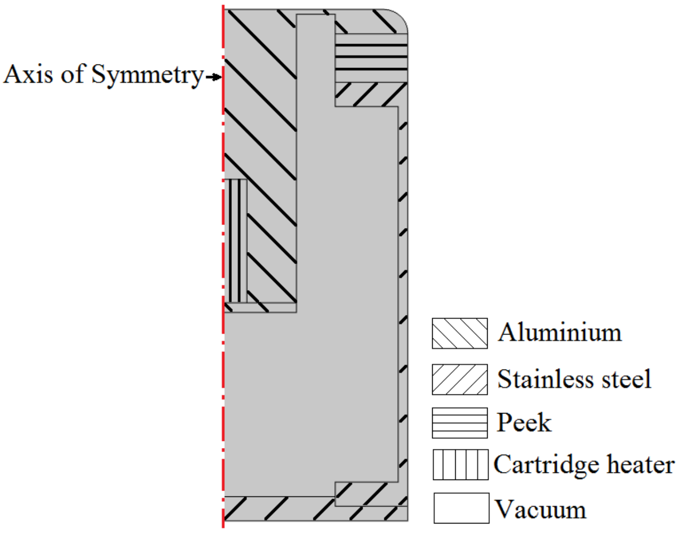

Figure 5.7 Modelling geometry and material filling

The modelling domains are filled with four materials, which are aluminium, stainless steel, peek and vacuum. The properties of each material are summarized in Table 5-1.

Table 5-1 Material properties

Properties	**Symbol**	**Aluminium**	**Stainless steel**	**Peek**	**Vacuum**
Thermal conductivity(W $m^{-1}K^{-1}$)	k	205	16	0.32	0
Density (kg m^{-3})	ρ	2600	7500	1300	0.00166
Heat capacity (J $kg^{-1}K^{-1}$)	Cp	910	490	1400	1004

Since there is no thermal convection or radiation in vacuum, the physics of the modelling domain is defined as heat transfer in solids. The temperature variation is only caused by thermal conduction and therefore the thermal Fourier equation is the governing equation applied to this model, i.e.

$$\rho\ Cp\frac{\partial T}{\partial t} = -\nabla \cdot (-k\nabla T) \tag{5.1}$$

where Cp the material specific heat capacitance and k is the thermal conductivity. In this model, the initial temperature of the electrode is 295 K.

The boundary indication is shown in Figure 5.8. The green line is the axis of symmetry; it allows the modelling slice to rotate along this axis. The black lines show the internal boundaries, which are considered to have a continuous thermal gradient across them. The thermal energy on this boundary is conserved and no extra energy supplied or removed across these boundaries. The blue line is defined as equal to a constant temperature which is equal to the saturated temperature of coolants (322.15 K for this model). The red line is the outer boundary of the cartridge heater, the magnitude of the heat flux is calculated by the ratio of heater power to heater surface area. It guarantees the heat power that implements in the model is identical with that of a real experiment. The heat fluxes on the heater boundary are summarised in Table 5-2.

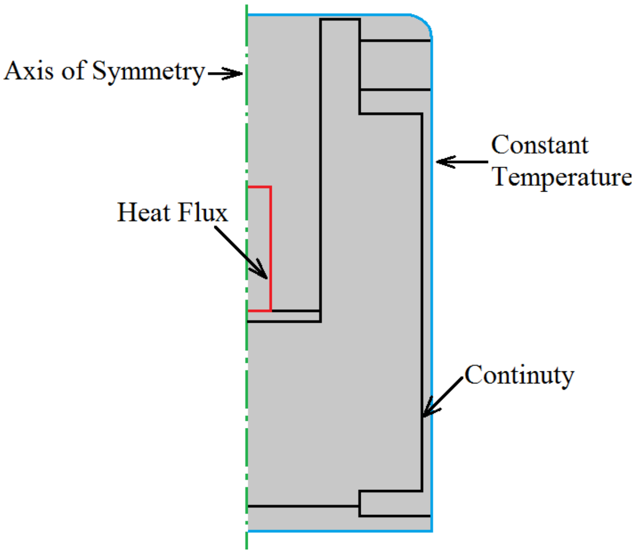

Figure 5.8 Mathematical boundary conditions of thermal physics

Table 5-2 Heat flux on the heater boundaries

Heater power P (W)	Boundaries heat flux q (W m^{-2})
50	65491.83
100	130983.66
150	196475.49
200	261967.32

The mesh setting, plotted in Figure 5.9, shows that a free triangular node was applied to create unstructured triangular meshes in all domains. In order to check the thermal obstructive groove performance, this area has the highest mesh density. The solid metal areas have high mesh density, it aims to provide an accurate thermal transfer profile. The vacuum area has low mesh density to reduce the computing time.

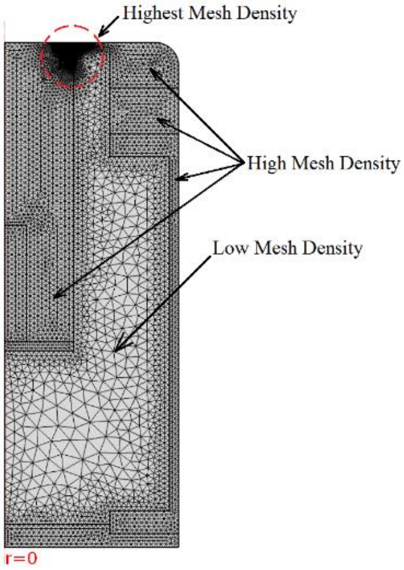

Figure 5.9 Mesh element of geometry

The temperature profile is shown in Figure 5.10 and Figure 5.11. It can be seen that the temperature contours are distributed in parallel in the aluminium block. These results indicate that there is a uniform temperature distribution in the heater radius direction. The line graph shows a good linear relationship between temperature magnitude and the central distance to the heater at the range of 0 to 40 mm, which covers the three-thermocouple positions.

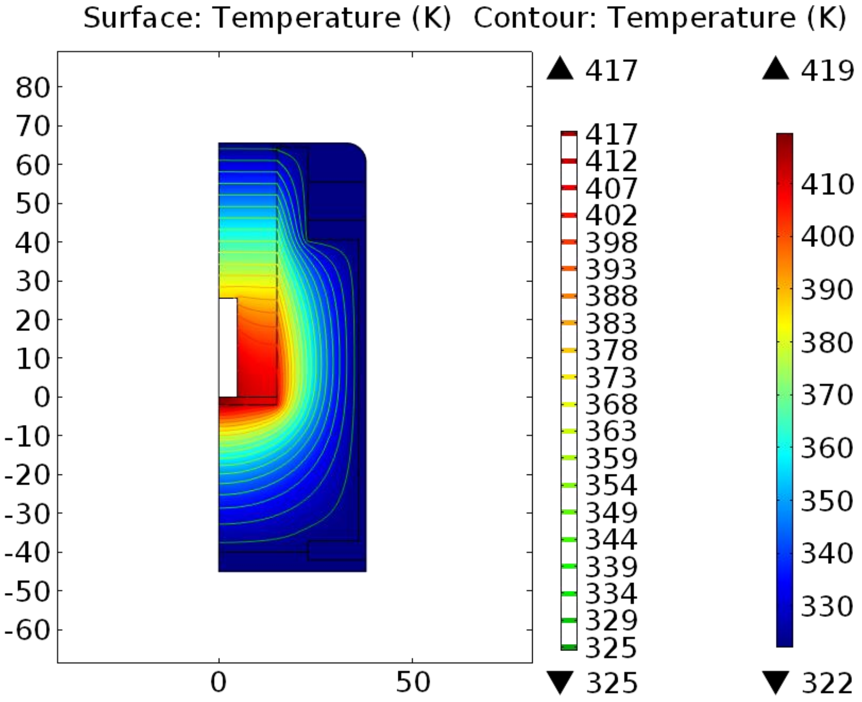

Figure 5.10 2-D axial symmetric surface plot, continuous plot of temperatures

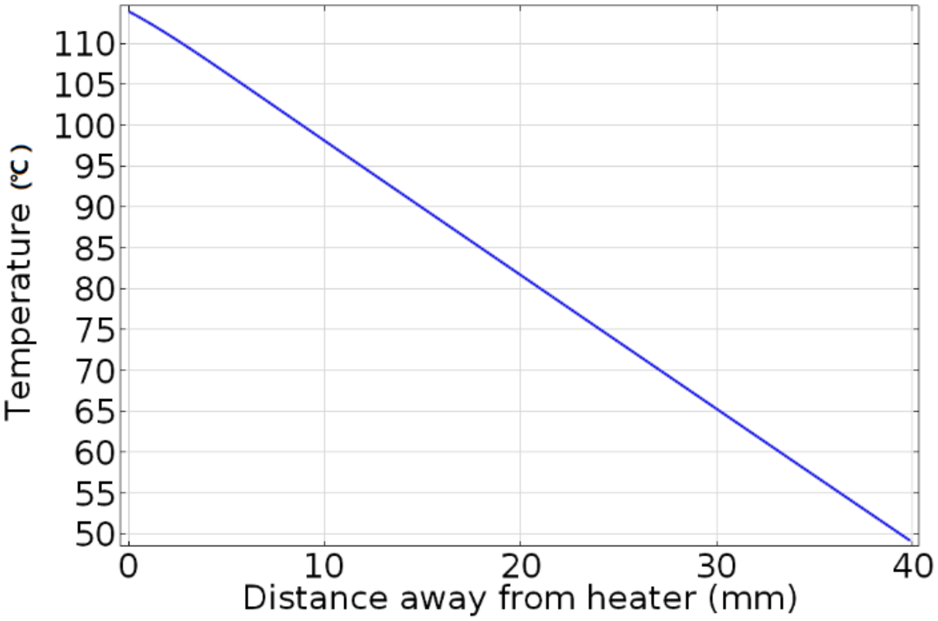

Figure 5.11 Temperature along the central axis from the heater to the boiling surface

The simulation results also examined the behaviour of the thermal obstructive groove. Results shown in the Figure 5.12 indicate that the heat flux uniformity of the boiling surface is excellent. Figure 5.13 details the heat flux along the boiling surface. It is seen that the heat flux reduced dramatically at the edge of the boiling surface, which indicates the vacuum thermal obstructive groove avoids heat loss efficiently.

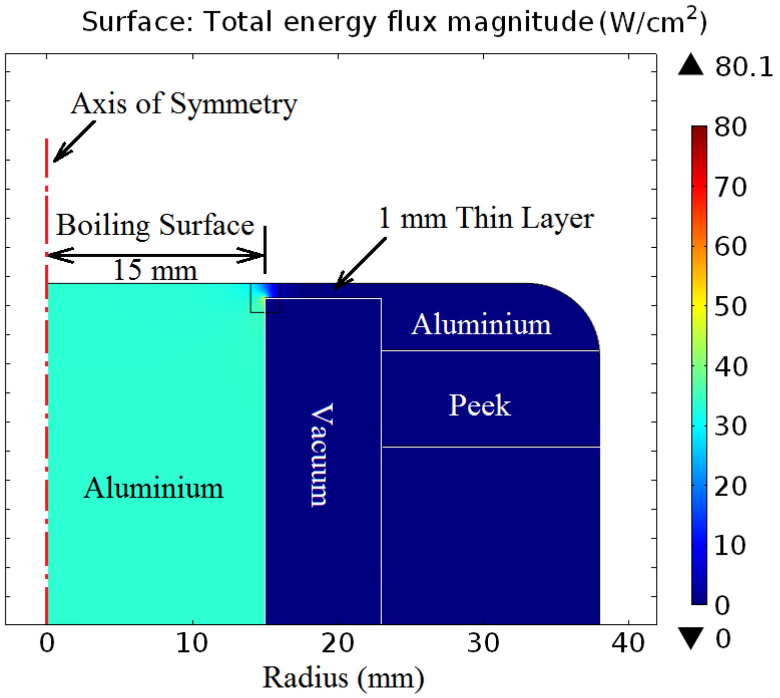

Figure 5.12 Heat flux on the top boiling surface

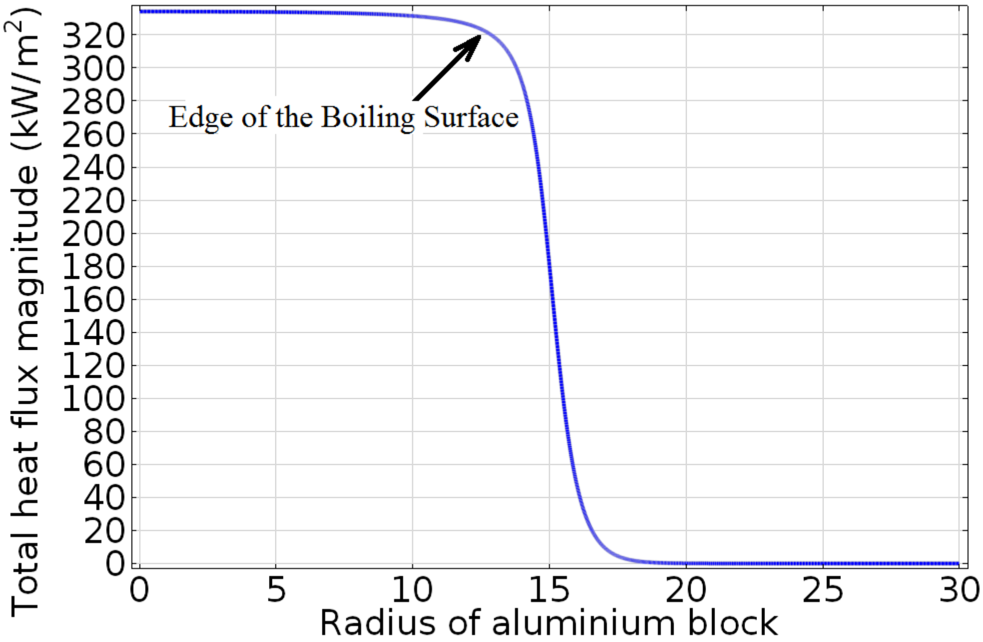

Figure 5.13 Heat flux magnitude along the boiling surface

In conclusion, the modelling results give three indications:

First, the temperature distribution is uniform on the boiling surface and the temperature magnitude is in a good linear relationship with the central distance to the heater. These two simulation results indicate the boiling surface temperature can be deduced by the temperature array.

Second, the uniform heat flux is on the boiling surface. The thermal obstructive groove can block heat flux efficiently.

Last, published literature has shown the critical heat flux (CHF) of both FK and HFE fluid is 208 W m^{-2} and 244.5 W m^{-2} respectably [47], [48]. The simulation result indicates that a 200 W heater has enough heat flux to exceed CHF of both FK and HFE fluids.

5.2.4 Polycarbonate Vessel and Support System

To allow visual observation, all experiments were conducted in a $246 \times 246 \times 400$ mm polycarbonate vessel, which provides a very good optical transparency (see Figure 5.15). A nylon frame was bolted on a laminated plastic lid. It is designed to support both HV and the grounded electrode. The separation between the HV and the grounded electrode can be varied vertically by adjusting nylon bolts. The sketch is shown in Figure 5.14. For this experiment, the electrode separation was set equal to 10 mm by a spacer, therefore the electric field that added to the boiling area can be varied by adjusting the applied electric potential

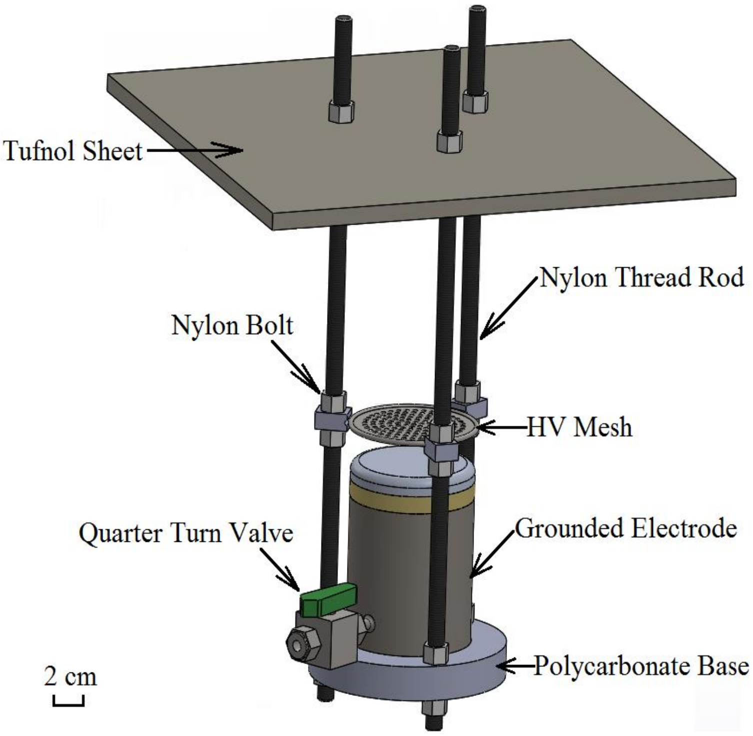

Figure 5.14 Nylon frame electrode support system

5.2.5 Temperature Control System

The temperature control system aims to maintain coolants saturation temperature. According to the target temperature, there are three different approaches that have been reported in the literature. The first method is to use a pumped closed circuit system [55], [60], [133]. The second approach is to use a water bath [45]. The third technique is to use a heater or hot plate [47], [136]. In this study, both passive and active approaches were applied to maintain the bulk liquid temperature always equal to saturation temperature. The passive approach is to attach calcium magnesium silicate sheets on the testing vessel outside surfaces. These sheets behave a very low thermal conductivity and therefore it can prohibit heat transfer efficiency. The active approaches include a hot plate, circulation pipe and a condenser which are shown in Figure 5.15.

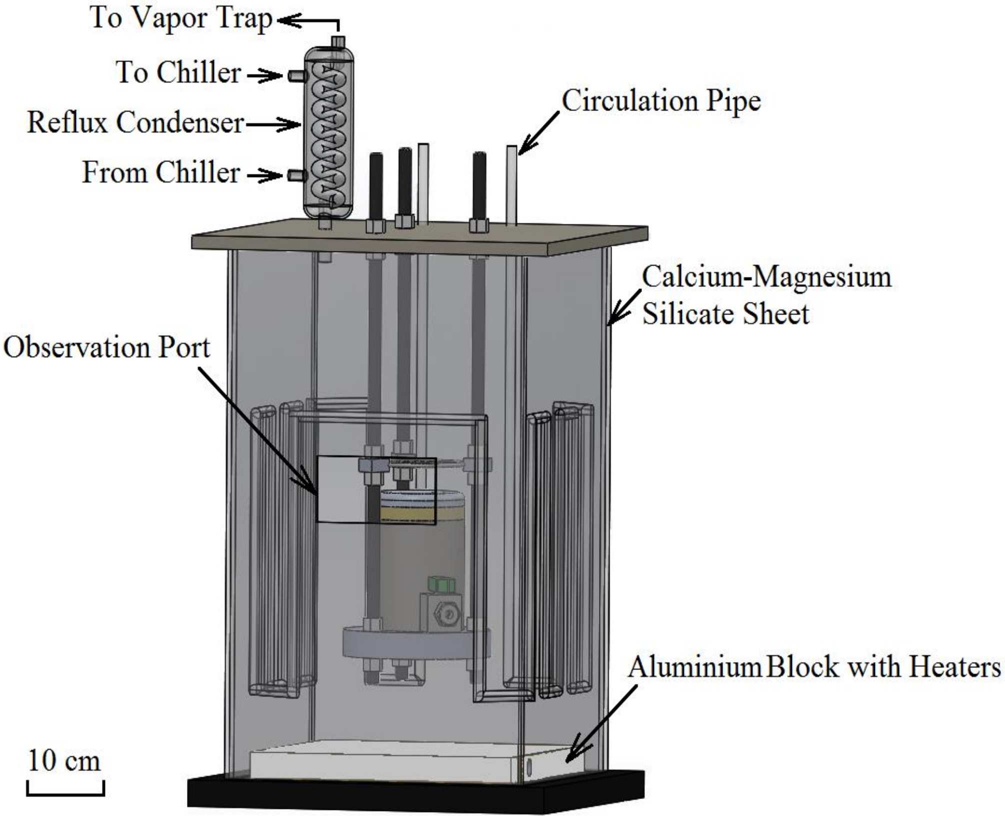

Figure 5.15 Temperature control system

The main heater is an aluminium hot plate which was placed on the bottom of the testing vessel. It aims to raise the coolant temperature. There are two cartridge heaters embedded in the aluminium plate. A proportional integral differential (PID) controller controlled the input power of these heaters. Circulation pipes were attached to the inside surface of the vessel that aims to unify bulk temperature. A condenser was located on the top cover of the vessel. It helps to condense the coolant vapour back to the liquid form.

5.2.6 Visual Observation System

A visual record system was applied with the aim to capture the coolant boiling behaviours. This system contains a high-speed digital camera (MotionXtra HG-100 K), a LED lamp and a diffuser. In this experiment, the frame rate of the camera was chosen equal to 1000 fps and the resolution was 800×600 pixels. The light source is a 100 W LED lamp, which provides enough light intensity for the high-speed camera.

5.3 Experimental Procedure

This section details the experimental procedures and verification results.

5.3.1 Experimental Procedures

The experiments can be divided into two parts, which are investigating coolants inherent boiling behaviour and studying EHD effect on FK coolant boiling behaviour. All the experiments were conducted at atmospheric pressure. Before each experiment, the grounded electrode was connected to a vacuum pump for 48 hours to create a 'vacuum jacket', which helps to keep thermal stability and limit heat loss during the experiments. Furthermore, to avoid any contamination that may affect heat transfer, both HV and grounded electrode were polished and cleaned with acetone. After installation of the electrode system, coolant was injected through a filter paper into the testing vessel until the liquid-vapour interface was 5 cm above the HV electrode. Then, the bulk liquid was heated up to the saturation temperature by the temperature control system.

The average heat flux q and boiling surface superheated temperature ΔT are the two parameters that required for plotting the boiling curves. The average heat flux was calculated from the heater input power (Q_{heater}) and boiling surface area ($A_{boiling}$). i.e.,

$$q = \frac{Q_{heater}}{A_{boiling}} \tag{5.2}$$

In this experiment, the heater input power was measured by a calibrated power meter and the boiling surface area was 7.07×10^{-4} m^2. The second parameter, which is boiling surface superheated temperature was calculated as;

$$\Delta T = T_w - T_{sat} \tag{5.3}$$

In the Equation 5.3, T_w is the wall temperature of the boiling surface. It is deduced from the three temperature sensors that are embedded inside the grounded electrode. T_{sat} is the coolant saturation temperature. Hence, it can be seen that the inherent boiling curve of coolants can be plotted by both gradually increasing the heater input power and decreasing the heater input power progressively.

The effective transfer coefficient (h) is defined to numerically evaluate thermal dissipation. It is the ratio between boiling surface heat flux (q) and superheated temperature (ΔT), i.e.

$$h = \frac{q}{\Delta T} \tag{5.4}$$

The larger transfer coefficient indicates that, with the same temperature differences, the coolant can dissipate larger thermal energy via the phase change process.

With the aim to obtain the EHD effect on FK coolant boiling heat transfer, a DC electric potential of 10 kV, 15 kV and 20 kV for both polarities were applied to the HV electrode in batches. The experimental procedures were the same as the zero-field experiments. To ensure repeatable properties, each experiment has been conducted at least twice.

5.3.2 Verification Results

There are three initial experiments to verify the arrangement used. The first experiment is to examine the gas tightness of the grounded electrode. The vacuum magnitude of the electrode as a function of time is shown in Figure 5.16.

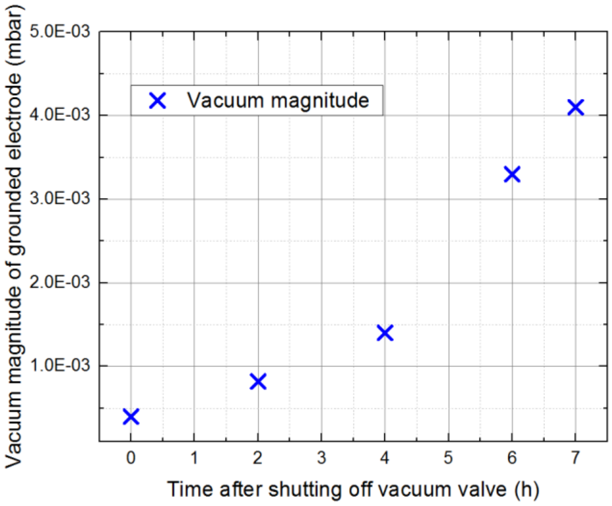

Figure 5.16 Vacuum magnitude as a function of time

It can be seen that after vacuuming the grounded electrode was under high vacuum ($\sim 10^{-3}$mbar) and after 7 hours the 'vacuum jacket' still existed to maintain thermal stability and limit the heat loss during the experiment.

The second initial experiment is to check the performance of the temperature control system. Two thermocouples were placed in the coolant. One of them was close to the hot plate and the other was close to the boiling surface. The targeting temperature was 49 ℃ and the test result is presented in Figure 5.17. It can be seen that initially there was a temperature overshoot of the hot plate. However, after a few minutes, the temperature has levelled off and it finally converges to the sample saturation temperature. This result indicates the temperature control system can control the bulk liquid temperature precisely and it meets the design requirements.

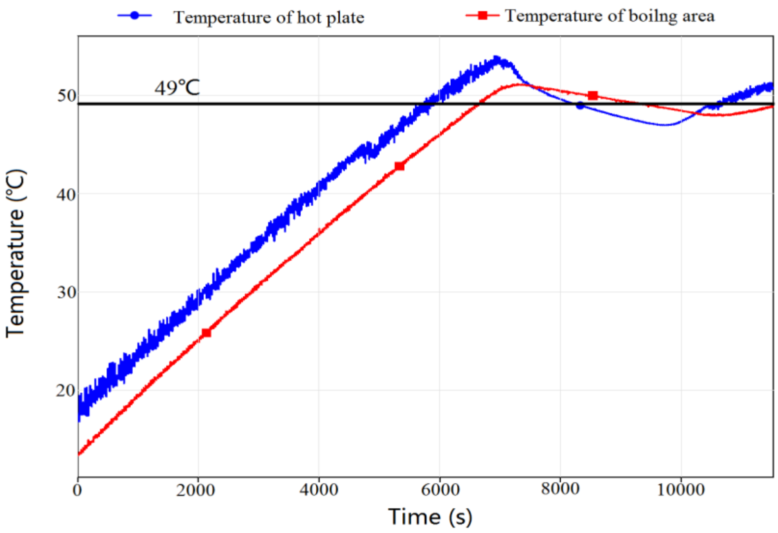

Figure 5.17 Coolant saturation temperature control

The last verification is to test the temperature sensor array that is embedded in the grounded electrode. The heater input voltage was varied by a variac and the input power was monitored by a power meter. The temperature profiles were shown in Figure 5.18.

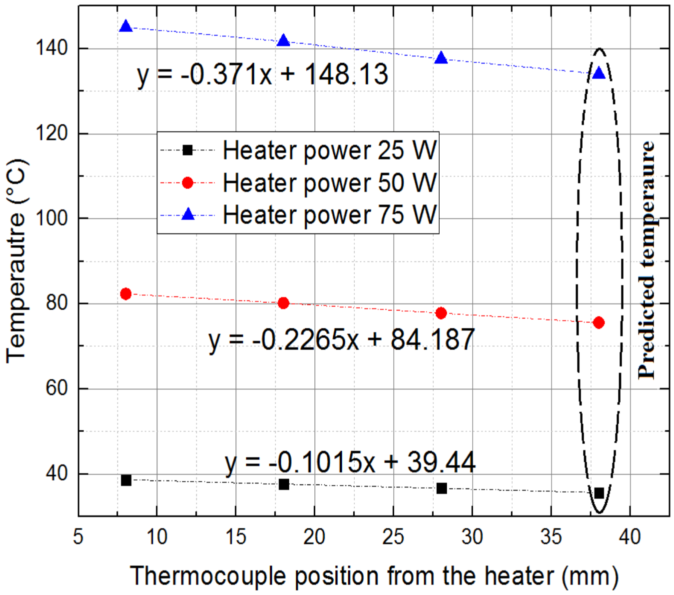

Figure 5.18 Temperature reading against the position to the heater

For this initial experiment, the grounded electrode was placed in the air, hence the temperature and power correlation was different with the electrode that placed in the coolants. The series results demonstrate that with different input power ranges, the temperature profile readings by the sensor array are always a good linear function. These results indicate the boiling surface temperature can be deduced precisely by the function that is given by the temperature data. In conclusion, the verification experiments have proven that the manufactured apparatus does meet the design requirements.

5.4 Results

The result section contains two parts. The first part characteristics the boiling curves of both HFE and FK coolants without the presence of the DC field. The effective heat transfer coefficients were obtained with the aim to compare these two candidate coolants' thermal properties.

The second part details the variation of the FK boiling curve caused by the DC field. The benefits given by the EHD phenomena on boiling behaviour are also discussed. In order to plot the coolant boiling curves, experiments were conducted with an increasing heat flux values, which is attributed to the heater power input. The heater input was increased in stages until the temperature to reach a steady state during the heat transfer. The boiling stages can be easily identified by either the visual record system or the temperature variations measured by temperature sensor array.

5.4.1 Boiling Curves without DC Field

Figure 5.19 and Figure 5.20 show the boiling curves for the parallel plate in HFE and FK coolants. For clarity, only the natural convection and nucleated boiling regimes are plotted. Note that the boiling curve is valid for corresponding heater arrangements; the boiling curve may change due to the different heater configurations.

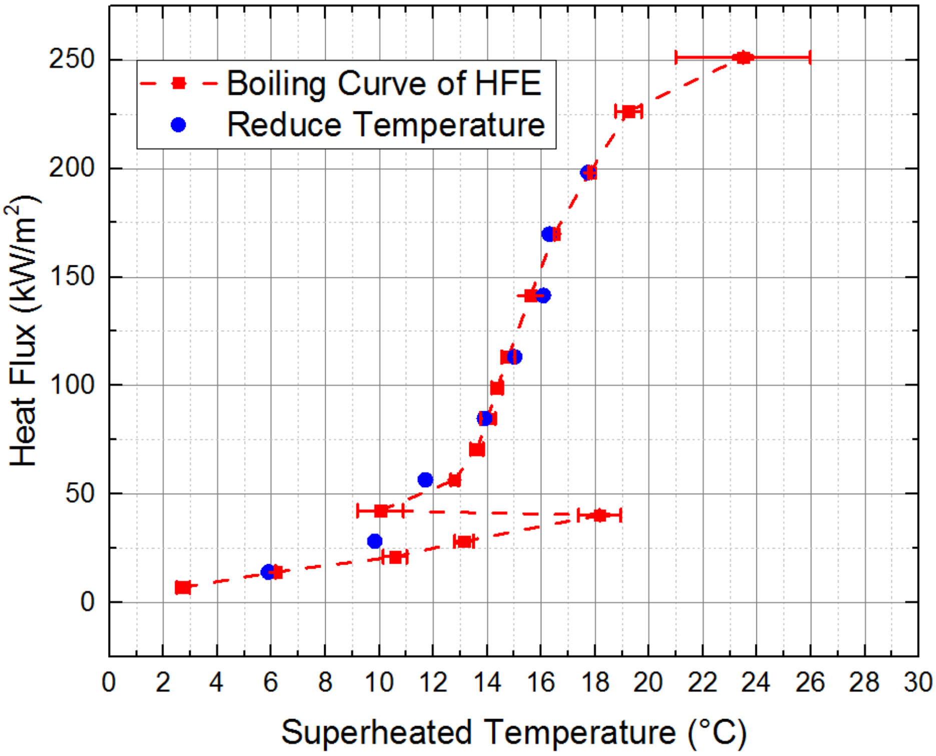

Figure 5.19 Pool boiling curve in saturated HFE coolant at atm

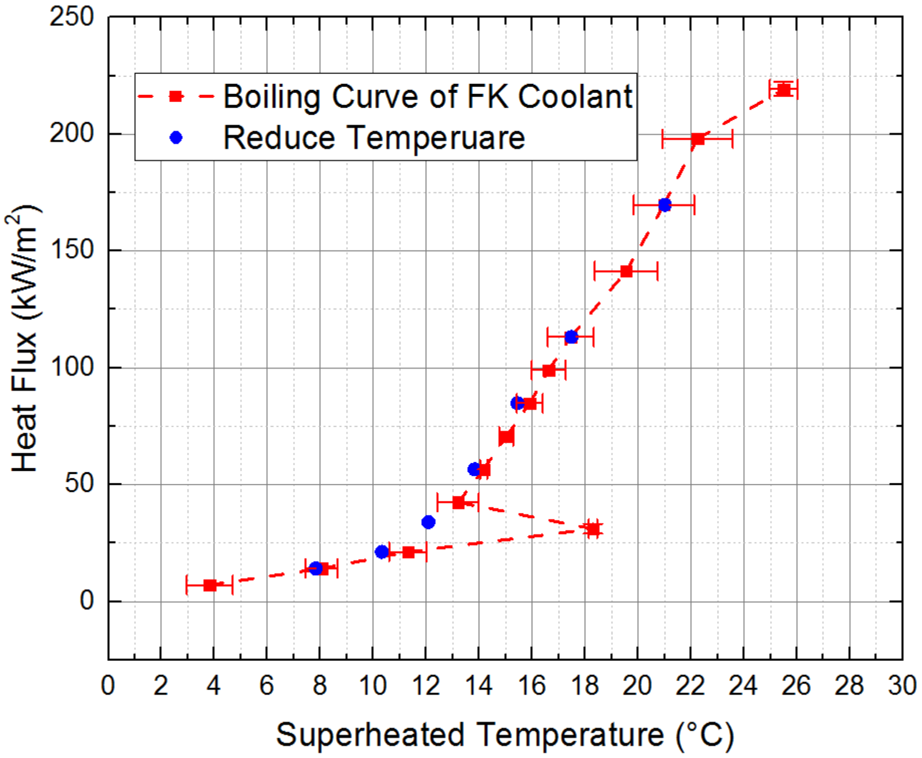

Figure 5.20 Pool boiling curve in saturated FK coolant at atm

The visual observation of boiling phenomena according to the different heat fluxes are plotted in Figure 5.21 and Figure 5.22.

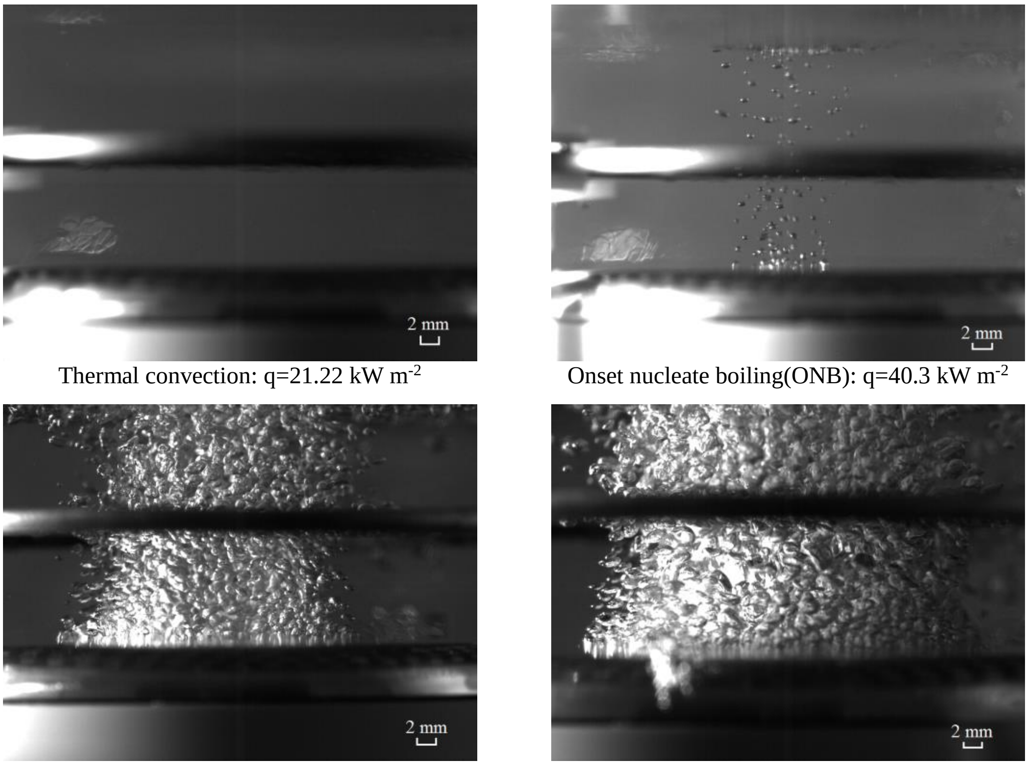

Thermal convection: q=21.22 kW m^{-2}

Onset nucleate boiling(ONB): q=40.3 kW m^{-2}

Nucleate boiling: q=141.47 kW m^{-2}

Critical heat flux (CHF): q=248.96 kW m^{-2}

Figure 5.21 HFE sample boiling phenomena of different heat transfer regimes

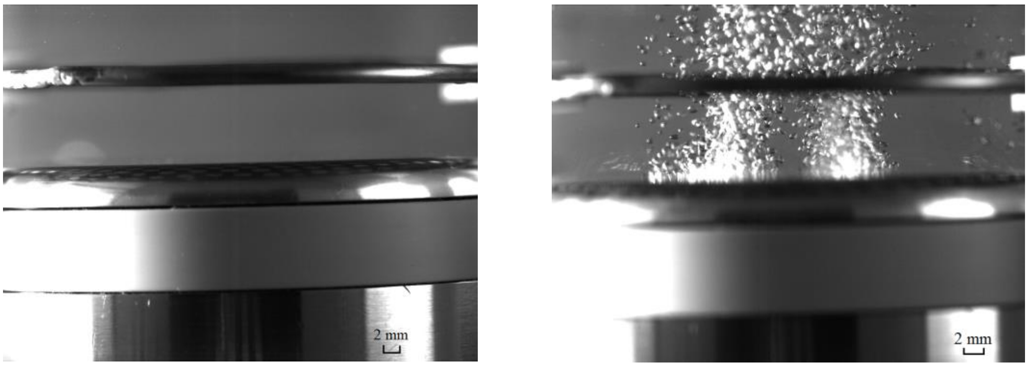

Thermal convection: q=21.22 kW m^{-2} Onset nucleate boiling (ONB): q=31.2 kW m^{-2}

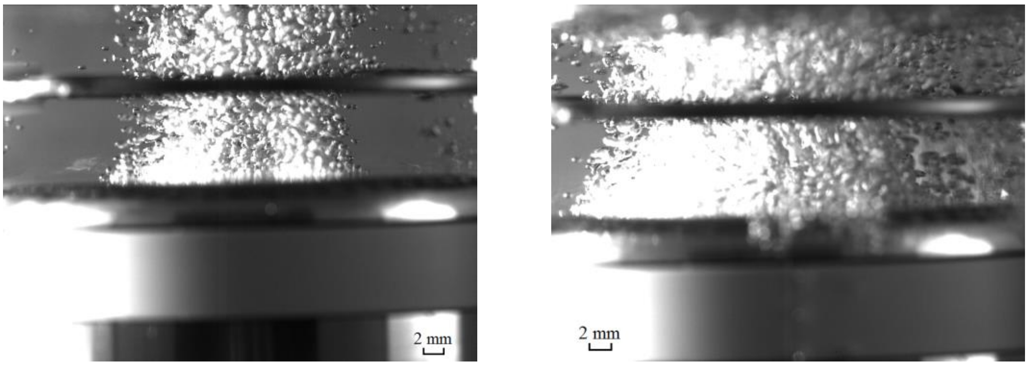

Nucleate boiling: q=141.47 kW m^{-2} Critical heat flux (CHF): q=219.28 kW m^{-2}

Figure 5.22 FK sample boiling phenomena of different heat transfer regimes

From the results, three observations can be made. Firstly, the 'boiling curve' and 'reducing temperature dots' do not always overlap. Specifically, it can be seen that there is an obvious boiling hysteresis for both HFE and FK coolants, while the reducing temperature dots do not demonstrate this. This is because both HFE and FK have relatively low surface tension. In this case, bubbles require a higher temperature gradient to initiate nucleate boiling. Secondly, there is a dramatic turn of the boiling curve occurs at the onset of nucleate boiling (ONB) point. When the heat flux achieved ONB point, with the formation of bubbles, the temperature of the boiling surface decreased significantly, the reason for this phenomenon is attributed to the phase change process that absorbs the thermal energy. Thirdly, the slope of the boiling curve of the nuclear boiling regime is much steeper than that of the convection regime, this indicates the phase-change process is more effective than convection on heat energy dissipation. Experiments overserved ONB heat fluxes are 40.3 kW m^{-2} and 31.2 kW m^{-2} for HFE and FK respectively with a corresponding superheated temperature of ~18.15 ℃ and 18.29 ℃. The critical heat flux (CHF) of HFE and FK are 248.96 kW m^{-2} and 219.28 kW m^{-2} respectively.

With the aim to compare HFE and FK boiling heat transfer behaviour, the effective heat transfer coefficient (*h*) as a function of heat flux is plotted in Figure 5.23. The result shows that with the increasing heat flux, HFE has a higher *h* than FK, which indicates with the same applied heat flux, larger thermal energy can be dissipated during the HFE boiling process.

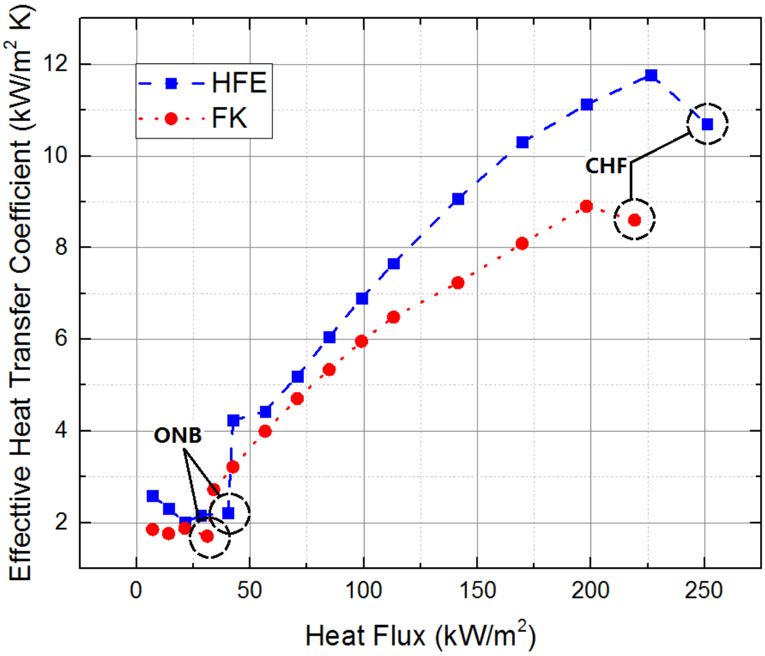

Figure 5.23 Effective heat transfer coefficient versus heat flux for HFE and FK

5.4.2 FK Boiling Curves under Uniform DC Field

The last section has shown the boiling curves of HFE and FK without any electric field. The results show that HFE has better performance in terms of thermal dissipation. However, due to the poor dielectric properties of HFE [135], this study only investigates FK heat transfer characteristic under different fields. The boiling curves of FK coolant under different electric fields are plotted in Figure 5.24 by both raising and decreasing input temperatures.

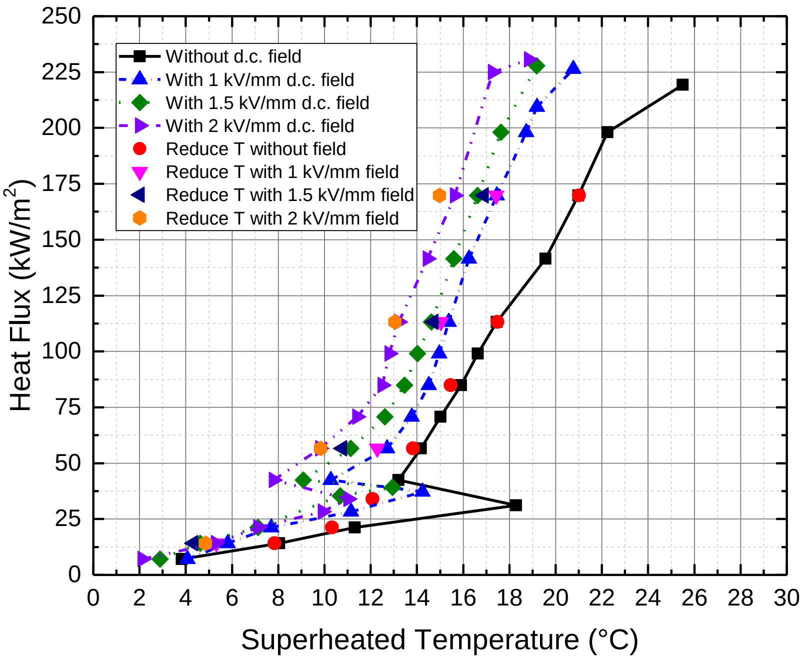

Figure 5.24 FK boiling curves under different electric fields

There are three observations. The first observation is the DC field effects on the ONB. The superheat temperature values at ONB under different fields are shown in Figure 5.25, it can be seen that in the presence of a DC field, the nucleate boiling begins at a lower superheated temperature.

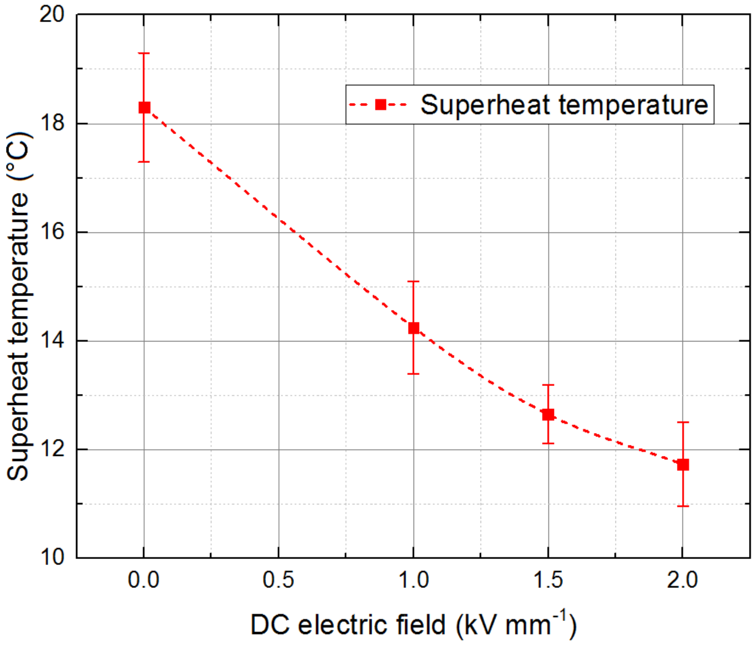

Figure 5.25 Electric field effect on superheat temperature of ONB

The second observation is that the DC field effects the nucleate boiling regime. This phenomenon can be reflected by the shifting boiling curves and effective heat transfer coefficients that are plotted in Figure 5.26.

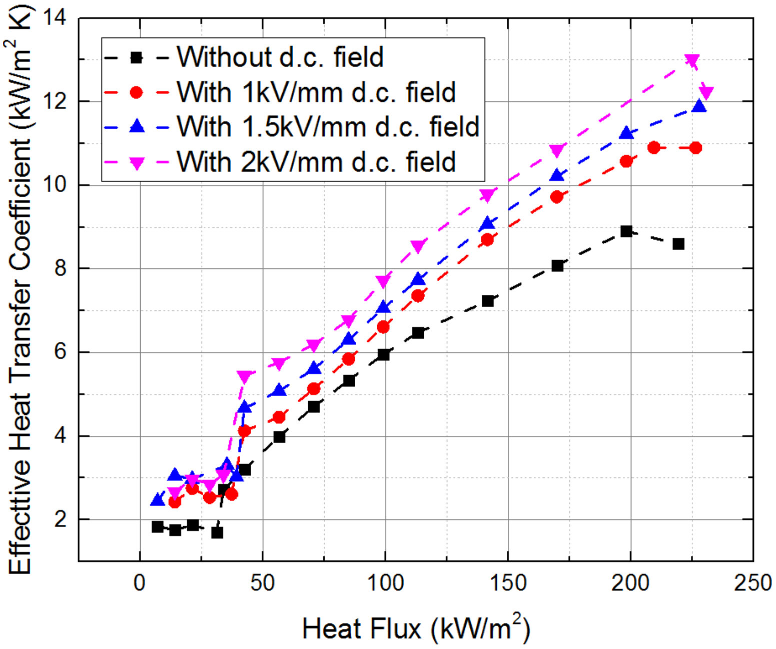

Figure 5.26 FK effective heat transfer coefficient in different fields

It can be seen that the boiling curves shift to the left with the increasing electric field, the reason for this phenomena is that less superheated temperature is required under the field to maintain nucleate boiling with the same heat flux. Furthermore, the effective heat transfer coefficient indicates that the DC field can effectively reduce the boiling hysteresis and further enhance thermal dissipation.

The last observation is that the DC field effect on the coolant critical heat flux (CHF). From Figure 5.27 it can be seen that the CHF value is increased with the enhancing electric fields. CHF is defined as the heat flux that causes the onset of film boiling that results in bubbles coalition and forming unstable vapour film. The vapour film covers the heater surface and increases the thermal resistance. Hence, CHF can be easily detected by the sudden increase of temperature sensors readings. The rapid temperature increase may cause the physical burnout of the heater surface and therefore CHF is defined as the maximum heat flux permissible for most heaters. As the consequence, a larger CHF value means higher thermal energy threshold, which also benefits to the thermal energy dissipation.

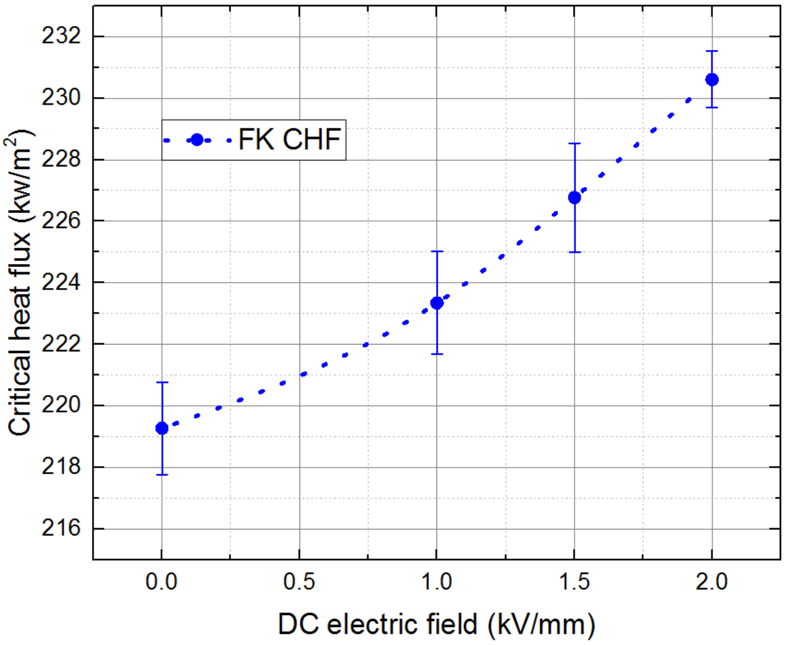

Figure 5.27 FK critical heat flux as a function of DC fields

The field polarity effect has also been investigated. The results are shown in Figure 5.28. It can be seen that the boiling curves are nearly overlapped under the same absolute value of the electric field and there is not an obvious variation on bubble characteristics. These results indicate that the electric field polarity does not have a significant effect on both FK coolant boiling behaviours and thermal dissipation.

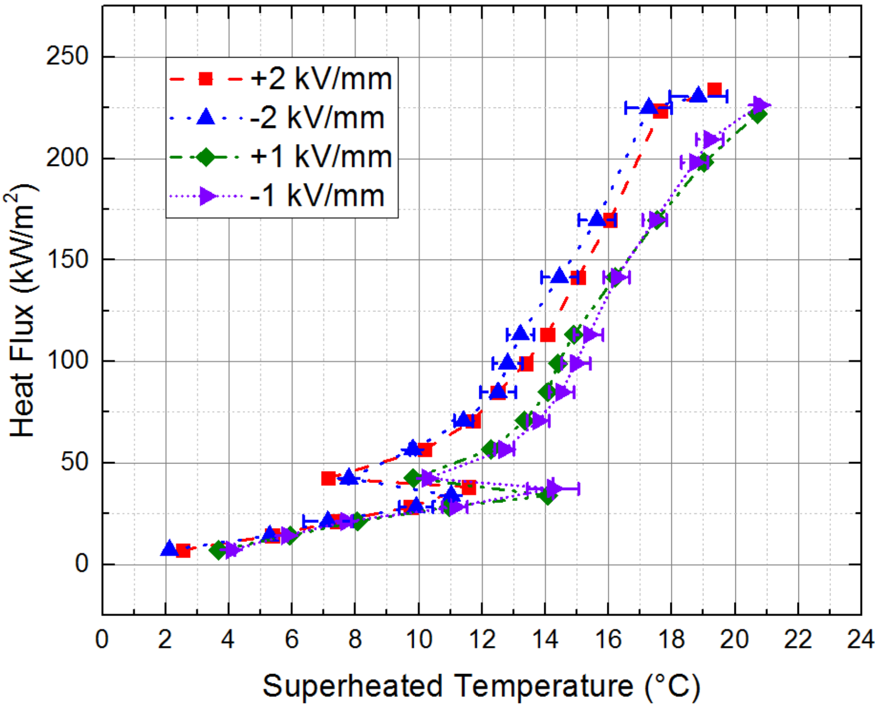

Figure 5.28 Field polarity effect on the FK boiling curves

5.5 Discussion

This section aims to discuss the physical reasons for all experimental results.

5.5.1 Boiling Curve of HFE and FK without DC Field

The results have shown that compared with FK, HFE has better thermal dissipation capability. It is reflected by the HFE sample's steeper nucleate boiling curve and higher effective heat transfer coefficient (see Figure 5.23). The different boiling heat transfer capability is attributed to the different material properties.

As discussed in Section 2.2.2 the thermal dissipation performance of a two-phase material can be characterised by the thermal dispassion factor (*N*). A higher thermal dispassion factor indicates greater permissible heat flux can be removed from the heat source during the phase change process. After checking the material data sheet [100], compared with FK HFE has the higher latent heat of evaporation, larger density and lower viscosity. Consequently, HFE having a higher thermal dissipation factor than FK, which results in the HFE sample has better cooling performance than FK.

5.5.2 Effect of DC Field on the Onset Nucleate Boiling (ONB) superheated Temperature of FK Coolant

The results shown in Figure 5.19, Figure 5.20 and Figure 5.24 demonstrate the phenomenon that the boiling surface has to achieve a high temperature in order to initiate the nucleate boiling. Since the temperature at the boiling surface is higher than the saturation temperature, this phenomenon is usually defined as the boiling temperature overshoot. This phenomenon is governed by the surface tension of the coolant. As both HFE and FK samples behave relatively low surface tension, the bubble nucleation sites are always ‘wet’. Therefore bubble sites require the larger surface temperature to activate [133], thus, forming a temperature overshoot.

The temperature overshoot is usually harmful to engineering applications [137], the reason for that is the superheat temperature is still in a linear or near correlation between heat flux and wall superheat. In contrast, the coolant can provide a much better performance once it turns into the nucleate boiling regime because the excess superheat can be released quickly during the phase-change process. Hence, reducing the overshoot temperature improves the two-phase system thermal dissipation efficiency.

Literature has shown that adding an electric field on the boiling region is one of the solutions to reduce the boiling temperature overshoot [69], [133], [138], which is also found in this study. From Figure 5.25 it can be seen that with the presence of a DC field the overshoot temperature of FK is decreased.

The physical basis of this improvement lies in the EHD force, which has been introduced in Section 2.4.2. Since the electric field is involved in the two-phase flow, the EHD term should be included in the Navier-Stokes equation [69], which for an incompressible liquid is:

$$\rho \frac{D\vec{v}}{Dt} = \rho\vec{g} + \overrightarrow{F_{EHD}} - \nabla P + \eta_l \nabla^2 \vec{v} \tag{5.5}$$

where $\frac{D\vec{v}}{Dt}$ represents the substantive acceleration consisting of the local contribution $\frac{\partial\vec{v}}{\partial t}$ and the convective term $(\vec{v}\cdot\nabla)\vec{v}$. The gravitational force per unit volume of the flow is denoted by the vector $\rho\vec{g}$; P is the pressure of the local fluid and the last term $\eta_l\nabla^2\vec{v}$ is the viscous factor.

It can be seen that the electric field induces an electroconvective movement in the FK sample and substantially enhances the thermal convection turbulence [69], [133]. This phenomenon further decreases the thermal boundary layer and consequently reduces the overshoot temperature.

5.5.3 Effect of DC Field on Nucleate Boiling Regime of FK Boiling Curves

The second finding from the experiments is the electric field effects on the nucleate boiling regime. Once boiling occurs, since the permittivity of the gas bubble and surrounding coolant are different, a non-uniform electric field is formed near the bubble coolant interface. This non-uniform field generates the interfacial EHD force and further affects bubble shape and boiling behaviours [57].

Without an electric field, when the bubble appeared at a bubble site, the thermal dissipation is governed by three mechanisms (see Figure 5.29i.) thermal conduction on the bubble microlayer, thermal absorption due to the phase change and thermal convection within the coolant adjacent to the bubble pocket.

With an electric field, due to the presence of the EHD force, bubble movement and shape are varied, which further influences the thermal dissipation mechanisms. Pohl proposed that the EHD forces act on a sphere bubble is determined by the bubble radius and the relative permittivity of bubble and liquid respectively [130]. Many studies have reported that the EHD force pushes the bubble against on the boiling surface, results in an intense evaporation in the bubble site and dramatically increases the bubble production and heat transfer [55].

Furthermore, many papers have reported that a bubble is elongated in the direction of the electric field [55], [67], [139] (see Figure 5.29ii.). The reason for this phenomenon is due to the electric stress caused by EHD, works on the bubble equator and towards the gas phase. With the same volume, the ellipsoidal bubble has a bigger surface area than a spherical bubble and therefore it increases the thermal conduction area on the bubble microlayer.

The last benefit given by the electric field is electro-convection. This additional convection cycle decreases the microlayer thickness meanwhile enhances the perturbation on the boiling surface. The perturbation further generates new bubbles by breaking-up the bubble microlayer [55].

It can be seen that the EHD force enhances both thermal conduction and convection within the two-phase system. Hence, a DC field can enhance the thermal dissipation, on the nucleate boiling regime and results in the boiling curve shifting to the left.

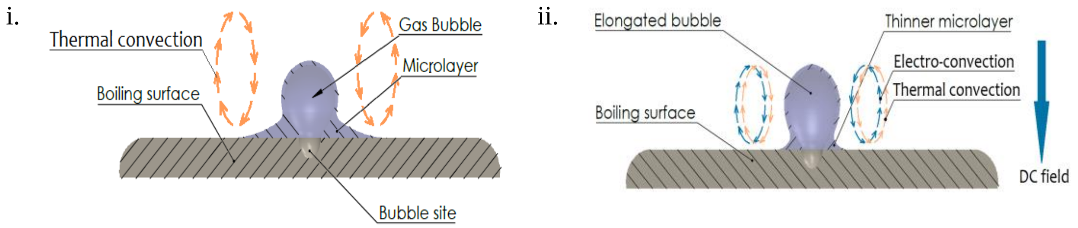

without DC field

with DC field

Figure 5.29 Nucleate boiling thermal dissipation mechanism

5.5.4 Effect of DC Field on the Critical Heat Flux (CHF) of FK Boiling Curves

The last indication given from experiments is that the DC field helps to increase the CHF value (see Figure 5.27). At CHF, bubbles form tempestuously. When the distance between bubble sites is smaller than the bubble diameter, neighbouring bubbles will coalesce and form a larger gas blanket [140]. This bubble blanket generates disturbance to the boiling surface, which is harmful to heat transfer and results in a rapid temperature increase on the boiling surface. The high temperature could cause the internal components failure of the cooling applications. Hence, the CHF is always defined as the max operational heat flux for the cooling equipment. An increased CHF value means a higher heat flux threshold of the cooling device, consequently, it can be seen as a method for cooling application optimization approach.

The EHD enhancing mechanism of the CHF can be explained by electric field effects on the liquid-gas interface stability [140]. As discussed in Section 2.4.2.4, with the involved electric field '*E*' the critical wavelength becomes smaller. Consequently, the bubble blanket is harder to form and therefore increases the value of CHF. This effect is inversely proportional to field squared, therefore, it is polarity independent.

5.6 Summary

This work has investigated the pool boiling behaviours of both Hydrofluoroethers (HFE), and Fluorinated ketone (FK). The effect of a DC uniform field on FK boiling performance also has been observed. From the application aspect, a novel hollowed electrode, which has a temperature sensor array in it, was manufactured to allow experiments to measure boiling temperature data. By using these data the boiling behaviours can be obtained that assists in plotting the boiling curves. The boiling curves provide the information on the complex two- phase boiling phenomena, which are valuable for the thermosyphon optimization design.

From a physical aspect, this study gives a detailed boiling and EHD mechanisms of candidate coolants from experiments. First, for both HFE and FK coolants there is a distinct boiling hysteresis before the ONB point. This phenomenon is embodied by the larger temperature overshoot. The reason for this is because both FK and HFE behave relatively low surface tension and therefore the 'wet bubble cavity' need more energy to initiate nucleate boiling. Second, a higher heat transfer coefficient indicates HFE can dissipate thermal energy more efficiently than FK coolant. Third, adding the uniform DC field is a realizable method to improve the boiling heat transfer of FK coolant. A 38% thermal dissipation enhancement was obtained under a 2 kV mm^{-1} electric field. The boiling enhancements are reflected in the EHD erasing boiling temperature overshoot, increasing the effectively boiling coefficient and raising the CHF point. Finally, different electric field polarities do not have a significant variation in boiling heat transfer enhancement.

Chapter 6

Numerical Simulation of Bubble Production

All models are wrong, but some are useful - George E.P. Box

Chapter 5 has shown that the two-phase boiling phenomenon provides highly effective thermal dissipation. In this chapter, a Finite Element Analysis (FEA) model has been developed. It simulates bubble production and two-phase heat transfer behaviours in both HFE and FK samples.

6.1 Introduction

The FEA model includes consideration of coupled thermal flux and multiple phase flow. The temperature patterns surrounding bubbles were plotted. This approach assists the analyzing of heat transfer of boiling behaviours. Simulated bubble production rates at different heat fluxes were also compared with experimental observations.

6.2 Modelling Process

The FEA model relies on defining partial differential equations (PDE) to represent the physical process. It can provide a reliable numerical prediction and becomes more popular over the last two decades due to the advances in computing. To develop an FEA model, there are four steps. The first step is to define the model geometry and material parameters. The second step is to specify the physical process by choosing the correct governing equations and defining proper boundary and domain conditions. The third step is to design an appropriate mesh to represent the model geometry and solve the governing equation. The last step is to analyze modelling results. This chapter introduces a two-phase/thermal complicated model by following these steps.

6.2.1 Define Model Geometry and Material Parameters

This model represents a glass beaker, which has a rod shape heating element located at the bottom centre. In order to compare with the experimental observations conveniently, the modelling geometry is identical with the experimental apparatus dimensions. Since the rotational symmetry of the apparatus, the spatial dimension of the model is defined as 2D axial symmetry, which is shown in Figure 6.1;

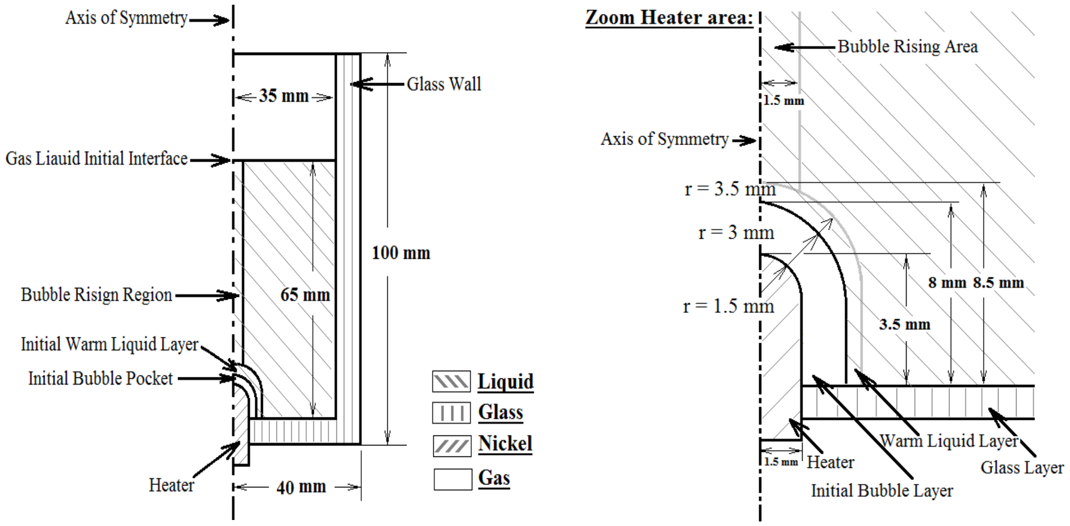

Figure 6.1 Modelling geometry

The inner and outer radii of the beaker are 37.5 and 40 mm respectively. The height of the beaker is 100 mm. In the beaker, the sample level is 65 mm.

To better explain the geometry that surrounding the heater, a close-up version of this area is plotted as shown in the right-hand side picture of Figure 6.1. In the model, in order to initiate the bubble production, three assumptions have to be made. First, a solid rod was assumed as the heating element to meet the definition of axial symmetry. This rod has a 1.5 mm radius and 3.5 mm height, the top of the rod is curved by 1.5 mm radius. Second, an initial bubble layer, which wraps the heater was defined. The thickness of this bubble layer is 1.5 mm and this layer defines the location where the initial phase change takes place. Third, a 3.5 mm thick warm liquid layer and 1.5 mm wide bubble rising channel was defined. This assumption defines more modelling domains, which are able to represent different physical settings. The boundaries of these areas are not real physical boundaries and therefore they are plotted in grey. After drawing the physical boundaries, the next step is to define the material properties of both HFE and FK. These parameters are summarised in Table 6-1. With the following exception, all the data is from the material data sheet [100]. Since no publication reports the specific heat capacity and thermal conductivity values of gas phase HFE and FK, these values were assumed as air properties at standard temperature and pressure (STP). In general, the gas phase material does not behave with high thermal conductivity. Hence, any error caused by the above assumptions can be neglected.

Table 6-1 Sample properties [100]

Properties	*Symbol*	*HFE*	*FK*
Molecular weight (kg mol^{-1})	M	0.25	0.316
Latent heat of vaporisation (J mol^{-1})	λ	28000	27808
The specific heat capacity of liquid (J kg^{-1}K^{-1})	Cp_l	1183	1103
The specific heat capacity of gas (J kg^{-1}K^{-1})	Cp_g	1000	1000
Coolant saturation temperature (K)	T_{sat}	334.15	322.15
The thermal conductivity of liquid (W m^{-1}K^{-1})	k_l	0.069	0.059
The density of Liquid (kg m^{-3})	ρ_l	1510	1600
The viscosity of the liquid (Pa s)	η_l	0.58×10^{-3}	0.64×10^{-3}
Surface tension (mN m^{-1})	σ_l	13.6	10.8
The thermal conductivity of vapour (W m^{-1}K^{-1})	k_g	0.17	

The thermal properties of solid materials are summarised in Table 6-2.

Table 6-2 Solid materials properties [141], [142]

Properties	*Symbol*	*Nickel (Heating element)*	*Glass*
Thermal conductivity (W m^{-1}K^{-1})	k_{Ni} / k_{Gl}	90	1.05
Density (kg m^{-3})	ρ_{Ni} / ρ_{Gl}	7810	2700
Specific heat capacity (J kg^{-1}K^{-1})	Cp_{Ni} / Cp_{Gl}	440	840

6.2.2 Governing Equation and Boundary Conditions of Physics

This section discusses the governing equations and boundary conditions of both thermal and multiple phase flow physics.

6.2.1.1 Thermal Transfer Physics

The complete model geometry is divided into seven subdomains as shown in Figure 6.2. Based on the materials, these subdomains can be subdivided into two groups. Subdomains 1- 2 are Nickel heating element and glass. They are uncompressed solids group. Subdomains 3-7 are a two-phase sample.

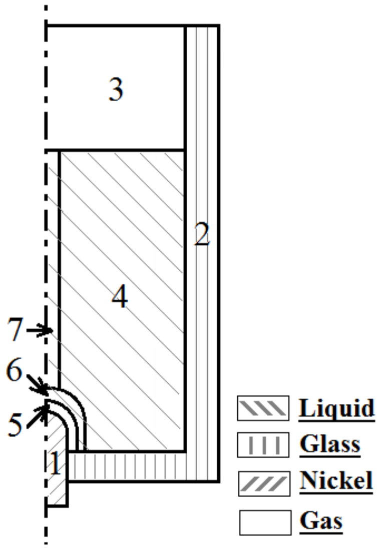

Figure 6.2 Subdomain pattern of thermal physics

Governing Equation of Solid Subdomains

Within solid materials, temperature variation is only caused by thermal conduction. The governing equation of these subdomains are defined as;

$$\rho C_p \frac{\partial T}{\partial t} = -\nabla \cdot (-k\nabla T) \tag{6.1}$$

The corresponding material properties have been summarized in Table 6-2. The initial temperature of the heating element is set equal to the liquid saturated temperature. The initial temperature of glass domain is set equal to 296.15 K.

Governing Equation of Fluid Subdomains

Within two-phase material, the thermal convection and heat sink is added into the thermal dissipation. The governing equation of these subdomains is:

$$\rho C_p \frac{\partial T}{\partial t} = \underset{\substack{\uparrow \\ \text{Thermal Conduction}}}{\boxed{-\nabla \cdot (-k\nabla T)}} \; \underset{\substack{\uparrow \\ \text{Thermal Convection}}}{\boxed{-\rho C_p v \cdot \nabla T}} \; \underset{\text{Heat Sink}}{\boxed{+Q}} \nwarrow \tag{6.2}$$

The thermal conduction process is as same as introduced by the Equation 6.1. The magnitude of the thermal convection is attributed to the fluid dynamic velocity v. The present of the heat sink 'Q' is attributed to the energy exchange during the phase change process.

To initiate the phase change process, the initial temperatures of subdomains are different. The initial temperature of bulk fluid domains (domain 3 and 4) is equal to 296.15 K. Subdomain 5 is the initial gas pocket, the initial temperature of this domain is set equal to samples' saturated temperature, which is 322.15 K and 334.15 K for FK and HFE respectively. Subdomain 6 and 7 are the warm liquid layer and the bubble rising channel; the initial temperature of these domains are 5 K higher than the ambient temperature i.e. 301.15 K. This setting allows the bubble to form and rises away from the heater instead of collapsing immediately.

Boundary Condition of Thermal Physics

After introducing subdomain conditions, Figure 6.3 shows the boundary conditions of thermal physics. Since both solid and two-phase materials are involved in the thermal transfer, all the boundaries should have a definition in the thermal physics.

In Figure 6.3, the green line is the axis of symmetry. The black lines show the internal boundaries, which are considered to have a continuous thermal gradient across them. The equation of these boundaries is:

$$-\vec{n}_{up} \cdot (-k_{up}\nabla T_{up}) = \vec{n}_{down} \cdot (-k_{down}\nabla T_{down}) \tag{6.3}$$

The heat transfer across the boundaries are calculated by the Fourier's law, where $\vec{n}$ is the unit normal vector to the interface pointed to the gas phase, subscript ‘up’ and ‘down’ denoting above and below the boundary surface respectively. This equation ensures that thermal energy is conserved.

The red line with the tag ‘heat source’ is the outer boundary of the heating element. This boundary is defined as;

$$-\vec{n}_{up}\cdot\left(-k_{up}\nabla T_{up}\right) = \vec{n}_{down}\cdot\left(-k_{down}\nabla T_{down}\right)+q_0 \tag{6.4}$$

In can be seen there is an inward heat flux ‘q_0’ was added on the heating boundary. The magnitude of this inward heat flux is calculated by:

$$q_0 = \frac{Q_{heater}}{A_{boilng}} \tag{6.5}$$

The boiling surface area in this model is estimated from the experimental apparatus. Therefore, with the same power input, the heat flux magnitude should identical with experiment. The value of the heat flux q_0 was summarised in the Table 6-3.

Table 6-3 Modelling heat flux magnitude

Heater power P (W)	Inward heat flux q_0 (kW m^{-2})
2 W	71
3 W	106
4 W	141

The bottom section of the heating element is for the electrical connection exposed to ambient. The grey colour line that is shown in Figure 6.3 shows this boundary. A thermal radiation term is added in the thermal equation of this boundary, which is defined as:

$$-\vec{n}\cdot\left(-k\nabla T\right) = \underset{\underset{\text{Inward Heat Flux}}{\uparrow}}{\boxed{q_0}} + \underset{\underset{\text{Thermal Convection}}{\uparrow}}{\boxed{h\left(T_{amb}-T\right)}} + \underset{\underset{\text{Thermal Radiation}}{\uparrow}}{\boxed{\varepsilon_{Surface}\sigma_{kB}\left(T_{amb}{}^{4}-T^{4}\right)}} \tag{6.6}$$

where $\varepsilon_{surface}$ the surface emissivity of nickel rod, in this model, it is 0.51. It can be seen that when the temperature of this boundary is higher than the ambient temperature, heat energy is dissipated to ambient by thermal radiation.

The external surface of the glass beaker also dissipates heat energy by thermal convection and radiation.

The blue lines (Heat flux 2) represent these boundaries. Equation 6.6 is also suitable for these boundaries. Nevertheless, there is no inward heat flux on these boundaries. Hence, q_0 is 0 and the $\varepsilon_{surface}$ value of glass is 0.95, which is according to the smooth glass surface [143].

The thermal condition of the purple boundary was defined as convective flux; this is because it is an outlet rather than a real a physical boundary.

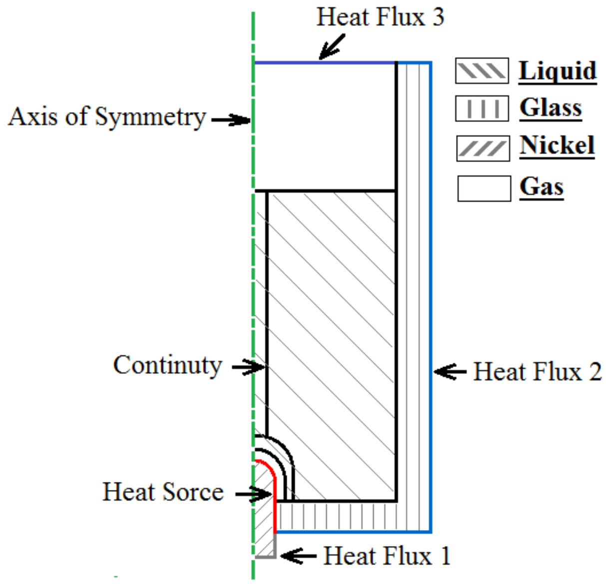

Figure 6.3 Mathematical boundary conditions of thermal physics

6.2.1.2 Multiple Phase Flow Physic

This section shows the governing equations and boundary conditions of multiple phase flow physics.

Governing Equation of Multiple Phase Flow

The five subdomains are involved in the phase flow physics. They are shown in Figure 6.4. Subdomain 1-2 are the gas phase domains and subdomain 3-5 are the liquid phase domains.

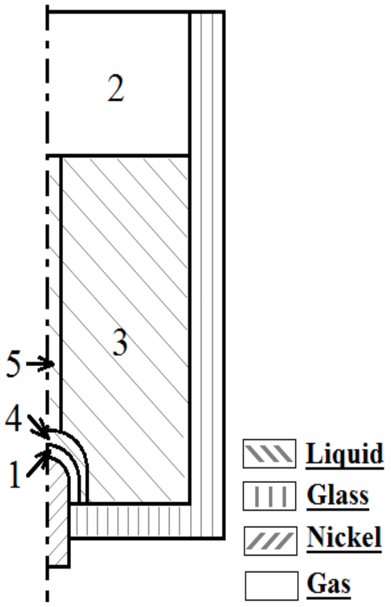

Figure 6.4 Subdomain pattern of multiple phases flow physics

The velocity field and pressure for all domains are described by considering incompressible Navier-Stokes formulation and the momentum equation, which is:

$$\underset{\substack{\uparrow\\ \text{Volumetric Momentum}}}{\boxed{\rho\frac{\partial v}{\partial t}}} + \underset{\substack{\uparrow\\ \text{Velocity Gradient}}}{\boxed{\rho\,(\vec{v}\cdot\nabla)\vec{v}}} = \nabla\cdot\left[\overset{\substack{\text{Pressure}\\ \downarrow}}{\boxed{-p\mathrm{I}}} + \underset{\substack{\uparrow\\ \text{Stokes's Stress}}}{\boxed{\eta(\nabla\vec{v}+(\nabla\vec{v})^{T})}}\right] + \overset{\substack{\text{Surface Tension Force}\\ \searrow}}{\boxed{\vec{\mathrm{F}}}} + \overset{\substack{\text{Density Gradient Force}\\ \downarrow}}{\boxed{\rho\vec{g}}} + \underset{\substack{\nwarrow\\ \text{Chemical Potential}}}{\boxed{\mathrm{G}\nabla\phi}} \tag{6.7}$$

where F is the extra force and G is the chemical potential, which is the partial molar Gibbs free energy. The matrix operating I is the identity matrix, *T* is the matrix transposition. From Equation 6.7, it can be seen that transient volumetric momentum is governed by the gradient of pressure, Stokes's stress, surface tension and density gradient. Stokes's stress reduces the fluid movement due to the fluid viscosity. The term F is the extra force act upon the bubble, in this study, it is determined by the surface tension on the gas-liquid interface. The material properties are according to the phase form. The involved parameters of both gas and liquid phase are summarised in Table 6-4.

Table 6-4 Material properties

Parameter	Subdomain 1-2 (Gas phase)	Subdomain 3-5 (Liquid Phase)	
		HFE	FK
Density (kg m^{-3})	ρ_g	1510	1600
Viscosity (Pa s)	4×10^{-5}	0.58×10^{-3}	0.64×10^{-3}
Surface tension (mN m^{-1})		13.6	10.8
Gravity acceleration (m s^{-2})	-9.81		

The gas density is calculated by the ideal gas law, which is:

$$\rho_g = (p+p_0)\times\frac{M}{R_{gas}}\times\frac{1}{T} \tag{6.8}$$

where p_0 is the atmospheric pressure, and R_{gas} is the molecular gas constant.

<u>Boundary Condition of Multiple Phase Flow Physics</u>

Compared with thermal transfer, the phase change phenomenon does not occur in every geometry subdomain. The required boundary conditions are outlined in Figure 6.5. As in the thermal model, the green boundary is the axis of symmetry. The orange coloured boundary is the initial gas-liquid interface. The equation of these boundaries was defined as:

$$\vec{n}\left[\underset{\substack{\uparrow\\ \text{Pressure}}}{\boxed{-p}} + \underset{\substack{\uparrow\\ \text{Stokes's Stress}}}{\boxed{\eta(\nabla\vec{v}+(\nabla\vec{v})^{T})}}\right] = 0 \tag{6.9}$$

This equation shows that the hydrostatic and viscosity condition on these boundaries are zero.

The top blue boundary is an outlet, there is no pressure and viscous stress applied on this boundary. Hence, the pressure term in Equation 6.9 is 0 and the equation transfers into:

$$\eta_l(\nabla\vec{v} + (\nabla\vec{v})^T)\,\vec{v} = 0 \tag{6.10}$$

The inner boundary of the heating element and glass beaker was defined as a no-slip wall. Such a condition enforces the fluid velocity on these boundaries to be 0. Hence, the bubble momentum on this boundary is determined by the fluid interface surface tension. Therefore only pressure, gravity force were applied for the fluid on these boundaries.

The purple coloured boundaries are internal continuity boundaries, where the pressure and Stokes's stress on the liquid and gas are balanced. Hence, the equation is defined as:

$$\vec{n}[-p_g\mathrm{I}+\eta_g(\nabla\vec{v} + (\nabla\vec{v})^T)] = \vec{n}[-p_l\mathrm{I}+\eta_l(\nabla\vec{v} + (\nabla\vec{v})^T)] \tag{6.11}$$

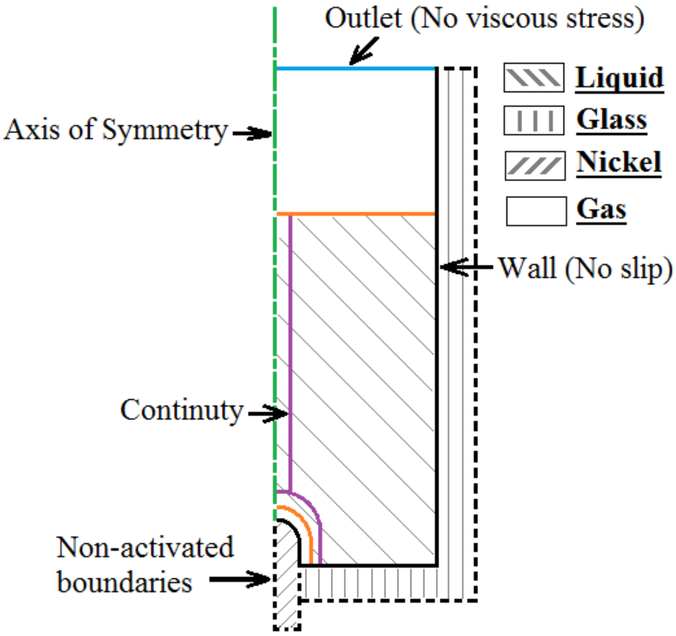

Figure 6.5 Mathematical boundary conditions of multiple phases flow physics

6.2.1.3 Coupling Thermal and Multiple Flow Physics

Last two sections have introduced boundary conditions and subdomain conditions of both thermal physics and multiple phase flow physics individually. This section aims to link them together thus representing dynamic phase change. The transient temperature is the 'bridge', which couples these two systems together and defines the phase condition of the material.

In reality, the liquid starts boiling when the liquid reaches its saturation point. Within this numerical model, the rate of the phase change occurs at any given calculating point is defined by a step function and with respect to temperature. These parameters are further related to a rate of vaporisation. To ensure that, Heaviside step function (*H*) is applied to the model. Such a function defines a condition derivate function by:

$$H = \begin{cases} 1\ (T > T_{sat}) \\ 0.5\ (T = T_{sat}) \\ 0\ (T < T_{sat}) \end{cases} \tag{6.12}$$

With the aid of the Heaviside step function, the rate of vaporization is defined by:

$$\dot{m} = -\frac{M}{\lambda}\ \vec{n}\ k_g\ \nabla T \approx C_k \rho_l \frac{(T - T_{sat}) \times (2H - 1)}{T_{sat}} \tag{6.13}$$

where $\dot{m}$ is the rate of vaporisation, C_k is a tuning parameter to control interface temperature. Practically, the value of C_k should large enough that the temperature at the interface remains at the liquid saturate temperature, but not so large that numerical instabilities results. In this study the, value of C_k is set equal to 0.03 m s^{-1}.

To ensure a phase change occurs, the model essentially involves rewriting the boundary conditions according to the volumetric sources. The equations governing the interface dynamics of a two-phase flow are described by the Cahn-Hilliard equation. In this study, the equation for the phase field variable is modified to allow for the phase change and is defined as [144]:

$$\frac{\partial \emptyset}{\partial t} + \vec{v}\ \cdot \nabla \emptyset - \dot{m}\delta_s(\frac{V_{fl}}{\rho_l} + \frac{V_{fg}}{\rho_g}) = \nabla \frac{\gamma \lambda_c}{\varepsilon_{int}}\ \nabla \Psi \tag{6.14}$$

where $\emptyset$ is the dimensionless phase field variable (-1<$\emptyset < 1$), V_{fl} and V_{fg} are the volume function of liquid and gas respectively, λ_c is the mixing energy density, ε_{int} is the interface thickness, γ is the mobility tuning parameter, Ψ is equation governing parameter and δ_s is the smoothed representation.

In the Equation 6.14, the term mixing energy density (λ_c) can be calculated by the surface tension (σ_l) and phase interface thickness (ε_{int}).

$$\lambda_c = \frac{3\sqrt{2}\ \varepsilon_{int}\ \sigma_l}{4} \tag{6.15}$$

The mobility tuning parameter γ determines the time scale of the Cahn-Hilliard diffusion and should be large enough to retain a constant interfacial thickness but small enough to avoid convective terms being overly damped. The equation governing parameter Ψ, which is determined by the two phase volume fraction and bubble interface thickness, i.e.:

$$\Psi = -\nabla \cdot {\varepsilon_{int}}^2 \nabla + (\phi^2 - 1)\phi \tag{6.16}$$

The smoothed factor δ_s represents the thickness of the diffuse interface of multiple phases and it is defined as;

$$\delta_s = 6\, V_{fl}\,(1 - V_{fl})\,\frac{|\nabla \emptyset|}{2} \tag{6.17}$$

After coupling thermal and two-phase flow physics, the governing equations of both are varied according to phase definition. The thermal parameters of bulk material are calculated depending on the phase volume function, which is introduced as follows.

Coupling Thermal Physics

The two-phase flow was then coupled into the thermal model via the latent heat of evaporation, which is implemented on fluids. The heat sink term 'Q' in the Equation 6.2 transfers into:

$$Q = -\frac{\dot{m}\,\lambda}{M} \tag{6.18}$$

Considering Equation 6.13 and 6.18, it can be seen that when the liquid instant temperature is higher than the saturated temperature, i.e. $T > T_{sat}$, the liquid phase turns into the gas phase. Meanwhile, the heat sink 'Q' term presents in the heat transfer equation and this negative heat sink term indicates that thermal energy is absorbed during the phase change process, vice versa. In addition, the thermal conductivity k and specific heat C_p within two-phase material was calculated according to their volume fraction by using;

$$k = (k_l - k_g)V_{fl} + k_g \tag{6.19}$$

$$C_p = (\mathrm{Cp}_l - \mathrm{Cp}_g)\, V_{fl} + \mathrm{Cp}_g \tag{6.20}$$

Coupling Two-Phase Flow Physics

Equation 6.14 shows that both mixing energy density and equation governing parameter are determined by the interface parameter, i.e. bubble wall thickness. In this model, the wall thickness of a thermal bubble was set equal to 3×10^{-5} m, this value was estimated from the images obtained from experiments. Meanwhile, in the two-phase system the velocity gradient in the Equation 6.7 becomes a function of mass flux, which is determined by the rate of evaporation and defined as:

$$\nabla \cdot \vec{v} = \dot{m}\,\delta_s\left(\frac{1}{\rho_g} - \frac{1}{\rho_l}\right) \tag{6.21}$$

6.2.3 Modelling Mesh Setting

An appropriate mesh setting results in a correct numerical prediction. This section introduces the mesh settings. The free triangular structure was selected to create unstructured meshes in all domains as shown in Figure 6.6. The surface tension force helps bubble to pinch off from the bubble pocket. To allow this physical phenomenon occurring in the model, the mesh size of bubble seed and rising areas must be smaller than the bubble wall thickness. The smallest size of mesh results in the highest mesh density in domain 1-3.

Since the bubble raises and forms only in the domain 1-3, a lower mesh density was applied to the other areas in order to reduce the computing time.

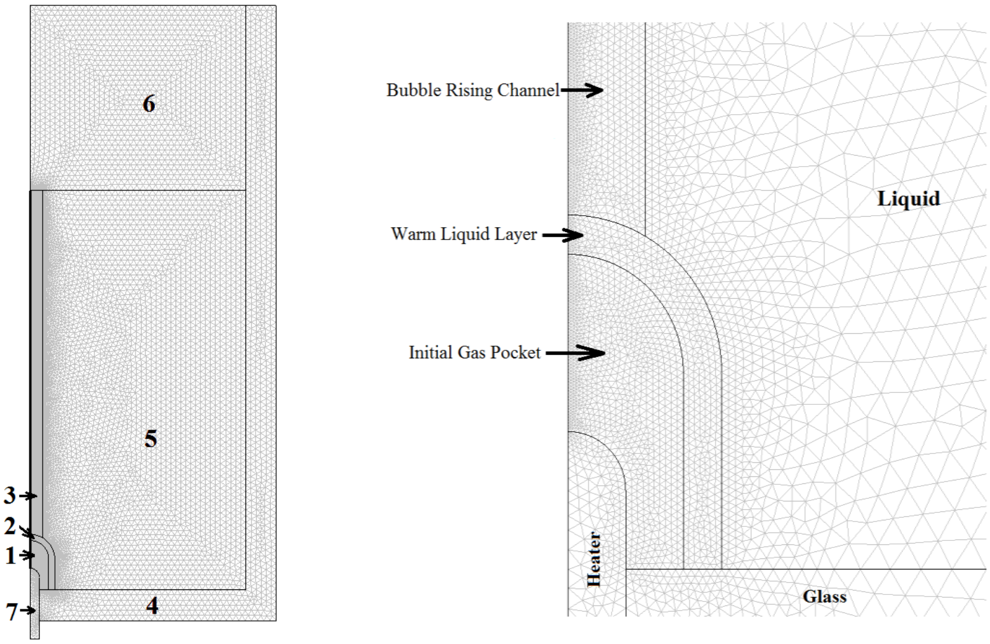

Figure 6.6 Mesh element of geometry

6.3 Modelling Results

In order to introduce the results clearly, this section is divided into two parts. The first part shows the result of bubble production in two-phase flow and the second part discusses the temperature distribution in two-phase flow.

6.3.1 Bubble Production in the Two-Phase Flow

The bubble production behaviours in the two-phase flow of HFE and FK samples are plotted in Figure 6.7 and Figure 6.8. The heat flux input of this example is 106 kW m^{-2} (corresponding to 3 W heating element input power).

In Figure 6.7 and Figure 6.8, fluid and bubble are represented by the blue and white region respectively. The initial bubble pocket rises after 0.05 second. A bubble seed remains on the top of the heating element. With the heat flux applied to the heater, the bubble seed grows bigger than before (see 0.2s pattern). The bubble volume becomes bigger and the buoyancy force elongates the bubble (see 0.4s pattern). Meanwhile, the surface tension force, which is acting on the elongated bubble bottom cross-section, pinches off the bubble from the parental bubble pocket. Then the bubble moves up due to the buoyancy force (see 0.6s pattern). The surface tension force works on the bubble and makes it in a spherical shape again. Under continuous heat flux, the above phenomena will repeat.

The FK sample behaves similar behaviour, but the bubble production rate is higher than HFE sample. The reason for that is the FK sample has lower saturation temperature and a smaller value of the latent heat of evaporation. Therefore, more bubbles were formed at the same heat flux.

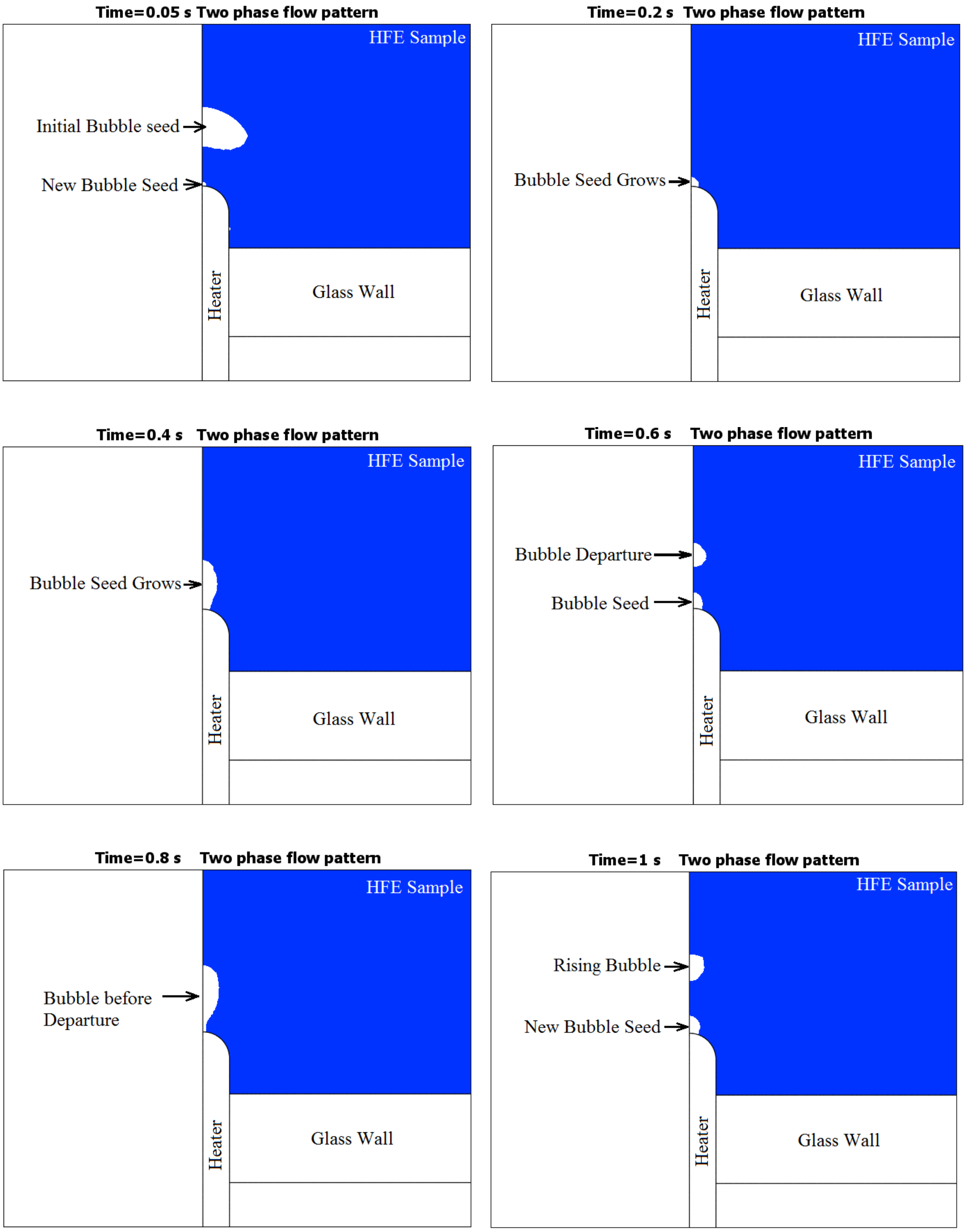

Figure 6.7 Two-phase flow pattern of HFE sample

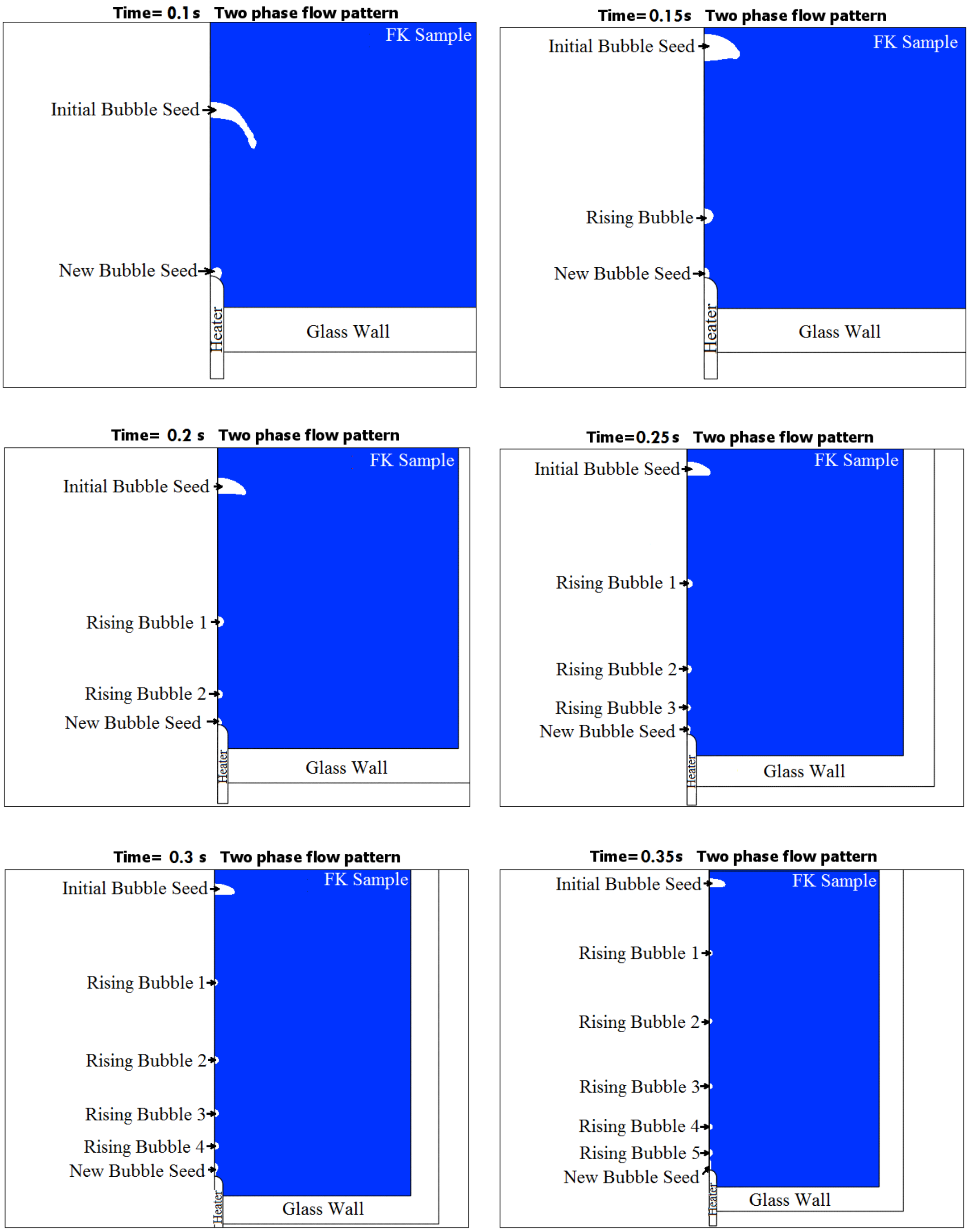

Figure 6.8 Two-phase flow pattern of FK sample

6.3.2 Temperature Dissipation in Two-Phase Flow

The temperature profiles of both HFE and FK are plotted in Figure 6.9 and Figure 6.11. The simulation results show that a two-phase system dissipates the thermal energy effectively. This is attributed to the thermal convection and latent heat absorption during the phase change process. The white arrows point out the thermal convective cycle. These arrows show that bubbles drag heat energy away from the heating element, in meantime, they push the cool fluid flowing back to the warm area and therefore forms a convective cycle. When the fluid temperature reaches the saturated temperature, a new bubble will be produced, which absorbs thermal energy during the phase change phenomenon. In order to quantify the effective thermal conductivity the temperature gradients of the bubble heater interface are plotted in Figure 6.10 and Figure 6.12.

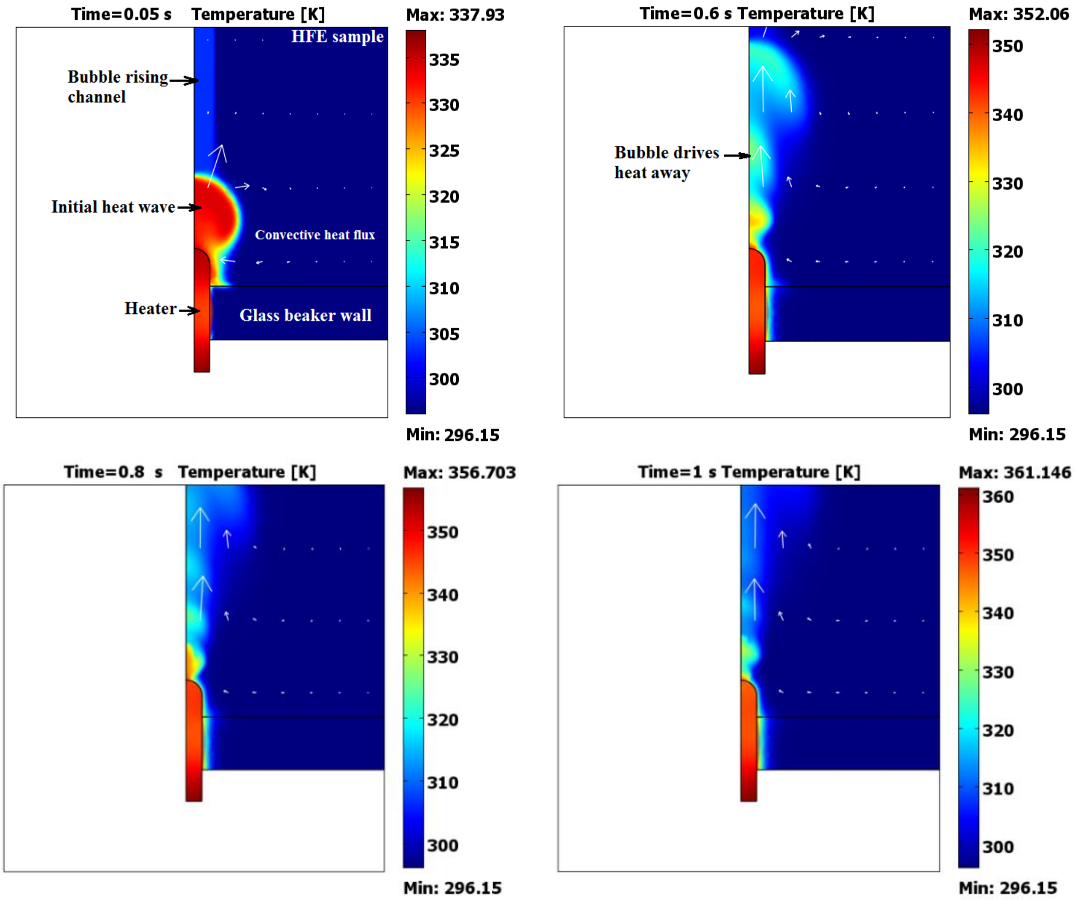

Figure 6.9 Temperature distribution in HFE sample

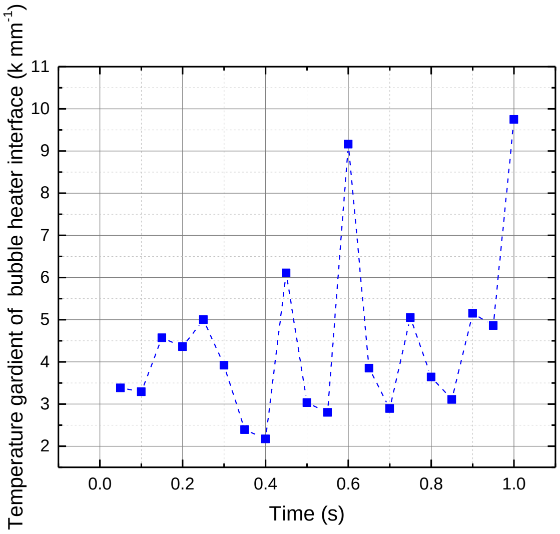

Figure 6.10 HFE sample temperature gradient of bubble heater interface

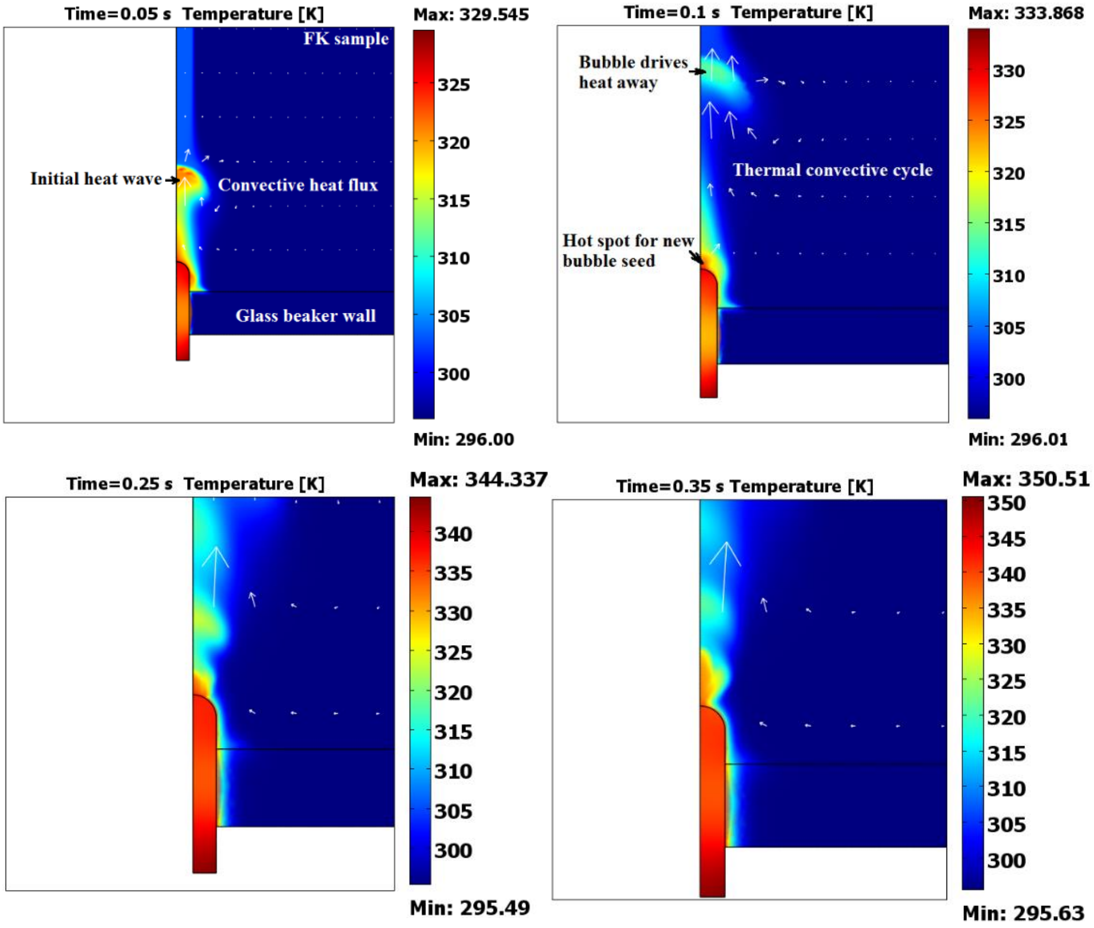

Figure 6.11 Temperature distribution in FK sample

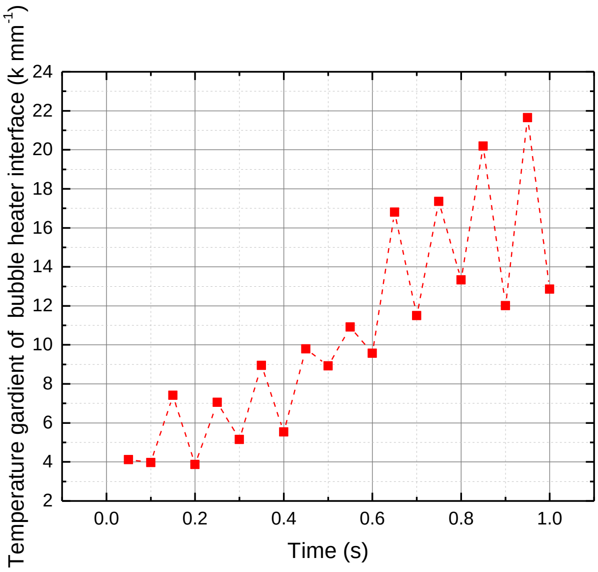

Figure 6.12 FK sample temperature gradient of bubble heater interface

The temperature gradient results help to draw three conclusions. Firstly, it can be seen that when the bubble departs from the heater surface, the temperature gradient becomes larger. The reason for this results is that the heating element is still hot, while the relatively cold fresh fluid, which is driven by the convective cycle, replaced the bubble site. The second finding is the effective thermal conductivity of boiling two-phase material is much higher than single liquid phase material. The effective thermal conductivity of two-phase HFE and FK materials within 1 second is 23.96 W $m^{-1}K^{-1}$ and 10.05 W $m^{-1}K^{-1}$ respectively. These values are deduced by the average temperature gradients. These values are more than 100 times higher than single-phase thermal conductivities. This is because in the two-phase material, instead of thermal conduction, thermal convection dominates the heat transfer. Thirdly, the HFE sample has lower average temperature gradient than FK sample, which results in a higher effective thermal conductivity. As a consequence, with same heat flux, HFE sample can dissipate higher thermal energy than FK sample. This model also proves the experimental conclusion that given by the last chapter, i.e. HFE is a better two-phase thermal transfer material than FK.

6.4 Experimental Validation

In order to validate the modelling results, the simulated bubble production rate has been compared with the experimental observations.

6.4.1 Apparatus

Figure 6.13 shows the apparatus diagram, a test beaker was manufactured, which is identical to the model geometry. A bubble generator, which detailed in section 4.3.3, was attached at the bottom of a beaker. A DC power supply was connected to the bubble generator in order to generate bubbles. The power input of the power supply was 2 W, 3 W and 4 W, they provided the same magnitude of heat flux within the model. The bubble production rate was calculated by the average bubble amount in 2 seconds with 5 individual measurements.

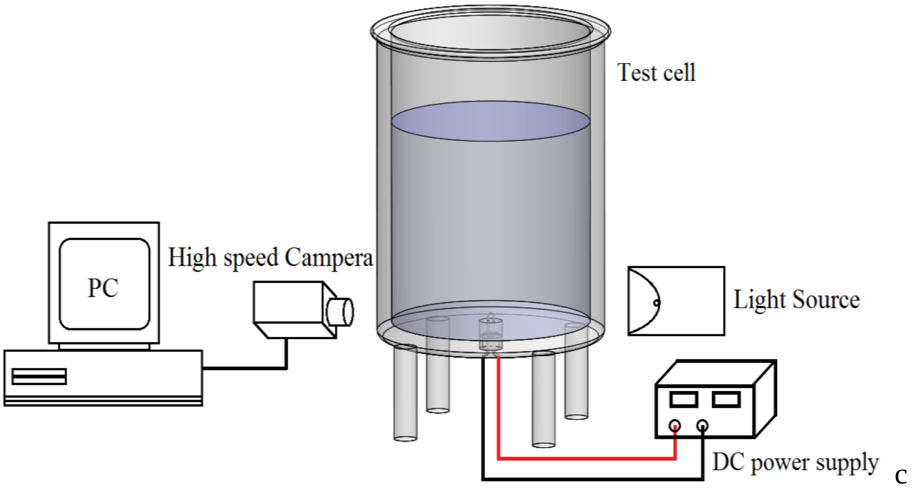

Figure 6.13 Bubble production rate experimental diagram

The comparison results of both HFE and FK sample are plotted in Figure 6.14. The error bars were calculated by the standard deviation of 5 experiments.

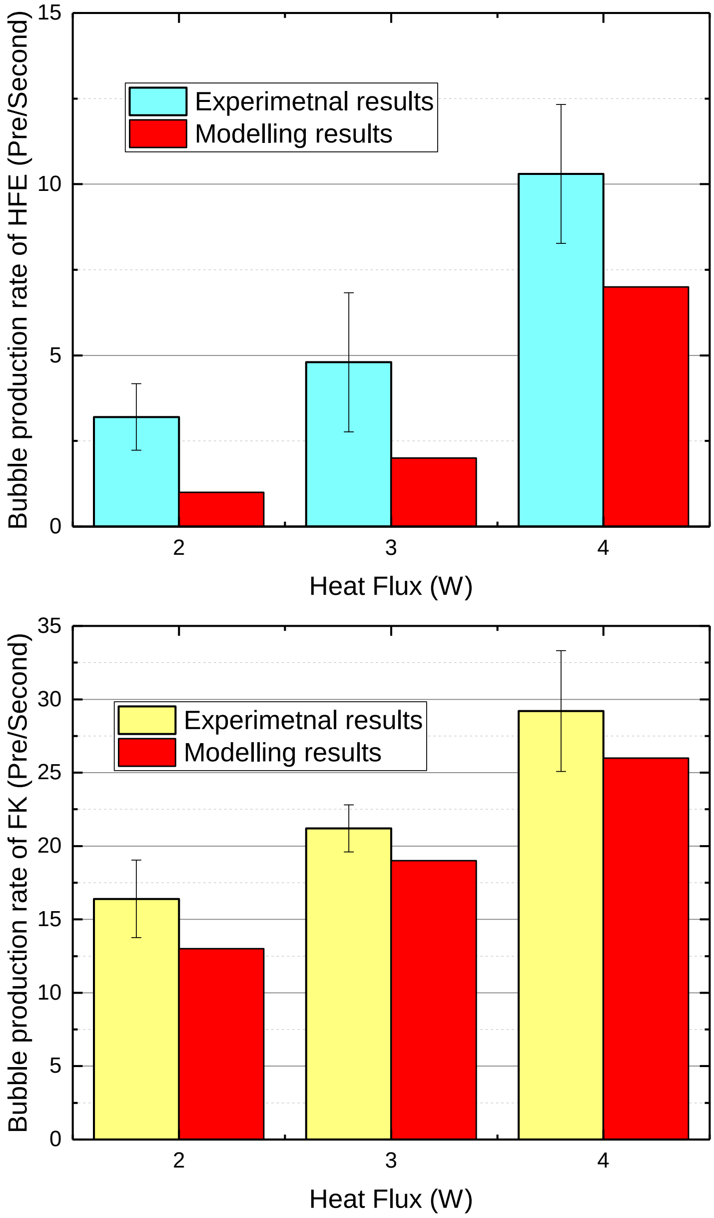

Figure 6.14 Comparison between experimental results and modelling results

Figure 6.14 shows that the model predictions are lower than the experimental observation. There are three possible reasons to explain the error.

The first reason is that there are more bubble nucleation sites in the real experiment. Specifically, the microcavities exist on the heating element, they are the potential hot spots and multiple bubbles may form on these locations. Therefore, in the experiment, multiple bubbles may appear on the bubble generator at the same time. In comparison, in the model new bubble was only formed at the top surface of the heater, which results in lower bubble amount and corresponding to a lower bubble production rate.

Second, there is an ill-defined initial condition in the model to initiate boiling. In the experiment, there is not a big volume initial gas pocket that surrounding the heating element. However, in the model, a gas pocket was defined to distinguish the two-phases domain. Due to the single gas phase behaviours very poor thermal conductivity, this setting may change the initial temperature distribution that around the heating element. Specifically, the large volume initial gas pocket may draw out higher thermal energy than reality.

Third, the material properties of both fluids could be temperature dependent, due to the lack of information from the material data sheet, the material properties were chosen as a constant value at ambient temperature. These different parameters may also affect the bubble production rate.

6.5 Summary

In this chapter, a numerical model was developed to simulate bubble production and heat dissipation. The model considered the thermal transfer and coupled with two-phase flow. It ensures the phase change process, meanwhile absorbs thermal energy from the heat source. There are two main outcomes of this study. First, the numerical prediction demonstrates that with the continual phase change process, thermal dissipation is increased significantly. This is because the thermal convection and phase change process can dissipate thermal energy more efficient than single-phase thermal conduction. Secondly, the bubble production rates predicted by the simulation for both HFE and FK samples have been compared to the experimental study. A comparison of any bubble production rate has shown a reasonable agreement. It indicates that the modelling procedure could be potentially applied to the other two-phase materials.

Chapter 7

Conclusions and Future Work

If you cannot explain simply, you do not understand it well enough - Albert Einstein

This thesis has presented a series of investigations on dielectric properties, effects of electrohydrodynamic on thermal bubble behaviours and heat transfer of Hydrofluoroethers (HFE) and Fluorinated Ketone (FK). The research outcomes are applicable to assist HV thermosyphon optimization design.

Although thermosyphon technology has been maturely applied to the electronics [145] and converters [146], HV thermosyphons are still in the development stage. For these applications, the presence of high electric fields is unknown and may significantly affect insulation and thermal dissipation. Using both experiments and theoretical analysis, this thesis has investigated this area. This chapter summarises the contribution made by this research, draws out the main outcomes, and discusses practicable future work.

7.1 Conclusion and Research Contribution

This thesis makes four significant contributions to assist coolant selection and optimization design for future HV thermosyphon applications.

First, the experimental data that shown in Chapter 3 forms a significant contribution to the literature in the dielectric material engineering. Although many publications have reported the dielectric properties of coolants, such as Chlorofluorocarbons (CFCs) and Hydrochlorofluorocarbons (HCFCs), these data are not applicable to the future thermosyphons. The reason is that both CFCs and HCFCs have been or will be phased out by 2030. Instead, HFE and FK are two relatively new coolants, this research as led to the publication of comprehensive material dielectric characteristics, including AC dielectric spectroscopy, DC conductivity and AC breakdown results. Furthermore, the electrical ageing effect, caused by the repeated AC breakdown, has also been investigated for these two materials. In order to guarantee correct data, all experiments were conducted multiple times under well-controlled conditionals and followed British standards. The experimental results show the distinct different dielectric behaviours of HFE and FK. AC and DC responses indicate that FK is an insulating coolant but HFE is far more electrically conductive. The AC breakdown measurements show that FK and HFE have comparable dielectric strength at ambient temperature and reducing temperature is a good strategy to increase FK AC dielectric strength. Electrical ageing did not affect AC dielectric strength of both HFE and FK sample, but the DC conductivity value of HFE sample increased significantly after ageing, due to the presence of conducting particles. From an industrial aspect, these results provide information on dielectric behaviours at different temperatures, which help manufacturers to define the maximum dielectric loss at operating frequencies and limit the electric field to avoid insulation failure. This obtained data also provided parameter values to assist numerical modelling of observed behaviours.

Second, this thesis gave an applicable numerical approach, which conditions in Chapter 4, to predict thermal bubble trajectories under different electric field. The previous study has reported that EHD phenomenon could be the one reason that causes electrical insulation failure, due to gas columns formation. Hence, understanding the bubble trajectories at different electric field circumstances is important. Before this study, there is no report on EHD force effects on FK material thermal bubble behaviour. The first numerical model, which was based on the FK material properties, has been developed by force analysis and establishing kinemics equations. A set of differential equations has been proposed and calculated to predicate the bubble trajectories under both uniform and non-uniform electric fields. Two experimental platforms were built to validate the theoretical results by using parallel plates and rod-plane arrangements. The results found that the bubble trajectory is significantly dependent on the bubble charge behaviour and field distribution. Specifically, the uniform field experimental results indicate that FK bubble is easily attracting electrons and behaves with negative polarity, thus ensuring an electrophoretic force acting on the bubble. Furthermore, non-uniform electric field results indicate that dielectrophoretic force also contributes to the bubble motions. The experimental results showed a good agreement between the theoretical prediction and practical observation. For the industrial aspect, these obtained results are valuable for the manufacturers to locate gas pockets and for developing approaches to remove undesired gas from HV thermosyphons.

Third, the boiling curves of both HFE and FK material presented in Chapter 5 are a contribution to the literature in terms of two-phase heat transfer technology. After a critical analysis of the previous experimental design, a novel electrode system was designed and manufactured. Both FEA simulation and initial validation results demonstrated that the novel electrode system not only meets the design requirements but also avoids limitations of previous designs. Consequently, this study delivered a much better and convenient engineering method to plot two-phase materials' boiling curves for future research. The experiment allowed measurement of both HFE and FK boiling curves, based on a flat boiling surface configuration. The flat boiling surface structure is more relevant to industrial applications, such as chips or evaporators. The main results have given the important heat flux points, which are ONB and CHF, and their corresponding overheated temperatures. What is more, the results have shown that both HFE and FK have a distinct boiling hysteresis. By comparing the effective thermal transfer coefficients, HFE has better thermal dissipation performance than FK material, but poor electrical insulation properties. Furthermore, the boiling curves for FK material have been obtained with different magnitude of DC electric fields, and the results have been analysed and discussed. The experimental results have shown that the electric field can alleviate the temperature overshoot phenomenon, which means that the higher the electric field is, the lower heat input required to initiate nucleate boiling. Furthermore, the electric field can enhance nucleate boing heat transfer, which is presented by the left shifted boiling curves. The results have demonstrated that a 38% thermal dissipation enhancement was obtained under a 2 kV mm^{-1} electric field. In addition, a 5% CHF value increase was obtained with 2 kV mm^{-1} electric field. Different field polarities did not influence boiling heat transfer. The experimental results indicate that EHD could be used to promote thermal dissipation in a thermosyphon. The data provided in this study give the information on two-phase boiling phenomena, which can assist the thermosyphon optimization design.

Last, an FEA model has been developed that considers both thermal and two-phase flow physics. The model simulated the two-phase boiling phenomenon, which is initiated by rising temperature. Standard Navier-Stokes, thermal convection and thermal conduction equations are the governing partial differential equations, which were implemented within corresponding physical boundaries. The boundary conditions are more complicated than most other single- phase models. The modelling results indicate that even though the applied heat flux is high, the excess temperature remains low. This is because the detaching bubbles drive liquid convection, the two-phase effective thermal conductivity of the coolant is 100 times higher than the single- phase thermal conductivity. Hence, the simulation results prove that two-phase boiling is an efficient method to dissipate thermal energy. Furthermore, an experimental platform according to the modelling geometry was built, to validate simulation results. By comparing the bubble production rate, the simulation and experimental results are in a reasonable agreement. In terms of applications, this modelling approach has benefits as it links thermal heat flux to bubble production rates.

7.2 Future Work

Despite the contribution made by this study, a number of unknowns have been identified, which need further investigation. To explain them clearly, these works are divided into experimental investigations and numerical studies.

7.2.1 Future Experimental Work

The following experiments may need to consider in the future:

Measure HFE and FK dielectric properties under different pressure conditions

Since the coolants' saturated temperature may change by varying the pressure, in the practical thermosyphon the coolants may not always boil at atmospheric pressure. Many publications have reported that the pressure is the other parameter, which also changes material dielectric response. Hence, it is important to measure the dielectric properties of both HFE and FK at different pressures.

To conduct this measurement, a sealed test cell is required. Since the volume of the test cell is fixed, the sample pressure will follow the temperature-pressure curve. At saturation condition, the higher temperature results in a higher sample pressure. The AC and DC dielectric responses can be measured by either measuring sample capacitance or conducting current. The measuring procedures refer to the study, which is shown in Chapter 3.

Effect of the bulk temperature on HFE and FK boiling heat transfer

From an industrial aspect, a manufacturer focuses on the saturation boiling curve, which means that bulk liquid temperature remains at the saturation temperature. However, the literature has shown that different bulk liquid temperature effect boiling curves. This variation can also be investigated by the same apparatus in the future. By setting the temperature control system the bulk liquid can maintain at any subcooled temperature that above the ambient temperature. Therefore, the FK and HFE samples' boiling curves can be investigated, at different bulk temperatures without and with an electric field.

Effect of boiling surface roughness on HFE and FK boiling heat transfer

As introduced in Chapter 2, increasing boiling surface roughness may also increase the boiling heat transfer. In the future, if it is necessary to investigate this variation, new boiling surfaces can be manufactured with different roughness and their effect on electrical performance as well as thermal performance assessed.

7.2.2 Future Numerical Study

The numerical study shown in Chapter 6 is not perfect. The 2D axial symmetric spatial dimension only allows bubble generation in the centre of axial symmetry. In the future, a 3D spatial dimension model should be constructed, therefore the advanced model can simulate the two-phase boiling phenomena on a flat boiling surface, which is closer to real applications.

The model developed in Chapter 6 only links thermal and two-phase flow physics. In the future, the electric field i.e. EHD could also be added to the simulations. Although it is a considerably complicated model and may need to take a long time to solve, the model can provide much useful information. If the model has good agreement with experimental results, some experimental investigations may become redundant.

References

[1] M. Palazzo, “Generator Circuit-Breakers Application Guide,” Zurich, Switzerland, 2012.

[2] D. Dufournet and J. M. Willieme, “Recent developments in generator circuit breakers,” in *IEEE/PES Transmission and Distribution Conference and Exhibition,Yokohama*, 2002, vol. 1, pp. 88–92.

[3] C.H.Flurscheim, *Power circuit breaker theory and design*. Salisbury: Peter Peregrinus Ltd, 1975.

[4] C. M. Franck, “HVDC circuit breakers: A review identifying future research needs,” *IEEE Trans. Power Deliv.*, vol. 26, no. 2, pp. 998–1007, 2011.

[5] S. M. Cary, “High voltage circuit breaker standards — comparative guide,” Cleveland, 2013.

[6] C. Renaud, “High strength, high conductivity, low radiation activation nanocomposite,” *IEEE Trans. Appl. Supercond.*, vol. 10, no. 1, pp. 1273–1276, 2000.

[7] A. Wagner, “Review of Thermosyphon Applications,” 2014.

[8] J. G. James, Van Fossen and F. S. Stepka, “Review and Technology Status of Liquid-Cooling for Gas Turbines,” 1979.

[9] M. Hara and H. Saito, “Thermal bubble breakdown in liquid nitrogen under nonuniform fields,” *IEEE Trans. Dielectr. Electr. Insul.*, vol. 1, no. 4, pp. 709–715, 1994.

[10] M. Hara, “Bubble-triggered breakdown of cryogenic liquids in pool-cooled superconducting apparatus,” in *International Symposium on Electrical Insulating Materials (ISEIM),* 2008, pp. 1–9.

[11] M. Hara and M. Kubuki, “Effect of thermally induced bubbles on the electrical breakdown characteristics of liquid nitrogen,” *Phys. Sci.*, vol. 4, pp. 209–216, 1990.

[12] M. Hara, T. Kaneko, and K. Honda, “Thermal-bubble initiated breakdown characteristics of liquid helium and nitrogen at atmospheric pressure,” *IEEE Trans. Electr. Insul.*, vol. 23, no. 4, pp. 769–778, 1988.

[13] T. Nguyen, M. Mochizuki, K. Mashiko, Y. Saito, L. Sauciuc, and R. Boggs, “Advanced cooling system using miniature heat pipes in mobile PC,” *IEEE Trans. Components Packag. Technol.*, vol. 23, no. 1, pp. 86–90, 2000.

[14] M. C. Zaghdoudi and a. Teytu, “Use of heat pipes for avionics cooling,” *Proc.*

3rd Electron. Packag. Technol. Conf. (EPTC 2000) (Cat. No.00EX456), pp. 425–430, 2000.

[15] J. Wang and I. Catton, “Biporous Heat Pipes for High Power Electronic Device Cooling,” in *IEEE SEMI-THERM Symposium*, 2001, pp. 211–218.

[16] H. Xie, A. Ali, and R. Bhatia, “The use of heat pipes in personal computers.,” in *Thermal and Thermomechanical Phenomena in Electronic Systems*, 1998, pp. 442–448.

[17] Braun Dieter, “Heat Pipes-A Novel Cooling Principle for Generator Circuit-breakers.,” in *VGB powertech*, 2009, pp. 69–72.

[18] G.P.Peterson, *An introduction to heat pipes: modeling,testing,and applications*. New York: John Wiley & Sons, 1994.

[19] Amir Faghri, *Heat Pipe Science And Technology*. London: Taylor & Francis, 1995.

[20] L.S.Tong and Y. S. Tang, *Boiling heat transfer and two-phase flow*, 2nd ed. New York: CRC Press, 2010.

[21] F. J. V Santos, R. S. Pai-Panandiker, C. A. Nieto De Castro, and U. V. Mardolcar, “Dielectric properties of alternative refrigerants,” *IEEE Trans. Dielectr. Electr. Insul.*, vol. 13, no. 3, pp. 503–510, 2006.

[22] Y. Tanaka, S. Matsuo, T. Sotani, T. Kondo, and T. Matsuo, “Relative Permittivity and Resistivity of Liquid HFC Refrigerants Under High Pressure,” *Int. J. Thermophys.*, vol. 20, no. 1, pp. 107–117, 1999.

[23] F. J. V. Santos, R. S. Pai-Panandiker, C. A. Nieto De Castro, and U. V. Mardolcar, “Dielectric properties of alternative refrigerants,” *IEEE Trans. Dielectr. Electr. Insul.*, vol. 13, no. 3, pp. 503–510, 2006.

[24] F. Dschung and J. Kindersberger, “Dielectric Dissipation Factor and Resistivity of Liquid Refrigerants and Dependency on Temperature,” *IEEE Trans. Dielectr. Electr. Insul.*, vol. 23, no. 2, pp. 859–865, 2016.

[25] V. Champa, A. N. Nagashree, B. V. Sumangala, and G. R. Nagabhushana, “Investigations on dielectric behaviour of a new ecofriendly dielectric coolant for transformers,” in *International Conference on Emerging Research in Electronics, Computer Science and Technology, ICERECT, Mandya*, 2016, pp. 435–440.

[26] T. Circus, T. Way, and M. L. Universit, “The dielectric strength of 1,1,1,2-C2H2F4 (Arcton 134a),” *J. Phys. D Appl. Phys.*, vol. i, p. 74001, 2013.

[27] V. Champa, A. N. Nagashree, B. V. Sumangala, and G. R. Nagabhushana, “Breakdown Behaviour of New Bio-degradable Dielectric Coolants under 50Hz AC for Different Electrode Configurations,” *Mater. Today Proc.*, vol. 5, no. 1, pp. 3099–3108, 2018.

[28] United Nations Environment Programme (UNEP), “The Montreal protocol on substances that deplete the ozone layer.,” 2000.

[29] United Nations Framework Convention on Climate Change (UNFCC), “Kyoto Protocol Reference Manual,” 2008.

[30] R. Schneider, “F gases regulation (EU),” White Paper IE 9, 2017.

[31] 3M, “Material Safety Data Sheet FC-72 Fluorinert Brand Electronic Liquid.” .

[32] National-Refrigerants, “Refrigerant Reference Guide,” 2004.

[33] T. Makita, Y. Tanaka, Y. Morimoto, M. Noguchi, and H. Kubota, “Thermal conductivity of gaseous fluorocarbon refrigerants R 12, R 13, R 22, and R 23, under pressure,” *Int. J. Thermophys.*, vol. 2, no. 3, pp. 249–268, 1981.

[34] W. Jiang, G. Ding, H. Peng, Y. Gao, and K. Wang, “Experimental and Model Research on Nanorefrigerant Thermal Conductivity,” *HVAC&R Res.*, vol. 15, no. 3, pp. 651–669, 2009.

[35] Dupont, “Technical Information HCFC-123,” 2004.

[36] M. J. Assael and L. Karagiannidis, “Measurements of the thermal conductivity of liquid R32, R124, R125, and R141b,” *Int. J. Thermophys.*, vol. 16, no. 4, pp. 851–865, 1995.

[37] I. M. Mahbubul, S. a. Fadhilah, R. Saidur, K. Y. Leong, and M. a. Amalina, “Thermophysical properties and heat transfer performance of Al2O3/R-134a nanorefrigerants,” *Int. J. Heat Mass Transf.*, vol. 57, no. 1, pp. 100–108, 2013.

[38] M. Mohsen-Nia, H. Rasa, and S. F. Naghibi, “Experimental and theoretical study of surface tension of n-pentane, n-heptane, and some of their mixtures at different temperatures,” *J. Chem. Thermodyn.*, vol. 42, no. 1, pp. 110–113, 2010.

[39] 3M, “3M Hydrofluoroethers Material Safety Data Sheet,” vol. 4, no. 1, p. 5, 2005.

[40] 3M, “3M Fluorinated ketone Material Safety Data Sheet,” 2008.

[41] G. Zhao, S. Bi, A. P. Fröba, and J. Wu, “Liquid viscosity and surface tension of R1234yf and R1234ze under saturation conditions by surface light scattering,” *J. Chem. Eng. Data*, vol. 59, no. 4, pp. 1366–1371, 2014.

[42] S. Fink and M. Noe, “A facility for testing the dielectric strength of liquid nitrogen,” in *2008 IEEE International Conference on Dielectric Liquids, ICDL 2008*, 2008.

[43] M. S. B. Frank Kreith, *Principles of Heat Transfer*. West Publishing Company, 1993.

[44] A. Asai, “Application of the Nucleation Theory on the Design of Bubble Jet Printers,” *J. Appl. Phys.*, vol. 28, pp. 909–915, 1989.

[45] Y. F. Xue, J. F. Zhao, J. J. Wei, J. Li, D. Guo, and S. X. Wan, “Experimental study of nucleate pool boiling of FC-72 on smooth surface under microgravity,” *Microgravity Sci. Technol.*, vol. 23, pp. 75–85, 2011.

[46] A. Ma, J. Wei, M. Yuan, and J. Fang, “Enhanced flow boiling heat transfer of FC-72 on micro-pin-finned surfaces,” *Int. J. Heat Mass Transf.*, vol. 52, no. 13–14, pp. 2925–2931, 2009.

[47] E. Forrest, L. W. Hu, J. Buongiorno, and T. McKrell, “Pool Boiling Performance of Novec TM 649 Engineered Fluid,” in *ECI International Conference on Boiling Heat Transfer, Florianopolis*, 2009, vol. 1, p. 7.

[48] M. S. El-Genk and H. Bostanci, “Pool boiling experiments for HFE-7100 dielectric liquid,” in *Thermal Challenges in Next Generation Electronic Systems*, 2002, pp. 179–186.

[49] P.J. Berenson, “Experiments on Pool-Boiling Heat Transfer,” *Int. J. Heat Mass Transf.*, vol. 5, pp. 985–999, 1962.

[50] R. L. Webb, *Heat Transfer Engineering*, 2nd ed. Taylor & Francis, 1981.

[51] L. Ventola, F. Robotti, M. Dialameh, F. Calignano, D. Manfredi, E. Chiavazzo, and P. Asinari, “Rough surfaces with enhanced heat transfer for electronics cooling by direct metal laser sintering,” *Int. J. Heat Mass Transf.*, vol. 75, pp. 58–74, 2014.

[52] R. . Y. and R.L.Hummel, “Improved Nucleate Boiling Heat Transfer,” *Chem. Eng. Progress*, vol. 60, pp. 53–58, 1964.

[53] P. E. Tuma, “Fluoroketone C2F5C(O)CF(CF3)2 as a heat transfer fluid for passive and pumped 2-phase applications,” in *IEEE Semiconductor Thermal Measurement and Management Symposium*, 2008, pp. 173–179.

[54] P. E. Tuma, “Evaporator/boiler design for thermosyphons utilizing segregated hydrofluoroether working fluids,” in *IEEE Semiconductor Thermal Measurement And Management Symposium*, 2006, pp. 69–77.

[55] O. JUNJI and Y. AKIRA, “Augmentation of boiling heat transfer by utilizing the EHD effect—EHD behaviour of boiling bubbles and heat transfer characteristics,” *Int. J. Heat Mass Transf.*, vol. 36, no. 3, pp. 783–791, 1993.

[56] M. C. Zaghdoudi and M. Lallemand, “Nucleate Pool Boiling Under DC Electric Field,” *Exp. Heat Transf.*, vol. 14, no. 3, pp. 157–180, 2001.

[57] M. C. Zaghdoudi and M. Lallemand, “Study of the behaviour of a bubble in an electric field :,” *Int. J. Therm. Sci.*, vol. 0729, pp. 39–52, 2000.

[58] C. Chen, L. He, X. Li, and L. Fu, “Experimental investigation of nucleate boiling heat transfer enhanced by non-uniform electric field,” in *Conference on Electrical Insulation and Dielectric Phenomena*, 2007, pp. 554–557.

[59] Q. Z. Chuntian Chen, Jiaxiang Yang, “Study of EHD effect on enhanced condensation heat transfer of dielectric fluid,” in *IEEE International Symposium on Electrical Insulation*, 2004, no. September, pp. 19–22.

[60] S.-D. OH and H.-Y. KWAK, “A Study of Bubble Behavior and Boiling Heat Transfer Enhancement under Electric Field,” *Heat Transf. Eng.*, vol. 21, no. 4, pp. 33–45, 2000.

[61] M. R. Pearson and J. Seyed-Yagoobi, “EHD conduction-driven enhancement of critical heat flux in pool boiling,” *IEEE Trans. Ind. Appl.*, vol. 49, no. 4, pp. 1808–1816, 2013.

[62] T. B. Jones and K. R. Hallock, “Surface wave model of electrohydrodynamically coupled minimum film boiling,” *J. Electrostat.*, vol. 5, pp. 273–284, 1978.

[63] P. H. G. Allen and T. G. Karayiannist, “Electrohydrodynamic enhancement of heat transfer and fluid flow,” *Heat Recover. Syst. CHP*, vol. 15, no. 5, pp. 389–

423, 1995.

[64] Y. C. Kweon and M. H. Kim, “Experimental study on nucleate boiling enhancement and bubble dynamic behavior in saturated pool boiling using a nonuniform de electric field,” *Int. J. Multiph. Flow,* vol. 26, no. 8, pp. 1351–1368, 2000.

[65] J. OGATA and A. YABE, “Basic study on the enhancement of nucleate boiling heat transfer by applying electric fields,” *Int. J. Heat Mass Transf.*, vol. 36, no. 3, pp. 775–782, 1993.

[66] T. G. Karayiannis, “EHD boiling heat transfer enhancement of R123 and R11 on a tube bundle,” *Appl. Therm. Eng.*, vol. 18, no. 9–10, pp. 809–817, 1998.

[67] P. Wang, D. J. Swaffield, P. L. Lewin, and G. Chen, “The effect of an electric field on behaviour of thermally induced bubble in liquid nitrogen,” in *IEEE International Conference on Dielectric Liquids*, 2008, pp. 1–4.

[68] M. Boger, F. Jaegle, G. Lamanna, A. Ferrari, and C. Munz, “Numerical and Experimental Investigation of Droplets in a Compressible Regime,” 2010.

[69] P. H. G. Allen and T. G. Karayiannist, “Electrohydrodynamic Enhancement of Heat Transfer and Fluid Flow,” *Heat Recover. Syst. CHP*, vol. 15, no. 94, pp. 389–423, 1995.

[70] V. S. Vorob’ev, S. P. Malyshenko, and A. B. Petrin, “The field-trap effect under conditions of boiling of dielectric liquids in nonuniform electric fields,” *High Temp.*, vol. 43, no. 2, pp. 240–246, Mar. 2005.

[71] P. Wang, D. J. Swaffield, P. L. Lewin, and G. Chen, “Thermal Bubble Motion in Liquid Nitrogen under Non- uniform Electric Fields,” *IEEE Trans. Dielectr. Electr. Insul.*, vol. 15, pp. 626–634, 2008.

[72] K. Takano, F. Shimokawa, and M.Hara, “Thermal bubble-triggered breakdown under DC, AC and impulse nonuniform electric fields in liquid nitrogen.,” in *High Voltage Engineering Symposium*, 1999, pp. 128–131.

[73] D. Phenomena, T. P. Hang, P. E. Frayssinesl, and F. Aitken, “Influence of vapor bubbles initiated by steady heating on the breakdown of liquid nitrogen,” in *Annual Report Conference on Electrical Insulation and Dielectric Phenomena*, 2003, pp. 313–316.

[74] Y. C. Kweon, M. H. Kim, H. J. Cho, and I. S. Kang, “Study on the deformation and departure of a bubble attached to a wall in d.c./a.c. electric fields,” *Int. J. Multiph. Flow*, vol. 24, no. 1, pp. 145–162, 1998.

[75] K. Y. S. Kweon Y.C. of a bubble, Kim M.H., Cho H.J., “Study on the deformation and departure attached to a wall in DC/AC electric fields,” *Int. J. Multiph. Flow 24*, pp. 145–162, 1998.

[76] H. J. Cho, I. S. Kang, Y. C. Kweon, and M. H. Kim, “Study of the behavior of a bubble attached to a wall in a uniform electric field,” *Int. J. Multiph. Flow*, vol. 22, no. 5, pp. 909–922, 1996.

[77] V. Asch, “Electrokinetic Phenomena in Boiling ``Freon-113’’,” *J. Appl. Phys.*, vol. 2654, 1966.

[78] I. Kano and Y. Takahashi, "Effect of Electric Field Generated by Microsized Electrode on Pool Boiling," *IEEE Trans. Ind. Appl.*, vol. 49, no. 6, pp. 2382–2387, 2013.

[79] C. Chen, G. Lan, G. Zhang, and X. Zhang, "Electrohydrodynamic enhancement condensation of dielectric liquid on the horizontal enhanced tube," in *Conference on Electrical Insulation and Dielectric Phenomena*, 2009, pp. 185–187.

[80] I. Kano and N. Okamoto, "Experimental Verification of a Prediction Model for Pool Boiling Enhanced by the Electrohydrodynamic Effect and Surface Wettability," *J. Heat Transfer*, vol. 139, no. 8, p. 084501, 2017.

[81] S. W. Ahmad, T. G. Karayiannis, D. B. R. Kenning, and A. Luke, "Compound effect of EHD and surface roughness in pool boiling and CHF with R-123," *Appl. Therm. Eng.*, vol. 31, no. 11–12, pp. 1994–2003, 2011.

[82] R. S. Neve and Y. Y. Yan, "Enhancement of heat exchanger performance using combined electrohydrodynamic and passive methods," *Int. J. Heat Fluid Flow*, vol. 17, no. 4, pp. 403–409, 1996.

[83] P. Wang, "Thermal Bubble Behaviour in Liquid Nirorgen under Electric Field," University of Southampton, 2008.

[84] I. W. Eames and H. M. Sabir, "Potential benefits of electrohydrodynamic enhancement of two-phase heat transfer in the design of refrigeration systems," *Appl. Therm. Eng.*, vol. 17, no. 1, pp. 79–92, 1997.

[85] J. OGATA and A. YABE, "Augmentation of nucleate boiling heat transfer by applying electric fields," in *Thermal engineering joint conference*, 1991, pp. 1–6.

[86] Y. V. Martynov and T. G. Karayiannis, "No Effect of an electrostatic field on the boiling of a liquid film," *Theor. Found. Chem. Eng.*, vol. 31, no. 4, pp. 312–320, 1997.

[87] C. Damianidis, T. G. Karayiannis, A. Al-Dadah, R. W. James, M. W. Collins, and P. H. G. Allen, "EHD boiling enhancement in shell-and-tube evaporators and its application in refrigeration plants," *ASHRAE Trans.*, vol. 98, no. pt 2, pp. 462–472, 1992.

[88] C. P. Allen PHG, *The potential of electrically enhanced evaporators Third international symposium on the large scale application of heat pumps*. UK: Oxford, 1987.

[89] A. K. JALALUDDIN and D. B. SINHA, "Effect of an Electric Field on the Superheat of Liquids," *Indian Journ. Phys.*, vol. 35, no. 311, pp. 234–237, 1998.

[90] M. Markels and R. L. Durfee, "Studies of boiling heat transfer with electrical fields," *AICHE*, vol. 11, pp. 716–721, 1965.

[91] M. Markels and R. L. Durfee, "The effect of applied voltage on boiling heat transfer," *AICHE*, vol. 11, pp. 106–110, 1964.

[92] I. A. Budov, V.M. ; Kir'yanov, V.A. ; Shemagin, "Heat transfer in the laminar-wave section of condensation of a stationary vapor," *J. Eng. Phys*, vol. 52, pp.

647–648, 1987.

[93] I. Grigorveva and V. E. Nakoryakov, “Exact solution of combined heat and mass transfer problem during film absorption,” *J. Eng. Phys.*, vol. 33, no. 5, pp. 1349–1353, 1977.

[94] V. Penev, V. . Krylov, C. Boyadjiev, and V. P. Vorotilin, “Wavy flow of thin liquid films,” *Int. J. Heat Mass Transf.*, vol. 15, pp. 1395–1406, 1972.

[95] Y. Tanaka, S. Matsuo, T. Sotani, T. Kondo, and T. Matsuo, “Relative Permittivity and Resistivity of Liquid HFC Refrigerants Under High Pressure 1,” *Int. J. Thermophys.*, vol. 20, no. 1, pp. 107–117, 1999.

[96] a. P. C. Ribeiro and C. a. Nieto De Castro, “Dielectric properties of liquid refrigerants: Facts and trends,” *Int. J. Refrig.*, vol. 34, no. 2, pp. 393–401, 2011.

[97] BSI, “Insulating liquids-Measurement of relative permittivity, dielectric dissipation factor (tan δ) and d.c. resistivity,” BS 60247, 2004.

[98] A. P. Abbott, C. A. Eardley, and R. Tooth, “Relative Permittivity Measurements of 1,1,1,2-Tetrafluoroethane (HFC 134a), Pentafluoroethane (HFC 125), and Difluoromethane (HFC 32),” *J. Chem. Eng. Data*, vol. 44, pp. 112–115, 1999.

[99] E. T. Hoch, “Electrode Effects in the Measurement of Power Factor and Dielectric Constant of Sheet Insulating Materials,” *Bell Syst. Tech. J.*, vol. 5, no. 4, p. 555–572c, 1926.

[100] 3M Electronics Materials Solutions Division, “Heat transfer applications using 3M ^{TM} Novec ^{TM} Engineered Fluids,” 2015.

[101] W. Eltringham and O. J. Catchpole, “Relative permittivity measurements of trifluoromethyl methyl ether and pentafluoroethyl methyl ether,” *J. Chem. Eng. Data*, vol. 52, pp. 1095–1099, 2007.

[102] J. K. Nelson, M. a. Brubaker, and J. a. Palmer, “The formulation of models for the description of streaming electrification in transformer structures,” *IEEE Trans. Dielectr. Electr. Insul.*, vol. 10, no. 6, pp. 920–932, 2003.

[103] T. Judendorfer, A. Pirker, and M. Muhr, “Conductivity measurements of electrical insulating oils,” in *IEEE International Conference on Dielectric Liquids*, 2011, no. 4, pp. 4–7.

[104] F. Schober, A. Küchler, and C. Krause, “Oil Conductivity – An Important Quantity for the Design and the Condition Assessment of HVDC Insulation Systems,” *FHWS Sci. J.*, vol. 1, no. 2, pp. 59–79, 2013.

[105] E. R. Bartnikas, *Engineering Dielectric Volume III: Electrical Insulating Liquids*. Philadelphia: ASTM, 1994.

[106] B. Abedian and K. N. Baker, “Temperature effects on the electrical conductivity of dielectric liquids,” *IEEE Trans. Dielectr. Electr. Insul.*, vol. 15, no. 3, pp. 888–892, 2008.

[107] L. I. Huaqiang, Z. Lisheng, Y. U. Qinxue, Z. Xuhai, C. Xiangdong, and C. Xiaolong, “The Effect of Temperature and Field Strength on the Resistivity of Transformer Oil,” in *International Symposium on Electrical Insulating Materials (ISEIM)*, 2011, pp. 429–432.

[108] J. H. and O. Hestad, “Field and Temperature Dependent Conductivity of Syndiotactic Polypropylene,” in *Electrical Insulation Conference*, 2014, pp. 33–37.

[109] A. A. S. Akmal, H. Borsi, E. Gockenbach, V. Wasserberg, and H. Mohseni, “Dielectric behavior of insulating liquids at very low frequency,” *IEEE Trans. Dielectr. Electr. Insul.*, vol. 13, no. 3, pp. 532–538, 2006.

[110] IEC, “Insulating liquids— Determination of the dielectric dissipation factor by measurement of the conductance and capacitance — Test method,” Standard no. 61620, 1998.

[111] IEC, “Measurement of relative permittivity , dielectric dissipation factor and d.c. resistivity of insulating liquids,” BS 60247, 1999.

[112] G. Jones and R. C. Josephs, “The measurement of the conductance of electrolytes. I. An experimental and theoretical study of principles of design of the wheatstone bridge for use with alternating currents and an improved form of direct reading alternating current bridge,” *J. Am. Chem. Soc.*, vol. 50, no. 4, pp. 1049–1092, 1928.

[113] M. Zenker, “Influence of Temperature on DC Conductivity of Dry Electrical Pressboard Impregnated with Synthetic Ester,” in *IEEE International Conference on Nanomaterials: Applications and Properties (NAP)*, 2017, pp. 1–5.

[114] J. H. T. Ransley, S. H. Mennema, G. Burnell, U. Balasumbramaniam, E. J. Tarte, M. G. Blamire, J. E. Evetts, J. I. Kye, and B. Oh, “Y-Ba-Cu-O grain boundary resistivity above and below the critical temperature,” *IEEE Trans. Appl. Supercond.*, vol. 13, no. 2, pp. 2886–2889, 2003.

[115] U. Gafvert, A. Jaksts, C. Tornkvist, and L. Walfridsson, “Electrical field distribution in transformer oil,” *IEEE Trans. Electr. Insul.*, vol. 27, no. 3, pp. 647–660, 1992.

[116] J. Gerhold, “Liquid helium breakdown as function of temperature and electrode roughness,” *IEEE Trans. Dielectr. Electr. Insul.*, vol. 1, no. 3, p. 432, 1994.

[117] C. M. Osburn and E. J. Weitzman, “Electrical Conduction and Dielectric Breakdown in Silicon Dioxide Films on Silicon,” *J. Electrochem. Soc.*, vol. 119, no. 5, p. 603, 1972.

[118] BSI, “Insulating liquids - Determination of the breakdown voltage at power frequency - Test method,” BS 60156, 2012.

[119] Phenix technologies, “Phenix Dielectric Breakdown Test Model Brochure,” Basel, Switzerland, 2015.

[120] R. Kurnianto, M. Taufan, Z. Nawawi, M. Nagao, and N. Hozumi, “Breakdown Strength of Biodegradable Dielectric Liquid : The effect of temperature and viscosity,” in *Australasian Universities Power Engineering Conference (AUPEC)*, 2012.

[121] M. Jovalekic, S. Tenbohlen, C. Perrier, and J. Harthun, “Performance of alternative insulating liquids at low temperature,” in *4th ETG Conference*, 2013, vol. 3, no. 4, pp. 4–8.

[122] Suwarno, M. Ilyas, and Rubadi, “Effects of temperature on dielectric properties of rhicinnus oils as insulating liquid,” in *Condition Monitoring and Diagnosis*, 2008, pp. 286–289.

[123] S. Nishimachi, N. Hayakawa, H. Kojima, M. Hanai, and H. Okubo, “Pressure and Temperature Dependence of Breakdown Characteristics of Sub-Cooled Liquid Nitrogen,” in *Conference on Electrical Insulation and Dielectric Phenomena (CEIDP)*, 2012, pp. 440–443.

[124] A. A. Abdelmalik, J. C. Fothergill, and S. J. Dodd, “Electrical conduction and dielectric breakdown characteristics of alkyl ester dielectric fluids obtained from palm kernel oil,” *IEEE Trans. Dielectr. Electr. Insul.*, vol. 19, no. 5, pp. 1623–1632, 2012.

[125] J. Wu, P. Traore, C. Louste, L. Dascalescu, F. B. Tian, and A. T. Perez, “Numerical investigation of electrohydrodynamic plumes for locally enhanced cooling in dielectric liquids,” *IEEE Trans. Ind. Appl.*, vol. 51, no. 1, pp. 669–678, 2015.

[126] H. Sadek, “Electrohydrodynamic Control of Convective Condensation Heat Transfer and Pressure Drop in a Horizontal Annular Channel,” vol. 16, no. 2, 2009.

[127] M. Pearson and J. Seyed-Yagoobi, “Advances in electrohydrodynamic conduction pumping,” *IEEE Trans. Dielectr. Electr. Insul.*, vol. 16, no. 2, pp. 424–434, 2009.

[128] M. Hara and Z. Wang, “An Analytical Study of Bubble Motion in Liquid Nitrogen under D.C. Non-uniform Electric Fields,” in *International Conference on Properties and Applications of Dielectric Materials*, 1994, pp. 459–462.

[129] T. B. Jones and G. W. Bliss, “Bubble dielectrophoresis,” *J. Appl. Phys.*, vol. 48, no. 4, pp. 1412–1417, 1977.

[130] H. A.Pohl, *Dielectrophoresis*. Chapter 4, Cambridge University Press, 1978.

[131] G. P. Peterson, “An introduction to heat pipes. Modeling, testing, and applications.,” *Wiley Ser. Therm. Manag. Microelectron. Electron. Syst.*, vol. 1, p. 15, 1994.

[132] Cooper, P., and Allen, P.H.G., “The potential of electrically enhanced condensers,” in *International Symposium on the Large Scale Applications of Heat Pumps*, 1984, pp. 295–309.

[133] P. Wang, P. L. Lewin, D. J. Swaffield, and G. Chen, “Electric field effects on boiling heat transfer of liquid nitrogen,” *Cryogenics (Guildf).*, vol. 49, no. 8, pp. 379–389, 2009.

[134] S. Laohalertdecha, P. Naphon, and S. Wongwises, “A review of electrohydrodynamic enhancement of heat transfer,” *Renew. Sustain. Energy Rev.*, vol. 11, no. 5, pp. 858–876, 1962.

[135] S. Wu, R. D. Chippendale, and P. L. Lewin, “Dielectric properties of Environmental Friendly Cooling Fluids,” in *Electrical Insulation Conference, Montréal*, 2016, pp. 601–604.

[136] J. P. McHale and S. V. Garimella, “Bubble nucleation characteristics in pool boiling of a wetting liquid on smooth and rough surfaces,” *Int. J. Multiph. Flow*, vol. 36, no. 4, pp. 249–260, Apr. 2010.

[137] J. B. Campbell, L. M. Tolbert, S. Member, C. W. Ayers, B. Ozpineci, and K. T. Lowe, “Two-Phase Cooling Method Using the R134a Refrigerant to Cool Power Electronic Devices,” *IEEE Trans. Ind. Appl.*, vol. 43, no. 3, pp. 648–656, 2007.

[138] P. M. Carrica and V. Masson, “Electric Field Enhancement and Deterioration of Boiling Heat Transfer and Critical Heat Flux in Dielectric Fluids,” *J. Therm. Eng.*, vol. 1, pp. 32–40, 2001.

[139] F. Veiplaetsen and J. Berghmans, “Study of the influence of an electric field on the liquid-vapor interface during film boiling of stagnant fluids,” in *Industry Applications Conference*, 1996, pp. 1755–1761.

[140] M. C. Zaghdoudi and M. Lallemand, “Electric Field Effects on Pool Boiling,” *Enhanc. Heat Transf.*, vol. 9, pp. 187–208, 2002.

[141] R. W. Powell, R. P. Tye, and M. J. Hickman, “The thermal conductivity of nickel,” *Int. J. Heat Mass Transf.*, vol. 8, no. 5, pp. 679–688, 1965.

[142] J. J. Blalock, “Effects of Electric and Magnetic Fields on Moving Liquid Paint on a Glass Surface by Declaration of Authorship,” Londwood University, 2013.

[143] R. GARDON, “The Emissivity of Transparent Materials,” *J. Am. Ceram. Soc.*, vol. 39, no. 8, pp. 278–285, 2006.

[144] Y. Sun and C. Beckermann, “Diffuse interface modeling of two-phase flows based on averaging: Mass and momentum equations,” *Phys. D Nonlinear Phenom.*, vol. 198, no. 3–4, pp. 281–308, 2004.

[145] F. Agostini, M. Habert, F. Molitor, R. Flueckiger, L. Kaufmann, A. Bergamini, M. Rossi, and S. Besana, “Double-loop thermosyphon for electric components cooling,” *IEEE Trans. Components, Packag. Manuf. Technol.*, vol. 4, no. 2, pp. 223–231, 2014.

[146] T. Gradinger, F. Agostini, and D. Cottet, “Two-phase cooling of hot-swappable modular converters,” *PCIM Eur. Conf. Proc.*, no. May, pp. 1157–1164, 2014.

Appendix A Publications

Conference:

1. S. Wu, R. D. Chippendale, P. L. Lewin, J. Hemrle, and L. Kaufmann, "Numerical study into the breakdown strength of a two-phase (gas-liquid) insulation system," *33rd Electr. Insul. Conf. EIC 2015*, no. June, pp. 13–16, 2015.

2. S. Wu, R. D. Chippendale, and P. L. Lewin, "Dielectric properties of Environmental Friendly Cooling Fluids," in *Electrical Insulation Conference*, 2016, pp. 601–604.

3. S. Wu, R. D. Chippendale, P. L. Lewin, J. Hemrle, and L. Kaufmann, "Bubble motion in high voltage thermosyphon fluid under the non-uniform electric field," *2017 IEEE Electr. Insul. Conf. EIC 2017*, no. June, pp. 417–420, 2017.

4. S. Wu, R. D. Chippendale, P. L. Lewin, J. Hemrle, and L. Kaufmann, "Electrical field effects on Boiling heat transfer of low global warming potential coolant" 2018 *IEEE International conference on dielectrics. ICD 2018*

Journal:

1. S. Wu, R. D. Chippendale, P. L. Lewin, J. Hemrle, and L. Kaufmann, "Dielectric Properties of Thermosyphon Cooling fluids for High Voltage Generator Circuit Breakers" *IET Science Measurement & Technology*

Journal under review:

1. S. Wu, R. D. Chippendale, P. L. Lewin, J. Hemrle, and L. Kaufmann, "DC Electrical Field Effects on Boiling Heat Transfer of Low Global Warming Potential Thermosyphon Fluids" *Journal of Applied Thermal Engineering*

Appendix B Blueprint of Apparatus

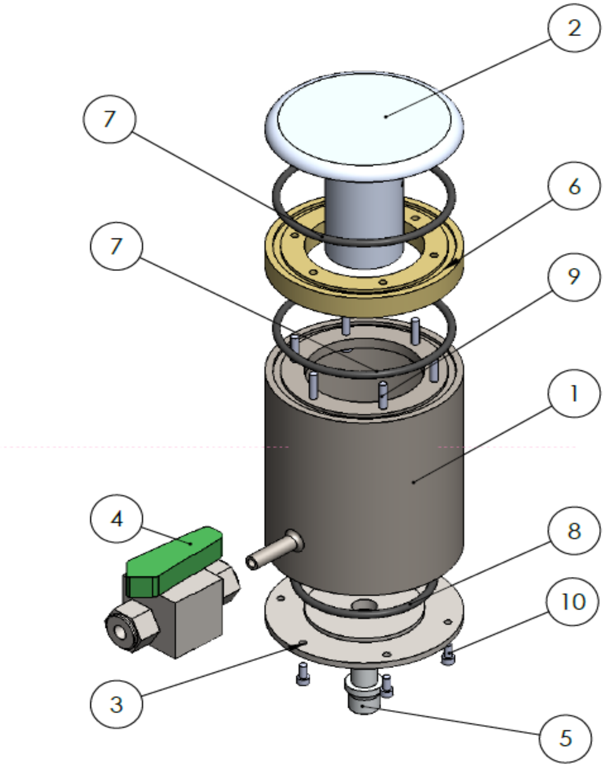

ITEM NO.	PART NUMBER	QTY.
1	Stainless steel base	1
2	Alminum Block	1
3	Bottom cap	1
4	Quarter turn valve	1
5	10 pins vacuum fitting	1
6	Peek Ring	1
7	O ring	2
8	O ring (small diameter)	1
9	Long M 3 bolt	6
10	Short M3 bolt	6

University of Southampton Tony Davies High Voltage Laboratory	Model Name: Bottom electrode exploded view	Date:30/05/2018	Third Projection
	Designer: Sijun Wu	Scale: 1:2	

B

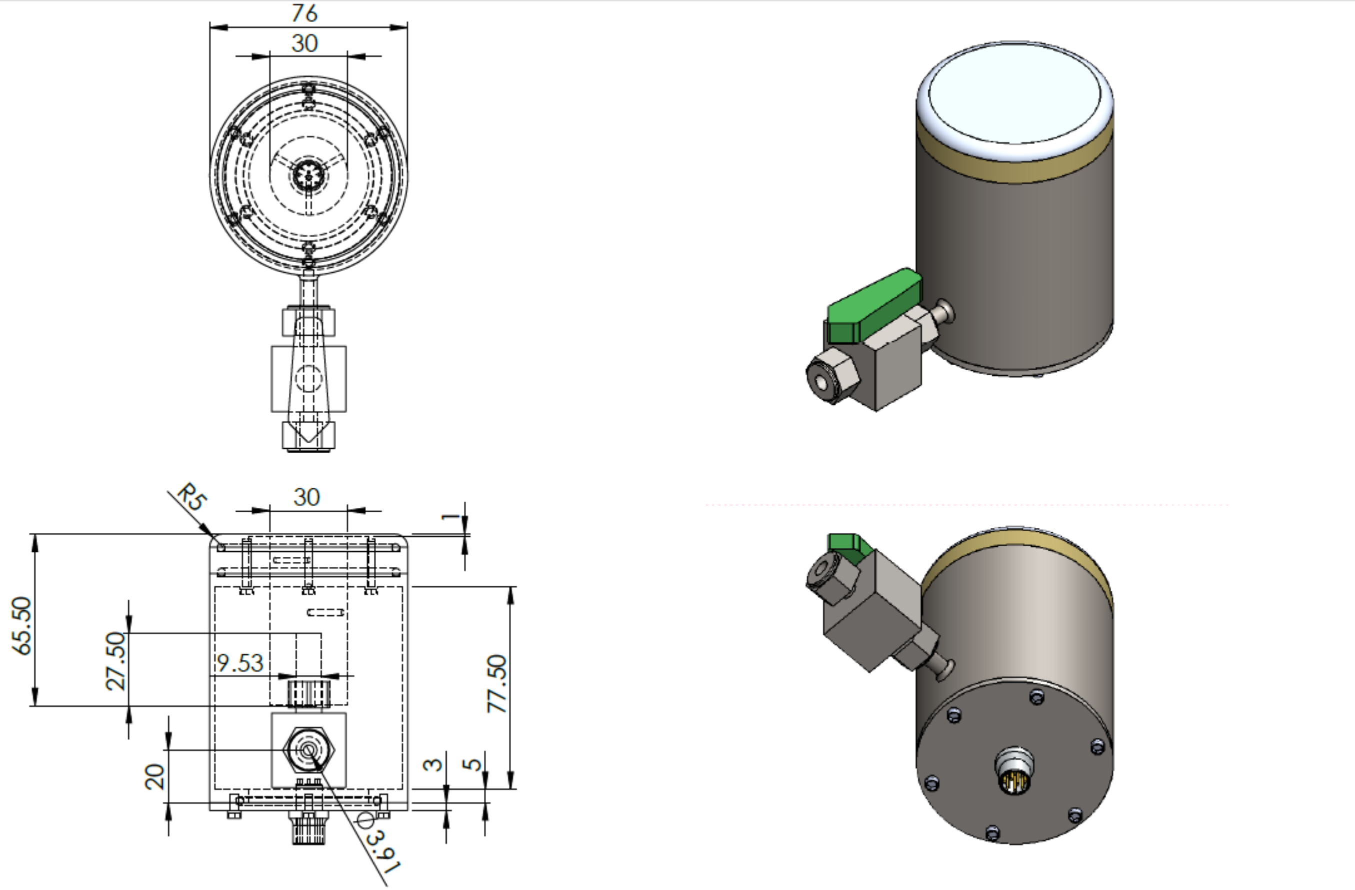

University of Southampton Tony Davies High Voltage Laboratory	Model Name:Bottom electrode	Date:30/05/2018	Third Projection
	Designer: Sijun Wu	Scale: 1:2	

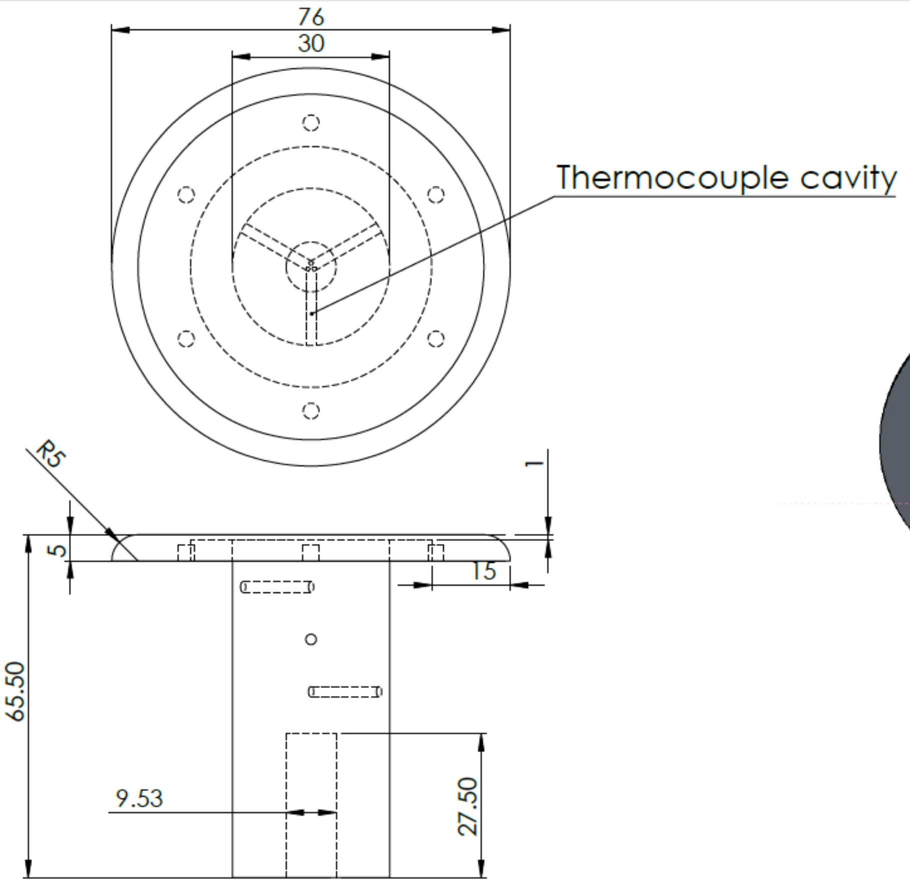

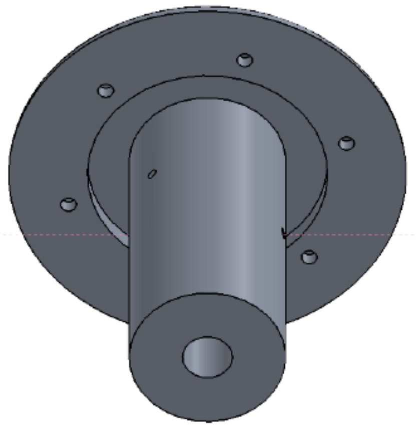

University of Southampton Tony Davies High Voltage Laboratory	Model Name:Aluminum block	Date:30/05/2018	Third Projection
	Designer: Sijun Wu	Scale: 1:1	

D

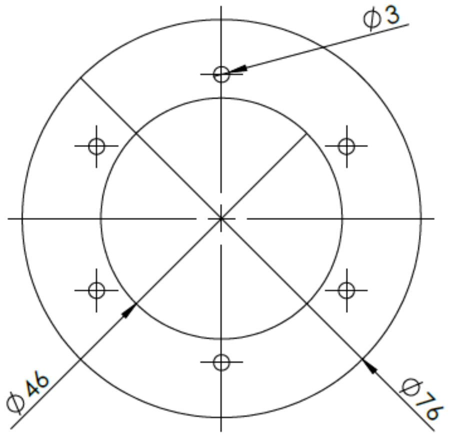

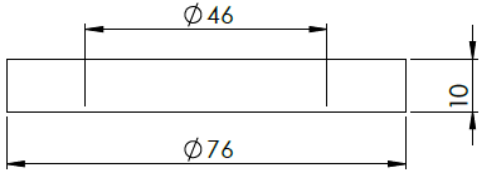

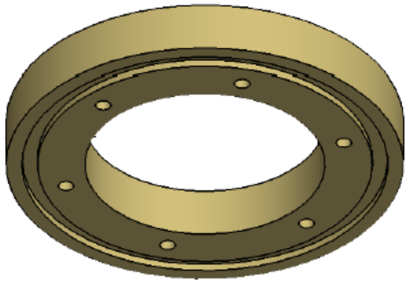

University of Southampton Tony Davies High Voltage Laboratory	Model Name:Peek Ring	Date:30/05/2018	Third Projection
	Designer: Sijun Wu	Scale: 1:1	

E

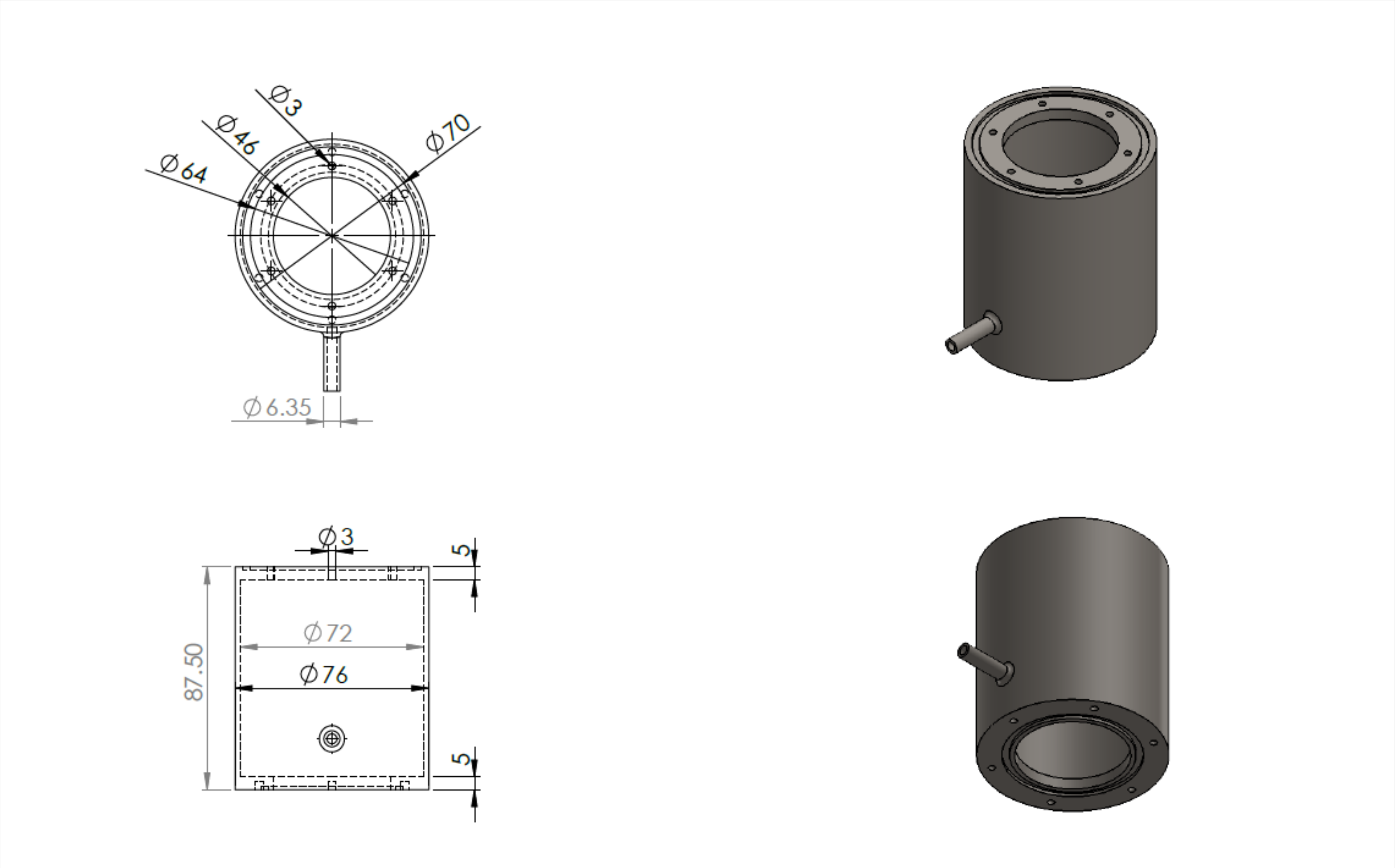

University of Southampton Tony Davies High Voltage Laboratory	Model Name:Stainless steel base	Date:30/05/2018	Third Projection
	Designer: Sijun Wu	Scale: 1:1	

F

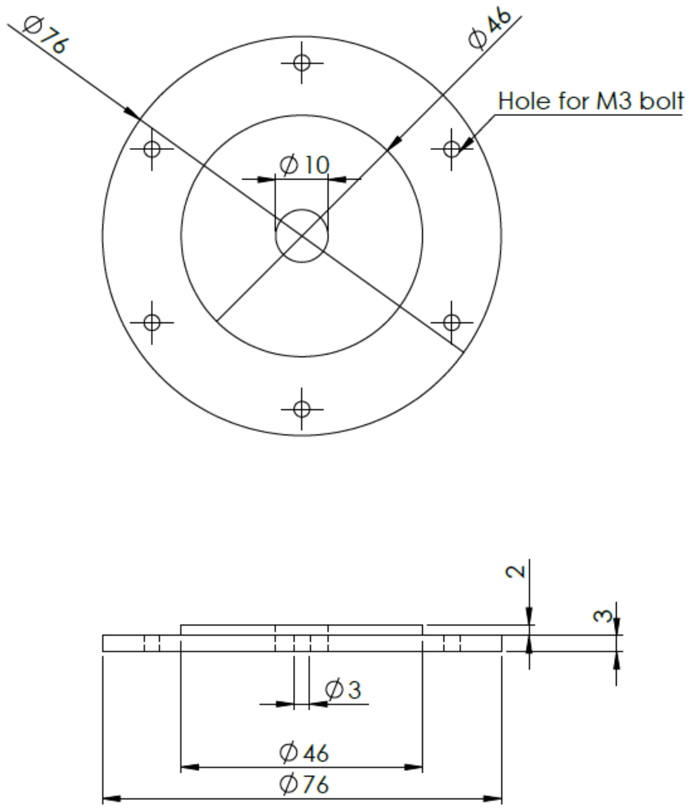

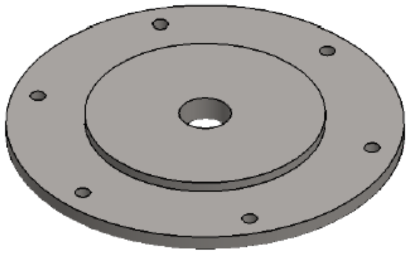

University of Southampton Tony Davies High Voltage Laboratory	Model Name:Bottom cap	Date:30/05/2018	Third Projection
	Designer: Sijun Wu	Scale: 1:1	

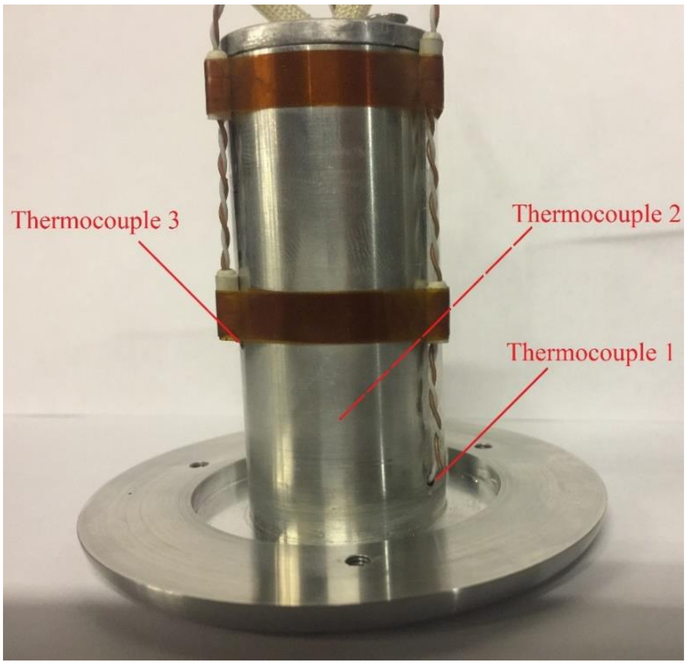

Figure i Aluminum Block

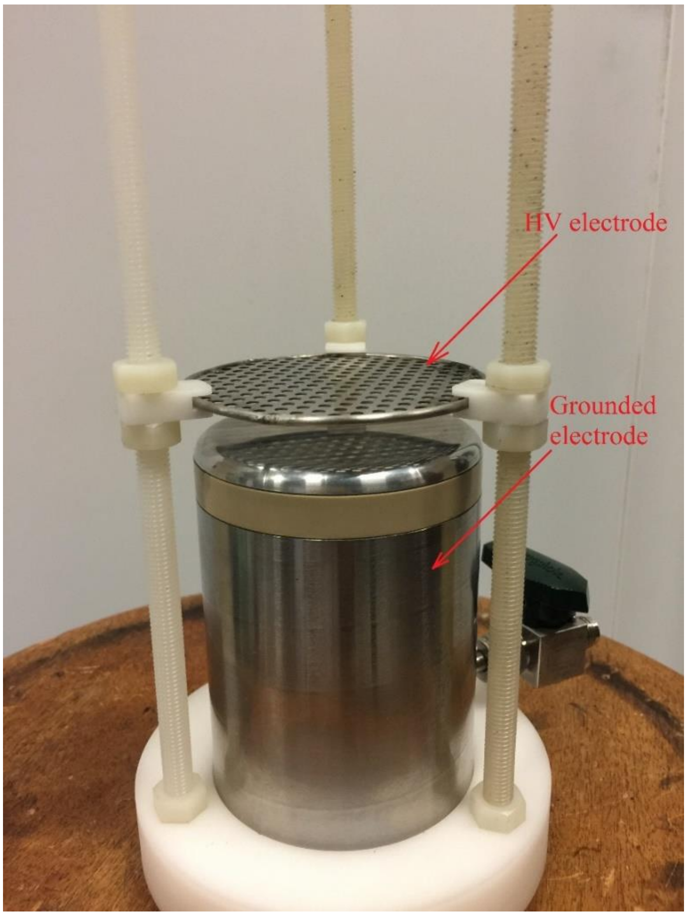

Figure ii Electrode System

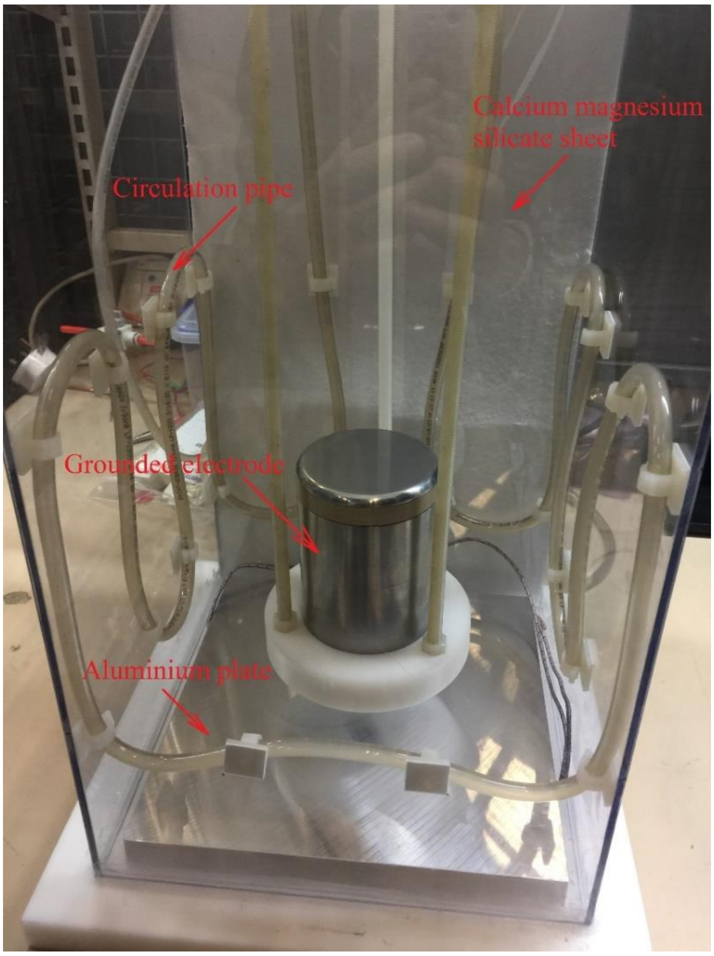

Figure iii Temperature Control System